



Showcasing research from Professor Su-Il In's laboratory,  
Department of Energy Science & Engineering, DGIST  
(Daegu Gyeongbuk Institute of Science and Technology),  
Daegu, Republic of Korea.

Solar fuels: research and development strategies to accelerate photocatalytic CO<sub>2</sub> conversion into hydrocarbon fuels

Climate change is an urgent issue requiring global cooperation, which is caused by the increased emission of CO<sub>2</sub> from fossil fuels usages. Solar-to-fuel conversion is a promising strategy to reduce atmospheric CO<sub>2</sub> concentration and produce eco-friendly fuels. In this article, we accomplish a comprehensive review of photocatalytic CO<sub>2</sub> conversion. We offer fundamentals, challenges, and important features of photocatalysts as well as provide future avenues for photocatalytic CO<sub>2</sub> reduction. In addition, economic and commercial viability is given to realize technology in the near future.

## As featured in:



See Su-Il In *et al.*,  
*Energy Environ. Sci.*, 2022, **15**, 880.



Cite this: *Energy Environ. Sci.*, 2022, 15, 880

## Solar fuels: research and development strategies to accelerate photocatalytic CO<sub>2</sub> conversion into hydrocarbon fuels

Eunhee Gong, † Shahzad Ali, Chaitanya B. Hiragond, Hong Soo Kim, † Niket S. Powar, Dongyun Kim, Hwapyong Kim and Su-Il In \*

Photocatalytic production of solar fuels from CO<sub>2</sub> is a promising strategy for addressing global environmental problems and securing future energy supplies. Although extensive research has been conducted to date, numerous impediments to realizing efficient, selective, and stable CO<sub>2</sub> reduction have yet to be overcome. This comprehensive review highlights the recent advances in CO<sub>2</sub> photoreduction, including critical challenges such as light-harvesting, charge separation, and the activation of CO<sub>2</sub> molecules. We present promising strategies for enhancing the photocatalytic activities and discuss theoretical insights and equations for quantifying photocatalytic performance, which are expected to afford a fundamental understanding of CO<sub>2</sub> photoreduction. We then provide a thorough overview of both traditional photocatalysts such as metal oxides and state-of-the-art catalysts such as metal-organic frameworks and 2D materials, followed by a discussion of the origin of carbon in CO<sub>2</sub> photoreduction as a means to further understand the reaction mechanism. Finally, we discuss the economic viability of photocatalytic CO<sub>2</sub> reduction before concluding the review with proposed future research directions.

Received 1st September 2021,  
Accepted 8th November 2021

DOI: 10.1039/d1ee02714j

rsc.li/ees

### Broader context

Research into CO<sub>2</sub> reduction has the potential to diminish our dependence on petroleum products and restrain global warming. Fossil fuels account for a large majority of global energy consumption, resulting in excessive emissions of CO<sub>2</sub> and other harmful gases. Furthermore, the current global economy and human society are heavily reliant on fossil fuels. Thus, there is an urgent need to develop renewable energy resources to generate energy and chemicals. Photocatalytic CO<sub>2</sub> reduction is one promising strategy for obtaining renewable energy and hydrocarbon fuels. However, we must first confront several challenges, such as limited light-harvesting and suboptimal photocatalytic activity. These challenges and potential solutions are the focus of the present review, alongside a discussion of our current theoretical understanding and consideration of the commercial/economic viability of CO<sub>2</sub> photoreduction technology.

Department of Energy Science & Engineering, Daegu Gyeongbuk Institute of Science and Technology (DGIST), 333 Techno Jungang-daero, Hyeonpung-eup, Dalseong-gun, Daegu 42988, Republic of Korea. E-mail: insuil@dgist.ac.kr, faraday.in@gmail.com

† These authors contributed equally to this work.



Eunhee Gong

Eunhee Gong received her BS degree in Fine Chemical Engineering from Chonnam National University, Republic of Korea, and her master's degree in Energy Science & Engineering from DGIST, Republic of Korea. She is currently a PhD candidate under the supervision of Professor Su-Il In at DGIST. Her current research is focused on the development of nanostructured materials for photocatalytic CO<sub>2</sub> conversion.



Shahzad Ali

Shahzad Ali received his BS and MS degrees in Chemical Engineering from COMSATS University Islamabad, Pakistan. He holds industrial and research experience related to power and renewable fuels and is currently a PhD candidate under the supervision of Professor Su-Il In at DGIST, Republic of Korea. His current research involves the development of economical systems and materials for photocatalytic CO<sub>2</sub> reduction.



## 1 Introduction

Global energy expenditure has skyrocketed in recent years, leading to the consumption of enormous amounts of fossil fuels such as coal, oil, and natural gas, which currently account for approximately 85% of primary energy supplies.<sup>1</sup> Fossil fuel combustion is associated with the excessive emission of harmful gases (e.g., CO<sub>2</sub>) that contribute to rising atmospheric temperatures, glacial melting, severe storms, ocean compositional changes, biodiversity loss, etc.<sup>2,3</sup> Therefore, global warming and its severe negative impacts on the earth have emerged as hotly discussed topics in recent decades. Over the past few years, the global average atmospheric CO<sub>2</sub> concentration has increased to over 410 ppm, which is approximately 45% higher than that prior to the Industrial Revolution.<sup>4,5</sup> According to the Intergovernmental Panel on Climate Change (IPCC), if this rate of CO<sub>2</sub> emission continues, atmospheric CO<sub>2</sub> levels will reach 590 ppm by 2100.<sup>6</sup> The IPCC proposed the goal of limiting the increase in global average temperature to within 1.5 °C of pre-industrial levels.<sup>7,8</sup> Thus, significant efforts have been undertaken worldwide to reduce atmospheric CO<sub>2</sub> emissions, such as the well-known Paris

Agreement under the United Nations Framework Convention on Climate Change (UNFCCC), in which more than 190 countries affirmed their commitment to decreasing CO<sub>2</sub> emissions.<sup>4,7</sup> There are three ways to control atmospheric CO<sub>2</sub>: (i) lowering CO<sub>2</sub> emissions, (ii) capture and storage, and (iii) converting it to value-added chemicals. One promising strategy for reducing CO<sub>2</sub> levels is using this waste product as a carbon feedstock to produce value-added compounds *via* catalytic reactions, opening the door to developing an artificial carbon cycle.<sup>9</sup> The potential of CO<sub>2</sub> to serve as a chemical feedstock has attracted considerable research attention in numerous fields, with a particular focus on photocatalytic,<sup>10–12</sup> biocatalytic,<sup>13,14</sup> electrochemical,<sup>15,16</sup> thermochemical,<sup>17,18</sup> and photothermal<sup>19,20</sup> CO<sub>2</sub> conversion.

With the aid of sunlight, plants capture CO<sub>2</sub> and convert it into various organic molecules (such as carbohydrates) and oxygen in a slow rate of chemical reaction known as “natural carbon fixation”.<sup>21</sup> Because CO<sub>2</sub> and water are both readily available on earth, their conversion into chemical fuels mediated by sunlight may provide an eco-friendly alternative to our present energy infrastructure.<sup>22</sup>



**Chaitanya B. Hiragond**

*Chaitanya B. Hiragond received his BS in Chemistry from Shivaji University, India, in 2012 and his MS in Organic Chemistry from Bharati Vidyapeeth Deemed University, India, in 2014. He is currently a PhD candidate under the supervision of Professor Su-Il In at DGIST, Republic of Korea. His current research focuses on developing photocatalytic materials for CO<sub>2</sub> conversion applications.*



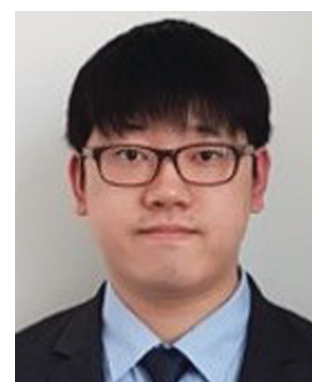
**Hong Soo Kim**

*Hong Soo Kim received his BS degree from Pusan National University in 2017. He is currently pursuing an integrated MS/PhD degree under the supervision of Professor Su-Il In at DGIST, Republic of Korea. His current research interests are focused on the electrical surface modification of electrode materials that can be used in a variety of applications.*



**Niket S. Powar**

*Niket S. Powar received his BS in chemistry and MS in Organic Chemistry from Shivaji University, India, in 2013 and 2015, respectively. He subsequently received his MTech in Nanotechnology and Renewable Energy at Amrita Vishwa Vidyapeetham University, India, in 2019. He is currently a PhD candidate under the supervision of Professor Su-Il In at DGIST, Republic of Korea. His current research interest lies in developing gas-phase photocatalysts for CO<sub>2</sub> photoreduction to generate value-added hydrocarbon products.*



**Dongyun Kim**

*Dongyun Kim received his BS degree from the Kumoh National Institute of Technology in 2019 and his MS degree from DGIST in 2021. He is currently working toward his PhD under the supervision of Professor Su-Il In at DGIST, Republic of Korea. His research interest is in the synthesis of photocatalysts for CO<sub>2</sub> conversion.*



Artificial photocatalysis under ambient conditions offers a promising alternative to thermocatalytic and electrochemical reactions, which are typically conducted at high temperatures and pressures or driven by an external electrical potential. In 1978, Halmann became the first to describe the conversion of  $\text{CO}_2$  into formic acid, formaldehyde, and methanol using an electrochemical cell with a GaP cathode under Hg arc lamp illumination.<sup>23</sup> Numerous attempts at  $\text{CO}_2$  photoconversion have subsequently been reported; nevertheless, significant problems remain with respect to activity and product selectivity owing to the inertness of  $\text{CO}_2$  molecules and the complexity of the process.<sup>24</sup>  $\text{CO}_2$  is a thermodynamically stable and chemically inert linear molecule, such that breaking the  $\text{C}=\text{O}$  bonds requires a substantial amount of energy to drive the process.<sup>25</sup> Furthermore, the reduction of  $\text{CO}_2$  with  $\text{H}_2\text{O}$  to form hydrocarbons, such as  $\text{CH}_4$ , is associated with a larger positive change in the Gibbs free energy ( $818.3 \text{ kJ mol}^{-1}$ ) than the conversion of  $\text{H}_2\text{O}$  into  $\text{H}_2$  and  $1/2\text{O}_2$  ( $232.2 \text{ kJ mol}^{-1}$ ) under ordinary conditions.<sup>25</sup> Although  $\text{CO}_2$  conversion is challenging, this waste product can be transformed into other value-added compounds by exploiting appropriate catalysts to overcome the kinetic and thermodynamic barriers and drive the process. In this respect, various photocatalytic materials, such as metal oxides, chalcogenides, carbon-based materials, metal complexes, metal-organic frameworks (MOFs), metal carbides, MXenes, polymers, perovskites, and plasmonic materials, have been frequently applied.<sup>4,26–32</sup>

In general, solar light harvesting, charge separation, and surface reaction are the crucial phases in effectively converting  $\text{CO}_2$  into chemical compounds such as  $\text{CO}$ ,  $\text{CH}_4$ ,  $\text{HCOOH}$ ,  $\text{HCHO}$ , and  $\text{CH}_3\text{OH}$ .<sup>33</sup> Possible reactions of  $\text{CO}_2$  reduction to various products and their standard redox potentials are listed in Table 1. A typical first step is single-electron transfer to  $\text{CO}_2$  to generate  $\text{CO}_2^{\bullet-}$  with a standard redox potential of  $-1.90 \text{ V}$  vs. normal hydrogen electrode (NHE), which is considered the rate-limiting step owing to its large energy requirement.<sup>2</sup> Although proton-assisted multi-electron processes require significantly lower potentials, suitable catalysts must be present to generate

**Table 1**  $\text{CO}_2$  reduction to various products and corresponding standard redox potentials vs. NHE (at pH 7)

Reaction	$E^0_{\text{redox vs. NHE (V)}}$	Main product	Eqn
$\text{CO}_2 + \text{e}^- \rightarrow \text{CO}_2^{\bullet-}$	-1.90	$\text{CO}_2^{\bullet-}$	(1)
$\text{CO}_2 + 2\text{H}^+ + 2\text{e}^- \rightarrow \text{CO} + \text{H}_2\text{O}$	-0.53	Carbon monoxide	(2)
$\text{CO}_2 + 2\text{H}^+ + 2\text{e}^- \rightarrow \text{HCOOH}$	-0.61	Formic acid	(3)
$\text{CO}_2 + 4\text{H}^+ + 4\text{e}^- \rightarrow \text{HCHO} + \text{H}_2\text{O}$	-0.48	Formaldehyde	(4)
$\text{CO}_2 + 6\text{H}^+ + 6\text{e}^- \rightarrow \text{CH}_3\text{OH} + \text{H}_2\text{O}$	-0.38	Methanol	(5)
$\text{CO}_2 + 8\text{H}^+ + 8\text{e}^- \rightarrow \text{CH}_4 + 2\text{H}_2\text{O}$	-0.24	Methane	(6)
$2\text{CO}_2 + 8\text{H}^+ + 8\text{e}^- \rightarrow \text{CH}_3\text{COOH} + 2\text{H}_2\text{O}$	-0.31	Acetic acid	(7)
$2\text{CO}_2 + 14\text{H}^+ + 14\text{e}^- \rightarrow \text{C}_2\text{H}_6 + 4\text{H}_2\text{O}$	-0.51	Ethane	(8)

the multiple electrons and protons needed to form the various products listed in Table 1.

Several challenges are associated with the aforementioned  $\text{CO}_2$  photoreduction that have impeded the wider application of photocatalytic technology. In particular, it is difficult to simultaneously realize both light absorption over a broad solar spectrum and reduction-oxidation processes using a single semiconducting material. First, wide-bandgap materials, such as  $\text{TiO}_2$ ,  $\text{ZnO}$ , and  $\text{CdS}$ , are primarily active in the ultraviolet (UV) region.<sup>28,34</sup> Second, although narrow-bandgap semiconductors such as  $\text{Cu}_2\text{O}$  are active in the visible–near-infrared (NIR) region,<sup>35</sup> their band potentials are unsuitable for simultaneously mediating reduction and oxidation reactions. Consequently, single-component systems have so far proved less satisfactory for photocatalysis, and numerous efforts have been made to overcome the tradeoff between these two beneficial properties of photocatalysts, such as through heterostructure formation.<sup>36</sup> Furthermore, spatial charge separation and charge transport from the catalyst surface to the reactants are important factors for reducing  $\text{CO}_2$ . However, it has been reported that the charge recombination process in semiconductors is faster than the surface redox process.<sup>37</sup> Charge recombination in semiconductors can often be attributed to Coulombic attraction, a lack of charge trapping states on the catalyst surface, *etc.*<sup>37,38</sup> Thus, if the charge carriers survive



*Hwapyong Kim received his BS degree from DGIST, Republic of Korea, in 2018. He is currently working toward his integrated MS/PhD degree under the supervision of Professor Su-Il In at DGIST. His current research interest lies in microbial fuel cells and catalysts for  $\text{CO}_2$  reduction/hydrogen evolution.*

**Hwapyong Kim**



**Su-Il In**

*Su-Il In is a professor at DGIST, Republic of Korea. He received his PhD in 2008 from the University of Cambridge, UK. He served as a postdoc at Technical University of Denmark and Penn State University (2008–2012) and later as a visiting scholar at the Department of Environmental Science & Engineering at Caltech, CA, USA (2019–2020). His current research interests are focused on energy and environmental issues, including photo/electrocatalytic  $\text{CO}_2$  conversion, betavoltaic cells, nano-bio hybrid technology, and microbial fuel cells.*



recombination, they can participate in the redox reaction. Charge separation, and interfacial charge separation in particular, can be enhanced by metal/non-metal doping, cocatalyst deposition, heterojunction formation, *etc.* Multicomponent systems have thus been constructed to restrict the recombination of electrons and holes. Apart from these issues, the amount of CO<sub>2</sub> adsorption on the catalyst surface greatly influences the catalytic performance. Catalysts with a large surface area provide more active sites for CO<sub>2</sub> adsorption. Meanwhile, the selectivity of photocatalytic CO<sub>2</sub> reduction is governed by a combination of known and unknown factors. CO<sub>2</sub> can be reduced to various products depending upon the availability of electrons (e<sup>-</sup>) and protons (H<sup>+</sup>) and the binding strength of the formed product.<sup>39</sup> Products with a greater binding strength can receive additional electrons and protons to form highly reduced products. This usually occurs for products arising from the partial reduction of CO<sub>2</sub>, *e.g.*, the transformation of CO to the highly reduced product CH<sub>4</sub>.<sup>40</sup> In addition to the variation in selectivity based on the degree of reduction, C-C coupling reactions are another crucial aspect governing the selectivity. In this case, the intermediate products, rather than desorbing, preferentially undergo coupling reactions, *e.g.*, •CH<sub>3</sub> radicals may couple to afford C<sub>2</sub>H<sub>6</sub>.<sup>5</sup> Under such circumstances, the optoelectronic and structural properties of the photocatalyst must both be considered during catalyst design for optimal selectivity. Furthermore, the stability of the photocatalyst is equally important, especially in terms of scale-up and catalyst reusability.<sup>41</sup> The major reported reason for catalyst instability is the strong oxidizing power of photogenerated holes, especially in the case of photocatalysts with a strong valence band (VB), such as TiO<sub>2</sub>.<sup>42</sup> These oxidizing holes or •OH radicals generated by water oxidation can oxidize the products/intermediates and photocatalyst metal atoms, leading to dramatically decreased photocatalytic yields.<sup>43,44</sup> Various strategies to overcome this issue have been explored, such as heterostructure formation and the use of hole scavengers.<sup>45,46</sup> However, these strategies have not yet been reported to provide prolonged stability. These approaches are one of the core subjects of the current review, with a particular focus on surface engineering, band alteration, heterojunction construction, and hybrid formation.

In addition to the aforementioned hurdles, the roles of the various reaction parameters have yet to be fully elucidated, despite numerous efforts during catalyst design. Factors such as reactor type, temperature, pressure, and light source can exert remarkable effects on catalytic activity and stability.<sup>47</sup> For example, in batch and flow reactors, the product yield may vary depending upon the reactant feed ratio, catalyst amount, flow rate, *etc.*<sup>47</sup> Furthermore, multi-sun system using a light concentrator affords enhanced photon flux, which can improve CO<sub>2</sub> conversion.<sup>48</sup> Evaluation of the catalytic activity in terms of efficiency and apparent quantum yield (AQY) is another critical consideration. Various parameters, such as reactor area, incident light, and collected light, should be factored into the efficiency calculation. As the catalytic yields described in the literature have been reported in a variety of units, such as ppm cm<sup>-2</sup> h<sup>-1</sup> and μmol g<sup>-1</sup> h<sup>-1</sup>, a fair comparison is required.<sup>47</sup> Here, we suggest the equation for fair comparison.

Next, understanding the complex reaction processes and mechanism of the CO<sub>2</sub> conversion process is vital, and quantitative isotopic measurements provide such a toolset for comprehending these aspects.<sup>49</sup> In conjunction with the analytical techniques of mass spectroscopy (MS) and nuclear magnetic resonance (NMR), which are frequently applied to study catalytic processes, isotopes, with their similar chemical properties, can help confirm the mechanism or product formation. For example, <sup>13</sup>C-labeled CO<sub>2</sub> and <sup>2</sup>H- or <sup>18</sup>O-labeled H<sub>2</sub>O are often used to investigate the processes of product formation, mitigating the influence of carbon impurities. Such mechanistic studies are also crucial for a comprehensive understanding of these processes.

In the past few years, research on photocatalytic CO<sub>2</sub> reduction has blossomed. Several review articles and perspectives have been published on the current status of photocatalytic CO<sub>2</sub> reduction, providing an overview of recent advances, material design, present challenges, potential solutions, and so on.<sup>4,24,31,39,50-55</sup> Fig. 1 shows the number of research papers and review articles published each year between 2010 and 2020 according to data collected from the Web of Science database on June 10, 2021, demonstrating that the scholarly community is becoming increasingly interested in this topic. Several international institutions have also been established that are providing valuable data for research and development efforts, such as the United Nations Environment Programme (UNEP),<sup>56</sup> the European Commission,<sup>56</sup> the Global Green Growth Institute (GGGI),<sup>56,57</sup> and the World Resources Institute (WRI).<sup>58</sup> In addition, several international conferences have been organized on a regular basis in recent decades, such as the International Conference on Carbon Dioxide Utilization (ICCDU)<sup>59,60</sup> and the International Conference on Greenhouse Gas Control Technologies (GHGT),<sup>61</sup> providing a forum for sharing and debating information on CO<sub>2</sub> emission, capture, and conversion to improve CO<sub>2</sub> reduction research and technologies. Furthermore, climate change has become a top priority for numerous government agencies, academic institutions, and technology companies. Therefore, we believe that

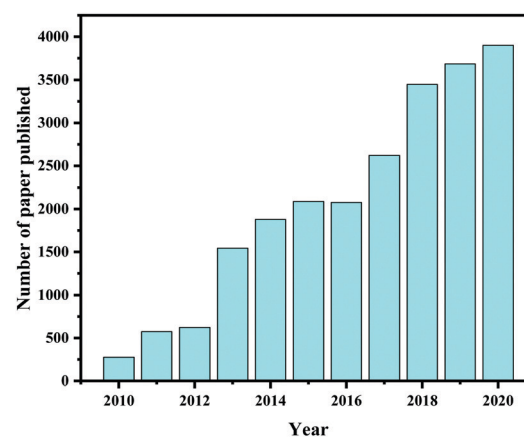


Fig. 1 The number of published articles on photocatalytic CO<sub>2</sub> conversion each year between 2010 and 2020, retrieved from the Web of Science database using the keywords (topic) of (photo\* or solar), (CO<sub>2</sub> or carbon dioxide), and (conversion or reduction) with several additional filters such as related field and journals.



CO<sub>2</sub> capture and conversion technology will continue to be a promising research topic in the coming decade.

Herein, we aim to provide a current overview of photocatalytic CO<sub>2</sub> conversion. The review begins with the fundamental aspects and key challenges of photocatalytic CO<sub>2</sub> reduction (Section 2) and then discusses the various strategies for overcoming these challenges (Section 3). Next, we summarize the performance of the various reported photocatalysts for CO<sub>2</sub> reduction and tabulate their activities and reaction parameters for quick understanding and evaluation (Section 5), after first providing a theoretical basis and the equations needed to calculate photocatalytic yields and efficiencies in a standardized manner (Section 4). We then discuss important insights into the nature of the carbon species involved in CO<sub>2</sub> photoreduction that has been gleaned from isotope labeling studies (Section 6). Next, we consider the commercial potential of photocatalytic CO<sub>2</sub> reduction based on current and future emission restrictions (Section 7). Finally, we propose likely future research directions based on our current understanding (Section 8). We believe that this review will serve as a valuable guide to researchers involved in the design and development of photocatalytic materials and systems.

## 2 Fundamentals and challenges of CO<sub>2</sub> photoreduction

The solar-light-driven conversion of the ubiquitous waste product CO<sub>2</sub> to chemical fuels in the gas phase has become a hot topic of research. Semiconductors are the most suitable materials for catalytic CO<sub>2</sub> conversion owing to their ability to simultaneously reduce CO<sub>2</sub> and oxidize H<sub>2</sub>O, and these materials play significant roles in all steps of the catalytic process, including adsorption, activation, dissociation, and product formation. Semiconductors possess two energy bands, namely, the VB, the highest energy band of occupied orbitals, and the conduction band (CB), the lowest energy band of vacant electronic states, which are separated by a quantum mechanically forbidden energy zone referred to as the bandgap ( $E_g$ ). When a semiconducting material is exposed to sunlight with an energy greater than or equal to the bandgap energy (*i.e.*,  $h\nu \geq E_g$ ), the electrons are excited from the VB to the CB, leaving behind holes in the VB (step I in Fig. 2).<sup>62</sup> The free electrons in the CB and holes in the VB transfer from the bulk to the catalyst surface (step II). Meanwhile, owing to the Coulombic force of attraction, a portion of the charges undergo recombination in the bulk before reaching the surface (step III). To complete the energy conversion process, the survived electrons and holes are transferred to surface-adsorbed CO<sub>2</sub> and H<sub>2</sub>O molecules, respectively, resulting in a simultaneous reduction–oxidation reaction to afford the solar fuel (step IV). To achieve the photon-induced uphill CO<sub>2</sub> conversion, the CB of the semiconductor should be more negative than the reduction potential of CO<sub>2</sub>, while the VB should be more positive than the oxidation potential of H<sub>2</sub>O. Because the recombination of electrons and holes is much faster than the process of charge transfer and consumption at

the catalyst interface, the lifetime of the photoexcited electrons must be sufficiently long for completion of the redox reaction. Higher photogenerated electron density at catalyst surfaces can be realized by the active separation of electrons and holes, which can robustly accelerate the rate of a redox reaction, leading to faster hydrocarbon production.<sup>39</sup> In addition, the characteristic features of the catalyst govern the product selectivity and catalyst stability; depending upon the reduction potential of the material, number of available electrons, active sites, adsorption of the intermediates, and various other factors (*e.g.*, gas or liquid phase, reaction conditions CO<sub>2</sub> in the presence of H<sub>2</sub>O), the CO<sub>2</sub> in the presence of H<sub>2</sub>O can be converted into a variety of products, such as CO, CH<sub>4</sub>, and C<sub>2</sub>H<sub>6</sub>. An effective catalyst (i) provides maximum solar light absorption to generate electrons and holes, (ii) contains sufficient active sites for CO<sub>2</sub> adsorption on its surface, and (iii) efficiently generates electron–hole pairs and mediates their migration to the catalyst surface. Numerous earlier studies focused on these factors in an effort to improve the catalytic performance of CO<sub>2</sub> reduction using various types of catalysts and different reaction conditions. However, because the reduction process entails several complex steps, it is not as straightforward as it may initially appear, with particular challenges being (i) limited light absorption, (ii) charge recombination, (iii) adsorption/activation of CO<sub>2</sub> molecules, (iv) photostability of the catalyst materials, (v) development of a facile and reasonable synthetic process, and (vi) underlying mechanism/C<sub>1</sub> and C<sub>2</sub> selectivity (Fig. 2). We will briefly discuss these challenges of photocatalytic CO<sub>2</sub> conversion in the remainder of this section.

### 2.1 Limited light absorption

The critical processes in CO<sub>2</sub> photoreduction reactions are (i) the formation of charge carriers through light absorption and electron excitation and (ii) the reaction of surface electrons with CO<sub>2</sub> molecules. As previously discussed, the electronic band structure of the catalyst is a crucial factor in light-driven CO<sub>2</sub> conversion, where a catalyst with appropriate redox potentials is required to drive the process smoothly from a thermodynamic standpoint. As depicted in Fig. 3, various semiconducting materials have been explored for this purpose.<sup>63–66</sup>

The solar spectrum comprises approximately 5% UV radiation, 43% visible radiation, and 52% infrared (IR) radiation; clearly, the visible and IR regions account for the majority. Thus, catalysts that primarily absorb visible/IR light can be expected to produce the maximum amount of charge to mediate the desired reaction. However, most of the commonly used semiconductors possess unsuitable bandgaps or band potentials to absorb sufficient sunlight for driving the process toward product formation. Although the band potentials of wide-bandgap semiconductors are suitable for mediating the redox process, they are only active in the shorter wavelength region. For example, TiO<sub>2</sub> is the most commonly applied semiconductor in this process; however, its wide bandgap (3.2 eV) limits light absorption to the UV region ( $\lambda = 390$  nm) and pristine TiO<sub>2</sub> is inactive with respect to visible-light-induced CO<sub>2</sub> conversion.

Various strategies have been investigated in an effort to overcome the limited light absorption ability of TiO<sub>2</sub>, which



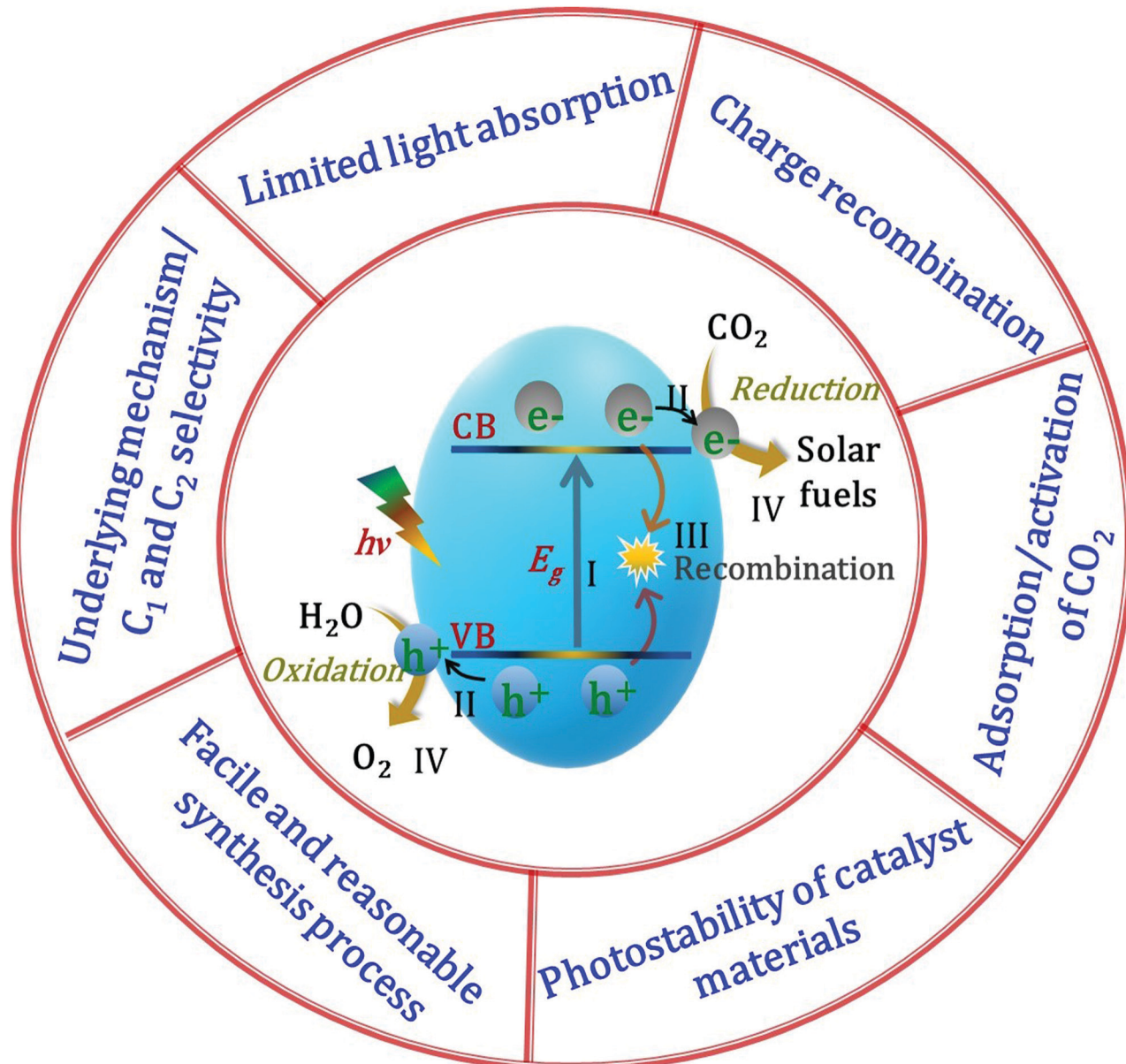


Fig. 2 Schematic illustration and challenges of the photocatalytic  $\text{CO}_2$  conversion process.

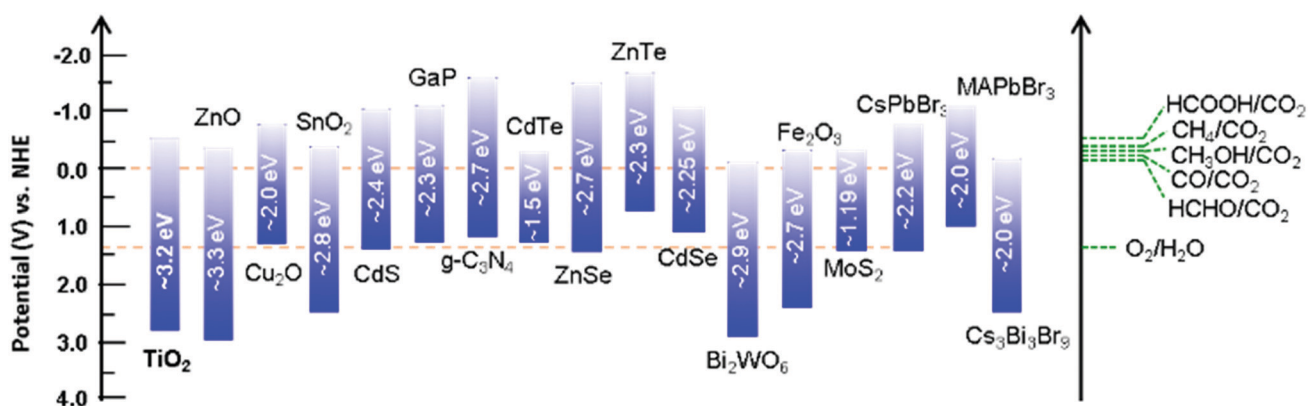


Fig. 3 Band potentials and corresponding bandgap energies of various selected photocatalysts relative to the redox potential involved in  $\text{CO}_2$  photoreduction to various products.

will be discussed in greater detail in the following sections (Section 5.1). Some narrow-bandgap semiconductors displaying strong light absorption in the visible region have been reported to convert  $\text{CO}_2$  into solar fuels; however, such a small bandgap inevitably leads to the simultaneous occurrence of reduction and oxidation processes on the surface and fast charge recombination, such that sacrificial agents are required to scavenge the holes.<sup>67</sup> For example,  $\text{Cu}_2\text{O}$  is a promising catalyst for  $\text{CO}_2$  conversion owing to its narrow bandgap (*ca.* 2.2 eV), which affords efficient photon absorption in the visible region of the solar spectrum. However, this narrow bandgap also causes rapid recombination of photogenerated charges, meaning that pristine  $\text{Cu}_2\text{O}$  still exhibits poor catalytic performance; in addition, the holes cause  $\text{Cu}_2\text{O}$  to self-oxidize, reducing its photostability.<sup>68</sup> Thus, by combining a narrow-bandgap material with a wide-bandgap semiconductor, light absorption in both the UV and visible regions can be effectively increased; such combinations have been widely documented in the literature.<sup>43,68</sup>

Another viable strategy for improving the photoconversion performance of photocatalysts is broadening their light absorption capability in the IR/NIR region;<sup>31</sup> however, few such catalysts have so far been reported, with the exception of  $\text{WO}_3$ ,<sup>67</sup>  $\text{B}_{13}\text{P}_2$ ,<sup>69</sup> *etc.* The real challenge associated with absorption in the NIR region is its low photonic energy, which can only provide low redox potentials in semiconductors.<sup>70</sup> However, considering current trends in nanotechnology, it is anticipated that NIR-active materials displaying superior catalytic properties to conventional semiconductors will ultimately be developed. Therefore, the primary challenge with respect to light absorption is developing catalysts that can function over a wide range of the solar spectrum including the UV, visible, and NIR regions.

## 2.2 Charge recombination

In photocatalytic  $\text{CO}_2$  conversion on semiconductors, stable charge separation on the catalyst surface plays a critical role in converting  $\text{CO}_2$  into value-added products. The relatively low quantum efficiency of most reported photocatalysts can be attributed to the occurrence of charge recombination before the surface reactions of electrons and holes with  $\text{CO}_2$  and water.<sup>71</sup> Thus, slow recombination or fast charge separation of the photoexcited carriers is a key factor in improving solar fuel production *via*  $\text{CO}_2$  reduction. Although electrons and holes are separated through the CB and VB, respectively, this process is quite tricky owing to the Coulombic force of attraction between the two species; Durrant and co-workers have demonstrated such recombination in organic solar cells.<sup>72</sup> Because there is no driving force to drag the bound electrons and holes apart in pristine semiconductors, they are vulnerable to recombination, which hinders their participation in surface redox reactions.<sup>73</sup> Moreover, the non-radiative relaxation of excited electrons to the ground state causes electron–hole recombination on the nanosecond timescale. In contrast, electron transfer at the semiconductor interface is typically two or three orders of magnitude slower than the electron–hole recombination rate. Consequently, the charge dynamics at the surface of semiconductors determine the rate of surface redox reactions and play

a crucial role in photocatalytic  $\text{CO}_2$  reduction. Charge recombination can interfere with charge separation and interfacial charge transfer, making it one of the main limiting factors in the solar-to-energy conversion process.<sup>71</sup> Recombination can occur both in the bulk and on the surface of the catalyst. In general, the charge carrier mobility is closely related to the distance from the bulk to the surface, which determines the rate of bulk recombination, while surface recombination can be caused by the absence of sufficient active sites or trapping states on the catalyst surface. As a result, catalysts with efficient charge separation and high intrinsic mobility can prevent recombination. To improve charge separation, nanoengineered materials have been explored that significantly reduce the distance between the point of charge generation and the catalyst surface.

Nanostructured semiconductors, because of their high surface-area-to-volume ratio, short charge migration distance, and tunable electronic properties, possess numerous advantages over their bulk counterparts for photocatalysis.<sup>74</sup> Previous studies have revealed that the characteristics of a catalyst, such as morphology, crystal structure, and particle size, effectively determine the rates of charge transport and recombination.<sup>75,76</sup> The morphology of a catalyst can significantly affect the charge carrier dynamics. For example, because of increased charge separation, 1D nanostructured  $\text{TiO}_2$  materials such as nanotubes, nanofibers, and nanorods exhibit far superior catalytic activity to  $\text{TiO}_2$  nanoparticles.<sup>77–79</sup> The distance between the point of charge generation and the catalyst interface can also be reduced using 1D nanostructures. Durrant and co-workers performed an interesting study on the relationship between charge recombination and the crystal phase using transient absorption spectroscopy (TAS), which elucidated the charge carrier dynamics in  $\text{TiO}_2$ .<sup>38</sup> The authors compared mesoporous  $\text{TiO}_2$  nanostructures (with a size of 20 nm) and bulk  $\text{TiO}_2$  (with a size of 50–200 nm) and found that the photogenerated charge carriers produced in the former easily reached the surface, whereas those in the latter did not and remained in the bulk. However, the results also revealed that nanostructuring did not improve the recombination rates, indicating that surface-state-mediated recombination is not a key pathway in the case of  $\text{TiO}_2$ . Instead, charge recombination was dependent on the crystal phase of  $\text{TiO}_2$ , as demonstrated by the rapid charge recombination in rutile  $\text{TiO}_2$  and superior charge separation capacity over time in anatase  $\text{TiO}_2$ . Similarly, Maity *et al.* analyzed the bulk charge carrier dynamics in single crystals of rutile and anatase  $\text{TiO}_2$  and discovered that the anatase phase exhibited a slower recombination rate than the rutile phase.<sup>80</sup> Various strategies have been explored over the years to avoid such recombination, including defect formation, doping with metals or non-metals, cocatalyst deposition, heterojunction formation, *etc.* For instance, a number of studies have demonstrated that the deposition of plasmonic nanoparticles (*e.g.*, Au, Ag, Pt) onto semiconductors can reduce charge recombination by creating a Schottky barrier, resulting in an increased excitons lifetime.<sup>81</sup>

## 2.3 Adsorption/activation of $\text{CO}_2$

As is well known,  $\text{CO}_2$  is a thermodynamically stable molecule with linear geometry; therefore, its reduction is challenging. However, it can be transformed into other value-added compounds under



appropriate conditions. In this respect, the adsorption and activation of  $\text{CO}_2$  molecules on catalyst surfaces are the critical kinetic factors in producing solar fuels. There are four key steps in this process: (i) adsorption of  $\text{CO}_2$  molecules on the catalyst surface, (ii) activation of the  $\text{CO}_2$  molecules to form partially charged  $\text{CO}_2^{\bullet-}$  anion radicals or intermediates, (iii)  $\text{C}=\text{O}$  bond dissociation to afford another chemical product after reaction with an electron and a proton, and (iv) desorption of the newly formed product from the catalyst surface.<sup>82</sup> Zou and co-workers described the possible configurations for the adsorption of  $\text{CO}_2$  molecules on

a catalyst surface (Fig. 4(a)).<sup>65</sup> For most metal oxides and sulfides, the C or O atoms of  $\text{CO}_2$  form weak bonds to single metal sites by hybridization of the 2p and 3d orbitals to generate intermediate products.<sup>83</sup> Compared to the highly stable  $\text{C}=\text{O}$  bonds of  $\text{CO}_2$ , the weak M-O or M-C bonds can be readily cleaved, enabling the formation of CO or higher hydrocarbons (after protonation). Moreover, the nature of the binding of  $\text{CO}_2$  molecules on the catalyst surface determines the activity and selectivity of the catalytic reaction. For example, in the case of  $\text{TiO}_2$ , several studies have shown that the binding energy of  $\text{CO}_2$  on a rutile surface

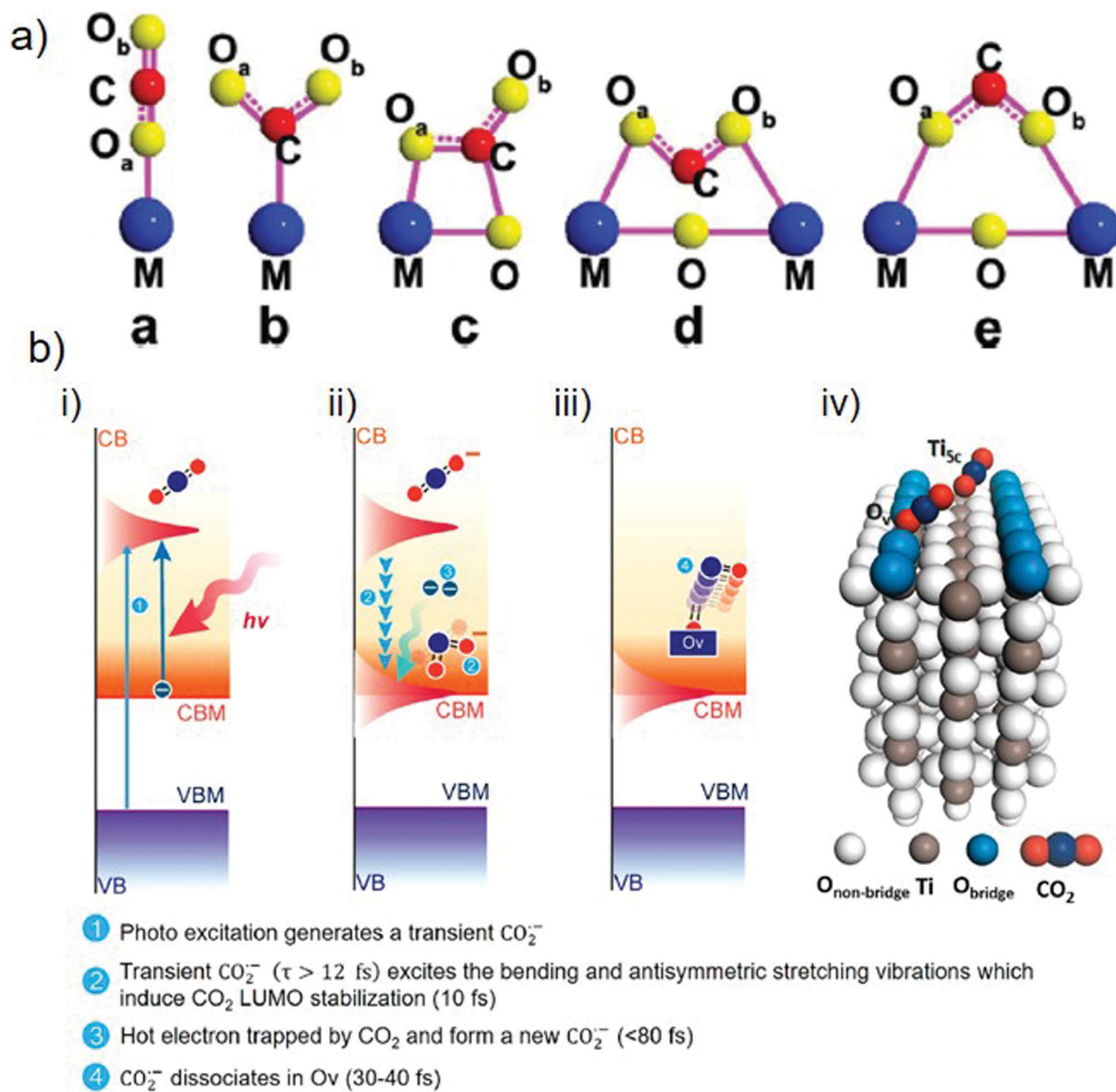


Fig. 4 (a) Various configurations of adsorbed  $\text{CO}_2$  molecules on a photocatalyst surface. Reproduced with permission from ref. 65, Copyright 2020, American Chemical Society. (b) Photocatalytic  $\text{CO}_2$  reduction over a  $\text{TiO}_2(110)$  surface showing the adsorption and activation of a  $\text{CO}_2$  molecule: (i)–(iii) stepwise activation of a  $\text{CO}_2$  molecule over time and (iv) adsorption of  $\text{CO}_2$  molecules at  $\text{O}_v$  and  $\text{Ti}_{5c}$  sites. Reproduced with permission from ref. 82, Copyright 2020, American Chemical Society.



is  $-0.34$  eV, while it increases to  $-1.08$  eV on defective  $\text{TiO}_2$ .<sup>84</sup> Therefore, defective  $\text{TiO}_2$  with oxygen vacancies or  $\text{Ti}^{3+}$  states offers more binding sites for  $\text{CO}_2$  molecules, which act as active sites for the desired reaction.

The activation of  $\text{CO}_2$  molecules is a vital step in the photocatalytic  $\text{CO}_2$  reduction process. Chu *et al.* used time-dependent *ab initio* simulations (nonadiabatic molecular dynamics (NAMD)) to investigate the activation of  $\text{CO}_2$  molecules on the surface of rutile  $\text{TiO}_2(110)$ .<sup>82</sup> According to the findings, once the electrons have been excited from the VB to the CB of  $\text{TiO}_2$ , the addition of an electron to the LUMO of the  $\text{CO}_2$  molecule results in the formation of a transient  $\text{CO}_2^{\bullet-}$  anion radical possessing a bent geometry (step 1, Fig. 4(b)-(i)). This bending originates from the repulsion between the free electrons of the oxygen atom and the added electron. If  $\text{CO}_2^{\bullet-}$  has a lifespan of more than 12 fs, with the help of oxygen vacancy, the excitation of vibrational modes (bending and antisymmetric stretching) will stabilize the LUMO of the  $\text{CO}_2$  molecules to below the conduction band minimum (CBM) of the catalyst within 10 fs (step 2, Fig. 4(b)-(ii)). This form of electronic state alignment can persist for more than 100 fs. Within a timescale of 80 fs,  $\text{CO}_2$  captures the electrons present on the catalyst surface (step 3, Fig. 4(b)-(ii)) and can subsequently dissociate to afford the product (*i.e.*, CO) within 30–40 fs after the trapping of the electrons (step 4, Fig. 4(b)-(iii)). Because the  $\text{Ti}_{5c}$  sites have lower adsorption energies for binding  $\text{CO}_2$  molecules, the results indicate that the association of  $\text{CO}_2$  with oxygen vacancies is more favorable for the excitation of the antisymmetric stretching mode (Fig. 4(b)-(iv)). The formation of products can differ according to the available electrons and protons participating in the chemical reaction.

Poor  $\text{CO}_2$  adsorption decreases the amount of  $\text{CO}_2$  available for the reduction. Hence, the efficiency of  $\text{CO}_2$  reduction can be significantly improved by enhancing  $\text{CO}_2$  adsorption on the catalyst surface. In addition to oxygen vacancies, as discussed above, surface functionalization of catalysts with hydroxyl ( $\text{OH}$ ) or amino ( $\text{NH}_2$ ) groups can increase  $\text{CO}_2$  adsorption. These functional groups are most likely to donate electrons to  $\text{CO}_2$  molecules, resulting in negatively charged  $\text{HCO}_2^{\delta-}$  species that enhance  $\text{CO}_2$  adsorption.<sup>85</sup> Increased  $\text{CO}_2$  adsorption ability has also been realized using catalysts with a large surface area, which provides more active sites for the catalytic reaction. Hiragond *et al.* reported hierarchical nanostructures that displayed increased  $\text{CO}_2$  adsorption owing to their unique structures and surface morphologies, including nanofibers, nanotubes/rods, nanosheets, nanoflowers, *etc.*<sup>86</sup> The deposition of alkali or alkaline-earth metals with a greater affinity toward acidic  $\text{CO}_2$  molecules on catalyst surfaces can also promote the adsorption of  $\text{CO}_2$  on photocatalysts.<sup>48</sup>

#### 2.4 Photostability of catalyst materials

Although several solar-active catalysts displaying significant activity for  $\text{CO}_2$  photoreduction have been reported, most of them suffer from instability. Therefore, photocatalyst stability is a major issue that has severely hampered the practical application of these catalysts. Photocatalyst instability may

originate from a number of sources, including transitions from active to inactive photocatalytic oxidation states, buildup of reaction intermediates that are difficult to reduce, oxidation of the products, and morphological changes.<sup>42,87</sup> In addition, reverse reactions may also play a role. For example, Punchihewa and co-workers observed the photoreduction of  $\text{CO}_2$  to formaldehyde and methanol in high yield after 30–45 min; however, the activity decreased after a specific time.<sup>88</sup> This decreased activity was caused by a hole-mediated back-reaction that was faster than the  $\text{CO}_2$  reduction.

Under light irradiation, equal amounts of electrons and holes should be formed on the catalyst; however, these electrons and holes may cause photocorrosion due to reduction or oxidation of the catalyst itself. For example, Xu and co-workers reported the degradation of  $\text{CdS}$  by photogenerated holes. Changes in the oxidation state typically occur when the redox potential of a photocatalyst lies within its bandgap, whereupon the photogenerated electrons and holes can reduce or oxidize the photocatalyst. In the case of  $\text{Cu}_2\text{O}$ , the holes were reported to have insufficient oxidizing ability for water oxidation and therefore preferentially oxidized  $\text{Cu}_2\text{O}$ , resulting in loss of the active oxidation state.<sup>44</sup> Similarly, inefficient utilization of the electrons for photocatalytic  $\text{CO}_2$  reduction led to the reduction of  $\text{Cu}_2\text{O}$  to  $\text{Cu}$ . In addition, some photocatalysts have very strong oxidizing power, resulting in the generation of active hydroxyl radicals from water, which can subsequently oxidize the intermediates of photocatalytic  $\text{CO}_2$  reduction to appreciably decrease the reaction yield.<sup>42</sup>

Catalyst stability is typically investigated by cycling tests in a batch/flow reactor in conjunction with various analytical techniques. Catalysts often become deactivated after repeated cycling for the reasons mentioned above, such that the surface active sites are no longer available to mediate the redox process.<sup>89</sup> Li and co-workers studied the deactivation mechanism of a  $\text{Cu}/\text{TiO}_2$  surface using *in situ* X-ray absorption spectroscopy (XAS) and diffuse reflectance infrared Fourier transform spectroscopy (DRIFTS).<sup>46</sup> The air-calcined  $\text{Cu}/\text{TiO}_2$  surface was dominated by the  $\text{Cu}^{2+}$  state, whereas the sample after treatment at  $200\text{ }^{\circ}\text{C}$  under  $\text{H}_2$  was rich in  $\text{Cu}^+$  and oxygen vacancies. The post-treatment sample ( $\text{Cu}/\text{Ti}(\text{H}_2)$ ) displayed 50% higher activity toward CO formation. The authors reported that the deactivation of  $\text{Cu}/\text{Ti}(\text{H}_2)$  was attributable to the consumption of OH groups and Cu active sites by holes. The  $\text{Cu}/\text{Ti}(\text{H}_2)$  catalytic activity decreased from a maximum of  $7.5\text{ }\mu\text{mol g}^{-1}\text{ h}^{-1}$  to  $3.5\text{ }\mu\text{mol g}^{-1}\text{ h}^{-1}$  after 7 h. *In situ* XAS results revealed that the photooxidation of  $\text{Cu}^+$  to  $\text{Cu}^{2+}$  altered the environment of Cu and led to the decrease in the  $\text{CO}_2$  photoreduction activity.

Various strategies have been applied to overcome these issues, including the use of hole scavengers to preserve the active oxidation states and intermediates. In addition, a variety of heterostructures and hybrid combinations have been developed to improve the stability of the  $\text{Cu}_2\text{O}$  catalyst; for example, the formation of  $\text{Cu}_2\text{O}/\text{TiO}_2$  heterostructures was reported to protect the  $\text{Cu}_2\text{O}$  from photocorrosion.<sup>43</sup> Recently, Ali *et al.* reported that a Z-scheme heterostructure based on reduced titania and  $\text{Cu}_2\text{O}$  displayed high photostability over 42 h (seven cycles) with

improved catalytic activity for the photoreduction of  $\text{CO}_2$  to  $\text{CH}_4$ .<sup>44</sup> This high stability was attributed to the Z-scheme charge transfer that successfully inhibited the photocorrosion of  $\text{Cu}_2\text{O}$ . In addition, thermal and oxidative/reductive treatments ( $\text{H}_2\text{O}_2$  or mild acid exposure) have also been applied to eliminate the adsorbed unwanted intermediates. Vacuum annealing can also restore the activity of a catalyst, which is likely attributable to the regeneration of oxygen vacancies or decomposition of adsorbed intermediates on the catalyst surface. The use of cocatalysts or shielding materials such as graphene to prevent oxidation is also an option. These techniques and their respective advantages will be discussed in the following sections.<sup>90</sup> Furthermore, Feng and co-workers suggested that increasing the light intensity using a solar concentrator can prevent catalyst deactivation owing to the influence of temperature under multi-sun conditions increasing product desorption.<sup>48</sup> Considering the crucial role of catalyst stability in photocatalytic  $\text{CO}_2$  reduction, more detailed research is necessary to elucidate the deactivation mechanisms.

## 2.5 Development of facile and reasonable synthetic processes

To date, a variety of photocatalytic materials have been investigated, each with unique size, shape, appearance, physicochemical properties, and so on. All of these properties are influenced by the synthetic strategy adopted to prepare the catalyst. For many years,  $\text{CO}_2$  conversion has been a central focus of research into semiconducting nanomaterials, especially in the case of  $\text{TiO}_2$ .<sup>91</sup> Advanced synthesis techniques can facilitate precise manipulation of the size, morphology, crystal facet, pore network, and structural periodicity. Thus, various rational design and synthesis methodologies have been explored for both single and multicomponent (hybrid) catalysts. For example, bandgap-engineered  $\text{TiO}_2$  has been reported to be beneficial for  $\text{CO}_2$  reduction. In addition, various studies have reported the synthesis of reduced titania using thermal treatment with aluminum or magnesium at high temperatures of 500–700 °C.<sup>92</sup> However, such high-temperature synthesis methodologies are not feasible for large-scale applications. In this respect, other studies have demonstrated the synthesis of reduced titania with abundant oxygen vacancies or  $\text{Ti}^{3+}$  states at lower temperatures (ca. 350 °C) using  $\text{NaBH}_4$  as a reducing agent.<sup>93</sup> Recently, MXenes have emerged as extremely promising materials for catalytic applications. In contrast to conventional 2D nanosheets that are typically obtained *via* an etching process involving hazardous acids such as hydrofluoric acid (HF), MXenes can also be synthesized in a convenient and facile manner through a hydrothermal approach in  $\text{NaOH}$  solution or electrochemical etching.<sup>94</sup>

In addition to the methods used to prepare the pristine semiconductors, the techniques used for cocatalyst deposition can also influence catalytic performance. Loading with a cocatalyst is typically accomplished using methods such as galvanic dispersion, photodeposition, wet chemical approaches, and impregnation.<sup>92</sup> Our previous studies demonstrated that flawless Schottky junctions between semiconductors and cocatalysts could be obtained using a simple photodeposition process at ambient temperature.<sup>5,93,95,96</sup> Most heterojunction combinations

have been widely synthesized using *in situ* hydrothermal, coprecipitation, solvothermal, vacuum annealing, and sonochemical approaches.<sup>97</sup> The synthetic procedure may vary depending upon the composition and heterostructure, *e.g.*, p-n junction, core-shell, Z-scheme, and S-scheme. Various studies have demonstrated that simple procedures can afford facile heterostructure combinations under ambient conditions. For example, in our recent study,  $\text{Cu}_2\text{O}$ -reduced titania heterojunctions were obtained *via* a facile, unique low-temperature thermochemical method followed by photodeposition.<sup>44</sup> All of these synthetic routes have been frequently applied over the years to prepare catalysts with optimal optoelectronic properties. Nevertheless, the continued development of comprehensive synthetic approaches that meet the requirements of simplicity, cost-effectiveness, high performance (*e.g.*, catalytic activity, selectivity, and physicochemical stability), and scalability remains necessary to satisfy engineering requirements for large-scale applications.

## 2.6 Underlying mechanism/ $\text{C}_1$ and $\text{C}_2$ selectivity

Understanding the mechanisms of  $\text{CO}_2$  photoreduction into various products is challenging owing to numerous known and unknown phenomena. Multiple factors, such as the catalyst properties, band potentials, surface defects,  $\text{CO}_2$  adsorption characteristics, and nature of the active sites and interface, can significantly influence the reaction pathway. The  $\text{CO}_2$  reduction pathway involves a series of steps after  $\text{CO}_2$  activation, which are dependent on the number of electrons produced, electron transfer to  $\text{CO}_2$  molecules, C–O bond breaking, the formation of intermediate species,  $\text{H}_2\text{O}$  oxidation to generate protons, coupling of intermediates with protons, new bond formation, *etc.* There exist various pathways for  $\text{CO}_2$  reduction to value-added products on a semiconductor surface, including the formaldehyde, carbene, and glyoxal pathways,<sup>9,98</sup> as depicted in Fig. 5. As explained above, all of these pathways begin with the adsorption and activation of  $\text{CO}_2$  molecules on the catalyst surface.

In the formaldehyde pathway,  $\text{CO}_2$  activation proceeds *via* binding of one of the O atoms to the active site of the catalyst. One electron transfer to the  $\text{CO}_2$  molecule leads to the formation of a  $\text{CO}_2\cdot^-$  radical, and subsequent addition of a proton generates a  $\cdot\text{COOH}$  radical intermediate. Next, the consecutive addition of a proton and an electron to  $\cdot\text{COOH}$  yields formic acid. Then, the formic acid accepts two protons to afford formaldehyde and water. It has been reported that the photoconversion of formic acid to formaldehyde has the most significant kinetic barrier in this pathway.<sup>99</sup> Methanol and methane can also be produced through this pathway in subsequent steps depending upon the available electrons and protons, where methane formation proceeds through the  $\cdot\text{CH}_3$  radical intermediate.

This route can account for the production of formic acid, formaldehyde, methanol, and methane but not CO, which is one of the most commonly generated products during the  $\text{CO}_2$  reduction process.

The carbene pathway can lead to CO formation with the consumption of two electrons, where the CO may be either a side product or an intermediate that reacts further to form



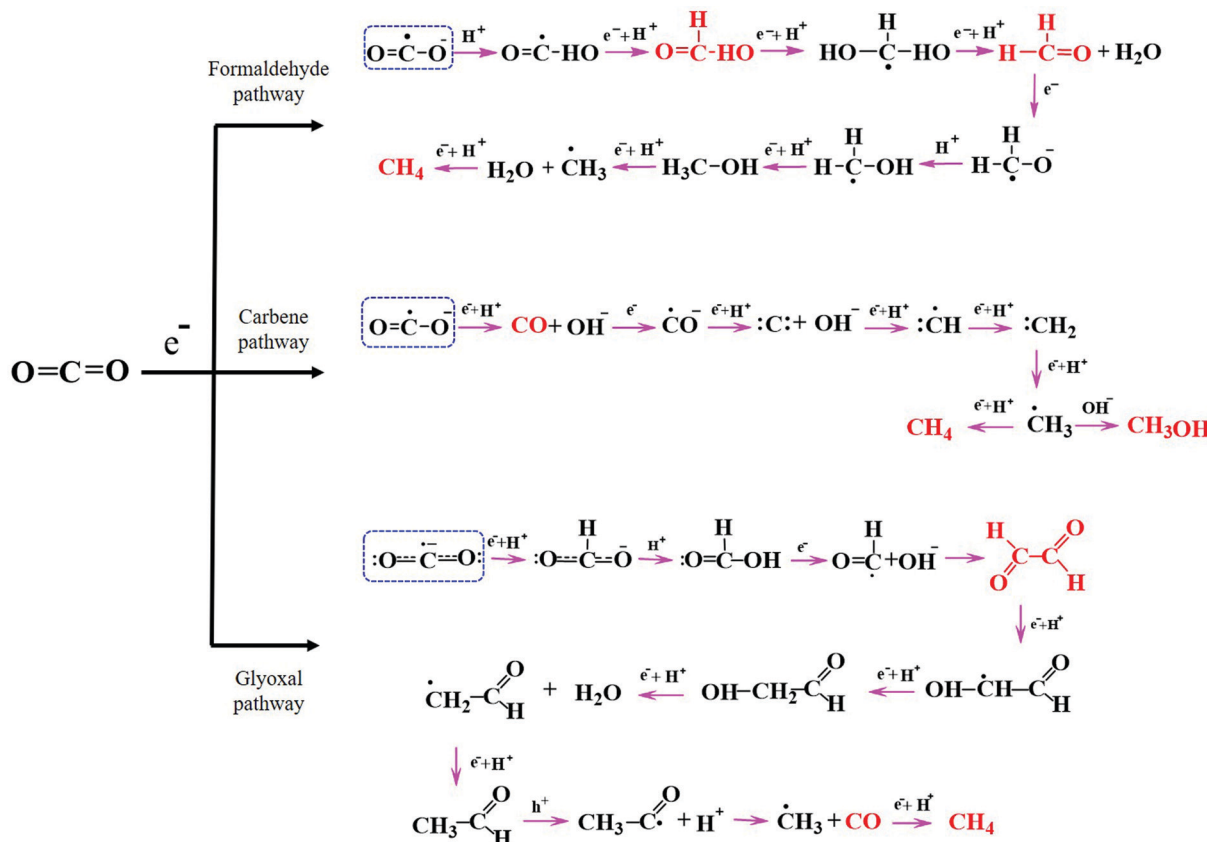


Fig. 5 General pathways for photocatalytic  $\text{CO}_2$  reduction: formaldehyde, carbene, and glyoxal. Adapted from ref. 9, Copyright 2020, Royal Society of Chemistry.

methane or methanol. Here, the active sites of the catalyst bind with the C atom of  $\text{CO}_2$ . The formation of methanol or methane *via* the CO intermediate is dependent upon the adsorption strength between CO and the catalyst surface; the CO may either rapidly desorb from the surface or accept electrons and protons to produce subsequent products. The subsequently generated  $\cdot\text{CH}_3$  radical may react with  $\text{OH}^-$  to form methanol or accept a proton and an electron to afford methane. According to the literature, the carbene pathway has been experimentally demonstrated to be the most commonly followed mechanism for the production of CO and other hydrocarbons, with the intermediates easily detectable using various advanced analytical techniques such as electron paramagnetic resonance (EPR).<sup>39</sup> The formation of such hydrocarbons *via* the carbene pathway is well known as a “proton-coupled electron transfer” (PCET), which is kinetically reliant on the partial electron density on the catalyst surface and the concentration of accessible protons. This pathway is complicated because  $\text{CO}_2$  requires two electrons and protons to generate CO, yet the production of higher hydrocarbons through PCET requires more electrons; for example, the generation of  $\text{CH}_4$  and  $\text{CH}_3\text{OH}$  requires eight and six electrons, respectively. Although significant progress in the photoreduction of  $\text{CO}_2$  to afford CO or  $\text{HCOOH}$  has been reported in the literature, there remains a gap in the research when it comes to converting  $\text{CO}_2$  into

higher hydrocarbons such as  $\text{C}_2\text{H}_5\text{OH}$ ,  $\text{C}_2\text{H}_4$ , and  $\text{C}_2\text{H}_6$  with high efficiency and selectivity.<sup>25</sup>

The third potential route for  $\text{CO}_2$  conversion is the glyoxal pathway, in which the two O atoms of  $\text{CO}_2$  coordinate to the catalyst active site in a bidentate manner to produce numerous products.<sup>100</sup> Initially, the  $\text{CO}_2\cdot^-$  radical interacts with  $\text{H}^+$  to generate a bidentate formate, which then couples with another  $\text{H}^+$  to afford formic acid. Subsequent electron and oxygen transfer lead to formyl radicals ( $\text{HCO}^\cdot$ ), which dimerize to generate glyoxal prior to the formation of  $\text{C}_2$  and  $\text{C}_3$  products. Similar to the previous two pathways, the combination of  $\cdot\text{CH}_3$  with a proton leads to  $\text{CH}_4$  formation with the elimination of CO as a byproduct. The  $\cdot\text{CH}_3$  radical can also form  $\text{C}_2$  products depending upon the presence of other intermediates in the system.

Although various studies have explored these  $\text{CO}_2$  reduction pathways both theoretically and experimentally, the multiple steps, intermediates, and byproducts involved in the reaction make the process more complex with respect to  $\text{C}_2$  selectivity. The density of the photogenerated electrons/holes and stabilization of the intermediates influence the  $\text{C}_2$  selectivity of the reaction; for instance, the stabilization of  $\cdot\text{CH}_3$  radicals is desirable for achieving  $\text{C}_2$  selectivity. However, this is hampered by (i) rapid hydrogenation of these intermediates to form  $\text{C}_1$  products and (ii) repulsive forces between the oppositely

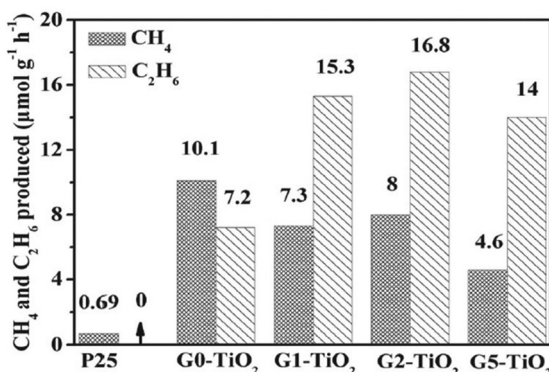


Fig. 6 Photocatalytic performance of graphene-wrapped  $\text{TiO}_2$  showing the formation of  $\text{C}_1$  and  $\text{C}_2$  products. Reproduced with permission from ref. 102, Copyright 2013, Wiley-VCH.

charged intermediates, which hinder C–C coupling. The creation of adjacent reaction sites displaying opposite charges could be used to weaken the repulsive forces between adsorbed reaction intermediates, especially  $\text{CO}_2^{\bullet-}$  or  $\text{CO}^*$ , and provide a platform for the coupling of these adsorbates. Therefore, such reaction sites are highly desirable, stabilizing the  $^{\bullet}\text{CH}_3$  radicals, and overcoming the interadsorbate repulsive forces.<sup>101</sup> For instance, as shown in Fig. 6, graphene has been reported to provide such sites and mediate the formation of a  $\text{C}_2$  product when coupled with  $\text{TiO}_2$ .

### 3 Strategies to improve $\text{CO}_2$ photoreduction

#### 3.1 Energy band structure engineering

As we discussed in Section 2.1, the electronic structure of the photocatalyst is crucial for improving the photocatalytic activity. The photocatalytic performance is highly dependent on the energy band structure (*i.e.*, bandgap and band positions) because the bandgap determines the range of light absorption while the appropriate band positions are required for the photocatalytic redox potentials. Various strategies for tuning the electronic structures of photocatalysts have been reported to date.<sup>54</sup> One such strategy is the introduction of defects to improve light absorption. For instance, Mao and co-workers first demonstrated the use of the disorder-engineering approach to prepare “black”  $\text{TiO}_2$  composed of crystalline  $\text{TiO}_2$  and disordered surface  $\text{TiO}_2$ , thereby introducing new energy levels.<sup>103</sup> Black  $\text{TiO}_2$  possesses a narrower bandgap (2.18 eV) compared to  $\text{TiO}_2$  (3.2 eV), which extends the light absorption. Several other approaches for synthesizing reduced  $\text{TiO}_2$  have since been explored, such as ion implantation,<sup>104</sup> the magnesiothermic method,<sup>105</sup> and hydride ball milling.<sup>106</sup> Here, not only the defects but also the midgap energy band, which refers to the additional electronic states under the CB of  $\text{TiO}_2$ , help to maximize the utilization of solar energy.

The electronic structure is highly influenced by band bending, which was first suggested for the metal–semiconductor contact by Schottky and Mott.<sup>107,108</sup> When a metal and semiconductor come

into contact, the work function difference between the two leads to electron transfer until the Fermi levels are aligned. At equilibrium, the concentration of free charge carriers is different for the metal and semiconductor, resulting in the formation of an electric field at the interface. Consequently, the energy band may bend upward or downward at the interface depending upon the work functions of the metal and semiconductor. For instance, downward band bending was reported for reduced  $\text{TiO}_2$  at the interface between N-doped graphene oxide and reduced  $\text{TiO}_2$ , which facilitated electron transfer and inhibited electron–hole recombination, resulting in improved photocatalytic activity.<sup>96</sup> Besides  $\text{TiO}_2$ , band structure engineering has been conducted for graphitic carbon nitride ( $\text{g-C}_3\text{N}_4$ ), an emerging polymeric photocatalyst, which possesses a moderate bandgap (2.7 eV) and an easily tunable electronic structure.<sup>109</sup> The CB of  $\text{g-C}_3\text{N}_4$  is composed of C  $p_z$  orbitals, while the VB consists of the N  $p_z$  orbitals.<sup>110</sup> Approaches for narrowing the bandgap include elemental doping,<sup>111</sup> variation of the linking monomer,<sup>112</sup> and copolymerization.<sup>113</sup>

#### 3.2 Non-metal doping and metal cocatalysts

Doping is one method for increasing the photocatalytic  $\text{CO}_2$  conversion efficiency by creating sub-energy levels within the bandgap, thereby extending the range of light absorption into the visible region. Non-metal dopants such as nitrogen (N), boron (B), carbon (C), sulfur (S), and phosphorus (P) in anatase  $\text{TiO}_2$  have been investigated.<sup>114</sup> For example, substitutional doping of the O atoms in anatase  $\text{TiO}_2$  with N atoms led to upward bending of the VB edge and a narrower bandgap owing to orbital mixing of the 2p states of O with the 2p states of N. Furthermore, Hashimoto and co-workers reported that N doping of  $\text{TiO}_2$  resulted in not only mixing of the orbitals but also an isolated N 2p band above the O 2p valence states, thereby improving the visible-light photocatalytic performance of  $\text{TiO}_2$ .<sup>115</sup> In addition to N doping, the effects of doping  $\text{TiO}_2$  with other non-metals, including B,<sup>116</sup> C,<sup>117</sup> P,<sup>118</sup> and S,<sup>119</sup> have also been investigated, leading to visible-light-active photocatalysts by reducing the bandgap.

Metal cocatalysts have also been extensively applied to improve  $\text{CO}_2$  photoreduction performance. These can act as electron traps that facilitate electron–hole separation and ultimately improve the photocatalytic activity of semiconductor materials.<sup>120</sup> In particular, noble-metal cocatalysts, such as copper (Cu),<sup>121</sup> gold (Au),<sup>122</sup> silver (Ag),<sup>123</sup> palladium (Pd),<sup>124</sup> and rhenium (Rh),<sup>125</sup> can enhance photocatalytic conversion. For example, Biswas and co-workers developed Pt– $\text{TiO}_2$  nanostructured films using a gas-phase deposition method and examined the correlation between the size of the Pt nanoparticles (NPs) and photocatalytic activity (Fig. 7).<sup>126</sup> When the size of the Pt NPs was too small, larger energy band separation occurred owing to the quantum confinement effect, inhibiting the electron transfer from  $\text{TiO}_2$  to Pt. Conversely, when the size of the Pt NPs was too large, the energy band position was similar to that of bulk Pt, thereby acting as a recombination site for the photoexcited electrons and holes.

Bimetallic cocatalyst systems have also been explored to improve photocatalytic activity and selectivity. For instance,

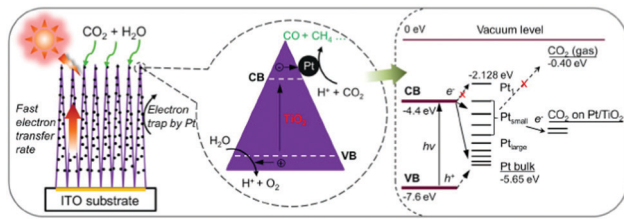


Fig. 7 Schematic diagram of  $\text{CO}_2$  photoreduction mechanism on Pt– $\text{TiO}_2$  nanostructured films. The magnified circle (center) shows that the photogenerated electrons can move rapidly inside the highly oriented  $\text{TiO}_2$  single crystals and flow to the deposited Pt NPs, where the redox reaction occurs to convert  $\text{CO}_2$  into  $\text{CO}$  and  $\text{CH}_4$ . The right side of the figure illustrates the energy levels of the Pt– $\text{TiO}_2$ – $\text{CO}_2$  system.  $\text{H}^+$  and  $\text{h}^+$  indicate protons and holes, respectively. Reproduced with permission from ref. 126, Copyright 2012, American Chemical Society.

the combination of Cu and Au has been reported, where Cu provided high affinity for  $\text{CO}_2$  to mediate the photocatalytic  $\text{CO}_2$  reduction while Au improved the visible-light absorption owing to its surface plasmonic effects.<sup>127</sup> In another example, a Pt@ $\text{Cu}_2\text{O}$  core–shell structured bimetallic system was studied, where the  $\text{Cu}_2\text{O}$  shell activated the  $\text{CO}_2$  molecules to enable photocatalytic  $\text{CO}_2$  conversion in the presence of  $\text{H}_2\text{O}$ , while the Pt core acted as an electron trap to extract electrons from  $\text{TiO}_2$ .<sup>128</sup> The  $\text{Cu}_2\text{O}$  shell on the Pt core also suppressed the reduction reaction of  $\text{H}_2\text{O}$  to  $\text{H}_2$ , which otherwise competes with the  $\text{CO}_2$  reduction reaction, thereby increasing the  $\text{CO}_2$  conversion activity. Similarly, Long *et al.* reported the alloying of Cu with Pd to achieve high selectivity for  $\text{CH}_4$  production by isolating the Cu atoms in a Pd matrix.<sup>129</sup> In this case, the Cu NPs served as the active sites for  $\text{CO}_2$  conversion, but these are susceptible to oxidation under ambient conditions. The alloying approach thus reduced the oxidation of Cu, while the Pd lattice inhibited the  $\text{H}_2\text{O}$  reduction reaction. Pd also exhibits strong binding to H atoms, thus suppressing the  $\text{H}_2$  evolution reaction and affording high selectivity for  $\text{CH}_4$  formation.

### 3.3 Heterostructure formation

Efficient photocatalytic  $\text{CO}_2$  reduction always requires a photocatalyst that can provide large amounts of photogenerated electrons and holes with strong redox potentials. However, by doing so, the optical response of the photocatalyst is compromised because only wide-bandgap photocatalysts can provide strong redox potentials.<sup>130</sup> On the contrary, a narrow-bandgap photocatalyst could be applied for enhanced light harvesting, but this requires choosing between a strong oxidation potential and a strong reduction potential. Hence, combining suitable narrow-bandgap photocatalysts could help overcome this tradeoff and realize synergistic effects.<sup>131</sup>

The classification of heterostructures with respect to their band alignment suggests that there exist three main types, namely, straddling alignment (type I), staggered alignment (type II), and broken alignment (type III), as depicted in Fig. 8. In type I heterostructures, the photogenerated charges originating from  $\text{S}_1$  tend to remain at  $\text{S}_2$ ; therefore, no charge separation is achieved. Although this type of charge transfer is beneficial

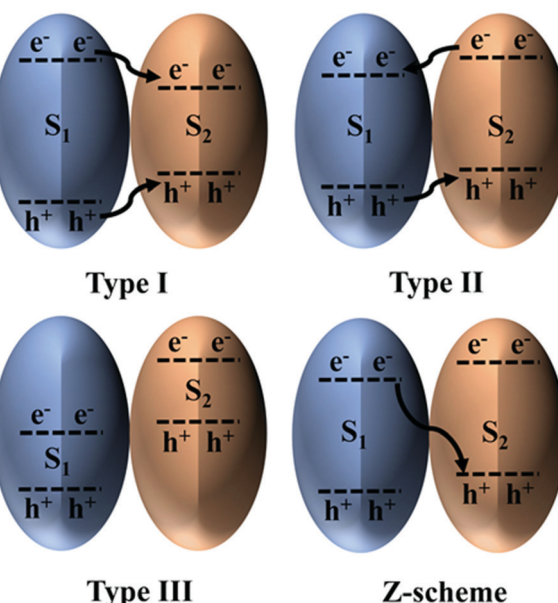


Fig. 8 Heterojunction classification based on the charge transfer mechanism. Reproduced with permission from ref. 132, Copyright 2016, Wiley-VCH.

for luminescent materials, it is ineffective for photocatalytic  $\text{CO}_2$  reduction. In stark contrast, for type III heterostructures, both the CB and VB edges of  $\text{S}_1$  lie below the CB of  $\text{S}_2$ . Finally, in type II heterostructures, charge separation is achieved but at the expense of lower redox potential. Therefore, type II heterostructures appear to be the most favorable for photocatalytic  $\text{CO}_2$  reduction and have been reported in various studies. Nonetheless, this is not regarded as an efficient scheme to combine two photocatalysts because the photogenerated charges lose energy during the transfer process.<sup>132</sup>

The Z-scheme charge transfer mechanism has the potential to solve the constraints of the aforementioned charge transfer. Under this scheme, the photogenerated charges of both photocatalysts with weak redox potentials recombine with each other while preserving the desired strong charges for photocatalytic  $\text{CO}_2$  reduction. This type of charge transfer seems justified because of the electrostatic force of attraction between two opposite charges. In addition to these beneficial attributes, this type of charge transfer is also advantageous for improving photocatalyst stability. For example, Cu is susceptible to facile oxidation because its oxidation potential lies within its bandgap. However, by constructing a Cu (*i.e.*,  $\text{S}_2$ ) Z-scheme heterostructure with a semiconductor possessing suitable band alignment (*i.e.*,  $\text{S}_1$ ), Cu oxidation can be avoided.<sup>133</sup>

In addition to the direction of the charge transfer, the geometry of the heterostructures also determines their classification. In this regard, interfacial contact between the constituent photocatalysts with high surface area confers beneficial features for the photocatalytic reactions. Various Z-scheme heterostructure geometries have been reported in the literature, which can be classified as (i) core–shell heterostructures, (ii) surface-deposited heterostructures, and (iii) Janus-like systems. The first type has limited exposure of the core to the reaction system, while



the second suffers from stability issues due to fast corrosion.<sup>43,134,135</sup> However, the synthesis of Janus structures is challenging. In this regard, Ali *et al.* developed reduced titania–Cu<sub>2</sub>O Z-scheme heterostructures, somewhat like Janus structures, by using the charge trapping ability of an amorphous shell of reduced titania.<sup>44</sup> Under irradiation, the photogenerated electrons accumulated in the amorphous core, causing Cu<sup>2+</sup> ions to preferentially accumulate at the edges. The resulting structure not only exposed both photocatalysts to the reactants but also maintained the stability of Cu owing to the higher concentration of electrons.

### 3.4 Surface modification

Surface characteristics play a major role in CO<sub>2</sub> adsorption and activation. Two important types of surface modification are surface functionalization and the deposition of metal complexes. Because CO<sub>2</sub> is electrophilic, the introduction of basic groups such as hydroxyl or amine moieties to a photocatalyst can enhance CO<sub>2</sub> adsorption.<sup>136,137</sup> Some studies have investigated the influence of alkalinization on the adsorption of CO<sub>2</sub> by TiO<sub>2</sub>. Treatment with different alkali solutions, such as NaOH, Na<sub>2</sub>CO<sub>3</sub>, KOH, and K<sub>2</sub>CO<sub>3</sub>, was reported to have various effects on CO<sub>2</sub> adsorption.<sup>138</sup> The use of NaOH afforded the highest CO<sub>2</sub> adsorption owing to the highest amount of free –OH groups. Furthermore, the preparation of layered hydroxide materials rich in surface hydroxyl groups *via* exfoliation also led to enhanced CO<sub>2</sub> uptake.<sup>139</sup> Similarly, amine functionalization (–NH species) enables the direct bonding of CO<sub>2</sub> molecules. Thus, Liao *et al.* described the covalent attachment of ethanamine to ZnO nanosheets *via* the hydroxyl groups to afford an amine-functionalized surface for the chemisorption of CO<sub>2</sub> molecules.<sup>140</sup> In addition, He *et al.* reported that the treatment of TiO<sub>2</sub> with HF modulated the ratio of crystal structure facets ((001)/(101)) to improve the dissociation of H<sub>2</sub>O and reduction of CO<sub>2</sub>.<sup>141</sup>

The deposition of metal complexes is another approach for surface modification. Early research focused on the combination of semiconductors and mononuclear metal complexes. However, such materials typically exhibit poor stability and insufficient oxidation ability, which has led to the consideration of hybrid materials as preferred alternatives. Nakada *et al.* revealed that a hybrid material based on g-C<sub>3</sub>N<sub>4</sub> and a Ru complex displayed high efficiency and selectivity for specific hydrocarbons.<sup>22,142</sup> By using 2-(1,3-dimethyl-2,3-dihydro-1H-benzimidazol-2-yl)benzoic acid as a sacrificial reducing agent, reverse electron transfer was suppressed to achieve a high quantum yield and selective CO formation.

The morphology/dimensionality of a material surface is another crucial issue that can be used to accelerate the kinetics of photocatalysis.<sup>143,144</sup> Low-dimensional materials, defined as nanostructured materials smaller than 100 nm, possess unique optical and electronic properties that originate from quantum confinement and plasmon resonance effects.<sup>144–148</sup> Low-dimensional materials can be classified into three categories, namely, (i) zero-dimensional (0D), (ii) one-dimensional (1D), and (iii) two-dimensional (2D) structures.

Zero-dimensional structures, such as nanoparticles, nanospheres, and quantum dots (QDs), are constrained on the

nanoscale in all three dimensions. For these structures, high photocatalytic CO<sub>2</sub> conversion can be achieved through the excellent light harvesting, satisfactory charge carrier density, and abundant surface sites.<sup>147–152</sup> Among such structures, the most extensively used are carbon QDs (CQDs), which exhibit a broad light absorption spectrum due to π-plasmon absorption in the core carbon nanocrystals, thereby enabling the π → π\* transition of conjugated carbon atoms in the UV-visible region.<sup>153–155</sup> It can be utilized not only in CQDs but also in semiconductor QDs and is advantageous for multi-electron and proton reduction.<sup>156,157</sup>

One-dimensional structures also possess an attractive morphology that provides excellent charge transfer and extended carrier lifetimes owing to the unique distribution of state density coupled with intrinsically higher reactivity.<sup>158–160</sup> In general, 1D structures have high aspect ratios with diameters ranging from 1 to 100 nm, and they include various morphologies such as nanowires, nanotubes, nanobelts, nanoribbons, and nanotubes. As 1D structures contain no grain boundaries, the electron transport distance is greatly reduced, thus improving the electron transfer efficiency and decreasing electron–hole recombination leading to high photocatalytic CO<sub>2</sub> conversion (Fig. 9(a)–(c)).<sup>159–161</sup> The unique characteristics of 1D structures, including relatively large specific surface areas and good chemical stability, can be used to assemble various heterogeneous surface structures.<sup>162–164</sup>

Two-dimensional structures, including nanosheets, nanoflakes, and thin films, have typical thicknesses ranging from several atoms to <100 nm, leading to larger surface-area-to-volume ratios compared to 1D structures. Furthermore, 2D structures display enhanced electron–hole separation, high charge carrier mobility, and reduced recombination.<sup>144,166</sup> Among the various 2D structural materials, graphene, which is composed of single-layer carbon nanosheets with a hexagonal packed lattice structure, has received a great deal of attention in the field of photocatalytic CO<sub>2</sub> conversion owing to its remarkably high surface area, excellent electrical conductivity (>10<sup>3</sup> S m<sup>-1</sup>), and good flexibility.<sup>90,167,168</sup> Liang *et al.* reported that the coupling of graphene with TiO<sub>2</sub> showed larger enhancement in photocatalytic CO<sub>2</sub> conversion, attributed to superior electric mobility of graphene (Fig. 9(d) and (e)).<sup>165</sup>

### 3.5 Reactor design

The design of reactors for photocatalytic CO<sub>2</sub> reduction also exerts an important influence on the CO<sub>2</sub> conversion efficiency. In addition, the use of different reactor geometries and reaction conditions can render it difficult to compare reaction rates and yields.<sup>47,169–171</sup> In general, photocatalytic CO<sub>2</sub> reduction is conducted in either batch reactor or continuous-flow reactor systems.

In the case of batch reactors, the reduction is typically performed in a pressurized reactor vessel equipped with an optically transparent window and an external temperature controller to adjust the sample temperature. However, there is always the possibility of the readsorption of products and subsequent reverse or side reactions, *e.g.*, re-oxidation to CO<sub>2</sub>.<sup>172,173</sup> Consequently, the yield during batch



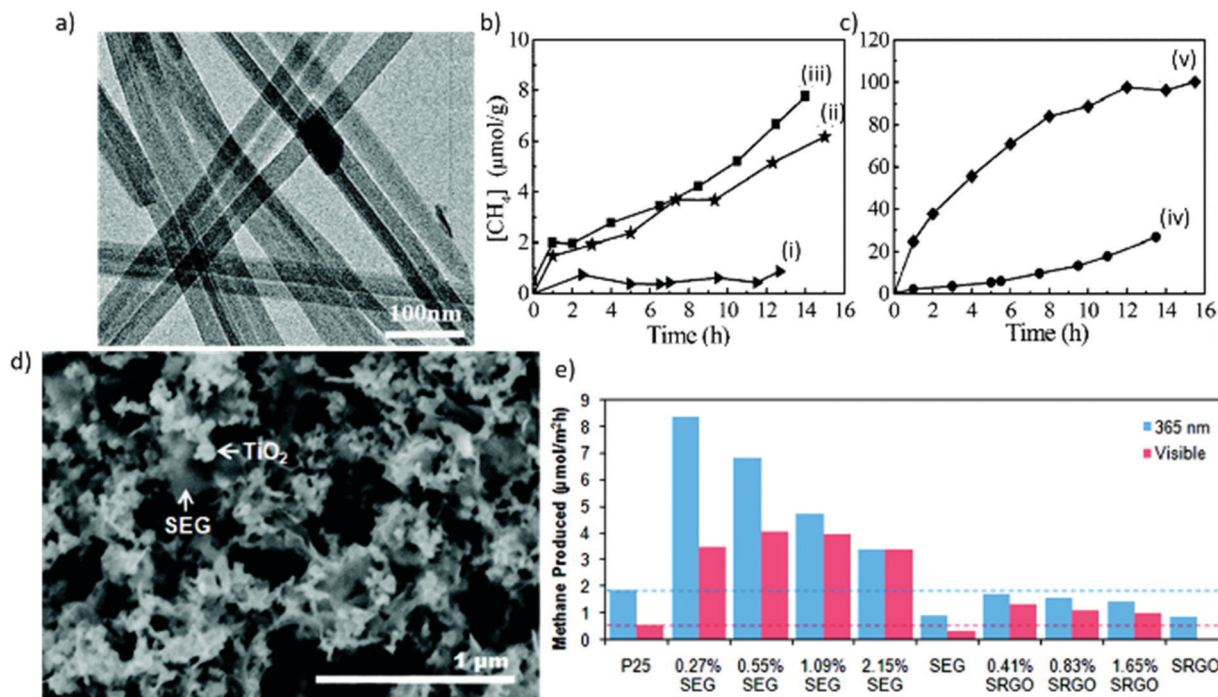


Fig. 9 (a) Transmission electron microscopy (TEM) image of Zn<sub>2</sub>GeO<sub>4</sub> nanoribbons, and (b and c) CH<sub>4</sub> generation over (i) bulk Zn<sub>2</sub>GeO<sub>4</sub>, (ii) nanoribbons, (iii) 1 wt% Pt-loaded nanoribbons, (iv) 1 wt% RuO<sub>2</sub>-loaded nanoribbons, and (v) 1 wt% RuO<sub>2</sub> + 1 wt% Pt-coloaded nanoribbons as a function of light irradiation time. Reproduced with permission from ref. 161, Copyright 2010, American Chemical Society. (d) Scanning electron microscopy (SEM) image of an annealed SEG-P25 nanocomposite, and (e) CO<sub>2</sub> photoreduction by SEG-P25 and SRGO-P25 nanocomposites under UV (365 nm) and visible illumination, where SEG and SRGO denote solvent-exfoliated graphene and solvent-reduced graphene oxide, respectively. Reproduced with permission from ref. 165, Copyright 2011, American Chemical Society.

reactions may decrease owing to the continuous accumulation of the target product as well as byproducts such as oxygen.<sup>174,175</sup> In this regard, one effort by Pipelzadeh *et al.* involved a pressure swing reactor in which the reaction mixture was periodically evacuated from the batch reactor and reinjected.<sup>176</sup> This continuous recycling of the products helped overcome the issues of product readsorption and limited mass transfer, increasing the CO production yield to 30–80%. In another effort to improve the photocatalytic yield, a specially designed twin reactor was employed where protons (H<sup>+</sup>)

generated in one compartment were transported to a separate compartment for CO<sub>2</sub> reduction, as shown in Fig. 10(a).<sup>177,178</sup> This configuration helped overcome the mass transfer limitation and thereby improve the photocatalytic yield. Overall, batch reactor systems make it difficult to compare photocatalytic performance and are often not a suitable option for applications involving prolonged and large-scale reactions.

On the other hand, in continuous-flow reactor systems, the reactants and products are moving at a constant flow rate

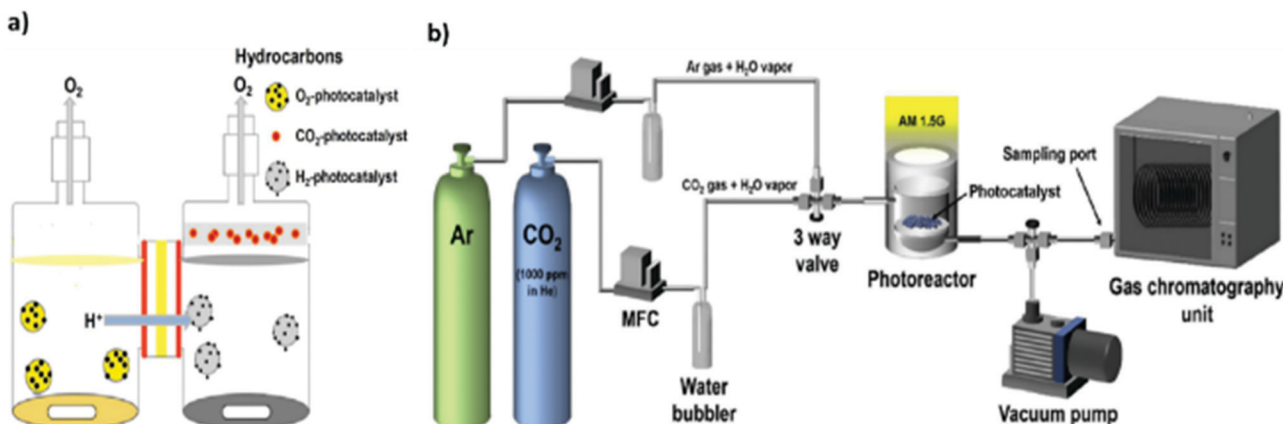


Fig. 10 Illustration of two setups for photocatalytic CO<sub>2</sub> reduction: (a) twin reactor. Reproduced with permission from ref. 177, Copyright 2018, Elsevier. (b) Continuous-flow reactor. Reproduced with permission from ref. 93, Copyright 2017, Elsevier.



inside the vessel while the reaction is in progress (Fig. 10(b)).<sup>5,93</sup> Continuous-flow reactor systems can avoid the problems of batch reactors, such as product readsorption on the photocatalyst surface,<sup>172,173</sup> but are also associated with the challenge of a very limited contact time between the reactants and photocatalyst surface owing to the short residence time.<sup>47,179,180</sup>

As shown in Fig. 11(a), a photoreactor using optical fibers to optimize the light path was developed.<sup>181</sup> In contrast to a conventional photoreactor composed of a cylindrical vessel equipped with a quartz window to allow light to enter, optical fibers coated with the catalyst were installed in such a manner as to occupy the maximum possible volume of the reactor, thus improving the contact between the catalyst, reactants, and light and affording high conversion efficiency.<sup>182</sup> However, optical fiber photoreactors are difficult to commercialize owing to several disadvantages, including low adhesion strength of catalyst on the fibers, relatively low surface area, and the effective utilization of only approximately 20–30% of the total reactor volume. To compensate for this, a monolith-type photoreactor was also reported as shown in Fig. 11(b).<sup>170</sup>

The use of the monolithic catalyst enabled efficient light harvesting and high photon flux owing to its unique structure and high surface-area-to-volume ratio.<sup>170,183</sup> Nevertheless, monolith-type photoreactors have the disadvantage that they cannot be used with visible light because of their low penetration depth through the microchannels. Therefore, a combination of a monolithic catalyst and optical fibers can be anticipated to overcome this issue.

In one such effort, Xiong *et al.* reported the use of a monolithic catalyst with a honeycomb structure through which optical fibers had been inserted.<sup>184</sup> This configuration successfully enhanced the photoreaction. In a similar manner, Liou *et al.* inserted carved polymethylmethacrylate (PMMA) optical fibers into a  $\text{NiO}/\text{InTaO}_4$ -coated monolith with a honeycomb structure.<sup>185</sup> This reactor afforded an improved product yield when applied to photocatalytic  $\text{CO}_2$  reduction owing to the large surface area, high photocatalyst loading, and effective light utilization. In another attempt, Cao and co-workers reported a double-chamber reactor as depicted in Fig. 12. Separation of the oxidation and reduction reactions helped to

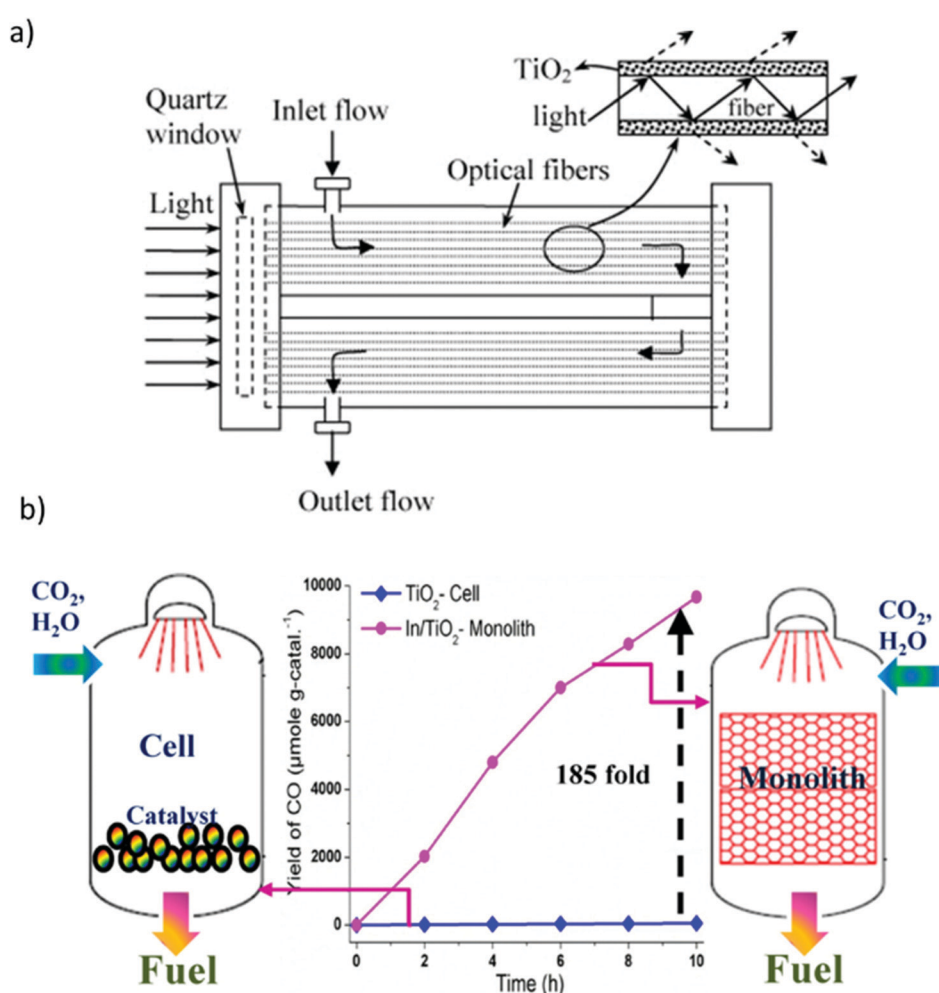


Fig. 11 (a) Schematic diagram of an optical fiber reactor, reproduced with permission from ref. 181, Copyright 2007, Elsevier. (b) Comparison of photocatalytic  $\text{CO}_2$  reduction with  $\text{H}_2\text{O}$  using cell- and monolith-type photoreactors. Reproduced with permission from ref. 170, Copyright 2013, Elsevier.



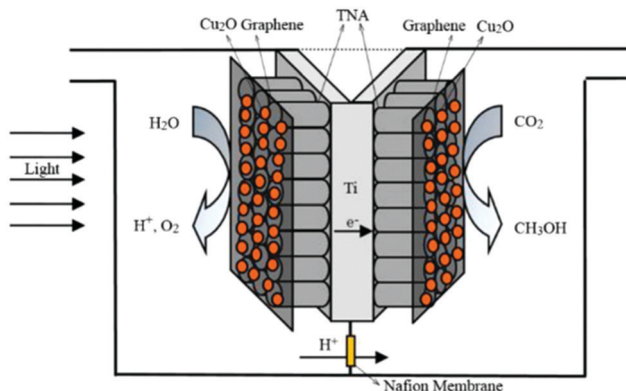


Fig. 12 Schematic diagram of a monolithic two-sided  $\text{Cu}_2\text{O}/\text{graphene}/\text{TNA}$  photoreduction reaction system. Reproduced with permission from ref. 186, Copyright 2016, Elsevier.

achieve stability of the monolithic two-sided  $\text{Cu}_2\text{O}/\text{graphene}/\text{TNA}$  photocatalyst for up to 60 h.<sup>186</sup>

### 3.6 Optimization of selectivity

As we discussed in Section 2, the  $\text{CO}_2$  photoreduction process occurs through a multistep reaction mechanism. Thus, optimization of the product selectivity is always a critical aspect. In general, formaldehyde, carbene, and glyoxal may be formed as intermediate products during the reaction. As such, it is essential for the practical applications of  $\text{CO}_2$  reduction technology to optimize the selectivity to obtain pure products.<sup>98</sup> The main obstacle here is that the reaction mechanism is not yet completely understood at the molecular level. However, several optimization strategies have been reported to date, such as modulating the bandgap, tailoring the surface composition, alkaline treatment of the catalyst, the loading of specific metals at a particular concentration, and improving the interfacial properties.<sup>52</sup> As discussed in Section 3.4, the  $\text{CO}_2$  photoreduction process can be improved by surface modification, and such strategies can also be applied to enhance the selectivity. For example, surface modification with hydrophobic-hydrophilic groups can favor the formation of specific hydrocarbons, in addition to influencing the reaction rate, by altering the affinity of the catalyst surface for  $\text{H}_2\text{O}$  molecules.<sup>187</sup> He *et al.* studied the fluorination of anatase  $\text{TiO}_2$  nanosheets, which introduced  $\text{Ti}^{3+}$  species on the catalyst surface that favored the conversion of  $\text{CO}_2$  to  $\text{CO}_2^{\bullet-}$ .<sup>141</sup> Subsequently, Xing *et al.* confirmed that the fluorination treatment had no effect on the  $\text{CO}_2$  adsorption.<sup>188</sup> Instead, fluorination treatment induces the built-in electric field by the substitutional F to surface oxygen vacancies. As a result, it increased the rate of  $\text{CH}_4$  and CO formation. However, the development of more eco-friendly strategies that avoid the use of fluorine would be desirable.

Moreover, the photocatalyst acidity or basicity can also contribute to product selectivity. Subrahmanyam *et al.* studied various metal oxide/metal composites, including  $\text{TiO}_2/\text{Pd}$ ,  $\text{CuO}/\text{ZnO}$ , and  $\text{Li}_2\text{O}/\text{TiO}_2$ , supported on  $\text{MgO}$ ,  $\text{Al}_2\text{O}_3$ , or  $\text{SiO}_2$ .<sup>189</sup> They found that the basic oxide supported systems displayed reasonable selectivity for the photoreduction of  $\text{CO}_2$

to  $\text{C}_1\text{--C}_3$  compounds. In contrast, the acidic oxide supported catalysts exhibited good selectivity for the generation of  $\text{C}_1$  compounds. More interestingly, the  $\text{C}_1\text{--C}_3$  selectivity remains independent of the confirmed photocatalyst. In conclusion, several strategies may be adopted to optimize the selectivity of  $\text{CO}_2$  photoreduction, but it remains necessary to understand the underlying reactions at the molecular level, including the heats of formation and the adsorption and desorption energies of the hydrocarbon products.

## 4 Theoretical insights and equations

### 4.1 Density functional theory for $\text{CO}_2$ photoreduction

Density functional theory (DFT) has attracted enormous attention over the last few decades as a means to understand the kinetics and thermodynamics of reaction mechanisms.<sup>190</sup> In the case of  $\text{CO}_2$  photoreduction, some crucial questions must be answered to overcome the barriers to commercialization, including (i) the nature of the reaction mechanism, (ii) the driving force behind  $\text{CO}_2$  photoreduction, and (iii) the optimal parameters for achieving the desired photoreduction efficiency. Although these questions seem challenging, it is essential to answer them to establish a robust foundation for  $\text{CO}_2$  photoreduction technology.<sup>89,191</sup>

To date, the development of semiconductor photocatalysts has been a primary focus of  $\text{CO}_2$  reduction technology; however, the anticipated efficiency has not yet been realized. Therefore, we need to understand the molecular-level reaction mechanisms responsible for the conversion of  $\text{CO}_2$  to hydrocarbons. For instance, the carbophilic and oxophilic interactions with the catalyst surface affect the product selectivity.

The kinetic model offers opportunities to design the photoreactor to avoid variable photon flux. In addition, the adsorption and desorption of  $\text{CO}_2$  molecules on the surface of the photocatalyst also affects other parameters such as light transport, temperature, and pressure.<sup>192,193</sup> In the initial stages of research, the microkinetic method was applied to understand the molecular-level interactions of  $\text{CO}_2$  molecules on the catalyst surface; however, this method does not consider the roles of heat and mass transfer. Thus, with quantum advanced computational modeling, most studies have discussed the reaction kinetics and adsorption energy (Gibbs free energy) of the  $\text{CO}_2$  molecules, intermediates, and products. Experimental kinetics studies have also been used to elucidate the reaction mechanism at the molecular level.<sup>89</sup> The Langmuir–Hinshelwood (LH)-based  $\text{CO}_2$  photoreduction kinetic model can be used to obtain insights into the reacting reagent species, with both the numerator and denominator terms in eqn (9):

$$r = kI^\alpha \times \frac{\prod_{i=1}^n k_i p_i}{\left(1 + \sum_{i=1}^z k_i P_i\right)} \quad (9)$$

where  $r$  is the rate of reaction ( $\mu\text{mol g}_{\text{cat}}^{-1} \text{h}^{-1}$ ),  $k$  is the rate constant ( $\mu\text{mol g}_{\text{cat}}^{-1} \text{h}^{-1}$ ),  $I$  is the irradiance ( $\text{W m}^{-2}$ ),  $\alpha$  is the reaction order of light intensity (dimensionless),  $K_i$  denotes the



equilibrium adsorption constants for the reactants and products (bar<sup>-1</sup>),  $P_i$  denotes the partial pressures of the reactants and products (bar),  $n$  denotes the adsorbed reactants involved in the primary surface reaction, and  $z$  designates all reactants and products.<sup>194</sup> Thus, to explain the microkinetics, the LH-based model has been used effectively under light transport, scattering, and the heat and mass transfer during the molecular rearrangements. The LH-based photoreduction model has also been applied to describe CO<sub>2</sub> and H<sub>2</sub>O diffusion inside the photocatalytic material.

Initially, this theory was primarily used to obtain insights into the electronic structure. Moreover, this theory is mainly dependent upon quantum calculations; it uses the exchange correlation functional to map the interaction electron to the non-interaction electron system, affording the ground state density. Two main types of approximation are used in these calculations, namely, the local density approximation and the generalized gradient approximation (GGA). In the former case, the calculation depends upon the functional electronic density at a given point in space, which leads to a substantial drawback.<sup>195,196</sup> Although the local density approximation provides an insight into the atomic energies and energy barriers, it has several disadvantages. Thus, a new approach referred to as the Hubbard model was introduced because the local density and generalized gradient approximations failed to explain the transition metals.<sup>197</sup> Various strategies have incorporated the gradient wave (GW) estimation, which yields excellent outcomes for bandgaps, and the Bethe-Salpeter equation (BSE) for absorption spectra.<sup>198</sup> These techniques are regularly used because of their unusually low computational expense. The precision of the DFT approach is heavily dependent upon the functionals used. In *ab initio* studies, the GGA is most commonly performed using the Perdew-Burke-Ernzerhof (PBE) functional. DFT can be used to evaluate the stability of a photocatalyst and the adsorption energies of CO<sub>2</sub> and the intermediate products. Here, we discuss some representative results involving theoretical calculations pertaining to CO<sub>2</sub> photoreduction.<sup>199</sup>

Li *et al.* performed DFT calculations to examine the catalytic activation of CO<sub>2</sub> on Cu<sub>2</sub>O(110) surfaces.<sup>200</sup> Cu<sub>2</sub>O has been identified as a remarkable candidate for CO<sub>2</sub> photoreduction owing to its unique electrical and optical properties. Different crystal facets often display distinct catalytic properties; for instance, Cu<sub>2</sub>O nanocrystals with (100) or (110) surfaces slowly decompose during the reaction, whereas the Cu<sub>2</sub>O(111) surface has been theoretically shown to possess high stability and rhombic dodecahedral nanocrystals exhibit optimum photocatalytic activity. The DFT study used the Vienna Ab initio Simulation Package (VASP) to simulate the Cu<sub>2</sub>O(110) surface morphology and calculate the energies during CO<sub>2</sub> and CO adsorption. Projector augmented-wave (PAW) atomic pseudopotentials were utilized with a cutoff energy of 400 eV for the plane wave basis set, while the GGA with the PBE parametrization was utilized for the exchange correlation functional. GGA is significantly affected by 3d electrons, so the development energies of 3d transition-metal oxides shows large in fault. Furthermore, to examine the active sites responsible for the catalytic activity, the authors

simulated the grazing-incidence X-ray absorption near-edge structure (XANES) by the Grazing-incidence X-ray absorption near-edge structure (GIXANES).<sup>200</sup> It is also matched in surface studies due to the limited penetration depth and small X-ray incident angle. In this work, to simulate the surface behavior, only several key layers of the Cu<sub>2</sub>O(110) section were considered for the slab model. The calculated spectra for the few layers of Cu particles on the ideal surface are presented in Fig. 13(a). The calculated spectra for ideal, O-deficient, and CO<sub>2</sub>-adsorbed (CO<sub>2,O-vac</sub>) surfaces utilizing the few layers, along with the corresponding second-derivative spectra, are shown in Fig. 13(b). These spectra were adjusted by coordinating with the edge positions of the surface slab. As shown in Fig. 13(b), the three types of surface displayed similar spectral shapes with small changes in the intrinsic energies. Compared with the ideal surface, the edge position (zero point of the second derivative) of the O-deficient surface displayed a shift toward lower energy of approximately 0.3 eV. After CO<sub>2</sub> adsorption, the edge position moved back toward higher energy, which validates the increase of the surface Cu oxidation states because of the charge transfer to the CO<sub>2</sub> atom. Hence, aligned spectra of before changing the oxidation state (Cu) and after changing the oxidation both spectra gives the information with rising the energy edges; the changes in the surface oxidation states manifest themselves as changes in the energy of the rising edges.

Tafreshi *et al.* performed DFT calculations for a Ag<sub>3</sub>PO<sub>4</sub>/g-C<sub>3</sub>N<sub>4</sub> nanocomposite to elucidate its electronic properties and photocatalytic activity.<sup>202</sup> The VB was composed of the d orbitals of Ag and the p orbitals of O, while the CB consisted of the p orbitals of C and N and the s orbital of Ag. The bandgap decreased from 2.75 eV for pristine Ag<sub>3</sub>PO<sub>4</sub> and 3.13 eV for single-layer g-C<sub>3</sub>N<sub>4</sub> to only 2.52 eV for the Ag<sub>3</sub>PO<sub>4</sub>/g-C<sub>3</sub>N<sub>4</sub> nanocomposite. The authors also studied the adsorption geometries and energies of the reaction intermediates for CO<sub>2</sub> photoreduction. The heterostructure was found to be thermodynamically favorable for CO<sub>2</sub> reduction and displayed high selectivity for CH<sub>4</sub>. The intermediates HCOOH\* and HOCOH\* were responsible for the generation of CH<sub>4</sub>. The most exothermic calculated reaction energy (-2.826 eV) was that for the conversion of *trans*-COOH to HCOOH\*, during the least reaction energy (-0.182 eV) for the hydrogenation of CH<sub>2</sub>O\* to CH<sub>2</sub>OH\* and HCO\* to *cis*-HCOH. The results revealed that the Ag atoms at the interface of Ag<sub>3</sub>PO<sub>4</sub> and C<sub>3</sub>N<sub>4</sub> served as charge recombination centers. In addition, the calculations indicated that the Ag atoms formed midgap states at the interface, leading to a smaller bandgap for this nanocomposite.

Furthermore, Zhao *et al.* conducted DFT calculations of metal/ZnO nanocomposites based on Au, Ag, or Pd and porous ZnO nanosheets (NSs) to investigate the molecular-level reaction mechanism.<sup>201</sup> The calculated potential energy diagrams for CO<sub>2</sub> to CH<sub>4</sub> conversion on the nanocomposites are presented in Fig. 13(c)-(f). The calculated adsorption energies were 0.29 eV on pristine ZnO NSs, -2.07 eV on Au/ZnO NSs, -1.89 eV on Ag/ZnO NSs, and -1.74 eV on Pd/ZnO NSs. A stable HCO<sub>2</sub> hydrogenation intermediate (CO<sub>2</sub>\* + H → HCO<sub>2</sub>\*) bonded with the ZnO nanosheet was considered for understanding the



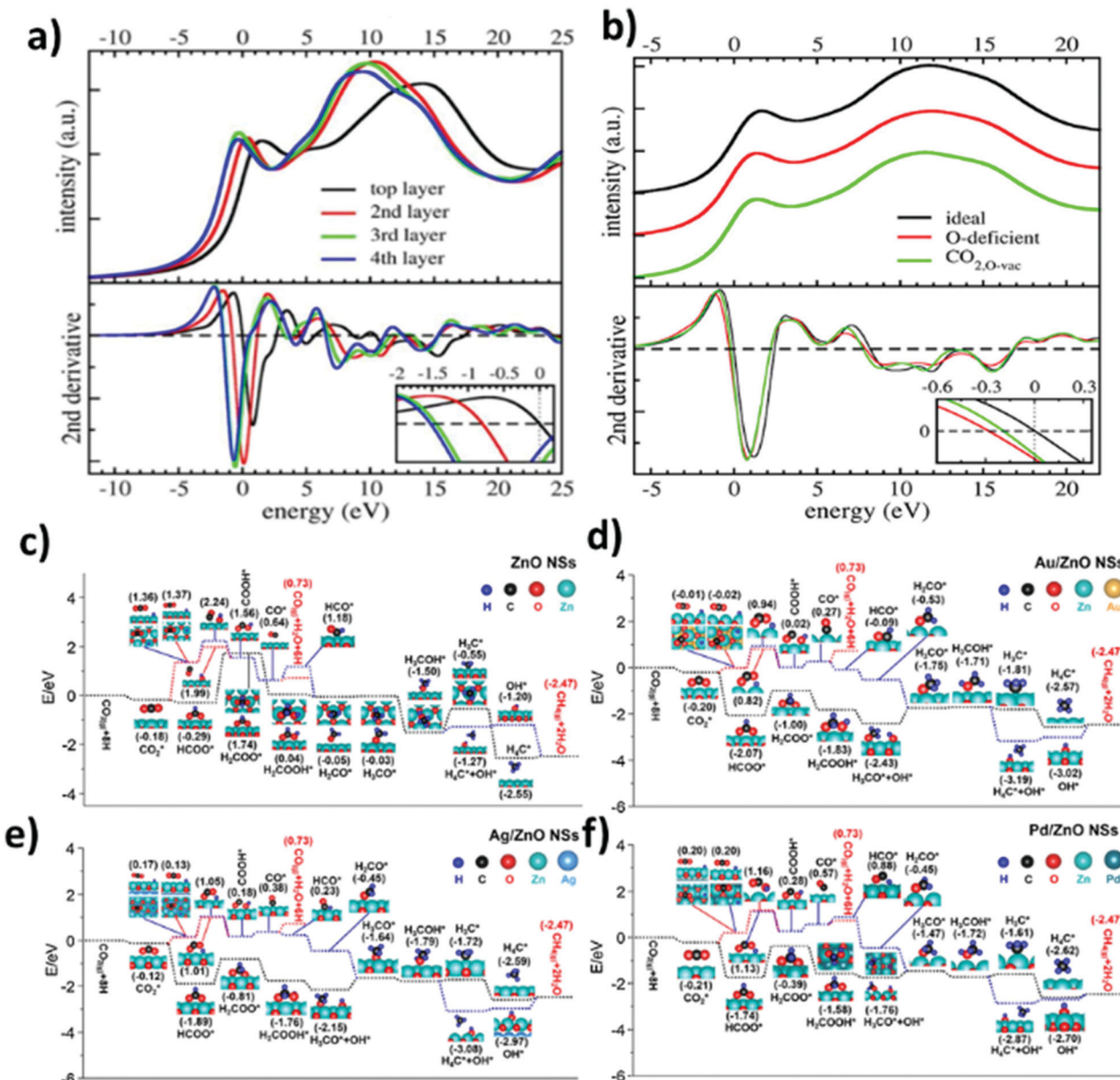


Fig. 13 Calculated Cu K-edge XANES spectra for (a) Cu atoms on a  $\text{Cu}_2\text{O}(110)$  surface and (b) ideal, O-deficient, and  $\text{CO}_2$ -adsorbed  $\text{Cu}_2\text{O}(110)$  surfaces. Reprinted with permission from ref. 200, Copyright 2018, American Chemical Society. (c)–(f) Calculated potential energy ( $E$ , eV) diagrams for the  $\text{CO}_2$  to  $\text{CH}_4$  reaction on (c)  $\text{Zn}_{49}\text{O}_{49}$ , (d)  $\text{Zn}_{49}\text{O}_{49}/\text{Au}_{128}(111)$ , (e)  $\text{Zn}_{49}\text{O}_{49}/\text{Ag}_{128}(111)$ , and (f)  $\text{Zn}_{36}\text{O}_{36}/\text{Pd}_{98}(111)$ . Reproduced with permission from ref. 201, Copyright 2019, Elsevier.

reaction mechanism. The loading of metals on the Zn nanosheets reduced the adsorption energy, confirming the thermodynamic feasibility of the first step of hydrogenation. After that new rate-determining reaction mechanism was studied, which is observed during the dehydroxylation process. The adsorption enthalpies decreased in the order of  $\text{Au/ZnO NSs}$  (+0.68 eV) >  $\text{Ag/ZnO NSs}$  (+0.51 eV) >  $\text{Pd/ZnO NSs}$  (+0.29 eV). Thus, it was concluded that the loading of metal nanoparticles altered the molecular pathway for the conversion of  $\text{CO}_2$  to  $\text{CH}_4$ .

Overall, the determination of precise reaction intermediates and pathways using DFT calculations remains challenging. However, this approach at least provides supporting evidence

for experimental observations. Furthermore, our understanding of the interactions of protons with photocatalyst surfaces is becoming more advanced, although there is still room for improvement. More investigation of the influence of electronically excited states and the solvent on photocatalyst performance is needed. Irrespective of their known limitations, GGA pseudopotentials with basic van der Waals corrections are the principal methodology. Later on, more extensive screening effects will be considered for realizing further improvements in photocatalysts. In addition, to enhance the photocatalytic performance to large scale production, we have to estimate the electronic distribution of catalyst.



## 4.2 Equations for gas-phase CO<sub>2</sub> photoreduction and CO<sub>2</sub> electrochemical reduction

**4.2.1 AQY/TON/TOF/faradaic efficiency.** Many of the terms and equations used in the field of photocatalysis are similar to those used in thermal catalysis. However, some problems can occur if they are directly applied to photocatalysts. For example, although the terms turnover number (TON) and turnover frequency (TOF) appear to have similar meanings,<sup>203</sup> they actually have different definitions in the context of catalysis.<sup>204</sup> TON is the ratio of the number of products ( $N$ ) per number of active sites (N<sub>a</sub>), whereas TOF is TON divided by time ( $t$ ), indicating the frequency of conversion:<sup>98,203,205</sup>

$$\text{TOF (s}^{-1} \text{ m}^{-2}\text{)} = \frac{1}{\text{Na}} \frac{\text{d}N}{\text{d}t} \quad (10)$$

Although this equation is convenient for homogeneous photocatalysts, it is not readily applicable to heterogeneous photocatalysts; because it is difficult to determine the actual active sites and the properties of a heterogeneous catalyst are not directly proportional to its area. In this regard, the efficiency of heterogeneous photocatalysts can be determined in a different way. In photochemistry, for example, the apparent quantum yield (AQY) is often used:<sup>5,93,203,206,207</sup>

$$\text{AQY (\%)} = \frac{\text{Number of reacted electrons}}{\text{Number of incident photons}} \times 100\% \quad (11)$$

$$\text{Number of reacted electrons} = \text{number of moles of product (mol)} \times \text{the number of required electron (8)} \times N_A \quad (12)$$

$$\text{Number of incident photons} = \frac{\text{Light absorbed by photocatalyst}}{\text{Average photon energy}} \times \text{time} \quad (13)$$

$$\text{Light absorbed by photocatalyst} = H (1000 \text{ W m}^{-2}) \times A (\text{m}^2) \quad (14)$$

$$\text{Average photon energy} = \frac{hc}{\lambda} \quad (15)$$

In these equations, N<sub>a</sub> is Avogadro's number ( $6.022 \times 10^{23} \text{ mol}^{-1}$ ),  $h$  is Planck's constant ( $6.626 \times 10^{-34} \text{ J s}^{-1}$ ),  $H$  is the incident light intensity,  $A$  is the irradiation area, and  $c$  is the speed of light ( $3 \times 10^8 \text{ m s}^{-1}$ ). AQY is defined as the ratio of the number of electrons participating in the photocatalytic reaction to the number of photons absorbed within a specified wavelength range, under the assumption that all photons are absorbed by the photocatalyst.<sup>98,203</sup> For example, the number of electrons required for the production of 1 mol of CH<sub>4</sub> by photocatalytic CO<sub>2</sub> reduction can be calculated using eqn (12). The incident photon flux can also be calculated from eqn (13)–(15). In eqn (14), the value of  $H$  for a given reactor can be reliably determined using a reference cell; this value is 1000 W m<sup>-2</sup> at AM 1.5. The average photon energy can be

determined from the incident light wavelength as expressed in eqn (15).<sup>5</sup>

Electrocatalysts have also received considerable attention in the field of CO<sub>2</sub> reduction for mediating specific redox reactions on an electrode surface.<sup>208</sup> Because these electrochemical processes involve electron transfer reactions, the performance is typically measured by the faradaic efficiency (FE):<sup>209–211</sup>

$$\text{FE} = \frac{v f_x P F \alpha}{RTI} \times 100\% \quad (16)$$

where  $x$  denotes the specific gaseous product,  $v$  is the CO<sub>2</sub> flow rate,  $f_x$  is the volume concentration of the product in the gas flow delivered to the gas chromatograph at a given sampling time,  $P$  is the ambient pressure ( $1.05 \times 10^5 \text{ Pa}$ ),  $R$  is the gas constant ( $8.314 \text{ J mol}^{-1} \text{ K}^{-1}$ ),  $T$  is room temperature (298 K),  $\alpha$  is the number of electrons transferred for the CO<sub>2</sub>-to-product conversion (e.g.,  $\alpha_{\text{CO}} = 2$ ),  $F$  is the Faraday constant ( $96\,485 \text{ C mol}^{-1}$ ), and  $I$  is the current at the given sampling time.<sup>209,212–214</sup>

$$\text{EE} = \frac{E^0 \times \text{FE}}{E^0 + \eta} \times 100\% \quad (17)$$

where  $E^0$  is the standard thermodynamic potential, FE is the faradaic efficiency, and  $\eta$  is the overpotential at the applied current density.<sup>212</sup> The denominator of eqn (17) can be derived from the cell voltage ( $E_{\text{cell}}$ ). The energetic efficiency (EE) is generally measured from the cell voltage of a two-electrode system because it is difficult to know the counter-electrode potential and voltage drop by electrolyte.<sup>213</sup> A high EE value means that little energy is required to produce the target product.<sup>214</sup> In the case of FE, we can obtain information about the number of electrons converted to the target product, but it is dependent on the applied potential of the electrochemical reaction. Although EE is the efficiency to consider energy input during electrochemical reaction, EE cannot make quantitative comparisons due to using only two electrode measurement. Jouny *et al.* listed the EE values for electrochemical CO<sub>2</sub> reduction to C<sub>1</sub>–C<sub>3</sub> compounds.<sup>214</sup>

**4.2.2 Efficiency/selectivity for CO<sub>2</sub> reduction.** The most precise method to determine photocatalytic activity is to measure the amount of product. For CO<sub>2</sub> reduction, the photocatalytic performance can be calculated by dividing the amount of product by the reaction time and mass of catalyst:<sup>95,98,207,215</sup>

$$\text{Product yield} (\mu\text{mol g}^{-1} \text{ h}^{-1}) = \frac{(C_{\text{final}} - C_{\text{initial}}) \times \text{volume of product mixture}}{\text{Amount of photocatalyst (g)} \times \text{photoreaction time (h)}} \quad (18)$$

$$\text{Rate of evolution} (\mu\text{mol cm}^2 \text{ h}^{-1}) = \frac{\text{Amount of product} (\mu\text{mol})}{\text{Exposed area of photocatalyst} (\text{cm}^2) \times \text{time (h)}} \quad (19)$$

where  $C$  is the concentration of the mixture.

The plot seems a saturation instead of linear graph because the product formation is not linear over time.<sup>98</sup> Therefore, the average efficiency of a catalyst depends upon the measurement time.



The irradiation time is related to catalytic stability, and it is recommended to use the same reaction time when attempting to compare different catalysts.<sup>216</sup>

When multiple products are present simultaneously, the selectivity for a particular product such as CH<sub>4</sub> or CO can be calculated:<sup>93</sup>

$$\text{Selectivity (\%)} = \frac{\text{Amount of desired product}}{\text{Total amount of all products}} \times 100\% \quad (20)$$

The efficiency can also be expressed by the input *vs.* output (e.g., in terms of energy).<sup>5</sup> In this case, the total mass is usually used as the denominator in eqn (21).<sup>98</sup> This can be calculated using the following equations:<sup>5,217</sup>

$$\eta_{\text{eff}} (\%) = \frac{\text{Thermodynamic energy of product}}{\text{Input light energy}} \times 100\% \quad (21)$$

Thermodynamic energy of product (cm<sup>-2</sup> h<sup>-1</sup>)

$$= [\text{CH}_4] (\text{mol cm}^{-2} \text{ h}^{-1}) \times \Delta H (810 \text{ kJ mol}^{-1}) \quad (22)$$

$$\text{Input light energy (for a 100 mW light source)} = 0.100 \text{ W cm}^{-2} \quad (23)$$

When the products of CO<sub>2</sub> reduction are analyzed by chromatography, the results are measured in ppm. However, when expressed in ppm, it is difficult to immediately understand the actual amount of product. Therefore, many researchers express the amount of product in molar units.<sup>44,218</sup> Some recent reports have confusion in calculation, for example, Sorcar *et al.* reported less accurate assumption and calculation results.<sup>5,93,95</sup> Therefore, we suggest better calculation method that extends the application to gas-phase reactions:<sup>44</sup>

$$\begin{aligned} \text{CH}_4 \text{ yield in } \mu\text{mole} &= [\text{CH}_4 \text{ yield in ppm}] \\ &\times [\text{moles of the gaseous mixture containing CH}_4] \end{aligned} \quad (25)$$

CH<sub>4</sub> yield in ppm

$$\begin{aligned} &= \frac{\mu\text{mol of CH}_4}{\text{moles of gaseous mixture}} \\ &= \frac{\text{Peak area of the CH}_4 \text{ from tested sample}}{\text{Peak area of the standard CH}_4} \times 100\% \end{aligned}$$

$$\text{Moles of gaseous mixture} = \frac{\text{Volume of gaseous mixture (L)}}{\text{Molar volume (L mol}^{-1}\text{)}}$$

$$\begin{aligned} \text{Molar volume} &= \frac{RT}{P} \\ &= \frac{0.08206 \text{ atm L mol}^{-1} \text{ K}^{-1} \times 298 \text{ K}}{1 \text{ atm}} \\ &= 24.45 \text{ L mol}^{-1} \end{aligned}$$

If the performance of photocatalysts can be reliably compared, it will be very beneficial to the field of solar fuel generation. We believe that the equations presented in this

review will prove valuable to researchers and encourage further progress in the field.

## 5 Materials for CO<sub>2</sub> photoreduction

### 5.1 Metal oxides

Metal oxides are widely used in photocatalysis because of their high earth-abundance and exceptional stability under various conditions. Several features of metal oxides are of particular relevance to photocatalysis, such as morphology/composition, light absorption characteristics, and charge transport properties. In 1972, Fujishima and Honda reported the production of hydrogen from TiO<sub>2</sub> under light illumination, which was the starting point for metal oxide-based photocatalysts and attracted worldwide attention.<sup>219</sup> Since then, numerous studies on metal oxide photocatalysts have been conducted. A comparison of metal oxide-based photocatalysts is presented in Table 2.

**5.1.1 Titanium dioxide (TiO<sub>2</sub>).** Besides the aforementioned strategies to improve the CO<sub>2</sub> reduction activity of TiO<sub>2</sub>, numerous other modification approaches have been investigated with respect to the crystal phase, crystal facet, surface defect, addition of cocatalyst, *etc.*

TiO<sub>2</sub> naturally exists in three polymorphs: anatase, brookite, and rutile. Among them, anatase, rutile, and anatase/rutile mixed phase (Degussa, P25) have been extensively studied for CO<sub>2</sub> photoreduction owing to their suitable optoelectronic properties. Brookite is the least commonly reported polymorph in photocatalysis as a result of the difficulty associated with obtaining high-purity brookite nanocrystallites.<sup>257</sup> In 2012, Andino and co-workers performed first-principles calculations on cluster and periodic slab systems to investigate the interaction between CO<sub>2</sub> and the brookite (210) surface.<sup>258</sup> The results indicated that perfect brookite is not a suitable catalyst for CO<sub>2</sub> photoreduction, whereas the oxygen-deficient brookite (210) surface displayed improved performance. Compared with the oxygen-deficient anatase (101) surface, the oxygen-deficient brookite (210) surface exhibited stronger interactions with CO<sub>2</sub>, favoring to form bent CO<sub>2</sub> molecules. In the same year, this group also experimentally studied the use of defective brookite for CO<sub>2</sub> photoreduction and reported that the surface defects (oxygen vacancies and Ti<sup>3+</sup>) provided additional active sites for CO<sub>2</sub> adsorption and activation, leading to improved performance compared to anatase and rutile.<sup>220</sup> *In situ* DRIFTS analysis revealed that the surface oxygen vacancies and Ti<sup>3+</sup> promoted the formation of the CO<sub>2</sub><sup>•-</sup> intermediate and facilitated its rapid reaction with H<sub>2</sub>O to afford higher CO<sub>2</sub> reduction activity to generate CH<sub>4</sub>.

Controlling the crystal facet is also an effective strategy for enhancing photocatalytic activity. Exposing high-energy surfaces, especially reactive crystal facets, has long been considered to increase photocatalytic activity. For instance, anatase TiO<sub>2</sub> is usually dominated by the {101} facet, which is thermodynamically stable. In 2008, a pioneering study by Lu and co-workers reported the synthesis of anatase TiO<sub>2</sub> with a high percentage of exposed {001} facets, which possess high surface energy and reactivity.<sup>259</sup> More recently, Jaroniec and co-workers investigated the



Table 2 Metal oxide-based materials for photocatalytic  $\text{CO}_2$  reduction

Catalyst	Feed gas composition	Light source	Reducing agent	Reaction conditions	Reactor type	Yield	Ref.
$\text{TiO}_{2-x}$	99.999% $\text{CO}_2$ , water bubbler ( $\text{H}_2\text{O}$ vapor)	150 W solar simulator (90 mW $\text{cm}^{-2}$ )	$\text{H}_2\text{O}$	100 mg sample	Flow reactor	$\text{CO}: 17 \mu\text{mol g}^{-1} \text{h}^{-1}$ $\text{CH}_4: 2 \mu\text{mol g}^{-1} \text{h}^{-1}$	220
$\text{TiO}_2$	<i>In situ</i> generated $\text{CO}_2 + \text{H}_2\text{O}$ vapor ( $\text{NaHCO}_3 + \text{HCl}$ )	300 W $\text{Xe}$ lamp	$\text{H}_2\text{O}$	100 mg sample in Pyrex reactor (200 mL)	Batch reactor	$\text{CH}_4: 1.35 \mu\text{mol g}^{-1} \text{h}^{-1}$	221
$\text{TiO}_{2-x}$	$\text{CO}_2 + \text{H}_2\text{O}$	300 W $\text{Xe}$ lamp (AM 1.5 filter)	$\text{H}_2\text{O}$	50 mg sample		$\text{CH}_4: 1.63 \mu\text{mol g}^{-1} \text{h}^{-1}$ $\text{CH}_4: 2.20 \mu\text{mol g}^{-1} \text{h}^{-1}$	188
$\text{TiO}_2/\text{Ni(OH)}_2$	<i>In situ</i> generated $\text{CO}_2 + \text{H}_2\text{O}$ ( $\text{NaHCO}_3 + \text{H}_2\text{SO}_4$ )	350 W $\text{Xe}$ lamp (40 mW $\text{cm}^{-2}$ )	$\text{H}_2\text{O}$			$\text{CO}: 0.71 \mu\text{mol g}^{-1} \text{h}^{-1}$	222
$\text{Pt}/\text{TiO}_2$	$\text{CO}_2 + \text{H}_2\text{O}$	400 W $\text{Xe}$ lamp (UV range, 250–388 nm, 19.6 mW $\text{cm}^{-2}$ )	$\text{H}_2\text{O}$	5 mg sample		$\text{CH}_4: 1361 \mu\text{mol g}^{-1}$ (5 h)	126
$\text{PdCu}/\text{TiO}_2$	$\text{CO}_2 + \text{H}_2\text{O}$	300 W $\text{Xe}$ lamp ( $\lambda < 400$ nm, 2 mW $\text{cm}^{-2}$ )	$\text{H}_2\text{O}$	5 mg sample		$\text{CH}_4: 19.6 \mu\text{mol g}^{-1} \text{h}^{-1}$	129
Au–Cu nanoalloy supported on $\text{TiO}_2$	99.995% $\text{CO}_2 + \text{H}_2\text{O}$	100 W $\text{Xe}$ lamp	$\text{H}_2\text{O}$	Sample film	Batch reactor	$\text{CH}_4: 2000 \mu\text{mol g}^{-1} \text{h}^{-1}$	127
$\text{g-C}_3\text{N}_4/\text{ZnO}$	<i>In situ</i> generated $\text{CO}_2 + \text{H}_2\text{O}$ ( $\text{NaHCO}_3 + \text{H}_2\text{SO}_4$ aqueous solution)	300 W simulated solar Xe arc lamp	$\text{H}_2\text{O}$	100 mg sample		$\text{CH}_3\text{OH}: 0.6 \mu\text{mol g}^{-1} \text{h}^{-1}$	223
$\text{ZnO}/\text{Au/g-C}_3\text{N}_4$	$\text{CO}_2$ (99.999% $\text{CO}_2 + \text{H}_2\text{O}$ )	300 W UV lamp	$\text{H}_2\text{O}$	Film-type sample		$\text{CO}: 862.1 \mu\text{mol m}^{-2} \text{h}^{-1}$	224
$\text{ZnO}/\text{ZnTe}$	$\text{CO}_2$ (99.999% $\text{CO}_2 + \text{H}_2\text{O}$ )	300 W $\text{Xe}$ lamp (420 nm cutoff)	$\text{H}_2\text{O}$	10 mg sample		$\text{CH}_4: 44.564 \mu\text{mol g}^{-1} \text{h}^{-1}$	225
Mo-Doped $\text{WO}_3\cdot0.33\text{H}_2\text{O}$	$\text{CO}_2$ (400 ppm, $\text{N}_2$ -based) + $\text{H}_2\text{O}$ (0.5 mL)	500 W $\text{Xe}$ lamp	$\text{H}_2\text{O}$	25 mg sample in closed Pyrex reactor (600 mL)		$\text{CH}_4: 5.3 \mu\text{mol g}^{-1} \text{h}^{-1}$	226
Ag-Modified $\text{ZnGa}_2\text{O}_4$	$\text{NaHCO}_3 + \text{CO}_2$	400 W high-pressure Hg lamp	$\text{H}_2\text{O}$	1.0 g sample	Flow reactor	$\text{CO}: 155.0 \mu\text{mol g}^{-1} \text{h}^{-1}$ $\text{H}_2: 8.5 \mu\text{mol g}^{-1} \text{h}^{-1}$ $\text{CH}_3\text{OH}: 74.3 \mu\text{mol g}^{-1} \text{h}^{-1}$	227
$\text{Ga}_2\text{O}_3$	$\text{NaHCO}_3 + \text{CO}_2$	UV light ( <i>ca.</i> 254 nm, 1.3 mW $\text{cm}^{-2}$ )	$\text{H}_2\text{O}$	100 mg sample		$\text{CO}: 100 \mu\text{mol g}^{-1} \text{h}^{-1}$	228
$\text{Pt/Zn-}\beta\text{-Ga}_2\text{O}_3$ nanorods	$\text{CO}_2/\text{H}_2\text{O}$ (99.999% $\text{CO}_2 + 20 \mu\text{L H}_2\text{O}$ )	15 mW UV-C lamps (5.94 mW $\text{cm}^{-2}$ )	$\text{H}_2\text{O}$	15 mg sample		$\text{CH}_3\text{OH}: 0.19 \mu\text{mol g}^{-1} \text{h}^{-1}$	229
$\text{Pt-RuO}_2/\text{Zn}_2\text{GeO}_4$	High-purity $\text{CO}_2 + 1 \text{ mL DI}$ 0.4 mL DI ( $\text{H}_2\text{O}$ vapor) High-purity $\text{CO}_2$	300 W $\text{Xe}$ lamp	$\text{H}_2\text{O}$	100 mg sample		$\text{CH}_4: 100 \mu\text{mol g}^{-1} \text{h}^{-1}$	161
$\text{InVO}_4$		300 W $\text{Xe}$ lamp	$\text{H}_2\text{O}$	0.1 g sample		$\text{CO}: 18.28 \mu\text{mol g}^{-1} \text{h}^{-1}$	230
$\text{Bi}_2\text{WO}_6$ (LSPR)	$\text{CO}_2 + \text{H}_2\text{O}$	UV-vis light (200 mW $\text{cm}^{-2}$ )	$\text{H}_2\text{O}$	5 mg sample with 0.2 mL pure water		$\text{CH}_3\text{OH}: 2.0 \mu\text{mol g}^{-1} \text{h}^{-1}$	231
$\text{CuO-Nb}_3\text{O}_8$	0.5 M $\text{KHCO}_3$ aqueous solution, adjusted to pH 12 with $\text{NaOH}$	UV ( $\text{Hg-Xe}$ lamp, 240–300 nm)	$\text{H}_2\text{O}$	Dispersed sample in glass reactor (500 mL)		$\text{CO}: 9.9 \mu\text{mol g}^{-1} \text{h}^{-1}$	232
$\text{CuO}_x\text{-ZnO}$	$\text{CO}_2 + \text{H}_2\text{O}$	300 W $\text{Xe}$ lamp (320–780 nm, 100 mW $\text{cm}^{-2}$ )	$\text{H}_2\text{O}$	5 mg sample		$\text{C}_2\text{H}_4: 2.7 \mu\text{mol g}^{-1} \text{h}^{-1}$ (32.9%)	233
$\text{Co}_3\text{O}_4$	0.5 mL DI (water vapor) 99.999% $\text{CO}_2$	200 W $\text{Xe}$ lamp (100 mW $\text{cm}^{-2}$ )	$\text{H}_2\text{O}$	5 mg sample		$\text{CH}_4: 2.2 \mu\text{mol g}^{-1} \text{h}^{-1}$ (26.9%)	
$\text{Cu-Pt/TiO}_2$	99.999% $\text{CO}_2$ water bubbler	Outdoor sunlight (normalized to a global AM 1.5 value of 100 mW $\text{cm}^{-2}$ )	$\text{H}_2\text{O}$			$\text{CO}: 3.3 \mu\text{mol g}^{-1} \text{h}^{-1}$ Stability: 4 cycles (1 cycle = 8 h)	234
$\text{MgO/Pt-TiO}_2$	$\text{CO}_2$ 4 mL water ( $\text{H}_2\text{O}$ vapor)	100 W $\text{Xe}$ lamp (320–780 nm, 60 mW $\text{cm}^{-2}$ )	$\text{H}_2\text{O}$	20 mg sample		$\text{CO}: 46.3 \mu\text{mol g}^{-1} \text{h}^{-1}$ Stability: 4 cycles (1 cycle = 5 h)	78
$\text{TiO}_{2-x}$	99.999% $\text{CO}_2$ water bubbler ( $\text{H}_2\text{O}$ vapor)	UV: 100 W Hg lamp Visible: 450 W $\text{Xe}$ lamp with UV filter (400–700 nm)	$\text{H}_2\text{O}$	40 mg sample 150 °C		$\text{CH}_4: 11 \mu\text{mol g}^{-1} \text{h}^{-1}$ $\text{CO}: 0.03 \mu\text{mol g}^{-1} \text{h}^{-1}$	235
Ag– $\text{TiO}_2$ (LSPR)	99.9999% $\text{CO}_2 + \text{H}_2\text{O}$	6 W UV lamp (47.23 mW $\text{m}^{-2}$ )	$\text{H}_2\text{O}$	100 mg sample		$\text{CH}_4: 54.5 \mu\text{mol g}^{-1} \text{h}^{-1}$ (1 cycle = 10 h)	236
						$\text{CH}_4: 86.5 \mu\text{mol g}^{-1}$ (15 h)	237

Table 2 (continued)

Catalyst	Feed gas composition	Light source	Reducing agent	Reaction conditions	Reactor type	Yield	Ref.
Pt <sub>1%</sub> -0.50-Graphene/reduced titania	CO <sub>2</sub> + H <sub>2</sub> O	100 W Xe solar simulator with AM 1.5 filter	40 mg sample	Flow reactor	CH <sub>4</sub> ; 37.0 $\mu\text{mol g}^{-1} \text{h}^{-1}$	95	
Cu <sub>1.00%</sub> -Pt <sub>0.35%</sub> -Blue titania	CO <sub>2</sub> + H <sub>2</sub> O	100 W Xe solar simulator with AM 1.5 filter	40 mg sample	Flow reactor	C <sub>2</sub> H <sub>6</sub> ; 11.0 $\mu\text{mol g}^{-1} \text{h}^{-1}$	5	
Hybrid carbon@TiO <sub>2</sub> hollow spheres	<i>In situ</i> generated CO <sub>2</sub> + H <sub>2</sub> O (NaHCO <sub>3</sub> + H <sub>2</sub> SO <sub>4</sub> )	300 W Xe arc lamp without filter	H <sub>2</sub> O	100 mg sample	CH <sub>4</sub> ; 3.0 $\mu\text{mol g}^{-1} \text{h}^{-1}$	238	
Au/TiO <sub>2</sub> /BiVO <sub>4</sub>	CO <sub>2</sub> + H <sub>2</sub> O	300 W Xe arc lamp (area of 3.5 cm <sup>2</sup> )	H <sub>2</sub> O	0.2 g sample	CH <sub>3</sub> OH; 9.1 $\mu\text{mol g}^{-1} \text{h}^{-1}$	239	
ZnFe <sub>2</sub> O <sub>4</sub> /RGO/ln <sub>2</sub> O <sub>3</sub>	CO <sub>2</sub> + H <sub>2</sub> O	300 W Xe arc lamp (area of 3.5 cm <sup>2</sup> )	H <sub>2</sub> O	0.1 g sample in cylindrical reactor (100 mL)	CH <sub>4</sub> ; 7.5 $\mu\text{mol g}^{-1} \text{h}^{-1}$	240	
SnS <sub>2</sub> /SnO <sub>2</sub>	CO <sub>2</sub> (400 mL 99.999% CO <sub>2</sub> + 0.5 mL H <sub>2</sub> O)	300 W Xe lamp	H <sub>2</sub> O	4 mg sample	CO: 8.85 $\mu\text{mol g}^{-1} \text{h}^{-1}$	240	
CeO <sub>2-x</sub> /Au/TiO <sub>2-x</sub>	CO <sub>2</sub> (99.999% CO <sub>2</sub> + H <sub>2</sub> O)	300 W UV (365 nm, 49.5 mW cm <sup>-2</sup> )	H <sub>2</sub> O	50 mg sample	CO: 48.01 $\mu\text{mol g}^{-1} \text{h}^{-1}$	241	
PDA-TiO <sub>2</sub> /UiO-66	CO <sub>2</sub> + H <sub>2</sub> O (NaHCO <sub>3</sub> + H <sub>2</sub> SO <sub>4</sub> )	300 W Xe lamp	H <sub>2</sub> O	50 mg catalyst	CO: 1.68 $\mu\text{mol g}^{-1} \text{h}^{-1}$	242	
PbO/TiO <sub>2</sub> HPJs	CO <sub>2</sub> + H <sub>2</sub> O (NaHCO <sub>3</sub> + H <sub>2</sub> SO <sub>4</sub> )	300 W Xe lamp	H <sub>2</sub> O	50 mg catalyst	CO: 7.52 $\mu\text{mol g}^{-1} \text{h}^{-1}$	243	
TiO <sub>2</sub> /AuCu/ZIF-8	CO <sub>2</sub> (99.999% CO <sub>2</sub> + H <sub>2</sub> O)	300 W Xe lamp (100 mW cm <sup>-2</sup> )	H <sub>2</sub> O	2 × 2 cm <sup>2</sup> film	CH <sub>4</sub> ; 3.57 $\mu\text{mol g}^{-1} \text{h}^{-1}$	244	
Flame-annealed TiO <sub>2</sub> /CuTCPP/P25m	CO <sub>2</sub> (99.999% CO <sub>2</sub> + H <sub>2</sub> O)	AM 1.5G (100 mW cm <sup>-2</sup> )	H <sub>2</sub> O	60 mg catalyst	C <sub>2</sub> H <sub>6</sub> ; 0.59 $\mu\text{mol g}^{-1} \text{h}^{-1}$	245	
PtRu/TiO <sub>2</sub>	CO <sub>2</sub> (99.999% CO <sub>2</sub> + H <sub>2</sub> O)	300 W Xe lamp (80 mW cm <sup>-2</sup> , 320 < $\lambda$ < 780 nm)	H <sub>2</sub> O	100 mg catalyst	CH <sub>4</sub> ; 1.50 $\mu\text{mol g}^{-1} \text{h}^{-1}$	246	
NQCDs/P25	CO <sub>2</sub> (99.999% CO <sub>2</sub> + H <sub>2</sub> O)	300 W Xe lamp	H <sub>2</sub> O	50 mg catalyst	CO: 2.0 $\mu\text{mol g}^{-1} \text{h}^{-1}$	247	
Au/Ag-TiO <sub>2</sub>	CO <sub>2</sub> + H <sub>2</sub>	35 W Xe lamp (20 mW cm <sup>-2</sup> )	H <sub>2</sub>	10 mg catalyst	CH <sub>4</sub> ; 53.21 $\mu\text{mol g}^{-1} \text{h}^{-1}$	248	
Au-MMT/TiO <sub>2</sub>	CO <sub>2</sub> + H <sub>2</sub>	200 W Hg reflector lamp (150 mW cm <sup>-2</sup> )	H <sub>2</sub>	Monolithic support	CH <sub>4</sub> ; 5.99 $\mu\text{mol g}^{-1} \text{h}^{-1}$	249	
ZIF-8/TiO <sub>2</sub>	CO <sub>2</sub> (99.999% CO <sub>2</sub> + H <sub>2</sub> O)	UV: 200 W Hg reflector lamp	H <sub>2</sub>	100 mg Xe lamp	CO: 83 $\mu\text{mol g}^{-1} \text{h}^{-1}$	250	
Pt-1.0-Reduced titania/Pt/TiO <sub>2</sub> /Au18@SiO <sub>2</sub>	1000 ppm CO <sub>2</sub> (He-based) + H <sub>2</sub> O	100 W Xe lamp (100 mW cm <sup>-2</sup> )	H <sub>2</sub> O	100 mg catalyst, 5 bar	UV: CO: 1223 $\mu\text{mol g}^{-1} \text{h}^{-1}$	251	
Coordination polymer of Oslo-27-Mg/TiO <sub>2</sub> /Mesoporous TiO <sub>2</sub>	CO <sub>2</sub> (99.999% CO <sub>2</sub> + H <sub>2</sub> O)	100 W Xe lamp (530 nm)	H <sub>2</sub> O	70 mg catalyst	CH <sub>4</sub> ; 12 $\mu\text{mol g}^{-1} \text{h}^{-1}$		
Cu/TiO <sub>2</sub> -SiO <sub>2</sub>	CO <sub>2</sub> (99.999% CO <sub>2</sub> + H <sub>2</sub> O)	5 W LED lamp (365 nm/365 nm)	H <sub>2</sub> O	32 mg catalyst	Vis: CO: 199 $\mu\text{mol g}^{-1} \text{h}^{-1}$		
Reduced titania-Cu <sub>2</sub> O/CuO-TiO <sub>2-x</sub> N <sub>x</sub>	1000 ppm CO <sub>2</sub> (He-based) + H <sub>2</sub> O	4 W UV lamp (365 nm)	H <sub>2</sub> O	10 mg catalyst	CH <sub>4</sub> ; 42 $\mu\text{mol g}^{-1} \text{h}^{-1}$		
	CO <sub>2</sub> (99.95% CO <sub>2</sub> + H <sub>2</sub> O)	250 W Xe lamp	H <sub>2</sub> O	100 mg catalyst	CO: 45.16 $\mu\text{mol g}^{-1} \text{h}^{-1}$	252	
	CO <sub>2</sub> (99.999% CO <sub>2</sub> + H <sub>2</sub> O)	150 W lamp (90 mW cm <sup>-2</sup> )	H <sub>2</sub> O	50 mg catalyst	CH <sub>4</sub> ; 1.13 $\mu\text{mol g}^{-1} \text{h}^{-1}$	253	
	CO <sub>2</sub> (99.999% CO <sub>2</sub> + H <sub>2</sub> O)	Xe lamp	H <sub>2</sub> O	100 mg catalyst	CO: 4.09 $\mu\text{mol g}^{-1} \text{h}^{-1}$	254	
	CO <sub>2</sub> (99.999% CO <sub>2</sub> + H <sub>2</sub> O)	100 W Xe lamp	H <sub>2</sub> O	40 mg catalyst	CH <sub>4</sub> ; 2.35 $\mu\text{mol g}^{-1} \text{h}^{-1}$	255	
	CO <sub>2</sub> (99.999% CO <sub>2</sub> + H <sub>2</sub> O)	300 W Xe lamp (100 mW cm <sup>-2</sup> )	H <sub>2</sub> O	100 mg catalyst	CO: 0.192 $\mu\text{mol g}^{-1} \text{h}^{-1}$		
			H <sub>2</sub> O	40 mg catalyst	CH <sub>4</sub> ; 0.145 $\mu\text{mol g}^{-1} \text{h}^{-1}$		
			H <sub>2</sub> O	100 mg catalyst	CO: 3.8 $\mu\text{mol g}^{-1} \text{h}^{-1}$	40	
			H <sub>2</sub> O	100 mg catalyst	CH <sub>4</sub> ; 0.68 $\mu\text{mol g}^{-1} \text{h}^{-1}$		
			H <sub>2</sub> O	40 mg catalyst	CO: 60 $\mu\text{mol g}^{-1} \text{h}^{-1}$	87	
			H <sub>2</sub> O	100 mg catalyst	CH <sub>4</sub> ; 10 $\mu\text{mol g}^{-1} \text{h}^{-1}$		
			H <sub>2</sub> O	100 mg catalyst	CH <sub>4</sub> ; 77 $\mu\text{mol g}^{-1} \text{h}^{-1}$	44	
			H <sub>2</sub> O	100 mg catalyst	CH <sub>4</sub> ; 41.3 ppm g <sup>-1</sup> h <sup>-1</sup>	256	

photocatalytic  $\text{CO}_2$  reduction activity of anatase  $\text{TiO}_2$  with co-exposed  $\{001\}$  and  $\{101\}$  facets.<sup>221</sup> DFT calculations of the electronic structures of the two facets revealed that their Fermi levels were located at distinct positions. Therefore, the  $\{001\}$  and  $\{101\}$  surfaces formed surface heterojunctions, which led to efficient photogenerated charge transfer and separation. Anatase  $\text{TiO}_2$  specimens with different ratios of exposed  $\{101\}$  and  $\{001\}$  facets were prepared by the addition of HF solution, and the optimal ratio for photocatalytic  $\text{CO}_2$  reduction was determined to be 45 : 55.

Defective  $\text{TiO}_2$  ( $\text{TiO}_{2-x}$ ) with oxygen vacancies and  $\text{Ti}^{3+}$  was reported to exhibit enhanced visible-light absorption owing to the induced mid-gap band.<sup>103</sup> Although the presence of  $\text{Ti}^{3+}$  improves the absorption of visible light by narrowing the bandgap, it also reduces the reduction potential, leading to slow kinetics for the photocatalytic  $\text{CO}_2$  reduction.<sup>25</sup> In 2018, Xing *et al.* reported that fluorination can improve the reduction potential of  $\text{TiO}_{2-x}$  crystals by replacing surface oxygen vacancies with doped F atoms, resulting in the formation of a built-in electric field (Fig. 14).<sup>188</sup> This finding was supported by DFT calculations indicating an upward shift in the  $\text{Ti}^{3+}$  energy level upon fluorination, leading to a methane production rate of  $1.63 \mu\text{mol g}^{-1} \text{h}^{-1}$  (13 times that for untreated  $\text{TiO}_{2-x}$ ). Recently, Sorcar *et al.* reported facile low-temperature synthesis techniques for reduced  $\text{TiO}_2$ . Reduced  $\text{TiO}_2$  showed narrow band gap, well-aligned band position for  $\text{CO}_2$  reduction reaction, and decreased charge recombination, promoting  $\text{CO}_2$  photoreduction. However, it showed poor reproducibility in  $\text{CO}_2$  conversion performance and less accuracy in equation.<sup>5,93,95</sup>

Morphological engineering has also been explored to increase the photocatalytic  $\text{CO}_2$  reduction efficiency of  $\text{TiO}_2$ . Properly designed structures can help overcome the inherent challenges of photocatalysis such as light absorption. Xu and co-workers found that 1D  $\text{TiO}_2$  nanofibers displayed remarkable photocatalytic  $\text{CO}_2$  reduction activity.<sup>222</sup> This was ascribed to the 1D

morphology enabling increased absorption of reflected and scattered light. Furthermore, the nanofiber structure maximized the number of exposed active sites, ultimately affording high photocatalytic performance. In addition, 2D nanostructured materials have recently attracted substantial attention owing to their remarkable intrinsic properties such as good charge transport and large surface area.<sup>260</sup> For example, compared to bulk materials, ultrathin  $\text{TiO}_2/\text{g-C}_3\text{N}_4$  structures provide short electron transfer pathways, leading to superior photocatalytic  $\text{CO}_2$  reduction activity.

**5.1.2 Other metal oxides.** Numerous studies have been conducted on other metal oxides. For example, Yu *et al.* reported the use of a binary  $\text{g-C}_3\text{N}_4/\text{ZnO}$  photocatalyst synthesized through a one-step calcination process for  $\text{CO}_2$  reduction.<sup>223</sup> UV-vis diffuse reflectance spectra revealed improved sunlight utilization and photocatalytic activity tests indicated enhanced production of  $\text{CH}_3\text{OH}$ . These results demonstrated the benefits of the intimate interfacial contact between the two phases. Moreover, DFT calculations were performed to confirm the electronic band structures and electron transport rates of  $\text{ZnO}$  and  $\text{g-C}_3\text{N}_4$ . The calculated charge carrier effective mass ( $m_c^*$ ) was greatly decreased by the interfacial contact in the binary photocatalyst, leading to more effective electron transfer during the photocatalytic reaction. Furthermore, Li *et al.* reported a  $\text{ZnO}/\text{Au}/\text{g-C}_3\text{N}_4$  (3-ZAC) microneedle film displaying local surface plasmon resonance (LSPR) effects.<sup>224</sup> The Au NPs added to the interface of  $\text{ZnO}/\text{g-C}_3\text{N}_4$  acted as an electron transfer bridge and LSPR excited source for the faster separation of electron-hole pairs. Furthermore, Ehsan and He reported the synthesis of a  $\text{ZnO}/\text{ZnTe}$  photocatalyst with a common cation heterostructure through a one-pot hydrothermal approach.<sup>225</sup> The  $\text{ZnO}/\text{ZnTe}$  photocatalyst possessed a flower-like nanostructure and displayed the heterojunction characteristics of both p-type  $\text{ZnTe}$  and n-type  $\text{ZnO}$ . Through this heterogeneous structure, charge transfer and photocatalytic activity were promoted, allowing the conversion of  $\text{CO}_2$  into  $\text{CH}_4$ . Meanwhile, Wang *et al.* studied homogeneous Mo-doped  $\text{WO}_3 \cdot 0.33\text{H}_2\text{O}$ , which displayed improved photocatalytic activity and selectivity for  $\text{CO}_2$  reduction to  $\text{CH}_4$ .<sup>226</sup> The Mo doping improved the ability of the material to store and localize photogenerated electrons and boosted the transfer of photoexcited electrons, leading to high levels of  $\text{CH}_4$  production.

Wang *et al.* reported a highly crystalline spinel-phase  $\text{ZnGa}_2\text{O}_4$  modified with Ag that exhibited high activity and selectivity toward photocatalytic CO evolution.<sup>227</sup> The optimized the crystal size and specific surface area of the  $\text{ZnGa}_2\text{O}_4$  photocatalyst was synthesized at a calcination temperature of 1123 K for 40 h. Also, by depositing Ag NPs on the  $\text{ZnGa}_2\text{O}_4$  sample surface through the chemical reduction method, well-formed metallic Ag NPs with a small size and good dispersion were obtained, thereby improving the selectivity and increasing CO evolution. Similarly, Akatsuka *et al.* reported the synthesis of a  $\text{Ga}_2\text{O}_3$  photocatalyst with coexisting  $\beta$  and  $\gamma$  phases under optimized calcination conditions, which played an important role in the photocatalytic reduction of  $\text{CO}_2$  and  $\text{H}_2\text{O}$  into CO.<sup>228</sup> The boundaries between the two phases served as active sites for the  $\text{CO}_2$  reduction, while

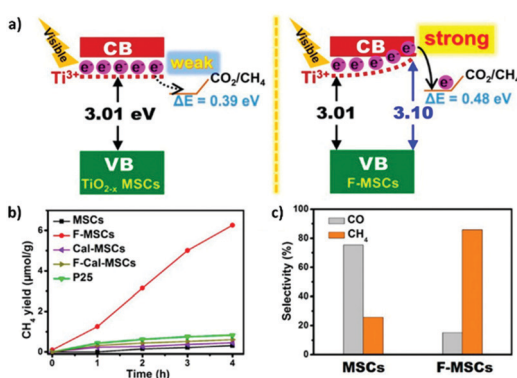


Fig. 14 (a) Schematic illustration of the influence of different  $\text{Ti}^{3+}$  impurity levels between MSCs (mesoporous single crystal) and F-MSCs (Fluorinated MSCs), where  $\Delta E$  represents the kinetic overpotential of the reduction process. (b) Time evolution of  $\text{CH}_4$  production over various samples under solar light irradiation for 4 h (300 W xenon lamp with an AM 1.5 filter,  $\text{CO}_2 + \text{H}_2\text{O}$ ). (c) Selectivity of photocatalytic reduction of  $\text{CO}_2$  and  $\text{H}_2\text{O}$  vapor over MSCs and F-MSCs. Reproduced with permission from ref. 188. Copyright 2018, American Chemical Society.



defects distributed on the  $\text{Ga}_2\text{O}_3$  surface acted as active sites for the water splitting. Furthermore, Yoon *et al.* studied Pt/Zn-embedded  $\beta\text{-Ga}_2\text{O}_3$  nanorods, which improved the reduction of  $\text{CO}_2$  into  $\text{CH}_3\text{OH}$  owing to the synergistic effect of increased defect sites and high charge transfer.<sup>229</sup> In another example, Liu *et al.* used a binary ethylenediamine (En)/water solvent system to synthesize single-crystalline  $\text{Zn}_2\text{GeO}_4$  nanoribbons with lengths of hundreds of micrometers, a thickness of approximately 7 nm (corresponding to five repeating cell units), and aspect ratios (length to width) of up to 10 000:1.<sup>161</sup> In addition, the photoactivity of  $\text{Zn}_2\text{GeO}_4$  was improved in terms of  $\text{CH}_4$  generation, which was ascribed to the following reasons: (i) a high specific surface area of 22.87  $\text{m}^2 \text{ g}^{-1}$ ; (ii) improved crystal quality, eliminating the possibility of any grain boundaries and/or other interfaces; (iii) the ultralong longitudinal dimensions of the nanoribbons, which provided sufficiently spacious transport channels for charge separation; and (iv) the ultrathin geometry of the nanoribbons, which allowed charge carriers to move rapidly from the interior to the surface for participation in the photoreduction reaction.

Layered  $\text{Bi}_2\text{WO}_6$  is another candidate catalyst and the most studied layered oxide material for photocatalytic applications owing to its suitable bandgap of 2.8 eV, which enables light harvesting in the visible region. Several studies on  $\text{Bi}_2\text{WO}_6$  materials in conjunction with other metal NPs, semiconductors, and carbon-based materials have been reported. For example,

Kong *et al.* anchored CQDs on ultrathin  $\text{Bi}_2\text{WO}_6$  (UBW) nanosheets using a single-step hydrothermal process.<sup>261</sup> This anchoring afforded extended light absorption in the visible-NIR region. In addition, the hybrid photocatalyst displayed several significant advantages for  $\text{CO}_2$  photoreduction, such as (i) the exposed active facets (001) of UBW improving  $\text{CO}_2$  adsorption, (ii) CQDs up-converted photoluminescence properties, and (iii) the electron-withdrawing nature of CQDs. Catalytic  $\text{CO}_2$  conversion was performed in a gas-phase flow reactor system under illumination from a 500 W Xe lamp. The optimized catalyst exhibited photocatalytic  $\text{CO}_2$  reduction into  $\text{CH}_4$  with a catalytic activity of 7.19  $\mu\text{mol g}^{-1}$ , which was approximately 9.5 and 3 times greater than those observed for bare  $\text{Bi}_2\text{WO}_6$  nanoplatelets and UBW, respectively. In 2019, Kong and co-workers demonstrated a surface-engineered 2D/2D p-n heterojunction catalyst based on  $\text{Bi}_2\text{WO}_6/\text{BiOI}$  (*i.e.*, BWO/BOI).<sup>262</sup> Oxygen-vacant BWO (BWO-OV) nanosheets were synthesized by a hydrothermal approach and then self-assembled with BOI. Fig. 15(a) shows the crystal structure of BWO-OV, which displayed intense light absorption in the visible region that extended into the NIR region. Furthermore, the p-n junction heterostructure enhanced the optical absorption over a broad range covering the UV-vis-NIR region (Fig. 15(b)). As a result, the optimized BWO-OV/BOI heterostructure exhibited the highest catalytic activity for  $\text{CO}_2$  reduction into  $\text{CH}_4$  (18.32  $\mu\text{mol g}^{-1}$ ) compared to other combinations under illumination from a 500 W Xe lamp (Fig. 15(c)). Thus, the coexistence of surface defects

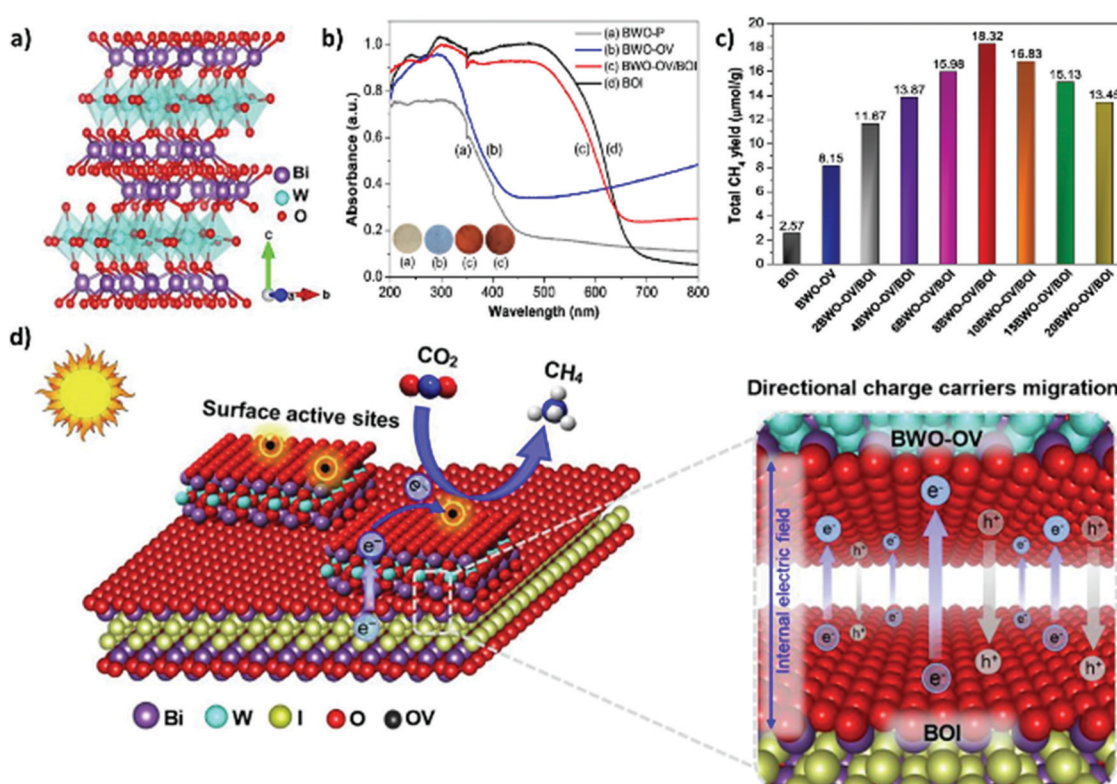


Fig. 15 (a) Crystal structure of oxygen-deficient  $\text{Bi}_2\text{WO}_6$ , (b) UV-vis absorption spectra of various samples, (c) photocatalytic  $\text{CO}_2$  reduction activity of various catalysts toward  $\text{CH}_4$  formation, and (d) schematic illustration of the  $\text{CO}_2$  reduction mechanism on the  $\text{Bi}_2\text{WO}_6/\text{BOI}$  composite. Reproduced with permission from ref. 262, Copyright 2019, Elsevier.



and p-n heterojunctions was demonstrated to effectively improve the optoelectronic performance of the catalyst and ultimately the catalytic activity. The mechanism of photocatalytic  $\text{CO}_2$  reduction to  $\text{CH}_4$  over BWO-OV/BOI is depicted in Fig. 15(d). The oxygen vacancies over BWO significantly enhanced the optical properties, and the p-n heterojunctions established an internal electric field between BWO and BOI that improved the charge separation and hindered electron-hole recombination.

Meanwhile, other researchers have attempted to improve the  $\text{CO}_2$  conversion efficiency of photocatalysts by using metal oxide materials in conjunction with organic and inorganic compounds. Li *et al.* studied a novel Z-scheme ternary hierarchical photocatalyst based on  $\text{ZnFe}_2\text{O}_4$ ,  $\text{In}_2\text{O}_3$ , and reduced graphene oxide (RGO).<sup>240</sup> The combination of  $\text{ZnFe}_2\text{O}_4$  and  $\text{In}_2\text{O}_3$  provided a wide visible-light absorption range and a suitable conduction bandgap position (*ca.*  $-1.5$  eV), while the addition of RGO promoted charge separation by serving as an electron mediator. The synthesis of  $\text{ZnFe}_2\text{O}_4/\text{RGO}/\text{In}_2\text{O}_3$  hollow tubules was confirmed by both steady-state and time-resolved surface photovoltage spectroscopy, which indicated a prolonged photogenerated charge carrier lifetime and improved charge carrier separation compared to bare  $\text{ZnFe}_2\text{O}_4$  and  $\text{In}_2\text{O}_3$ . The most exciting fact is that neither bare  $\text{ZnFe}_2\text{O}_4$  nor  $\text{ZnFe}_2\text{O}_4/\text{In}_2\text{O}_3$  exhibited  $\cdot\text{OH}$  generation in a series of reaction processes, whereas bare  $\text{In}_2\text{O}_3$  and  $\text{ZnFe}_2\text{O}_4/\text{RGO}/\text{In}_2\text{O}_3$  displayed strong signals corresponding to  $\cdot\text{OH}$  as confirmed by EPR analysis. This finding suggests that the photogenerated electrons were transferred from the CB of  $\text{In}_2\text{O}_3$  to the VB of  $\text{ZnFe}_2\text{O}_4$ , resulting in a large quantity of  $\cdot\text{OH}$  groups. These properties allowed the Z-scheme  $\text{ZnFe}_2\text{O}_4/\text{RGO}/\text{In}_2\text{O}_3$  catalyst to exhibit high  $\text{CO}_2$  conversion. Meanwhile, Yin *et al.* reported the synthesis of Cu(II)-grafted  $\text{Nb}_3\text{O}_8$  nanosheets.<sup>232</sup> The small size of the Cu(II) nanoclusters ( $<3$  nm), which were composed of amorphous oxides, promoted the accumulation of excited electrons to drive the efficient multi-electron reduction of oxygen. By grafting the  $\text{Nb}_3\text{O}_8$  nanosheets and Cu(II) cocatalysts, which not only increased the specific surface area of the catalyst but also shortened the electron transport distance,  $\text{CO}_2$  was more effectively converted to CO.

Recently, numerous studies have been conducted on the evolution of  $\text{C}_2$  (*e.g.*,  $\text{C}_2\text{H}_4$ ) and higher hydrocarbons during the photocatalytic  $\text{CO}_2$  reduction.<sup>263</sup> However, this is associated with many challenges owing to the relatively low efficiency of multi-electron transfer and slow dynamics of C-C coupling. The formation of the key intermediates of  $\cdot\text{OC-CO}$  and  $\cdot\text{OC-COH}$  required for the production of  $\text{C}_2$  and higher hydrocarbons from  $\text{CO}_2$  over photocatalysts is also very difficult compared to electrocatalytic reactions.<sup>264,265</sup> Because photocatalysts produce lower electron densities upon light irradiation.<sup>266,267</sup> Wang *et al.* reported the use of  $\text{CuO}_x@\text{p-ZnO}$  to convert  $\text{CO}_2$  into  $\text{C}_2\text{H}_4$ .<sup>233</sup> The authors synthesized the hybrid material by replacing some of the  $\text{Zn}^{2+}$  ions in ZIF-8 with  $\text{Cu}^{2+}$  to afford a uniform Cu/Zn atomic ratio as shown in Fig. 16(a)–(f). XAFS analysis revealed the occurrence of surface changes during the photocatalytic reaction, as shown in Fig. 16(g)–(i). During the photocatalytic  $\text{CO}_2$  reduction, partial reduction of  $\text{Cu}^{2+}$  occurred owing to the transfer of electrons from p-ZnO, resulting in the formation of a  $\text{Cu}^+$  surface layer on the

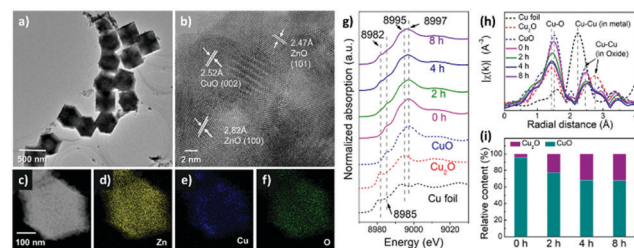


Fig. 16 (a) TEM image, (b) high-resolution TEM image, (c) annular dark-field TEM image, and (d)–(f) elemental mapping images of  $\text{CuO}_x@\text{p-ZnO}$ . (g) Copper K-edge X-ray absorption near-edge structure (XANES) spectra for pristine Cu foil,  $\text{Cu}_2\text{O}$ ,  $\text{CuO}$ , and  $\text{CuO}_x@\text{p-ZnO}$  collected after 0, 2, 4, and 8 h of photoreaction. (h) Fourier-transformed  $k^2$ -weighted ( $\chi(k)$ ) EXAFS spectra and (i) relative contents of  $\text{CuO}$  and  $\text{Cu}_2\text{O}$  on  $\text{CuO}_x@\text{p-ZnO}$  after 0, 2, 4, and 8 h of photoreaction. Reproduced with permission from ref. 233. Copyright 2021, American Chemical Society.

$\text{CuO}_x$  matrix.  $\text{CO}_2$  reduction then took place on the  $\text{CuO}_x$  matrix; following the two-electron reduction to CO, a portion of the generated  $\cdot\text{CO}$  species desorbed to form gaseous CO, while other  $\cdot\text{CO}$  species remained trapped on the  $\text{CuO}_x$  matrix. This enabled subsequent electron transfer to further reduce the surface-bound  $\cdot\text{CO}$  into  $\text{CH}_4$  and  $\text{C}_2\text{H}_4$  *via* the intermediates  $\cdot\text{CHO}$  and  $\cdot\text{OC-COH}$ , respectively. The results indicated that the hybrid  $\text{CuO}_x@\text{p-ZnO}$  catalyst had a lower binding energy than ordinary  $\text{Cu}_2\text{O}$  and a high Gibbs free energy ( $\Delta G$ ) for the formation of the  $\cdot\text{OC-CO}$  intermediate.

## 5.2 Graphene-based photocatalysts

In recent years, graphene, a valuable carbon-based 2D material composed of a single sheet of  $\text{sp}^2$ -hybridized C atoms arranged in a hexagonal lattice,<sup>168</sup> has been the subject of rigorous research owing to its diverse range of potential applications. Graphene exhibits a variety of desirable characteristics, such as electrical conductivity, high surface area (*ca.*  $2600\text{ m}^2\text{ g}^{-1}$ ), and the ability to activate molecules.<sup>268–270</sup> The addition of graphene to photocatalysts has proved beneficial for (i) suppressing the recombination of photogenerated electrons and holes, (ii) enhancing  $\text{CO}_2$  adsorption owing to  $\pi-\pi$  conjugation between graphene and  $\text{CO}_2$ , (iii) activating  $\text{CO}_2$  molecules, (iv) improving the corrosion resistance, (v) increasing the surface area, and (vi) enhancing light absorption,<sup>167,271–276</sup> all of which are advantageous for photocatalysis.

Highly-mobile electrons, which are usually called  $\pi$  electrons, are used to mediate the bonding with other graphene sheets or metals or metal oxides. As a result of this bonding, a strong interaction is developed between the graphene and semiconductor through which the former can readily take away the photogenerated electrons.<sup>277–279</sup> The abundant literature on graphene-based photocatalysts indicates that the Fermi level/work function (0 V *vs.* NHE) of these photocatalysts remains below the CB of many metal oxide-based photocatalysts. Owing to this band alignment, the photogenerated electrons are transferred to the graphene surface, while the holes preferentially remain on the surface of the metal oxide, thereby affording spatial separation of the electrons and holes at the interface.



In contrast, only a few studies have considered the role of graphene as a hole conductor.<sup>95</sup> Illustrative examples of such charge separation by graphene/TiO<sub>2</sub> systems are presented in Fig. 17(a) and (c), in which the presence of graphene remarkably suppressed the charge recombination confirmed by TRPL and PL.

Graphene absorbs the entire solar spectrum owing to its zero bandgap and black color. However, despite this extended range of light absorption, it is unable to provide the photo-generated charges required for CO<sub>2</sub> reduction. To exploit the light harvesting, it is essential to load an appropriate amount of

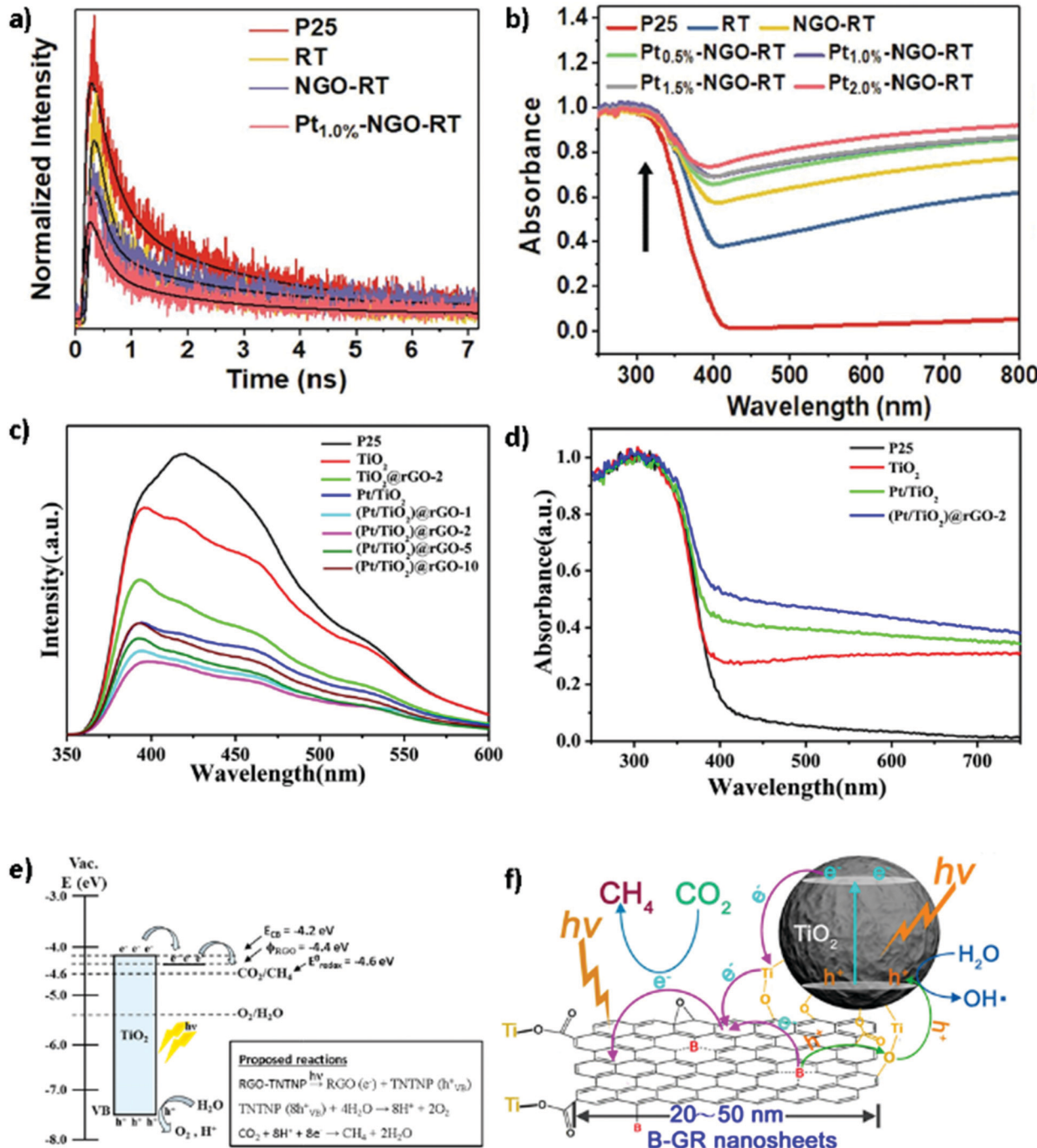


Fig. 17 (a) Time-resolved photoluminescence (PL) spectra and (b) UV-vis spectra for graphene added to reduced TiO<sub>2</sub> (RT). Reproduced with permission from ref. 96, Copyright 2020, Elsevier. (c) PL spectra and (d) UV-vis spectra for graphene added Pt/TiO<sub>2</sub>. Reproduced with permission from ref. 280, Copyright 2016, Elsevier. Illustrative examples of (e) a graphene derivative–metal oxide composite with bandgap alignment and proposed proton-assisted multi-electron reactions, reproduced with permission from ref. 281, Copyright 2013, Elsevier, and (f) TiO<sub>2</sub>/B-GR (boron doped graphene nanosheets) showing the proposed electron–hole transfer reaction, reproduced with permission from ref. 282, Copyright 2013, American Chemical Society.



graphene onto the metal oxide semiconductor. Otherwise, it shields the surface of the photocatalyst and thus obstructs the light absorption and other photocatalytic properties as well by curtailing the generation of the photogenerated pairs. This optimal graphene amount engages in electronic interactions with photocatalysts, *e.g.*,  $\text{TiO}_2$ , by which the absorption is enhanced.<sup>102,283</sup> Almost all of the studies pertaining to grapheme–metal oxide photocatalysts have reported this behavior.<sup>284,285</sup> For example, Li and co-workers reported that the addition of graphene enhanced the light absorption of  $\text{Pt-TiO}_2$ , respectively, as shown in Fig. 17(d).<sup>280</sup> Similar study was also reported by Hiragond and co-workers for hydrothermally grown graphene over reduced  $\text{TiO}_2$  (RT), respectively (Fig. 17(b)).<sup>96</sup>

In addition to the outstanding optoelectronic properties of graphene, its specific surface area is regarded as the maximum among all synthesized materials. Consequently, the use of graphene to prepare photocatalysts can be expected to considerably increase the surface area and therefore the number of exposed reaction sites. These reaction sites of graphene enable  $\pi$ – $\pi$  interactions with  $\text{CO}_2$ , thus increasing its adsorption. In addition,  $\pi$ – $\pi$  conjugation can further destabilize and activate  $\text{CO}_2$ , leading to an appreciable enhancement in the  $\text{CO}_2$  reduction activity.<sup>90,286</sup> Under light irradiation, graphene is known to receive electrons from metal oxides, where they reduce the  $\text{CO}_2$  in the presence of protons, while the leftover holes at the metal oxide oxidize water to generate protons, which is necessary for the  $\text{CO}_2$  reduction. Fig. 17(e) shows the proposed charge transfer and reaction scheme when graphene is used as a cocatalyst or to form heterostructures. In these studies, various geometries of graphene have been used, including QDs and few layers of 2D sheets. In all of these circumstances, the addition of graphene has proved efficacious for improving the optoelectronic properties of the photocatalysts, where the graphene-based photocatalysts were found to harvest light at longer wavelengths. As a result, abundant photogenerated charges were generated and efficiently utilized for  $\text{CO}_2$  reduction owing to the additional role of graphene in preventing these charges from undergoing recombination.<sup>287</sup>

Doped graphene materials, *e.g.*, boron-doped graphene<sup>288</sup> or nitrogen-doped graphene,<sup>289</sup> have also proved efficacious for  $\text{CO}_2$  reduction. Boron doping has been found to alter the morphology of the photocatalyst to afford nanoribbons, which facilitates directional charge transfer, while nitrogen doping enhanced the  $\text{CO}_2$  adsorption. The mechanism of the charge transfer and band alignment for B-GR is depicted in Fig. 17(f).<sup>282</sup>

Some studies have also reported the use of graphene oxide (GO) for photocatalytic  $\text{CO}_2$  reduction through bandgap engineering. In this regard, studies by Chen and co-workers described Cu-modified GO, where the Fermi level of the Cu became more negative owing to electron transfer to Cu, while holes accumulated on the graphene surface.<sup>290</sup> Therefore, this study completely contradicts the previous reports. Sorcar *et al.* reported similar results, where the upward band bending of the  $\text{TiO}_2$  compelled the electrons to remain in the reduced titania while the holes were transferred to GO.<sup>95</sup> The performance of graphene-based photocatalysts is summarized in Table 3.

The combination of graphene with other photocatalytic materials has also been reported to enhance the  $\text{C}_2$  selectivity. For example, Chen and co-workers reported the formation of  $\text{CH}_3\text{CHO}$  over Cu NPs (4–5 nm) anchored on GO, which they ascribed to the effective charge separation at the Cu–GO interface in which the electrons accumulated at Cu while the holes tended to remain on the graphene.<sup>290</sup> Sorcar *et al.* reported a similar type of hole accumulation for their graphene-wrapped blue titania (BT), and they also reported the formation of a  $\text{C}_2$  product ( $\text{C}_2\text{H}_6$ ).<sup>95</sup> They proposed that synergistic effects involving the graphene and electron-enriched  $\text{Ti}^{3+}$  states of BT generated  $\cdot\text{CH}_3$  radicals, which underwent “radical substrate reactions” to form  $\text{C}_2\text{H}_6$ . Zou and co-workers also reported  $\text{C}_2\text{H}_6$  formation owing to these synergistic effects for their graphene– $\text{TiO}_2$  hybrid material.<sup>102</sup>

The literature suggests that graphene wrapping is also conducive for improving photocatalyst stability. One possible reason for this could be the oxidation of water on the graphene surface, which avoids the contact of the photocatalyst with both holes and water. Sorcar *et al.* reported such example, where they used graphene-wrapped reduced BT (G/RBT) deposited with Pt and found that holes were transferred to graphene upon light irradiation.<sup>95</sup> During photocatalytic  $\text{CO}_2$  reduction tests, this material remained stable for six cycles (42 h in total). Another study by Tang and co-workers also reported the efficacy of graphene wrapping for sustaining the photocatalytic performance of  $\text{Cu}_2\text{O}$ .<sup>178</sup> The authors noted that graphene addition allowed the photocatalysts to exhibit continuous and enhanced CO production for almost 20 h, which was longer than that observed for pristine  $\text{Cu}_2\text{O}$  and air-oxidized  $\text{Cu}_2\text{O}$  (Fig. 18(a)). One possible reason for this could be the prevention of oxidation of the  $\text{Cu}_2\text{O}$ . A similar study by Cao and co-workers reported the role of graphene in mitigating Cu oxidation.<sup>186</sup> Upon comparison of the pristine  $\text{Cu}_2\text{O}/\text{TNA}$  with post-reaction (10 h) samples of  $\text{Cu}_2\text{O}/\text{TNA}$  and  $\text{Cu}_2\text{O}/\text{graphene}/\text{TNA}$ , the authors observed the oxidation of Cu for the graphene-free samples. Owing to this beneficial effect of the graphene,  $\text{Cu}_2\text{O}/\text{graphene}/\text{TNA}$  exhibited stable performance over 10 consecutive cycles with a performance loss of only 18%, as shown in Fig. 18(b).

### 5.3 Metal–organic frameworks

Metal–organic frameworks (MOFs) are micro/mesoporous hybrid crystalline materials in which organic linker ligands coordinate and interconnect metal ions or metal cluster nodes. As a result of this coordination network, MOFs possess a porous structure with high pore volume and large surface area. These materials can display physisorption due to van der Waals forces. Thus, MOFs can serve as good absorbents for capturing chemicals such as  $\text{CO}_2$ . To date, MOFs have been applied in numerous research fields, such as gas purification,<sup>302</sup> hydrogen storage,<sup>303</sup> carbon capture,<sup>304</sup> electrocatalysis,<sup>305</sup> photocatalysis,<sup>306</sup> semiconductors,<sup>307</sup> and drug delivery.<sup>308</sup>

Both the organic linker ligands and the metal ions or cluster nodes of MOFs can be tailored for photocatalytic applications. For example, Zecchina and co-workers reported that the metal ions or metal cluster nodes can act as semiconductor QDs,

Table 3 Graphene-based materials for photocatalytic  $\text{CO}_2$  reduction

Catalyst	Feed gas composition	Light source	Reducing agent	Reaction conditions	Reactor type	Yield	Ref.
Graphene-Zn <sub>0.5</sub> Cd <sub>0.5</sub> S	<i>In situ</i> generated $\text{CO}_2$ + $\text{H}_2\text{O}$ (NaHCO <sub>3</sub> + HCl)	300 W Xe arc lamp (400 nm cutoff filter)	$\text{H}_2\text{O}$	100 mg sample in reactor (200 mL)	Gas phase	$\text{CH}_3\text{OH}$ : 1.96 $\mu\text{mol g}^{-1} \text{h}^{-1}$	291
Cu <sub>2</sub> O/graphene/TNA		300 W Xe arc lamp (400 nm cutoff filter)		Double-chamber reactor (250 mL), two-sided sample (calculated area of 1 $\text{cm}^2$ ), proton exchange reaction for 10 h	Liquid phase	$\text{CH}_3\text{OH}$ : 45 $\mu\text{mol cm}^{-2} \text{h}^{-1}$ Stability: 6 cycles	186
Cu/GO	Moist $\text{CO}_2$	300 W halogen lamp (100 mW $\text{cm}^{-2}$ )	$\text{H}_2\text{O}$	100 mg of sample, 300 mL, 2 h	Gas phase	$\text{AQY} = 5.7\%$ $\text{CH}_3\text{CHO}$ : 3.88 $\mu\text{mol g}^{-1} \text{h}^{-1}$ $\text{CH}_3\text{OH}$ : 2.94 $\mu\text{mol g}^{-1} \text{h}^{-1}$ $\text{CH}_4$ : 1.98 ppm $\text{cm}^{-2} \text{h}^{-1}$	290
G-TNT (titania nanotubes)	1000 ppm moist $\text{CO}_2$	100 W Xe arc lamp	$\text{H}_2\text{O}$	Reactor volume: 15.4 $\text{cm}^3$	Gas-phase batch reactor		215
G-Ti <sub>0.91</sub> O <sub>2</sub> hollow spheres	Highly pure moist $\text{CO}_2$	300 W Xe arc lamp	$\text{H}_2\text{O}$	10 mg of sample dispersed in 230 mL reactor	Gas-phase batch reactor	$\text{CH}_4$ : 1.14 $\mu\text{mol g}^{-1} \text{h}^{-1}$ CO: 8.91 $\mu\text{mol g}^{-1} \text{h}^{-1}$	279
RGO-CdS	<i>In situ</i> generated $\text{CO}_2$ + $\text{H}_2\text{O}$ (NaHCO <sub>3</sub> + HCl)	300 W Xe arc lamp ( $\lambda \geq 420$ nm)	$\text{H}_2\text{O}$	100 mg sample in distilled water (10 mL) in glass reactor	Gas phase	$\text{CH}_4$ : 2.51 $\text{g}^{-1} \text{h}^{-1}$ $\text{AQY} = 0.8\%$	275
Graphene-TiO <sub>2</sub>	Moist pure $\text{CO}_2$	300 W Xe arc lamp	$\text{H}_2\text{O}$	0.1 g sample in reactor (230 mL)		$\text{CH}_4$ : 8 $\mu\text{mol g}^{-1} \text{h}^{-1}$ $\text{C}_2\text{H}_6$ : 16.8 $\mu\text{mol g}^{-1} \text{h}^{-1}$ $\text{CH}_4$ : 41.3 $\mu\text{mol g}^{-1} \text{h}^{-1}$ CO: 0.4 $\mu\text{mol g}^{-1} \text{h}^{-1}$	102
(Pt/TiO <sub>2</sub> )/rGO	Moist pure $\text{CO}_2$	300 W Xe arc lamp (320–780 nm)	$\text{H}_2\text{O}$	8 h	Continuous-flow gas-phase reactor	$\text{H}_2$ : 5.6 $\mu\text{mol g}^{-1} \text{h}^{-1}$ $\text{AQY} = 1.93\%$	280
Pt/G/RBT	1000 ppm moist $\text{CO}_2$	100 W Xe arc lamp	$\text{H}_2\text{O}$	40 mg of photocatalyst dispersed over ceramic disc, illuminated for 7 h	Continuous-flow gas-phase reactor	$\text{CH}_4$ : 259 $\mu\text{mol g}^{-1}$ $\text{C}_2\text{H}_6$ : 77 $\mu\text{mol g}^{-1}$ $\text{AQY} = 7.9\%$	95
SEG-P25 nanocomposites	Moist pure $\text{CO}_2$	100 W Hg vapor lamp ( $\lambda = 365$ nm) and 60 W daylight bulb	$\text{H}_2\text{O}$	Teflon reactor (25 mL)	Gas phase	P25 under UV 7.2 times more $\text{CH}_4$ than for P25 under visible 7.2 times more $\text{CH}_4$ than for P25 under visible	165
GR/TiO <sub>2</sub> (graphene-supported $\text{TiO}_2$ nanocrystals)	Moist pure $\text{CO}_2$ (99.999%)	300 W Xe arc lamp ( $300 < \lambda < 400$ nm)	$\text{H}_2\text{O}$	10 mg photocatalyst in reactor (85 mL)		$\text{CH}_4$ : 27.8 $\mu\text{mol g}^{-1} \text{h}^{-1}$ $\text{CO}$ : 70.8 $\mu\text{mol g}^{-1} \text{h}^{-1}$ $\text{AQY} = 0.0847\%$	272
GO-OTiO <sub>2</sub> binary composite	Moist pure $\text{CO}_2$ (99.999%)	15 W daylight bulb	$\text{H}_2\text{O}$		Continuous-flow gas-phase reactor	$\text{CH}_4$ : 1.718 $\mu\text{mol g}^{-1} \text{h}^{-1}$	292
GR/g-C <sub>3</sub> N <sub>4</sub>	Highly pure moist $\text{CO}_2$	15 W daylight bulb	$\text{H}_2\text{O}$	Under ambient temperature and pressure for 10 h	Continuous-flow gas-phase reactor	$\text{CH}_4$ : 5.87 $\mu\text{mol g}^{-1}$	293
Pt-NGO-RT	1000 ppm moist $\text{CO}_2$	100 W Xe arc lamp	$\text{H}_2\text{O}$	40 mg photocatalyst dispersed over ceramic disc, illuminated for 7 h	Gas-phase flow reactor	$\text{CH}_4$ : 252.0 $\text{nmol g}^{-1}$ Stability: 5 cycles	96
Cs <sub>4</sub> PbBr <sub>6</sub> /rGO	Ethyl acetate (solvent)	300 W Xe arc lamp ( $\lambda > 420$ nm)	$\text{H}_2\text{O}$	5 mg sample dispersed in 5 mL of ethyl acetate and 5 $\mu\text{L}$ of water in sealed Pyrex bottle (35 mL), 10 h reaction time	Liquid phase	$\text{CO}$ : 11.4 $\mu\text{mol g}^{-1} \text{h}^{-1}$ Stability: 6 cycles	294
CsPbBr <sub>3</sub> -USGO- $\alpha$ -Fe <sub>2</sub> O <sub>3</sub> (ultrathin and small-size graphene oxide)	Pure $\text{CO}_2$	300 W Xe arc lamp (400 nm filter)	$\text{H}_2\text{O}$	4 mg as-prepared nanomaterial in acetonitrile/deionized water (200: 1 (v/v), 5 mL) in sealed Pyrex bottle (12 mL), 4 h	Gas-phase batch reactor	$\text{CO}$ : 14.6 $\mu\text{mol g}^{-1} \text{h}^{-1}$	295
ZnO/graphene	<i>In situ</i> generated $\text{CO}_2$ + $\text{H}_2\text{O}$ (NaHCO <sub>3</sub> + H <sub>2</sub> SO <sub>4</sub> )	300 W Xe arc lamp	$\text{H}_2\text{O}$	50 mg photocatalyst, 200 mL		$\text{CO}$ : 3.38 $\mu\text{mol g}^{-1} \text{h}^{-1}$ $\text{CH}_4$ : 0.59 $\mu\text{mol g}^{-1} \text{h}^{-1}$ $\text{CH}_3\text{OH}$ : 0.09 $\mu\text{mol g}^{-1} \text{h}^{-1}$ Stability: 5 cycles	296
Ni@GC	High-purity $\text{CO}_2$ (99.999%)	300 W Xe arc lamp (420 nm long-pass cutoff filter)	$\text{H}_2\text{O}$	Triethanolamine (TEOA)	Liquid phase	$\text{CO}$ : 27.0 $\mu\text{mol g}^{-1}$ $\text{H}_2$ : 9.0 $\mu\text{mol g}^{-1}$ Stability: 5 cycles	297



Table 3 (continued)

Catalyst	Feed gas composition	Light source	Reducing agent	Reaction conditions	Reactor type	Yield	Ref.
AgCuInS <sub>2</sub> -graphene-TiO <sub>2</sub>	Pure CO <sub>2</sub> gas (filling for 500 W metal halide lamp 30 min)		Na <sub>2</sub> SO <sub>3</sub> (hole scavenger)	100 mg photocatalyst dissolved in 50 mL of 0.04 M NaHCO <sub>3</sub> , under UV light	Liquid-phase batch reactor	CH <sub>3</sub> OH: 15.21% of reaction mixture	298
LaYAgO <sub>4</sub> -Graphene-TiO <sub>2</sub>	Carbonated water	500 W metal halide lamp		150 mg in 50 mL carbonated water, 48 h		AQY = 1.175%	299
rGO-CuO	CO <sub>2</sub> saturated with water/DMF	20 W white LED bulb (85 W m <sup>-2</sup> )	H <sub>2</sub> O/DMF	24 h	Liquid phase	CH <sub>3</sub> OH: 1945.9 nmol g <sup>-1</sup> h <sup>-1</sup> (12.27% of reaction mixture)	299
rGO-TiO <sub>2</sub> NPs	1000 ppm moist CO <sub>2</sub>	100 W Xe arc lamp	H <sub>2</sub> O	2.0 × 2.0 cm <sup>2</sup> photocatalyst film in reactor (15.4 mL)	Gas phase	CH <sub>4</sub> : 1228.0 μmol g <sup>-1</sup> h <sup>-1</sup> Stability: 6 cycles	300
N-Doped graphene-CdS	Moist pure CO <sub>2</sub>	350 W Xe arc lamp (420 nm cutoff filter)		50 mg photocatalyst, 3 h	Gas phase	CH <sub>4</sub> : 5.67 ppm cm <sup>-2</sup> h <sup>-1</sup> CO: 2.59 μmol g <sup>-1</sup> h <sup>-1</sup> CH <sub>4</sub> : 0.33 μmol g <sup>-1</sup> h <sup>-1</sup> Stability: 4 cycles	301

while the organic ligand linkers can play the role of antennas for sensitizing the QDs.<sup>309</sup> In terms of functionalizing MOFs, post-synthesis modification (PSM) is the general method for anchoring catalytic sites to MOFs to increase their photocatalytic activity. MOFs can be modified with proper combination of nodes and organic linking groups by anchoring photocatalytically active species. This affords a single photocatalytic reaction site, in contrast to other PSM methods that lead to heterogeneously scattered sites. Catalytically active species supported on MOFs prepared *via* PSM methods have been designed to meet a variety of catalytic applications. However, MOFs may lose their catalytic selectivity or performance if the anchored catalytic sites on the ligands induce unexpected forms by interactions between the metal complexes and a solid surface.

To solve this problem, Dengrong *et al.* used MOF-253-Ru(CO)<sub>2</sub>Cl<sub>2</sub>, which is constructed by MOF-253 supported Ru carbonyl complex.<sup>310</sup> MOF-253 was adopted as a platform for constructing a photocatalytic system that displayed improved charge transfer. MOF-253-Ru(CO)<sub>2</sub>Cl<sub>2</sub> exhibited a photocatalytic CO<sub>2</sub> conversion rate of 8.23 μmol g<sup>-1</sup> h<sup>-1</sup> for HCOO<sup>-</sup> under visible-light irradiation for 8 h. Ru(bpy)<sub>2</sub>Cl<sub>2</sub> was used to photo-sensitize MOF-253-Ru(CO)<sub>2</sub>Cl<sub>2</sub> in the visible region through *N,N*-chelation of the Ru(bpy)<sub>2</sub>Cl<sub>2</sub> by the MOF-253 surface sites to afford immobilized [Ru(bpy)<sub>2</sub>(X<sub>2</sub>bpy)]<sup>2+</sup> on the MOF surface. Li *et al.* synthesized a Cu<sub>3</sub>(BTC)<sub>2</sub>@TiO<sub>2</sub> hybrid photocatalyst possessing the unique structure shown in Fig. 19(a), consisting of a Cu<sub>3</sub>(BTC)<sub>2</sub> octahedral microcrystal core and TiO<sub>2</sub> shell. The TiO<sub>2</sub> semiconductor shell underwent facile photoexcitation to produce excitons. In addition, the TiO<sub>2</sub> shell and Cu<sub>3</sub>(BTC)<sub>2</sub> core afforded a microporous structure that favored the capture of gas molecules in the catalyst core and provided photocatalytic reaction sites. The photoexcited electrons produced on the TiO<sub>2</sub> shell were transferred to the interface state of Cu<sub>3</sub>(BTC)<sub>2</sub>@TiO<sub>2</sub> (Fig. 19(b)), whereupon they activated CO<sub>2</sub> on the Cu sites of Cu<sub>3</sub>(BTC)<sub>2</sub>. Cu<sub>3</sub>(BTC)<sub>2</sub>@TiO<sub>2</sub> showed a CH<sub>4</sub> production of 2.64 μmol g<sup>-1</sup> h<sup>-1</sup> (Fig. 19(c)). In other words, the core–shell structure of this MOF-based semiconductor was well constructed to produce excitons and provide a microporous core for gas molecule capture.<sup>311</sup>

In another study, Kong and co-workers designed a core–shell halide perovskite@MOF composite with enhanced CO<sub>2</sub> reduction activity.<sup>312</sup> Coating of the ZIF shell onto the surface of CsPbBr<sub>3</sub> was achieved *in situ* by dispersing CsPbBr<sub>3</sub> QDs in a mixture of the metal precursor and imidazole ligand (Fig. 19(d)). This coating and the increased charge separation efficiency were key factors underlying the observed CH<sub>4</sub> selectivity. where the improved moisture stability of the CsPbBr<sub>3</sub> QDs, CO<sub>2</sub> capture ability, and charge separation efficiency contributed to the enhanced photoconversion efficiency of CO<sub>2</sub> into CO and CH<sub>4</sub>. Two different ZIFs were prepared: (i) ZIF-8 using a Zn precursor and (ii) ZIF-67 using a Co precursor. CsPbBr<sub>3</sub> was then coated onto the ZIFs, as demonstrated by TEM images, STEM images, and elemental mapping data. The Co-based ZIFs acted as a cocatalyst for CsPbBr<sub>3</sub> to improve the optical properties of the hybrid sample CsPbBr<sub>3</sub>/ZIF-67 compared to pristine CsPbBr<sub>3</sub> and the Zn-based

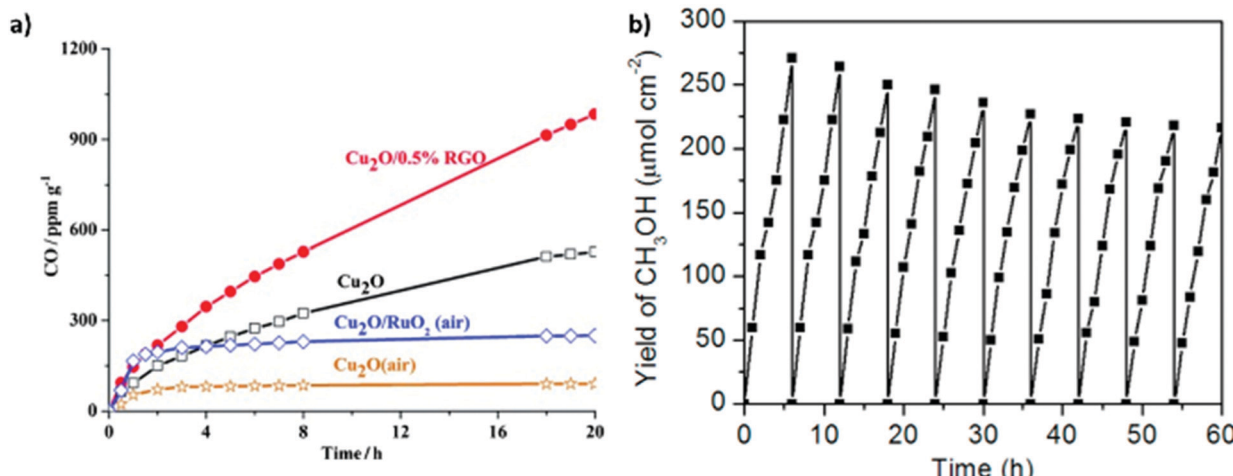


Fig. 18 Stability exhibited by (a) Cu<sub>2</sub>O upon the addition of graphene. Reproduced with permission from ref. 178, Copyright 2014, NCBI and (b) stability exhibited by Cu<sub>2</sub>O/TNA upon the addition of graphene. Reproduced with permission from ref. 186, Copyright 2016, Elsevier.

composite, resulting in high catalytic activity for CO<sub>2</sub> reduction into CO and CH<sub>4</sub> with an electron consumption rate of 29.630 μmol g<sup>-1</sup> h<sup>-1</sup>. The catalyst also displayed high stability over six cycles.

Xu *et al.* synthesized a photocatalytically activated porphyrin-based semiconducting PCN-222 system (Fig. 19(e)) that exhibited superior efficiency to the ligand alone.<sup>313</sup> The high CO<sub>2</sub> capture ability of the MOF in acetonitrile effectively increased the photocatalytic efficiency. Furthermore, the results of PL spectroscopy and ultrafast transient absorption spectroscopy revealed that highly stable electron trap states of PCN-222 suppressed electron–hole recombination, thus improving the photocatalytic CO<sub>2</sub> conversion efficiency.

Dong *et al.* reported the bimetallic MOF PCN-250-Fe<sub>2</sub>M (M = Mn, Zn, Ni, Co), which displayed improved photocatalytic activity and selectivity for reducing CO<sub>2</sub> into CO compared to the monometallic analogue PCN-250-Fe<sub>3</sub>.<sup>314</sup> PCN-250-Fe<sub>3</sub> and PCN-250-Fe<sub>2</sub>M were synthesized by a solvothermal method (Fig. 19(f)), in which the Fe<sup>II</sup> metal ions of the Fe<sub>2</sub><sup>III</sup>Fe<sup>II</sup> metal cluster of PCN-250-Fe<sub>3</sub> could be replaced with other M<sup>II</sup> species (M = Mn, Zn, Ni, Co). In the conversion of CO<sub>2</sub> to CO, formation of the carboxyl intermediate (\*COOH) is the rate-limiting step for CO<sub>2</sub> reduction. DFT calculations indicated that doping with the second metal enhanced the adsorption of CO<sub>2</sub> molecules and restrained the hydrogen evolution reaction (HER). Therefore, the photocatalytic efficiency and selectivity for the conversion of CO<sub>2</sub> to CO improved for all of the bimetallic PCN-250-Fe<sub>2</sub>M derivatives compared to PCN-250-Fe<sub>3</sub>. In particular, the Mn-containing bimetallic catalyst PCN-250-Fe<sub>2</sub>Mn displayed the highest photocatalytic CO formation rate of 21.51 mmol h<sup>-1</sup> g<sup>-1</sup> under visible-light irradiation, as shown in Fig. 19(g).

Various approaches have been explored for increasing the photocatalytic efficiency of MOF-based photocatalysts, such as the use of semiconductors and perovskites, regulating the combination of metal ion or complex, and the introduction of trap sites. It is also possible to enhance the efficiency by tuning the light absorption sites through bandgap engineering. Meanwhile, the

selectivity can be improved by modifying the CO<sub>2</sub> adsorption sites. However, long-term stability is still a key limitation of MOF-based photocatalysts. The photocatalytic CO<sub>2</sub> reduction performance of MOF-based photocatalysts is summarized in Table 4.

#### 5.4 Transition-metal dichalcogenides

Two-dimensional materials are emerging nanomaterials that possess interesting electrical and optical properties. These materials may consist of a single layer or several layers but are typically less than 5 nm in thickness. In contrast, the lateral size may be several hundred nanometers. Transition-metal dichalcogenides (TMDCs) are superior 2D materials such as MoS<sub>2</sub>, WS<sub>2</sub>, SnS<sub>2</sub>, MoSe<sub>2</sub>, and WSe<sub>2</sub>.<sup>316</sup> TMDCs have attracted substantial attention owing to their low cost and excellent catalytic activity, which is comparable to that of noble metals. The TMDC nanostructure contains active sites on both edges and basal planes that provide opportunities for electrocatalysis and photocatalysis.<sup>317,318</sup> Optimization of the semiconductor and metallic phases can alter the chemical kinetics, electrical transport, and intrinsic catalytically active sites. The fundamental structural features of TMDCs and strategies for enhancing their catalytic activity were recently reviewed.<sup>319</sup> TMDCs can be represented by the general formula MX<sub>2</sub>, where M is a transition-metal atom belonging to groups IVB–VIIB of the periodic table and X is a chalcogen atom such as S, Se, or Te. The typical structure can be denoted X–M–X, in which a central layer of metal atoms is sandwiched between two layers of chalcogen atoms.<sup>320</sup> The monolayer of TMDCs can be stacked owing to van der Waals forces of attraction between each layer. The unit cell structure may possess trigonal prismatic or octahedral geometries. The trigonal prismatic geometry may exist as 2H or 3R polymorphs, which attributes the same metal element but atomic configuration difference in structure. The 2H and 3R phases exhibit hexagonal and rhombohedral symmetry, respectively. In addition, the metallic 1T phase displays tetragonal symmetry with octahedral coordination of the metal

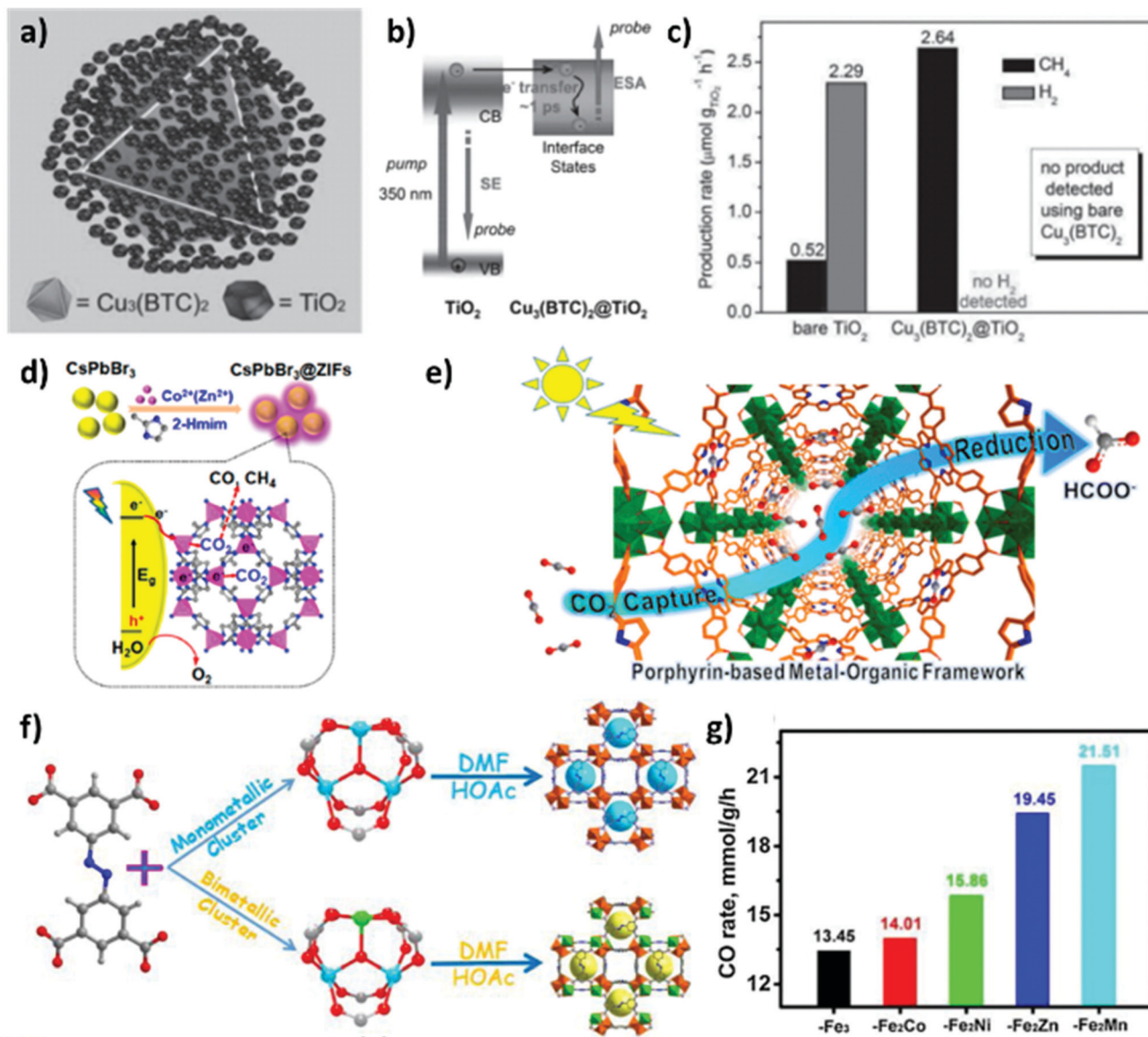


**Fig. 19** (a) Core–shell structure, (b) charge transfer mechanism, and (c) production rates of  $\text{CH}_4$  and  $\text{H}_2$  from  $\text{CO}_2$  for  $\text{Cu}_3(\text{BTC})_2$ @ $\text{TiO}_2$ . Reproduced with permission from ref. 311, Copyright 2014, Wiley-VCH. (d) Synthetic procedure and  $\text{CO}_2$  reduction process for  $\text{CsPbBr}_3$ /ZIFs. Reproduced with permission from ref. 312, Copyright 2018, American Chemical Society. (e) Schematic illustration of photocatalytic  $\text{CO}_2$  reduction by PCN-222. Reproduced with permission from ref. 313, Copyright, 2015 American Chemical Society. (f) Synthetic route to PCN-250- $\text{Fe}_3$  and PCN-250- $\text{Fe}_2\text{M}$  ( $\text{M} = \text{Mn, Zn, Ni, Co}$ ) by the reaction of  $\text{Fe}_3$  (or  $\text{Fe}_2\text{M}$ ) clusters and 3,3',5,5'-azobenzene tetra-carboxylic acid ( $\text{H}_4\text{abtc}$ ) ligand, and (g) comparison of photocatalytic reaction results for PCN-250- $\text{Fe}_3$  and PCN-250- $\text{Fe}_2\text{M}$  in terms of CO production. Reproduced with permission from ref. 314, Copyright 2020, Elsevier.

atom. The electronic structures of these phases vary depending on the filling of the d orbitals, which alters the energy band structure to afford semiconductor or metallic characteristics.<sup>321</sup>

Overall, these aspects determine the type of structure that can be obtained for a specific application. TMDCs have been extensively used in electrodes for electrochemical and photo-electrochemical  $\text{CO}_2$  reduction owing to their high electronic conductivity and redox surface area.<sup>315,322</sup> In contrast, there have been few reports describing their use as photocatalysts for  $\text{CO}_2$  reduction. The most important considerations in regard to photocatalysis are exciton generation and charge separation; however, the intrinsic mobility of electrons and holes can be

limited in TMDCs.<sup>323</sup> Cheng and Liu studied the electron and hole mobility in these materials using density functional perturbation theory and Wannier interpolation of the electron-phonon matrix.<sup>324</sup> This study revealed that two types of scattering processes (*i.e.*, longitudinal optical and longitudinal acoustic phonon scattering) limit the charge mobility and are not dependent upon the effective mass of the atoms. However, the charge mobility was found to be influenced by the electrical polarization changes induced by atomic vibration. Furthermore, the two types of scattering processes impede the charge carriers. This investigation indicated that  $\text{MoS}_2$  and  $\text{WS}_2$  exhibit higher charge carrier mobility with respect to other chalcogens because they exclusively



Table 4 MOF-based materials for photocatalytic  $\text{CO}_2$  reduction

Catalyst	Feed gas composition	Light source	Reducing agent	Reaction conditions	Reactor type	Yield	Ref.
Sensitized MOF-253- $\text{Ru}(\text{CO})_2\text{Cl}_2$	Moist $\text{CO}_2$ + MeCN/TEOA (10:1, 6 mL)	Xe lamp ( $\lambda = 420\text{--}800\text{ nm}$ )	TEOA	5 mg photocatalyst	Gas phase	$\text{HCOO}^-$ : 8.23 $\mu\text{mol}$ (8 h)	310
$\text{Cu}_3(\text{BTC})_2@\text{TiO}_2$	$\text{CO}_2$ + $\text{H}_2\text{O}$ (5 mL)	UV irradiation ( $\lambda > 400\text{ nm}$ )	$\text{H}_2\text{O}$	300 mg photocatalyst in batch reactor (100 mL)	Batch reactor (100 mL)	$\text{CH}_4$ : 2.64 $\mu\text{mol g}^{-1}\text{h}^{-1}$	311
$\text{CsPbBr}_3@\text{ZIF-67}$	$\text{CO}_2$ + $\text{H}_2\text{O}$ (10 $\mu\text{L}$ )	100 W Xe lamp (150 mW $\text{cm}^{-2}$ )	$\text{H}_2\text{O}$	4.5 mg photocatalyst in sealed Pyrex reactor (40 mL)	Pyrex reactor (40 mL)	Electron consumption rate: 29.630 $\mu\text{mol g}^{-1}\text{h}^{-1}$ (3 h)	312
PCN-222	MeCN/TEOA (10:1 (v/v), 60 mL) degassed with $\text{CO}_2$	300 W Xe lamp ( $\lambda = 420\text{--}800\text{ nm}$ )	TEOA	50 mg photocatalyst	Gas phase	$\text{HCOO}^-$ : 3 $\mu\text{mol h}^{-1}$	315
PCN-250-Fe <sub>2</sub> Mn	$\text{CO}_2$ (1 atm) + MeCN/ $\text{H}_2\text{O}$ (15:1) with TIPA	300 W Xe lamp ( $\lambda > 420\text{ nm}$ )	$\text{H}_2\text{O}$	5 mg photocatalyst	Pyrex reactor (100 mL)	CO: 21.51 $\text{mmol g}^{-1}\text{h}^{-1}$ AQY = 2.60%	314

display acoustic phonon scattering, whereas other chalcogenides exhibit both types of scattering. Therefore, most studies have been performed using  $\text{MoS}_2$  and  $\text{WS}_2$ . Meier *et al.* investigated tuning of the bandgap for  $\text{MoS}_2$  nanoflowers to achieve  $\text{CO}_2$  conversion to  $\text{CO}$ .<sup>325</sup> The  $\text{MoS}_2$  nanoflowers were synthesized using single- and three-zone furnaces (SZF and TZF, respectively) with different temperature ramping rates, which led to changes in the bandgap. A high ramping rate influenced the development of the flake surface and edges containing the coordinated atoms, and edges rich in Mo displayed high catalytic activity. However, further increasing the ramping rate resulted in the formation of  $\text{MoS}_2$  nanosheets, which exhibited reduced photocatalytic activity. Among the various synthetic approaches, the optimized SZF procedure afforded *ca.* 0.21  $\mu\text{mol g}^{-1}\text{h}^{-1}$  of CO formation, as illustrated in Fig. 20(a). Furthermore, to enhance the CO evolution,  $\text{MoS}_2$  was treated with  $\text{H}_2$ , which reduced the oxidation state for the Mo, resulting in the highest rate of CO production at 100 °C, as shown in Fig. 20(b).

Despite the above efforts, the CO production has remained limited, and  $\text{MoS}_2$  is typically used as a cocatalyst or composite component to enhance charge transfer. Hence, Tu *et al.* reported the *in situ* growth of  $\text{MoS}_2$  nanosheets on  $\text{TiO}_2$ , resulting in close contact between the two components to improve the interfacial area.<sup>331</sup> This close contact afforded nanojunctions that reduced electron–hole recombination. Furthermore, the Mo edges exhibited metallic characteristics with a high d-electron density and stabilized the intermediates through electrostatic attraction to enhance the yield of  $\text{CH}_3\text{OH}$  during  $\text{CO}_2$  reduction. Different morphologies of  $\text{TiO}_2$  can also be exploited to further improve the charge separation and transport. In this regard, Xu *et al.* developed the 1D  $\text{TiO}_2$  and  $\text{MoS}_2$  heterostructure illustrated in Fig. 20(c).<sup>326</sup> They optimized the ratio of  $\text{TiO}_2$  and  $\text{MoS}_2$  for photocatalytic  $\text{CO}_2$  reduction to form  $\text{CH}_4$  and  $\text{CH}_3\text{OH}$ . The pure  $\text{TiO}_2$  nanofibers exhibited  $\text{CH}_3\text{OH}$  production rate of 0.72  $\mu\text{mol g}^{-1}\text{h}^{-1}$ . But, after loading with  $\text{MoS}_2$ , the production of  $\text{CH}_4$  and  $\text{CH}_3\text{OH}$  was enhanced by 2.86 and 2.55  $\mu\text{mol g}^{-1}\text{h}^{-1}$ , respectively. The origin of the improved  $\text{CO}_2$  photoreduction may be the higher Fermi level of  $\text{MoS}_2$  with respect to  $\text{TiO}_2$ , enabling the transfer of excited electrons from  $\text{TiO}_2$  to the  $\text{MoS}_2$  sheets and then to adsorbed  $\text{CO}_2$  molecules under UV-vis irradiation.

Nevertheless, the expected photocatalytic performance has not yet been realized. Jung *et al.* reported the synthesis of a hierarchical structure composed of mesoporous  $\text{TiO}_2$  on graphene with a few layers of  $\text{MoS}_2$ .<sup>327</sup> The mesoporous  $\text{TiO}_2$  facilitated the adsorption of  $\text{CO}_2$  and also decreased the electron diffusion length.  $\text{TiO}_2$  and  $\text{MoS}_2$  comprised the heterostructure in this hierarchical structure, while graphene assisted in the separation of photoinduced electron–hole pairs. Few-layered  $\text{MoS}_2$  was used because it has active edges that reduce the electron transfer path and have larger amount of the unsaturated S atoms at the edges, thereby improving the  $\text{CO}_2$  reduction performance. Moreover, few-layered  $\text{MoS}_2$  exhibits quantum confinement, leading to the more negative CB shown in Fig. 20(d). Increasing the number of  $\text{MoS}_2$  layers to more than 5 or 6 resulted in an unsuitable CB alignment for  $\text{CO}_2$  reduction. Upon applying this structure to  $\text{CO}_2$  photoreduction, the

authors observed CO as the main product and subsequently compared the performance with the non-mesoporous and non-macroporous structures of  $\text{TiO}_2$  with  $\text{MoS}_2$  as a heterostructure. The resulting CO yields were  $92.33 \mu\text{mol g}^{-1} \text{ h}^{-1}$  for the mesoporous  $\text{TiO}_2/\text{MoS}_2/\text{graphene}$  structure and  $70.09$  and  $27.09 \mu\text{mol g}^{-1} \text{ h}^{-1}$  for the non-mesoporous and non-macroporous structures of  $\text{TiO}_2$ , respectively. This study demonstrates the roles of synergistic effects, surface area, and a porous support heterostructure.<sup>327</sup> Furthermore, the above discussion shows that  $\text{CO}_2$  fixation and CB alignment are crucial aspects of  $\text{CO}_2$  photoreduction.

Long *et al.* studied the influence of the S/Se ratio in a  $\text{MoS}_x\text{Se}_y/\text{TiO}_2$  heterostructure, and found that this parameter changed the band edges and  $\text{C}_1$  and  $\text{C}_2$  product selectivity.<sup>328</sup> The  $\text{CO}_2$  photoreduction performance was examined for different S/Se ratios, and photocatalyst formed the  $\text{CH}_3\text{CH}_2\text{OH}$  as a  $\text{C}_2$  product. Adjusting the S/Se ratio to 2:3 increased the formation of formic acid as a  $\text{C}_1$  product. The influence of the S/Se ratio on the product selectivity is shown in Fig. 20(e). The metallic character was governed by the S/Se ratio, which thus determined the  $\text{MoS}_x\text{Se}_y$  bandgap. The increase in the CBM of  $\text{MoS}_x\text{Se}_y$  with increasing Se content mirrored the decrease in electronegativity from S to Se, which also led to a diminishing electric potential. Then again, consistently specific photocatalytic  $\text{CO}_2$  fixation requires an excellently tunable energetic site of the photocatalyst. The S/Se ratio-dependent CBM of  $\text{MoS}_x\text{Se}_y$  enables the selective production in photocatalytic  $\text{CO}_2$  fixation.

The applications of TMDCs in  $\text{CO}_2$  reduction are not limited to  $\text{TiO}_2$  but have also been extended to other metal oxides such

as  $\text{SnO}_2$ . Bilawal *et al.* studied the  $\text{SnO}_2/\text{Ag}/\text{MoS}_2$  heterostructure to enhance the charge separation and  $\text{CO}_2$  reduction performance.<sup>329</sup> Here, they used  $\text{MoS}_2$  nanoflowers owing to their high surface area and appropriate conduction band for  $\text{SnO}_2$ , and added Ag NPs to obtain a suitable work function. The resulting heterostructure facilitated the photon-to-electron charge transfer through the cascade band alignment. Fig. 20(f) shows the observed yields of CO and  $\text{CH}_4$ , which varied upon changing the ratio of  $\text{SnO}_2$  to  $\text{MoS}_2/\text{Ag}$ .

The p-n junction of p- $\text{MoS}_2$ /n- $\text{Bi}_2\text{S}_3$  nanorods has also been studied for  $\text{CO}_2$  reduction. The treatment of  $\text{MoS}_2$  at high temperature affords sulfur vacancies that lead to high  $\text{CO}_2$  adsorption. Kim *et al.* exploited these sulfur vacancies in  $\text{MoS}_2$  to obtain a p-n junction catalyst with improved optical properties by heterostructure formation with  $\text{Bi}_2\text{S}_3$ .<sup>330</sup> They observed CO and  $\text{CH}_4$  yields of  $40$  and  $42.5 \mu\text{mol g}^{-1}$ , respectively, after 10 h of light illumination. In addition, Wang *et al.* reported a unique marigold-like  $\text{SiC}@\text{MoS}_2$  nanoflower structure for photocatalytic  $\text{CO}_2$  reduction.<sup>332</sup> In this case, the  $\text{MoS}_2$  was responsible for  $\text{H}_2\text{O}$  oxidation owing to its high hole mobility, while the high electron mobility of SiC contributed to the  $\text{CO}_2$  reduction. The authors measured the photocatalytic activity under visible light and observed a  $\text{CH}_4$  production rate of  $323 \mu\text{L g}^{-1} \text{ h}^{-1}$  and  $\text{O}_2$  evolution rate of  $620 \mu\text{L g}^{-1} \text{ h}^{-1}$ . As shown in Fig. 20(g), two paths were available for  $\text{CO}_2$  reduction, namely, hydrogenation ( $\text{CO}_2 \rightarrow \text{HCOOH} \rightarrow \text{HCHO} \rightarrow \text{CH}_3\text{OH} \rightarrow \text{CH}_4$ ) and deoxygenation ( $\text{CO}_2 \rightarrow \text{CO} \rightarrow \text{C}^* \rightarrow \cdot\text{CH}_3 \rightarrow \text{CH}_3\text{OH}/\text{CH}_4$ ). The stability of the  $\text{SiC}@\text{MoS}_2$  photocatalyst was dependent upon the stability of the  $\text{MoS}_2$  nanosheets. Dai *et al.* studied a

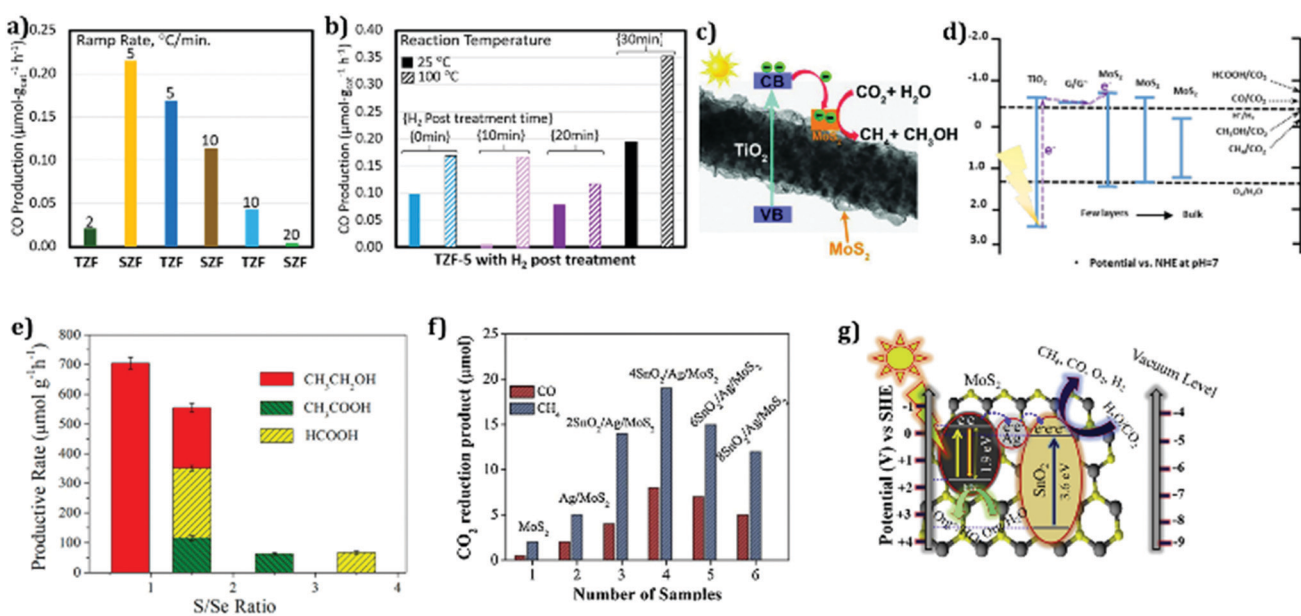


Fig. 20 (a)  $\text{CO}_2$ -to-CO photoreduction performance of  $\text{MoS}_2$  nanoflowers synthesized using the SZF and TZF approaches and (b) influence of  $\text{H}_2$  post-treatment on the  $\text{CO}_2$  reduction activity. Reproduced with permission from ref. 325, Copyright 2018, American Chemical Society. (c) Photocatalytic  $\text{CO}_2$  reduction by a  $\text{TiO}_2/\text{MoS}_2$  heterostructure. Reproduced with permission from ref. 326, Copyright 2018, Wiley-VCH. (d) Charge separation and transport phenomena in  $\text{TiO}_2/\text{MoS}_2/\text{graphene}$ . Reproduced with permission from ref. 327, Copyright 2018, American Chemical Society. (e) Influence of the S/Se ratio on  $\text{C}_1$  and  $\text{C}_2$  product selectivity during  $\text{CO}_2$  photoreduction. Reproduced with permission from ref. 328, Copyright 2020, American Chemical Society. (f) Photocatalytic performance of  $\text{SnO}_2/\text{Ag}/\text{MoS}_2$  for  $\text{CO}_2$  reduction to generate CO and  $\text{CH}_4$ . Reproduced with permission from ref. 329, Copyright 2020, Elsevier. (g) Reaction pathway for  $\text{CH}_4$  formation on the surface of  $\text{SiC}@\text{MoS}_2$ . Reproduced with permission from ref. 330, Copyright 2019, MDPI.



Table 5 TMDC-based materials for photocatalytic CO<sub>2</sub> reduction

Catalyst	Feed gas composition	Light source	Reducing agent	Reaction conditions	Reactor type	Yield	Ref.
MoS <sub>2</sub> nanoflowers	CO <sub>2</sub> + H <sub>2</sub> O	1600 W Xe arc lamp	H <sub>2</sub> O	Reaction temperature maintained at 16 °C	—	CO: 0.22 μmol g <sup>-1</sup> h <sup>-1</sup> CH <sub>4</sub> : 0.17 μmol g <sup>-1</sup> h <sup>-1</sup> CH <sub>3</sub> OH: 10.6 μmol g <sup>-1</sup> h <sup>-1</sup>	325
MoS <sub>2</sub> -TiO <sub>2</sub>	CO <sub>2</sub> + 1 M NaHCO <sub>3</sub>	350 W Xe lamp	—	Catalyst treated at 300 °C under Ar for 2 h	—	CH <sub>3</sub> OH: 2.55 μmol g <sup>-1</sup> h <sup>-1</sup> CH <sub>4</sub> : 2.86 μmol g <sup>-1</sup> h <sup>-1</sup>	331
1D/2D TiO <sub>2</sub> /MoS <sub>2</sub>	CO <sub>2</sub> + H <sub>2</sub> O	350 W Xe lamp	H <sub>2</sub> O	50 mg sample in 10 mL H <sub>2</sub> O	—	CH <sub>3</sub> OH: 2.55 μmol g <sup>-1</sup> h <sup>-1</sup> CH <sub>4</sub> : 2.86 μmol g <sup>-1</sup> h <sup>-1</sup>	326
Mesoporous TiO <sub>2</sub> / few-layered MoS <sub>2</sub> / graphene	CO <sub>2</sub> + H <sub>2</sub> O	350 W Xe lamp	H <sub>2</sub> O	Reaction mixture kept for several hours at 40 °C	—	CO: 92.33 μmol g <sup>-1</sup> h <sup>-1</sup>	327
TiO <sub>2</sub> -MoS <sub>x</sub> Se <sub>y</sub>	CO <sub>2</sub> + NaHCO <sub>3</sub>	350 W Xe lamp	—	0.2 MPa CO <sub>2</sub> and 0.1 M NaHCO <sub>3</sub> (H <sub>2</sub> source), room temperature	—	CH <sub>3</sub> CH <sub>2</sub> OH: 704.38 μmol g <sup>-1</sup> h <sup>-1</sup>	328
SnO <sub>2</sub> /Ag/MoS <sub>2</sub>	CO <sub>2</sub> + H <sub>2</sub> O	350 W Xe lamp	H <sub>2</sub> O	0.1 g catalyst dispersed in 6 mL H <sub>2</sub> O	Flow reactor	CO: 9 μmol g <sup>-1</sup> h <sup>-1</sup> CH <sub>4</sub> : 20 μmol g <sup>-1</sup> h <sup>-1</sup>	329
Bi <sub>2</sub> S <sub>3</sub> /MoS <sub>2</sub>	99.99% CO <sub>2</sub> + H <sub>2</sub> O	Xe lamp (150 mW cm <sup>-2</sup> )	H <sub>2</sub> O	Reaction temperature 60 °C	Batch reactor	CO: 40 μmol g <sup>-1</sup> (10 h) CH <sub>4</sub> : 42.5 μmol g <sup>-1</sup> (10 h)	330
3D-SiC@2D-MoS <sub>2</sub>	CO <sub>2</sub> + H <sub>2</sub> O	300 W Xe lamp	H <sub>2</sub> O	40 mL reaction mixture at 298 K	Schlenk flask reactor	CH <sub>4</sub> : 323 μL g <sup>-1</sup> h <sup>-1</sup>	332
MoS <sub>2</sub> /Bi <sub>2</sub> WO <sub>6</sub>	99.99% CO <sub>2</sub> + H <sub>2</sub> O	350 W Xe lamp	H <sub>2</sub> O	50 mg catalyst in 50 mL DI water	—	CH <sub>3</sub> OH: 36.7 μmol g <sup>-1</sup> h <sup>-1</sup> C <sub>2</sub> H <sub>5</sub> OH: 36.6 μmol g <sup>-1</sup> h <sup>-1</sup>	333
MoS <sub>2</sub> nanosheets	99.99% CO <sub>2</sub> + 0.5 M NaHCO <sub>3</sub> , 0.5 M NaOH, or 0.5 M NaCl	UV light	H <sub>2</sub> O	0.1 g MoS <sub>2</sub> in 50 mL DI water	—	CH <sub>3</sub> OH: 27.4/11.2/7.8 μmol g <sup>-1</sup> h <sup>-1</sup> CH <sub>3</sub> CHO: 2.2/2.5/4.8 μmol g <sup>-1</sup> h <sup>-1</sup> (for NaHCO <sub>3</sub> /NaOH/NaCl)	334

MoS<sub>2</sub>/Bi<sub>2</sub>WO<sub>6</sub> composite photocatalytic material for CO<sub>2</sub> photoreduction.<sup>333</sup> The hierarchical flower-like structure displayed significant activity in the visible spectrum, and the MoS<sub>2</sub> acted as a cocatalyst. Thus, after 4 h of light illumination, methanol and ethanol were produced as the primary products with yields of 36.7 and 36.6 μmol g<sub>cat</sub><sup>-1</sup>, respectively.

Considerable progress is still needed to realize satisfactory performance from TMDCs, and the stability of exfoliated 2D nanosheets in particular remains a massive challenge. After all, the bulk forms possess indirect bandgaps, and chalcogens based on transition metals do not usually exhibit high charge carrier mobility. Successfully overcoming these challenges may allow 2D TMDCs to find practical applications in photocatalytic CO<sub>2</sub> reduction. The photocatalytic activities of TMDCs are summarized in Table 5.

## 5.5 MXenes

Recently, MXenes, another class of 2D materials, have received enormous attention owing to their high electrical conductivity, large specific surface area, hydrophilicity, and tunable composition.<sup>335–339</sup> MXenes possess a lamellar structure with anisotropic properties and can be represented by the general formula M<sub>n+1</sub>AX<sub>n</sub>, where M is a transition metal, n = 1, 2, or 3, A is an A-group in the periodic table (mostly IIIA and IVA), and X is C or N.<sup>340</sup> The MAX phase is hexagonally stacked where the tight M layer is inserted with the pure A-group layer, and the X elements fill the octahedral sites.<sup>341</sup> The first MXene to be discovered was Ti<sub>3</sub>C<sub>2</sub>T<sub>x</sub>, where T<sub>x</sub> represents a surface terminated group and since then more than 30 other compositions have also been reported.<sup>342</sup> Ti<sub>3</sub>C<sub>2</sub> is primarily synthesized by the exfoliation of Ti<sub>3</sub>AlC<sub>2</sub> with HF. This method is expected to afford various compositions.<sup>341,342</sup> To date, MXenes have been exploited in

applications such as lithium-ion batteries,<sup>343</sup> electrochemical supercapacitors,<sup>344</sup> and fuel cells.<sup>345</sup> In addition to these energy storage applications, they have also been explored as promising photocatalytic materials.<sup>346–349</sup> The 2D structure of MXenes affords a high surface area and good pore structure, making these materials an excellent choice for enhanced CO<sub>2</sub> adsorption and photocatalytic activity. Moreover, MXenes may serve as efficient cocatalysts in photocatalysis owing to their good electronic conductivity, adjustable bandgap, and strong metallic characteristics.<sup>350</sup> The Ran group reported the use of Ti<sub>3</sub>C<sub>2</sub>/CdS for H<sub>2</sub> generation and demonstrated that Ti<sub>3</sub>C<sub>2</sub> is a promising cocatalyst for photocatalytic applications, providing an alternative to noble metals.<sup>351</sup>

To date, several Ti<sub>3</sub>C<sub>2</sub>-based heterostructured photocatalysts have been studied for CO<sub>2</sub> conversion. For example, Low *et al.* prepared TiO<sub>2</sub>/Ti<sub>3</sub>C<sub>2</sub> by *in situ* calcination and successfully applied it to photocatalytic CO<sub>2</sub> conversion.<sup>336</sup> Ultrathin layered 2D Ti<sub>3</sub>C<sub>2</sub> was first synthesized and then combined with TiO<sub>2</sub> using simple calcination at various temperatures. The composite exhibited a high surface area with a unique rice crust-like structure. The high electronic conductivity of Ti<sub>3</sub>C<sub>2</sub> was found to be beneficial for the migration of photogenerated electrons from TiO<sub>2</sub> to Ti<sub>3</sub>C<sub>2</sub>. Photocatalytic CO<sub>2</sub> reduction mainly afforded CH<sub>4</sub> along with a small amount of other products such as CH<sub>3</sub>OH and C<sub>2</sub>H<sub>5</sub>OH, and the catalytic activity for CH<sub>4</sub> formation was approximately 3.1 times higher than that for pristine TiO<sub>2</sub>. The enhanced catalytic activity was ascribed to the large surface area, improved CO<sub>2</sub> adsorption, and the heterogeneous interface between TiO<sub>2</sub> and Ti<sub>3</sub>C<sub>2</sub>, which improved the charge separation. In another study, Pan *et al.* presented a functional MXene/CsPbBr<sub>3</sub> system for CO<sub>2</sub> reduction to CO and CH<sub>4</sub>, in which the CsPbBr<sub>3</sub> was grown *in situ* on 2D Ti<sub>3</sub>C<sub>2</sub> NSs.<sup>352</sup> In this study,



HCl–HF solution was used to etch  $\text{Ti}_3\text{AlC}_2$  to obtain  $\text{Ti}_3\text{C}_2\text{T}_x$  NSs, upon which cubic  $\text{CsPbBr}_3$  was grown *in situ* to afford the final nanocomposites. The PL and time-resolved PL quenching was observed for the composite sample, indicating efficient charge transfer through the  $\text{CsPbBr}_3/\text{MXene}$  interface. The optimized composite mediated the reduction of  $\text{CO}_2$  to  $\text{CO}$  ( $26.32 \mu\text{mol g}^{-1} \text{h}^{-1}$ ) and  $\text{CH}_4$  ( $7.25 \mu\text{mol g}^{-1} \text{h}^{-1}$ ). Therefore, such perovskite/2D composites can be used to realize efficient photocatalysis.

It is well known that the combination of 2D/2D heterojunctions provides superior structural stability owing to the substantial interfacial contact.<sup>336</sup> In this regard, Yu and co-workers reported the heterostructure combination of 2D  $\text{Bi}_2\text{WO}_6$  with 2D  $\text{Ti}_3\text{C}_2$  NSs.<sup>353</sup> The incorporation of  $\text{Ti}_3\text{C}_2$  led to enhanced  $\text{CO}_2$  adsorption owing to the increased surface area. The 2D/2D sandwich-like  $\text{Ti}_3\text{C}_2/\text{Bi}_2\text{WO}_6$  system displayed excellent charge transfer for  $\text{CO}_2$  reduction. Under light irradiation, the photoexcited electrons transferred from the CB of  $\text{Bi}_2\text{WO}_6$  to  $\text{Ti}_3\text{C}_2$  through the ultrathin layered heterostructure and reacted with adsorbed  $\text{CO}_2$  molecules. Therefore, the photocatalytic  $\text{CO}_2$  reduction activity toward  $\text{CH}_4$  and  $\text{CH}_3\text{OH}$  was significantly improved. Moreover, DFT calculations revealed that the excellent conductivity of  $\text{Ti}_3\text{C}_2$  was beneficial for rapid charge transport. Subsequently, Yang *et al.* demonstrated that  $\text{Ti}_3\text{C}_2/\text{g-C}_3\text{N}_4$  nanosheet heterojunctions exhibited improved catalytic activity for  $\text{CO}_2$  reduction into  $\text{CO}$  and  $\text{CH}_4$ .<sup>335</sup> The intimate contact between two 2D materials also leads to good charge separation. Hence, the catalytic activity of  $\text{Ti}_3\text{C}_2/\text{g-C}_3\text{N}_4$  for  $\text{CO}_2$  reduction toward  $\text{CO}$  and  $\text{CH}_4$  reached rates of  $5.19$  and  $0.044 \mu\text{mol h}^{-1} \text{g}^{-1}$ , respectively. This catalytic activity was approximately eightfold higher than that for pristine  $\text{g-C}_3\text{N}_4$ . Significantly, BET isotherm experiments revealed higher chemical affinity between  $\text{CO}_2$  molecules and the catalyst surface, which contributed to the improved catalytic performance.

In addition to these binary composites, Wu *et al.* also described the ternary heterostructure composition  $\text{Ti}_3\text{C}_2\text{T}_x/(001)\text{TiO}_2/\text{C}_3\text{N}_4$ , which was synthesized by *in situ* oxidation/electrostatic self-assembly.<sup>350</sup> The heterojunction composed of  $\text{Ti}_3\text{C}_2\text{T}_x/(001)\text{TiO}_2$  NSs with highly exposed  $\{001\}$   $\text{TiO}_2$  facets was first synthesized by the *in situ* oxidation of  $\text{Ti}_3\text{C}_2\text{T}_x$  NSs. Next, the ternary composite with  $\text{C}_3\text{N}_4$  was obtained by exploiting the electrostatic attraction between the opposite charges.

This 2D/2D heterojunction combination provided broad electron transfer channels that significantly enhanced the charge separation properties, while the incorporation of the 2D MXene into  $\text{TiO}_2/\text{C}_3\text{N}_4$  increased the catalytic activity. The heterojunction catalyst displayed threefold higher  $\text{CO}_2$  conversion activity compared to pristine  $\text{TiO}_2$  or  $\text{C}_3\text{N}_4$ . A similar  $\text{TiO}_2/\text{C}_3\text{N}_4/\text{Ti}_3\text{C}_2$  composite was explored in another study by combining 0D  $\text{Ti}_3\text{C}_2$  QDs with 2D/2D core–shell  $\text{TiO}_2/\text{C}_3\text{N}_4$  heterojunctions.<sup>260</sup> First, ultrathin  $\text{C}_3\text{N}_4$  was deposited on the  $\text{TiO}_2$  nanosheets by the thermal condensation of urea to form a core–shell structure. Then, the as-prepared  $\text{Ti}_3\text{C}_2$  QDs were electrostatically assembled on the  $\text{C}_3\text{N}_4$  shell. The close attachment of the  $\text{Ti}_3\text{C}_2$  QDs on the  $\text{TiO}_2/\text{C}_3\text{N}_4$  is due to van der Waals interactions. Theoretical and experimental results indicated that the charge transfer in the ternary composite occurred *via* a dual heterojunction involving the S-scheme for  $\text{TiO}_2/\text{C}_3\text{N}_4$  and the Schottky scheme for the  $\text{C}_3\text{N}_4/\text{Ti}_3\text{C}_2$  QDs. The QDs extracted the electrons from  $\text{C}_3\text{N}_4$ , enabling S-scheme charge transfer between  $\text{TiO}_2$  and  $\text{C}_3\text{N}_4$ . As a result, the composite exhibited a  $\text{CO}$  evolution rate of  $4.39 \mu\text{mol g}^{-1} \text{h}^{-1}$ .

Therefore, MXenes can be fruitfully applied as cocatalysts for photocatalytic  $\text{CO}_2$  conversion. In particular, their 2D nature affords a large surface area, providing a promising alternative option to expensive noble metals. Until recently, most studies have focused on the synthesis of MXenes with HF, which may represent one of the primary drawbacks of these systems; the use of such hazardous chemicals may not be desirable for large-scale MXene production. However, various studies are underway to replace such chemicals. For example, Shah and co-workers reported the synthesis of MXenes by electrochemical etching in HCl solution.<sup>354</sup> In time, this research may permit the large-scale synthesis of MXenes by environmentally friendly approaches using less hazardous chemicals.

The photocatalytic  $\text{CO}_2$  reduction performance of MXene-based materials is summarized in Table 6.

## 5.6 Perovskites

Perovskite materials ranging from oxides to halides have stimulated enormous interest for catalytic applications owing to their exciting features such as cost-effectiveness, tunable bandgaps, high surface area, and surface defects for charge trapping.<sup>50</sup> Moreover, in terms of altering the redox potentials, the

Table 6 MXene-based materials for photocatalytic  $\text{CO}_2$  reduction

Catalyst	Feed gas composition	Light source	Reducing agent	Reaction conditions	Reactor type	Yield	Ref.
$\text{Ti}_3\text{C}_2/\text{g-C}_3\text{N}_4$	$\text{CO}_2 + \text{H}_2\text{O}$ ( $\text{H}_2\text{SO}_4 + \text{NaHCO}_3$ )	300 W Xe lamp (420 nm cutoff)	$\text{H}_2\text{O}$	20 mg catalyst	—	$\text{CH}_4: 0.044 \mu\text{mol g}^{-1} \text{h}^{-1}$ $\text{CO}: 5.19 \mu\text{mol g}^{-1} \text{h}^{-1}$	335
$\text{TiO}_2/\text{Ti}_3\text{C}_2$	$\text{CO}_2 + \text{H}_2\text{O}$ ( $\text{HCl} + \text{NaHCO}_3$ )	300 W Xe lamp	—	50 mg catalyst in Pyrex reactor (200 mL)	—	$\text{CH}_4: 0.22 \mu\text{mol h}^{-1}$	336
$\text{Ti}_3\text{C}_2\text{T}_x/(001)\text{TiO}_2/\text{C}_3\text{N}_4$	$\text{CO}_2 + \text{H}_2\text{O}$ ( $\text{H}_2\text{O} + 15 \text{ vol\% TEOA}$ )	—	TEOA	5 mg catalyst on glass in reactor (80 mL)	—	$\text{CH}_4: 1.97 \text{ ppm h}^{-1}$ $\text{CO}: 15.0 \text{ ppm h}^{-1}$	350
$\text{CsPbBr}_3/\text{Ti}_3\text{C}_2\text{T}_x$	$\text{CO}_2$ (ethyl acetate)	300 W Xe lamp ( $>420 \text{ nm cutoff}$ )	—	—	—	$\text{CH}_4: 7.25 \mu\text{mol g}^{-1} \text{h}^{-1}$ $\text{CO}: 26.32 \mu\text{mol g}^{-1} \text{h}^{-1}$	352
$\text{Ti}_3\text{C}_2/\text{Bi}_2\text{WO}_6$	$\text{CO}_2 + \text{H}_2\text{O}$ ( $\text{H}_2\text{SO}_4 + \text{NaHCO}_3$ )	300 W Xe lamp	—	100 mg catalyst in Pyrex glass reactor (200 mL)	Batch	$\text{CH}_4: 1.78 \mu\text{mol g}^{-1} \text{h}^{-1}$ $\text{CH}_3\text{OH}: 0.44 \mu\text{mol g}^{-1} \text{h}^{-1}$	353
$\text{TiO}_2/\text{C}_3\text{N}_4/\text{Ti}_3\text{C}_2$	$\text{CO}_2 + \text{H}_2\text{O}$ ( $\text{H}_2\text{SO}_4 + \text{NaHCO}_3$ )	350 W Xe lamp	$\text{H}_2\text{O}$	30 mg catalyst in two-neck Pyrex reactor	—	$\text{CH}_4: 1.20 \mu\text{mol g}^{-1} \text{h}^{-1}$ $\text{CO}: 4.39 \mu\text{mol g}^{-1} \text{h}^{-1}$	260

structural flexibility of perovskites makes them quite different from traditional semiconductors. The ideal perovskite has the general formula  $ABX_3$ , in which A and B are different cations and X denotes oxide/halide anions surrounded by B cations.

$\text{CaTiO}_3$  was the first perovskite material discovered, and this formula has since been extended to a variety of new forms, such as  $A_2\text{BX}_6$ ,  $A_2\text{BB}'\text{X}_6$ , and so on.<sup>355</sup> This structure allows the formation of lattice deficiencies, which can be advantageous for tuning the optoelectronic properties. Besides simple perovskites, layered perovskites and their derivatives display excellent properties such as structural stability and low cost. Previously, oxide perovskites were primarily used as catalyst materials; however, halide perovskites are now one of the most commonly used materials for photocatalytic  $\text{CO}_2$  conversion. Therefore, we will first discuss recent progress in oxide perovskite photocatalysts before considering halide perovskites.

Depending on the type and composition of the A and B sites, oxide perovskites exhibit different band structures and optoelectronic properties. In addition, replacing or doping the A, B, or O sites with other metal or non-metal elements can change the chemical composition and symmetry of oxide perovskites, which can be beneficial for tuning the material properties, such as band potentials, light absorption, and  $\text{CO}_2$  adsorption.<sup>356</sup> Consequently, the photocatalytic performance of oxide perovskites can be altered by changing their composition, structure, morphology, and heterostructure combination. In 1978, Hemminger and colleagues demonstrated the photo-assisted conversion of  $\text{CO}_2$  into  $\text{CH}_4$  on the surface of  $\text{SrTiO}_3(111)$  for the first time without using an electrochemical cell.<sup>357</sup> Since this pioneering work, various perovskites have been examined for  $\text{CO}_2$  conversion applications. However, pure  $\text{SrTiO}_3$  is not considered a suitable catalyst because of its large bandgap ( $>3.0$  eV) and light absorption mainly in the UV region; thus, surface modification, heterostructure formation, and metal NP deposition have frequently been applied to increase its sensitivity to visible light. For instance, Luo *et al.* prepared Ti-rich and  $\text{Sr}(\text{OH})_2$ -decorated  $\text{SrTiO}_3$  catalysts and explored the effects of surface modification on  $\text{CO}_2$  photoreduction.<sup>358</sup>

The results revealed that Ti-rich  $\text{SrTiO}_3$  possesses a narrow bandgap due to a lower Ti 3d ground-state level, which increased light harvesting in the visible region. Therefore, it exhibited high photocatalytic activity toward CO formation ( $26.4 \mu\text{mol g}^{-1}$ ) compared to pristine  $\text{SrTiO}_3$  ( $18.4 \mu\text{mol g}^{-1}$ ) and  $\text{Sr}(\text{OH})_2$ -modified  $\text{SrTiO}_3$  ( $13.8 \mu\text{mol g}^{-1}$ ). In another study, oxygen-deficient self-doped  $\text{SrTiO}_{3-\delta}$  was utilized for the photoconversion of  $\text{CO}_2$  into  $\text{CH}_4$ .<sup>359</sup> To obtain  $\text{Ti}^{3+}$  states accompanied by oxygen vacancies, the catalyst was synthesized by a combustion process with high-temperature heat treatment. This resulted in improved  $\text{CO}_2$  adsorption on the surface of the oxygen-deficient catalysts and thus increased  $\text{CO}_2$  reduction activity. Metal NPs have also been employed in this field owing to their unique features originating from surface plasmon resonance (SPR). For example, Li *et al.* demonstrated the synergistic effects of metal cocatalysts on oxide perovskites, which significantly enhanced the response to visible light as a result of the plasmonic effect and electron extraction properties of the metal NPs.<sup>360</sup> In this study, Rh

metal was grafted onto  $\text{SrTiO}_3$  prior to the loading of Au NPs as a photosensitizer. With 99.4% selectivity for CO formation, the optimized  $\text{SrTiO}_3$ , *i.e.*,  $\text{Rh}(\text{PD})\text{-Au}@\text{SrTiO}_3$ , demonstrated 153- and 22-fold higher catalytic activity than pristine  $\text{Rh}@\text{SrTiO}_3$  and  $\text{Au}@\text{SrTiO}_3$  samples, respectively.

As discussed earlier, the integration of two semiconducting materials to form a heterojunction combination can be a promising strategy for improving catalytic activity owing to the efficient charge separation *via* the closely connected interface. In one study,  $\text{RuO}_2$  NPs were supported on  $\text{SrTiO}_3$  and the resulting composites were found to exhibit improved catalytic activity for  $\text{CO}_2$  photoreduction with  $\text{H}_2$  in a flow reactor system.<sup>361</sup> Remarkably, the authors also studied the influence of the photothermal behavior of the catalyst toward  $\text{CH}_4$  formation at  $150^\circ\text{C}$ . The improved catalytic activity was attributed to the high  $\text{CO}_2$  adsorption by  $\text{SrTiO}_3$  and efficient charge separation between  $\text{RuO}_2$  and  $\text{SrTiO}_3$ . Heterojunction combinations of oxide perovskites with  $\text{TiO}_2$  (*e.g.*,  $\text{CaTiO}_3/\text{TiO}_2$ ) have also been reported.<sup>362</sup> Later, additional oxide perovskites with A site substitution were found to mediate photocatalytic  $\text{CO}_2$  conversion. For example, Teramura and co-workers studied the photoreduction of  $\text{CO}_2$  over  $\text{ATaO}_3$  ( $\text{A} = \text{Li, Na, K}$ ) using  $\text{H}_2$  as a reductant.<sup>363</sup> The strong chemisorption of  $\text{CO}_2$  molecules was observed on the surface of  $\text{LiTaO}_3$ , and the catalytic activity followed the order  $\text{LiTaO}_3 > \text{NaTaO}_3 > \text{KTaO}_3$ . Similarly, Zhou *et al.* investigated photocatalytic  $\text{CO}_2$  reduction over alkaline tantalates, *i.e.*,  $\text{MTaO}_3$  ( $\text{M} = \text{Li, Na, K}$ ), with 3D hierarchical structure obtained using activated carbonized wood as a template.<sup>364</sup> The template provided a high surface area that enhanced the light harvesting and gas diffusion properties. The results indicated that the CO and  $\text{CH}_4$  formation rates upon  $\text{CO}_2$  reduction were enhanced by 3.1 and 8.4 times, respectively, by the deposition of the Au cocatalyst on  $\text{NaTaO}_3$ . The formation of CO and  $\text{CH}_4$  over  $\text{NaTaO}_3$  was attributed to the suitable band potentials that simultaneously reduced  $\text{CO}_2$  and oxidized  $\text{H}_2\text{O}$ . Both of these studies demonstrated that alkaline  $\text{NaTaO}_3$  has a synergistic effect on reducing  $\text{CO}_2$  to CO and  $\text{CH}_4$ . Although CO selectivity was observed under a  $\text{H}_2$  environment, the presence of  $\text{H}_2\text{O}$  led to the formation of both CO and  $\text{CH}_4$ . In another study, the lanthanum-based oxide perovskite  $\text{LaCoO}_3$  was utilized as a cocatalyst on a Ru complex for the reduction of  $\text{CO}_2$  to CO under light irradiation.<sup>365</sup> The results revealed 20-fold higher activity compared to the system lacking  $\text{LaCoO}_3$ , in addition to 76% selectivity for CO formation and an AQY of 1.36%. Similarly,  $\text{MnCo}_2\text{O}_4$  microspheres have been utilized as a stable cocatalyst for the conversion of  $\text{CO}_2$  to CO.<sup>366</sup>

The morphology of perovskite nanocrystals is another crucial factor in tuning the properties of the catalyst to improve the catalytic reaction rate. In this regard, Shi *et al.* prepared Pt-loaded  $\text{g-C}_3\text{N}_4/\text{NaNbO}_3$  nanowires and studied their photocatalytic  $\text{CO}_2$  reduction behavior.<sup>367</sup> The resulting composite displayed improved catalytic activity for  $\text{CH}_4$  formation ( $6.4 \mu\text{mol g}^{-1} \text{h}^{-1}$ ) compared to Pt-loaded  $\text{g-C}_3\text{N}_4$  and Pt-loaded  $\text{NaNbO}_3$ , which originated from the improved charge separation through the closely connected interface, increased surface area due to the nanowire morphology of  $\text{NaNbO}_3$ , efficient charge transport through the heterostructure, and suitable band



potentials for  $\text{CO}_2$  reduction to  $\text{CH}_4$ . In addition, Kumar and co-workers designed the UV-vis-NIR-active catalyst  $\text{Ag}_2\text{CrO}_4/\text{Ag}/\text{BiFeO}_3@\text{RGO}$ , composed of a Ag-mediated  $\text{Ag}_2\text{CrO}_4/\text{BiFeO}_3$  heterojunction on an RGO matrix.<sup>368</sup> Each of the components made a significant contribution to improving the conversion of  $\text{CO}_2$  into  $\text{CO}$  and  $\text{CH}_4$ . For example, the  $\text{BiFeO}_3$  and  $\text{Ag}_2\text{CrO}_4$  served as the photoreduction and photooxidation systems, respectively, while the plasmonic Ag NPs mediated the electron donation and the RGO improved the redox capabilities by enhancing the electron mobility. In another study, Wang and colleagues synthesized Ag-deposited  $\text{H}_2\text{SrTa}_2\text{O}_7$  (HST) using a polymerizable complex and an ion-exchange method.<sup>369</sup> Owing to the anisotropy of the layered HST perovskite structure, photoinduced electrons and holes gathered on the edges and basal plane. The Ag NPs reduced the kinetic barrier to  $\text{CO}$  formation and captured more electrons from the perovskite to reduce  $\text{CO}_2$  to  $\text{CO}$ , thereby impeding the reduction of  $\text{H}^+$  to  $\text{H}_2$ . The optimal Ag-loaded sample (Ag/HST) displayed twofold higher reduction ability than pure HST with approximately 60% selectivity for  $\text{CO}$  formation. In an effort to improve the charge separation, Tu *et al.* reported a layered ferroelectric perovskite of  $\text{SrBi}_4\text{Ti}_4\text{O}_{15}$  NSS for  $\text{CH}_4$  evolution in a gas-solid phase system without the use of any cocatalyst or sacrificial agent.<sup>370</sup> The ferroelectric characteristics of  $\text{SrBi}_4\text{Ti}_4\text{O}_{15}$  (SBTO-1) afforded efficient bulk charge separation and high charge mobility. The catalyst was synthesized *via* a soft chemical method by adding NaOH as a mineralizer. Post-treatment annealing was then conducted at 350 °C (SBTO) and 650 °C (SBTO-2) to tune the ferroelectric polarization. Notably,  $\text{SrBi}_4\text{Ti}_4\text{O}_{15}$  displayed significant photocatalytic performance in the reduction of  $\text{CO}_2$  to  $\text{CH}_4$  with a rate of 19.8  $\mu\text{mol g}^{-1} \text{h}^{-1}$ , along with a small amount of  $\text{CO}$  formation (Fig. 21(a) and (b)).

The catalyst was found to be 8- and 283-fold more active than the reference samples of  $\text{Bi}_4\text{Ti}_3\text{O}_{12}$  and  $\text{BiOBr}$ , respectively, with a  $\text{CH}_4$  selectivity of 93% and an AQY of 1.33% at 365 nm. Time-dependent *in situ* DRIFTS analysis confirmed the conversion of  $\text{CO}_2$  into  $\text{CH}_4$  and  $\text{CO}$  on the SBTO surface (Fig. 21(c)). According to the calculated band potential value, the negative CB of  $\text{SrBi}_4\text{Ti}_4\text{O}_{15}$  provided a strong driving force for improving  $\text{CO}_2$  conversion (Fig. 21(d)). Remarkably, the layered nanocrystal structure with well-aligned distorted polyhedra enhanced the charge separation because the electrons and holes migrated separately to the  $\text{TiO}_2$  and  $\text{Bi}_2\text{O}_2^{2+}$  layers (Fig. 21(e)).

Another type of material is metal halide perovskites, which are represented by the general formula  $\text{ABX}_3$ , where A and B are cations and X is an anion.<sup>12</sup> Following the successful utilization of methylammonium lead halide perovskites in solar cell and LED applications in 2009, halide perovskites have attracted considerable attention in the field of photocatalysis. To date, several halide perovskites with various compositions have been reported where A = methylammonium (MA), formamidinium (FA), or Cs, B = Pb, Bi, or Sn, and X = Cl, Br, or I. However, similar to pristine metal oxides or any other semiconductors, pristine metal halide perovskites are associated with several drawbacks, such as poor light absorption, poor charge separation, and rapid charge recombination. In an effort to improve

these aspects, halide perovskites have been combined with various secondary materials or cocatalysts such as graphene, metal NPs, metal oxides, and metal carbides. In particular, the moisture stability of these perovskites has been significantly improved by embedding them into polymers or metal oxides/complexes. For example, Xu *et al.* established heterojunctions based on  $\text{TiO}_2$  nanofibers and  $\text{CsPbBr}_3$  QDs that promoted electron-hole separation and improved the photoconversion efficiency compared to the pristine perovskite.<sup>373</sup> Such hybridization enabled the preparation of heterojunctions with the highest redox ability.

Similarly, some other heterostructure combinations have been reported. For example, in 2017 Xu *et al.* reported that the rate of electron consumption increased by 25.5% upon combining  $\text{CsPbBr}_3$  with graphene oxide.<sup>374</sup> In addition, Jiang and co-workers described an ingenious ternary heterostructure based on  $\text{CsPbBr}_3$  nanocrystals and a hierarchical branched  $\text{ZnO}$  nanowire/macroporous graphene oxide composite.<sup>375</sup> In this case, the RGO played an important role by simultaneously adsorbing and activating  $\text{CO}_2$  molecules *via*  $\pi$ - $\pi$  interactions and conjugation, which most likely accelerated the catalytic  $\text{CO}_2$  conversion. The 3D cross-linked morphology provided a larger active surface area as well as pathways for rapid electron transport and mass transfer. Furthermore, 1D branched  $\text{ZnO}$  is simple to synthesize, inexpensive, and has ideal energy band potentials for  $\text{CO}_2$  reduction. In contrast to pristine  $\text{CsPbBr}_3$ , which reduced  $\text{CO}_2$  to  $\text{CO}$  and  $\text{CH}_4$  with reasonable activity, the hybrid composite displayed an increased rate of  $\text{CH}_4$  formation. Hence, the selectivity for  $\text{CH}_4$  formation correspondingly increased from 78.2% for  $\text{CsPbBr}_3$  to 96.7% for the ternary composite. Similarly, Wang *et al.* synthesized  $\text{Cs}_4\text{PbBr}_6$  wrapped with defective RGO hybrids through antisolvent precipitation and applied these materials to  $\text{CO}_2$  photoconversion.<sup>294</sup>

The presence of oxygen defects in the rGO nanosheets ultimately extended the lifetime of the electron-hole pairs. Here, COOH and OH moieties acted as anchor points for the hybridization of rGO with  $\text{CsPbBr}_3$  through forming Pb–O–C bonds. Some additional combinations of metal halide perovskites with graphene oxide have also been reported.<sup>376</sup> For example, the MOF nanocomposite  $\text{CsPbBr}_3\text{-UiO-66(NH}_2\text{)}$  has been studied for photocatalytic  $\text{CO}_2$  conversion and was found to display high catalytic activity for  $\text{CO}$  formation (98.57  $\mu\text{mol g}^{-1}$ ).<sup>377</sup> The increased activity and stability were driven by the high surface area, enhanced visible-light absorption, efficient charge separation in the QDs, and presence of the  $\text{UiO-66(NH}_2\text{)}$  nanocomposites. The selective formation of  $\text{CO}$  upon  $\text{CO}_2$  photoreduction was attributed to the dynamically favorable band potentials of  $\text{CsPbBr}_3$  and the HOMO/LUMO levels of  $\text{UiO-66(NH}_2\text{)}$  for efficiently mediating the  $2\text{H}^+/2\text{e}^-$  process. In another work, Kong and co-workers designed a core-shell halide perovskite@MOF composite that exhibited enhanced  $\text{CO}_2$  reduction activity.<sup>312</sup> In this work, coating of the ZIF shell onto the surface of the  $\text{CsPbBr}_3$  QDs was achieved *in situ* by dispersing the latter into a solution of the metal ion precursor and imidazole ligand. This coating improved the moisture stability of the  $\text{CsPbBr}_3$  QDs in addition to the  $\text{CO}_2$  capture ability and charge separation efficiency, ultimately resulting in enhanced photoconversion efficiency of  $\text{CO}_2$  to  $\text{CO}$  and  $\text{CH}_4$ .



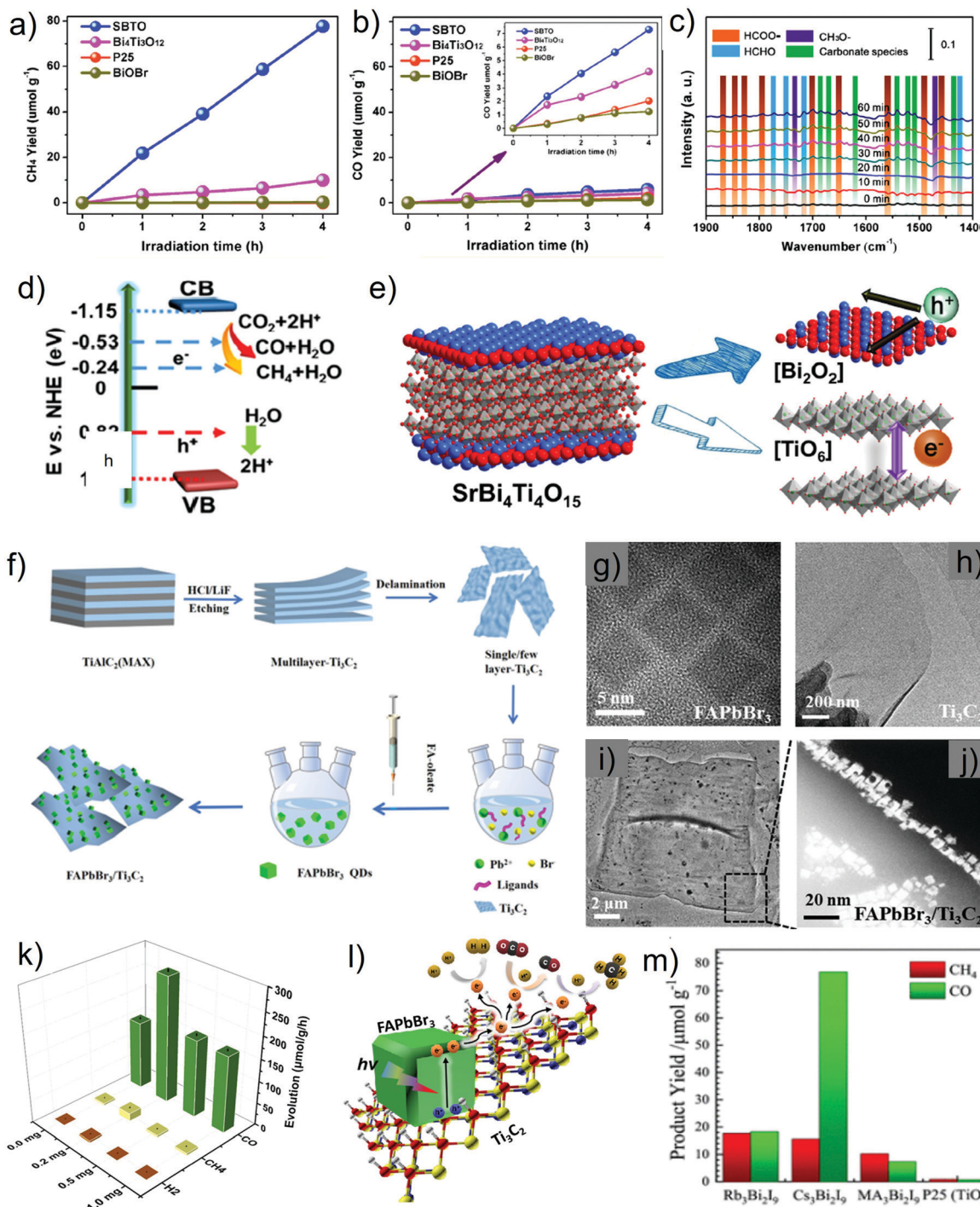


Fig. 21 (a) CH<sub>4</sub> and (b) CO evolution over SrBi<sub>4</sub>Ti<sub>4</sub>O<sub>15</sub> (SBTO) catalysts and several reference samples, (c) *in situ* DRIFTS analysis showing the intermediate products formed on SBTO catalysts under light irradiation at various time intervals, (d) energy band diagram for an SBTO catalyst, and (e) structure of the SBTO units showing electron–hole separation in different directions. Reproduced with permission from ref. 370, Copyright 2019, Elsevier. (f) Synthetic route to FAPbBr<sub>3</sub>/Ti<sub>3</sub>C<sub>2</sub>. (g)–(i) TEM images of FAPbBr<sub>3</sub>, Ti<sub>3</sub>C<sub>2</sub>, and their heterojunction, (j) dark-field STEM image of FAPbBr<sub>3</sub>/Ti<sub>3</sub>C<sub>2</sub>. (k) photocatalytic CO<sub>2</sub> reduction performance of FAPbBr<sub>3</sub>-x-Ti<sub>3</sub>C<sub>2</sub> samples (x is mg of Ti<sub>3</sub>C<sub>2</sub>). (l) structure of FAPbBr<sub>3</sub>/Ti<sub>3</sub>C<sub>2</sub> heterojunction for CO<sub>2</sub> reduction. Reproduced with permission from ref. 371, Copyright 2021, American Chemical Society. (m) CO and CH<sub>4</sub> formation over various Bi-based perovskite nanocrystals. Reproduced with permission from ref. 372, Copyright 2019, American Chemical Society.

Tang *et al.* conducted a theoretical study on the mechanism of CO<sub>2</sub> reduction by performing DFT calculations of Fe- and Co-doped CsPbBr<sub>3</sub>.<sup>378</sup> The results showed that the doped

perovskite displayed better adsorption ability of the activated intermediate CO<sub>2</sub><sup>•-</sup> that led to improved catalytic activity. Free energy calculations suggested that the product selectivity of the



pristine perovskite lay toward CO formation, whereas the selectivity shifted toward CH<sub>4</sub> formation upon Fe or Co doping. Shyamal *et al.* also investigated Fe(II)-doped CsPbBr<sub>3</sub> perovskite and observed enhanced catalytic activity and selectivity toward CH<sub>4</sub> formation.<sup>379</sup> The formation of CH<sub>4</sub> was drastically improved upon Fe doping, while the pristine perovskite was selective toward CO evolution. The product selectivity of doped CsPbBr<sub>3</sub> was related to the adsorption-desorption characteristics, where the more positive adsorption energy of the CH<sub>4</sub> molecule enabled it to desorb rapidly from the catalytic surface, which was the major reason for the high selectivity. Similarly, other studies have reported the Co, Ni, and Mn doping of perovskite nanocrystals.<sup>380,381</sup> Apart from metal doping, a composite based on CsPbBr<sub>3</sub> nanocrystals and 2D Pd NSs has been reported as a highly efficient and stable catalyst for gas-phase photocatalytic CO<sub>2</sub> reduction with H<sub>2</sub>O vapor.<sup>382</sup> This combination formed a Schottky contact and improved the electron consumption rate compared with the pristine perovskite nanocrystals. Subsequently, the transition-metal complex Ni(tpy) was immobilized on CsPbBr<sub>3</sub> nanocrystals, which provided abundant active sites for capturing CO<sub>2</sub> molecules through the metal complexes.<sup>383</sup> Meanwhile, the polypyridyl rings efficiently captured and stored electrons for the CO<sub>2</sub> reduction process. As a result, the efficiency of CO<sub>2</sub> photoreduction to CO/CH<sub>4</sub> increased by a factor of 26.

Cesium-based metal halide perovskites are commonly used for photocatalytic CO<sub>2</sub> reduction; however, changing the metal component (A site) may alter the optoelectronic properties of the catalyst. In this regard, Wu and co-workers encapsulated CH<sub>3</sub>NH<sub>3</sub>PbI<sub>3</sub> (MAPbI<sub>3</sub>) QDs in the pores of the Fe-porphyrin-based MOF PCN-221(Fe<sub>x</sub>) and studied its photocatalytic CO<sub>2</sub> reduction behavior to afford CO/CH<sub>4</sub>.<sup>384</sup> The encapsulation improved the perovskite stability and the close contact between these materials shortened the charge transfer distance, resulting in very high catalytic activity. In another case, formamidinium lead bromide (FAPbBr<sub>3</sub>) perovskite QDs were applied to CO<sub>2</sub> photoreduction in various reaction media, where water acted as a proton source and the solvent allowed maximum CO<sub>2</sub> saturation.<sup>385</sup> Similarly, improved catalytic activity was reported upon Schottky heterojunction formation between FAPbBr<sub>3</sub> and Ti<sub>3</sub>C<sub>2</sub> nanosheets.<sup>371</sup> The excellent metallic conductivity and high surface area of Ti<sub>3</sub>C<sub>2</sub> were beneficial for improving the optoelectronic properties of the catalyst. Briefly, FAPbBr<sub>3</sub> QDs were grown in the presence of Ti<sub>3</sub>C<sub>2</sub> using the hot injection method (Fig. 21(f)). Spectroscopic analysis confirmed the strong interaction between FAPbBr<sub>3</sub> and Ti<sub>3</sub>C<sub>2</sub>, facilitating separation of the photogenerated electrons through the interface. The formation of FAPbBr<sub>3</sub>/Ti<sub>3</sub>C<sub>2</sub> could also be observed in the TEM and STEM images (Fig. 21(g)–(j)). Analysis of the optoelectronic properties revealed that the Ti<sub>3</sub>C<sub>2</sub> nanosheets acted as an electron acceptor, allowing for the rapid transfer of photoexcited electrons in FAPbBr<sub>3</sub>. The electron consumption rate for FAPbBr<sub>3</sub>/Ti<sub>3</sub>C<sub>2</sub> was reported to be 717.18 μmol g<sup>-1</sup> h<sup>-1</sup>, which was approximately two-fold higher than that for the bare FAPbBr<sub>3</sub> sample (Fig. 21(k) and (l)).

Although a variety of metal halide perovskites have shown promise as materials for photocatalytic CO<sub>2</sub> reduction, the

mass production of lead-based perovskite materials remains problematic owing to the unavoidable issue of lead toxicity, obstructing the long-term viability of this technology. As a result, numerous research efforts have been dedicated to creating environmentally safe lead-free halide perovskite materials for photocatalytic applications. In this regard, Zhou and co-workers studied nanocrystals of the halide double perovskite Cs<sub>2</sub>AgBiBr<sub>6</sub> synthesized *via* a hot-injection method, which displayed excellent electron consumption (105 μmol g<sup>-1</sup>) under AM 1.5 G illumination.<sup>386</sup> The synthesized nanocrystals were reported to be highly stable in mild polar solvents for more than three weeks, even in the presence of light and humidity. Another recent study used the injection of a precursor at room temperature followed by heating of the reaction mixture to construct 2D multilayered Cs<sub>2</sub>AgBiX<sub>6</sub> (X = Cl, Br, I) nanoplatelets.<sup>387</sup> Nanoplatelets possess several desirable characteristics such as exposed facets, well-arranged surface atomic symmetries, and quantum confined photocarriers. The authors synthesized a series of double perovskites by varying the halide composition and combinations, and Cs<sub>2</sub>AgBiBr<sub>6</sub> was found to display efficient photocatalytic performance. To investigate the influence of the nanoplatelet morphology, the catalytic performance of the Cs<sub>2</sub>AgBiBr<sub>6</sub> nanoplatelets was compared to that of simple nanocrystals. The results revealed that the nanoplatelets exhibited higher CO and CH<sub>4</sub> production rates than the nanocrystals (eight-fold higher electron consumption rate over 6 h). NPLs have anisotropically confined charge carriers and long diffusion length, resulted in such an improved catalytic performance.

Besides these materials, Cs<sub>2</sub>AgBiBr<sub>6</sub> nanocrystals were combined with g-C<sub>3</sub>N<sub>4</sub> to form Z-scheme and type-II heterojunction systems using toluene and CH<sub>2</sub>Cl<sub>2</sub>, respectively.<sup>388</sup> Interestingly, by altering the CB of g-C<sub>3</sub>N<sub>4</sub> and the VB of Cs<sub>2</sub>AgBiBr<sub>6</sub>, the Z-scheme combination displayed superior photocatalytic CO<sub>2</sub> reduction to CH<sub>4</sub>, whereas the type-II heterojunction system exhibited CO selectivity. In 2020, Lu *et al.* reported the photoconversion of CO<sub>2</sub> upon changing the B site to the aforementioned layered double halide perovskite, *i.e.*, Cs<sub>3</sub>Sb<sub>2</sub>Br<sub>9</sub>.<sup>389</sup> The surface-exposed Sb sites led to higher reactivity for CO<sub>2</sub> reduction and thus improved catalytic activity. Changing the cation may also lead to different catalytic behavior; for example, Bhosale *et al.* fabricated Bi-based perovskite photocatalysts (*i.e.*, Cs<sub>3</sub>Bi<sub>2</sub>I<sub>9</sub>, Rb<sub>3</sub>Bi<sub>2</sub>I<sub>9</sub>, and MA<sub>3</sub>Bi<sub>2</sub>I<sub>9</sub>) using a top-down ultrasonication approach.<sup>372</sup> They revealed that the cation and crystal structure of the perovskite play important roles in determining the catalytic activity and CO<sub>2</sub> reduction pathway using EPR and diffuse-reflectance infrared spectra. The photocatalytic CO<sub>2</sub> reduction activities toward CO and CH<sub>4</sub> of the perovskite nanocrystals followed the order Cs<sub>3</sub>Bi<sub>2</sub>I<sub>9</sub> > Rb<sub>3</sub>Bi<sub>2</sub>I<sub>9</sub> > MA<sub>3</sub>Bi<sub>2</sub>I<sub>9</sub> > TiO<sub>2</sub> (Fig. 21(m)). In addition, the EPR results indicated that Cs<sub>3</sub>Bi<sub>2</sub>I<sub>9</sub> displayed higher catalytic activity than the other perovskites owing to its greater ability to generate electron-hole pairs.

The studies discussed above suggest unique strategies for obtaining lead-free perovskite-based catalytically active materials for mediating efficient photocatalytic CO<sub>2</sub> conversion reactions. The photocatalytic CO<sub>2</sub> reduction performance of perovskite-based catalysts is summarized in Table 7.



Table 7 Perovskite-based materials for photocatalytic  $\text{CO}_2$  reduction

Catalyst	Feed gas composition	Light source	Reducing agent	Reaction conditions	Reactor type	Yield	Ref.
Ti-Rich SrTiO <sub>3</sub> SrTiO <sub>3-<math>\delta</math></sub> Au/Rh@SrTiO <sub>3</sub>	$\text{CO}_2$ (10 mL) + $\text{H}_2\text{O}$ (10 $\mu\text{L}$ ) 98% $\text{CO}_2$ + 2% $\text{H}_2\text{O}$ $\text{CO}_2$ + $\text{H}_2\text{O}$	300 W Xe lamp (0.190 W $\text{cm}^{-2}$ ) 300 W Xe lamp (420 nm filter) 300 W Xe lamp (142 filter)	$\text{H}_2\text{O}$ $\text{H}_2\text{O}$	20 mg sample 0.3 g sample 75 mg sample	Gas phase Gas phase Gas-phase batch reactor	CO: 26.4 $\mu\text{mol g}^{-1}$ (6 h) CH <sub>4</sub> : 0.25 $\mu\text{mol m}^{-2}\text{h}^{-1}$ CO: 369.2 $\mu\text{mol g}^{-1}\text{h}^{-1}$ H <sub>2</sub> : 69.4 $\mu\text{mol g}^{-1}\text{h}^{-1}$ CH <sub>4</sub> : 2.8 $\mu\text{mol g}^{-1}\text{h}^{-1}$ CH <sub>4</sub> : 14.6 $\mu\text{mol g}^{-1}\text{h}^{-1}$	358 359 360
RuO <sub>2</sub> -SrTiO <sub>3</sub>	$\text{CO}_2$ + $\text{H}_2$ (4 : 1 (mol/mol))	300 W UV-vis Xe lamp (1000 W $\text{m}^{-2}$ ) 300 W Xe lamp	—	50 mg sample	Gas-phase flow reactor	CO: 11.72 $\mu\text{mol g}^{-1}\text{h}^{-1}$	361
CaTiO <sub>3</sub> /TiO <sub>2</sub>	$\text{CO}_2$ + $\text{H}_2\text{O}$	$\text{H}_2\text{O}$	10 mg sample in quartz tube (43 mL)	Gas-phase batch reactor	CO: 0.42 $\mu\text{mol g}^{-1}$ (10 h)	362	
Li/K/Na-TaO <sub>3</sub>	$\text{CO}_2$ (150 $\mu\text{mol}$ ) + $\text{H}_2$ (50 $\mu\text{mol}$ )	200 W Hg-Xe lamp	—	2.0 g sample in quartz reactor (150 mL)	Gas phase	CO: 173 $\mu\text{mol g}^{-1}\text{h}^{-1}$ CH <sub>4</sub> : 36 $\mu\text{mol g}^{-1}\text{h}^{-1}$ CO: 28.5 $\mu\text{mol}$ (1 h)	364
NaTaO <sub>3</sub>	$\text{CO}_2$ + $\text{H}_2\text{O}$ (80 kPa of $\text{CO}_2$ , 2 mL $\text{H}_2\text{O}$ )	200 W Hg-Xe arc lamp	—	50 mg sample in Pyrex reaction cell, 2 mL DI water	Gas phase	AQY = 1.36%	365
LaCoO <sub>3</sub>	$\text{CO}_2$ -saturated MeCN/ $\text{H}_2\text{O}$ /TEOA (3:2:1)	300 W Xe lamp (420 nm cutoff) $\text{H}_2\text{O}$ filter	$\text{H}_2\text{O}$	1 mg sample with Ru-complex and TEOA as photosensitizer and electron donor, respectively, reaction controlled at 30 °C	Gas phase		
MnCo <sub>2</sub> O <sub>4</sub>	High purity of $\text{CO}_2$ in solvent (5 mL, 2:3 $\text{H}_2\text{O}$ /acetonitrile) $\text{CO}_2$ + $\text{H}_2\text{O}$	300 W Xe lamp (420 nm cutoff) 300 W Xe arc lamp	$\text{H}_2\text{O}$	4 $\mu\text{mol}$ sample, Ru-complex, and TEOA in reactor (80 mL) 50 mg sample, 2 mL $\text{H}_2\text{O}$ in Pyrex glass vessel	Gas-phase batch reactor	CO: 27 $\mu\text{mol}$ (1 h) CO: 0.39 $\mu\text{mol g}^{-1}$	366 367
Ag <sub>2</sub> CrO <sub>4</sub> /Ag/ BiFeO <sub>3</sub> @rGO	99.99% $\text{CO}_2$ + $\text{H}_2\text{O}$	UV, visible, NIR	$\text{H}_2\text{O}$	40 mg sample, 40 mL DI water in Pyrex reactor vessel	Gas phase	CH <sub>4</sub> : 180 $\mu\text{mol g}^{-1}$ (8 h) CO: 38 $\mu\text{mol g}^{-1}$ (8 h) CH <sub>4</sub> : 19.8 $\mu\text{mol g}^{-1}\text{h}^{-1}$ CO: 1.74 $\mu\text{mol g}^{-1}\text{h}^{-1}$ AQY = 1.33% (365 nm)	368 370
Ag/H <sub>2</sub> SrTa <sub>2</sub> O <sub>7</sub>	$\text{CO}_2$ (95% Ar, 5% $\text{CO}_2$ ) + $\text{H}_2\text{O}$	300 W Xe lamp ( $\lambda$ > 200 nm)	—	100 mg sample dispersed in DI $\text{H}_2\text{O}$ and dried at 80 °C	Gas-phase batch reactor	CO: 0.39 $\mu\text{mol g}^{-1}\text{h}^{-1}$	369
TiO <sub>2</sub> /CsPbBr <sub>3</sub>	High-purity $\text{CO}_2$ (99.99%)	300 W Xe arc lamp	$\text{H}_2\text{O}$	200 mg sample	Gas-phase flow reactor	CO: 9.02 $\mu\text{mol g}^{-1}\text{h}^{-1}$	373
CsPbBr <sub>3</sub> QDs/GO	Ethyl acetate (10 mL) + $\text{CO}_2$	100 W Xe lamp (AM 1.5 filter)	—	10 mg sample, 30 mL acetonitrile, 100 $\mu\text{L}$ $\text{H}_2\text{O}$ in quartz/Pyrex hybrid reaction cell	Gas phase	CO: 58.7 $\mu\text{mol g}^{-1}$ (12 h) CH <sub>4</sub> : 29.6 $\mu\text{mol g}^{-1}$ (12 h) H <sub>2</sub> : 1.58 $\mu\text{mol g}^{-1}$ (12 h) CH <sub>4</sub> : 6.29 $\mu\text{mol g}^{-1}\text{h}^{-1}$ (3 h) CO: 0.8 $\mu\text{mol g}^{-1}\text{h}^{-1}$ (3 h)	374
CsPbBr <sub>3</sub> /BZNW/ MRGO	$\text{CO}_2$	150 W Xe lamp (AM 1.5 G and 420 nm optical filter, 100 mW $\text{cm}^{-2}$ )	$\text{H}_2\text{O}$	4 mg sample in sealed Pyrex bottle (40 mL)	Gas phase	CO: 58.7 $\mu\text{mol g}^{-1}$ (12 h) CH <sub>4</sub> : 29.6 $\mu\text{mol g}^{-1}$ (12 h) H <sub>2</sub> : 1.58 $\mu\text{mol g}^{-1}$ (12 h) CH <sub>4</sub> : 6.29 $\mu\text{mol g}^{-1}\text{h}^{-1}$ (3 h) CO: 0.8 $\mu\text{mol g}^{-1}\text{h}^{-1}$ (3 h)	294
Cs <sub>4</sub> PbBr <sub>6</sub> /rGO	$\text{CO}_2$ + ethyl acetate	300 W Xe lamp (420 nm filter, 100 mW $\text{cm}^{-2}$ )	$\text{H}_2\text{O}$	5 mg sample, 5 mL ethyl acetate, and 5 $\mu\text{L}$ water mixed in sealed Pyrex bottle (35 mL)	Gas phase	CO: 11.4 $\mu\text{mol g}^{-1}\text{h}^{-1}$	376
CsPbBr <sub>3</sub> /USGO/ $\alpha$ -Fe <sub>2</sub> O <sub>3</sub>	$\text{CO}_2$	300 W Xe lamp (420 nm filter, 100 mW $\text{cm}^{-2}$ )	$\text{H}_2\text{O}$	4 mg sample mixed with acetonitrile/ — deionized water (200:1 (v/v), 5 mL) in sealed Pyrex bottle (12 mL)	Gas phase	CO: 73.8 $\mu\text{mol g}^{-1}\text{h}^{-1}$	376
CsPbBr <sub>3</sub> QDs/UiO- 66(NH <sub>2</sub> )	High-purity $\text{CO}_2$ + ethyl acetate	300 W Xe lamp (420 nm UV cutoff filter)	$\text{H}_2\text{O}$	10 mg sample dispersed in $\text{H}_2\text{O}$ /ethyl acetate (1 : 300 (v/v)), 10 $\mu\text{L}$ $\text{H}_2\text{O}$ in Pyrex reaction cell	Gas phase	CO: 98.57 $\mu\text{mol g}^{-1}$ CH <sub>4</sub> : 3.08 $\mu\text{mol g}^{-1}$ (12 h)	377
CsPbBr <sub>3</sub> @zeolitic imidazolate	$\text{CO}_2$ + $\text{H}_2\text{O}$ vapor ( $\text{H}_2\text{O}$ evaporated at 120 °C for 2 min)	100 W Xe lamp (AM 1.5G filter, 150 mW $\text{cm}^{-2}$ )	$\text{H}_2\text{O}$	4.5 mg sample (film) in sealed Pyrex bottle (40 mL)	Gas phase	Electron consumption rate: 312 AQY = 0.035%	378
Co- and Fe-CsPbBr <sub>3</sub>	Theoretical DFT study using DMol <sub>3</sub>	300 W Xe lamp (150 mW $\text{cm}^{-2}$ )	$\text{H}_2\text{O}$	5 mg sample mixed with $\text{CO}_2$ and 10 $\mu\text{L}$ $\text{H}_2\text{O}$ in sealed Pyrex bottle (25 mL)	Gas phase	CO: 6.1 $\mu\text{mol g}^{-1}\text{h}^{-1}$ (3 h) CH <sub>4</sub> : 3.2 $\mu\text{mol g}^{-1}\text{h}^{-1}$ (3 h)	379
Fe( <i>n</i> )-CsPbBr <sub>3</sub>							

Table 7 (continued)

Catalyst	Feed gas composition	Light source	Reducing agent	Reaction conditions	Reactor type	Yield	Ref.
Co-CsPbBr <sub>3</sub> /Cs <sub>4</sub> PbBr <sub>6</sub>	CO <sub>2</sub> + acetonitrile (methanol as hole scavenger)	300 W Xe lamp (100 mW m <sup>-2</sup> ) H <sub>2</sub> O	4 mg sample added to acetonitrile/H <sub>2</sub> O/MeOH (5 : 15 : 15 $\mu$ L) in sealed Pyrex bottle (12 mL)	—	CO: 1835 $\mu$ mol g <sup>-1</sup> (15 h)	380	
Ni- and Mn-doped CsPbCl <sub>3</sub> nanocrystals	CO <sub>2</sub>	300 W Xe lamp (AM 1.5 filter) H <sub>2</sub> O vapor	6 mg sample (film) and 500 $\mu$ L H <sub>2</sub> O in Gas phase sealed Pyrex bottle (120 mL)	CO: 169.37 $\mu$ mol g <sup>-1</sup> h <sup>-1</sup> (for Ni) CO: 152.49 $\mu$ mol g <sup>-1</sup> h <sup>-1</sup> (for Mn)	381		
CsPbBr <sub>3</sub> /Pd nanosheets	CO <sub>2</sub> + H <sub>2</sub> O (H <sub>2</sub> O evaporated at 120 °C for 3 min)	150 W Xe lamp (Zolix, AM 1.5 G and 420 nm optical filter, 100 mW cm <sup>-2</sup> )	H <sub>2</sub> O vapor 5.3 mg catalyst (film) and 10 $\mu$ L water Gas phase sealed Pyrex bottle (40 mL)	CO: 12.63 $\mu$ mol g <sup>-1</sup> (3 h) CH <sub>4</sub> : 10.41 $\mu$ mol g <sup>-1</sup> (3 h)	382		
[Ni(terpy) <sub>2</sub> ] <sup>2+</sup> (Ni(terpy)) CsPbBr <sub>3</sub> nanocrystals	CO <sub>2</sub> + ethyl acetate	300 W Xe lamp (SolarEdge 700, 100 mW cm <sup>-2</sup> , $\lambda$ > 400 nm)	5 mg catalyst in ethyl acetate/water solution (5 mL, 49:1 (v/v)) in Pyrex photoreactor (reactor maintained at 25 °C)	CO + CH <sub>4</sub> : 1724 $\mu$ mol g <sup>-1</sup> (4 h)	383		
Ni(terpy)-CsPbBr <sub>3</sub> Fe/CH <sub>3</sub> NH <sub>3</sub> PbI <sub>3</sub> (MAPbI <sub>3</sub> ) QDs	CO <sub>2</sub> + ethyl acetate	300 W Xe lamp	H <sub>2</sub> O 4 mg catalyst, 5 mL ethyl acetate and H <sub>2</sub> O (1 : 0.012 (v/v)) injected into sealed Pyrex bottle (10 mL)	CO + CH <sub>4</sub> : 1559 $\mu$ mol g <sup>-1</sup> (384)	384		
FAPbBr <sub>3</sub> QDs	CO <sub>2</sub>	300 W Xe lamp (100 mW cm <sup>-2</sup> )	H <sub>2</sub> O 4 mg catalyst in 1 mL H <sub>2</sub> O or ethyl acetate in sealed Pyrex bottle (40 mL)	CO: 181.25 $\mu$ mol g <sup>-1</sup> h <sup>-1</sup> (385)	385		
FAPbBr <sub>3</sub> /Ti <sub>3</sub> C <sub>2</sub>	CO <sub>2</sub>	300 W Xe lamp (100 mW cm <sup>-2</sup> )	H <sub>2</sub> O 3 mg catalyst, 0.5 mL H <sub>2</sub> O in sealed Pyrex bottle (40 mL)	CO: 283.41 $\mu$ mol g <sup>-1</sup> h <sup>-1</sup> CH <sub>4</sub> : 17.67 $\mu$ mol g <sup>-1</sup> h <sup>-1</sup> H <sub>2</sub> : 1.33 $\mu$ mol g <sup>-1</sup> h <sup>-1</sup> CO: 14.1 $\mu$ mol g <sup>-1</sup> (6 h) CH <sub>4</sub> : 9.6 $\mu$ mol g <sup>-1</sup> (6 h)	371		
Cs <sub>2</sub> AgBiBr <sub>6</sub>	Pure CO <sub>2</sub> + ethyl acetate (pretreated with 4 A molecular sieves to remove residual water) Dry ethyl acetate + CO <sub>2</sub> (99.9%)	100 W Xe lamp (AM 1.5 G filter) 405 nm laser diode	— Xe lamp (80 mW cm <sup>-2</sup> )	CO: ca. 25.06 $\mu$ mol g <sup>-1</sup> (6 h) CH <sub>4</sub> : ca. 40.06 $\mu$ mol g <sup>-1</sup> (6 h) AQY = 0.035% CO + CH <sub>4</sub> : 2.0 $\mu$ mol g <sup>-1</sup> h <sup>-1</sup> (387)	386		
Cs <sub>2</sub> AgBiX <sub>6</sub>	Pure CO <sub>2</sub> + ethyl acetate + methanol	—	2 mg catalyst, 10 mL ethyl acetate in sealed headspace reactor (20 mL)	CO: 25.06 $\mu$ mol g <sup>-1</sup> (6 h) CH <sub>4</sub> : 9.6 $\mu$ mol g <sup>-1</sup> (6 h)	388		
Cs <sub>3</sub> Sb <sub>2</sub> Bi <sub>9</sub>	Pure CO <sub>2</sub>	300 W Xe lamp with AM 1.5 irradiation	— 15 mg catalyst, 4 mL ethyl acetate, 1 mL methanol in Schlenk glass bottle (25 mL) ca. 50–100 mg catalyst, pre-dried octadecene in water-jacketed Pyrex photoreactor (reaction maintained at 25 °C)	CO: 510 $\mu$ mol g <sup>-1</sup> (4 h)	389		
Bi-Based perovskite nanocrystals	99.99% CO <sub>2</sub> + H <sub>2</sub> O vapor	32 W UV lamp (305 nm)	H <sub>2</sub> O Catalyst in 1 mL trichloromethane and dried by N <sub>2</sub> gas flow in quartz reactor (230 mL)	Gas phase For Cs <sub>3</sub> Bi <sub>2</sub> I <sub>9</sub> (10 h): CO: 77.6 $\mu$ mol g <sup>-1</sup> CH <sub>4</sub> : 14.9 $\mu$ mol g <sup>-1</sup> For Rb <sub>3</sub> Bi <sub>2</sub> I <sub>9</sub> (10 h): CO: 18.2 $\mu$ mol g <sup>-1</sup> CH <sub>4</sub> : 17.0 $\mu$ mol g <sup>-1</sup> For MA <sub>3</sub> Bi <sub>2</sub> I <sub>9</sub> (10 h): CO: 7.2 $\mu$ mol g <sup>-1</sup> CH <sub>4</sub> : 9.8 $\mu$ mol g <sup>-1</sup>	372		

### 5.7 Plasmonic materials

The LSPR permits NPs to harvest light it is dependent upon the size of nanoparticles. The resulting interaction of the light and free electrons in the CB of the NPs causes oscillation of the surface electrons with the incident light. LSPR permits the gathering of light photons and creates energized charge transporters and heat. These charge transporters can be utilized to drive chemical reactions. In plasmonic catalysis, the exchange of photoexcited charge transporters from metal NPs to the reactants. The formation of heterostructures based on LSPR and photocatalysts is an exciting approach for  $\text{CO}_2$  photoreduction.<sup>390</sup> Recently, several studies have attempted to apply plasmonic engineering to  $\text{CO}_2$  photoreduction.<sup>391–393</sup> Under light irradiation, free electrons produce an electrical dipole moment by displacing the electrical field to nuclei. Concurrently, the Coulombic attraction between the electrons and nuclei generates a restoring force to produce the resonant oscillation of electrons. This phenomenon is called the quasi-static effect and it significantly enhances light absorption.<sup>394,395</sup> In this regard, Kumari *et al.* reported the use of Ag plasmonic NPs for  $\text{CO}_2$  reduction under visible-light irradiation.<sup>396</sup> They studied discrete adsorbates by *in situ* surface-enhanced Raman spectroscopy and estimated the product formation energy using DFT simulations.

Fig. 22(a) shows the results for a physisorbed  $\text{CO}_2$  molecule, which was found to lie a considerable distance (3.4 Å) from the Ag surface in the simple structure form with a somewhat out-of-plane geometry for OCO (108.7°). To represent the effect of plasmonic excitation, the authors considered a charge-separated condition of the  $\text{CO}_2$ /metal complex with a -1 charge along the  $\text{CO}_2$  molecule and a +1 charge on the Ag surface. After geometry

relaxation, the  $\text{CO}_2$  held an electronic charge of -0.4 (balanced by a positive charge of +0.4 on Ag). Reliant upon the binding motif of  $\text{CO}_2^{\delta-}$  on the surface, O atoms facing catalyst surface (Fig. 22(b)) or C atom facing catalyst surface (Fig. 22(c)), the structure of adsorbate, free energy, and registered Raman spectrum changed. However, the OCO vibration mode was estimated to be in the range of 1200–1300  $\text{cm}^{-1}$  range, which was not observed in this study. This charged  $\text{CO}_2^{\delta-}$  exhibited a bent geometry, the activated type of  $\text{CO}_2$ . Indeed, energy optimization of  $\text{CO}_2^{\delta-}$  on Ag in the vicinity of a surface-adsorbed  $\text{H}^{\delta+}$  induced the development of a surface-adsorbed  $\text{HOCO}^*$  intermediate (Fig. 22(d) and (e)). However, the O and H atoms pointed away from the surface. The CO vibration stretching mode at 2231  $\text{cm}^{-1}$  (Fig. 22(f)) showed that adsorbed CO is formed.

Furthermore, the decoration of bimetallic Au/Ag NPs on the top of  $\text{TiO}_2$  nanowires was reported to synergistically enhance the light absorption.<sup>250</sup> The surface electrons of Au/Ag become excited and transferred to the CB of  $\text{TiO}_2$ . While Au/Ag NPs could act as electron sink and allow a longer lifetime for photoexcited electrons. Therefore, the authors observed the evolution of CO ( $1813 \mu\text{mol g}_{\text{cat}}^{-1} \text{h}^{-1}$ ) as the primary product with 98% selectivity. In addition, the plasmonic effects of Au in  $\text{CO}_2$  photoreduction have also been studied. Collado *et al.* demonstrated that the deposition of small Au nanoparticles on  $\text{TiO}_2$  resulted in the formation of  $\text{C}_1$  and  $\text{C}_2$  products under UV irradiation.<sup>397</sup> Upon increasing the amount of Au from 0.5 to 3.0 wt%, the production of  $\text{CH}_4$  improved with respect to  $\text{CH}_3\text{OH}$ ,  $\text{H}_2$ , and CO owing to the better charge separation and a number of electrons. Furthermore, Zeng *et al.* reported the controlled fabrication of a plasmonic Z-scheme Au/ $\text{TiO}_2$

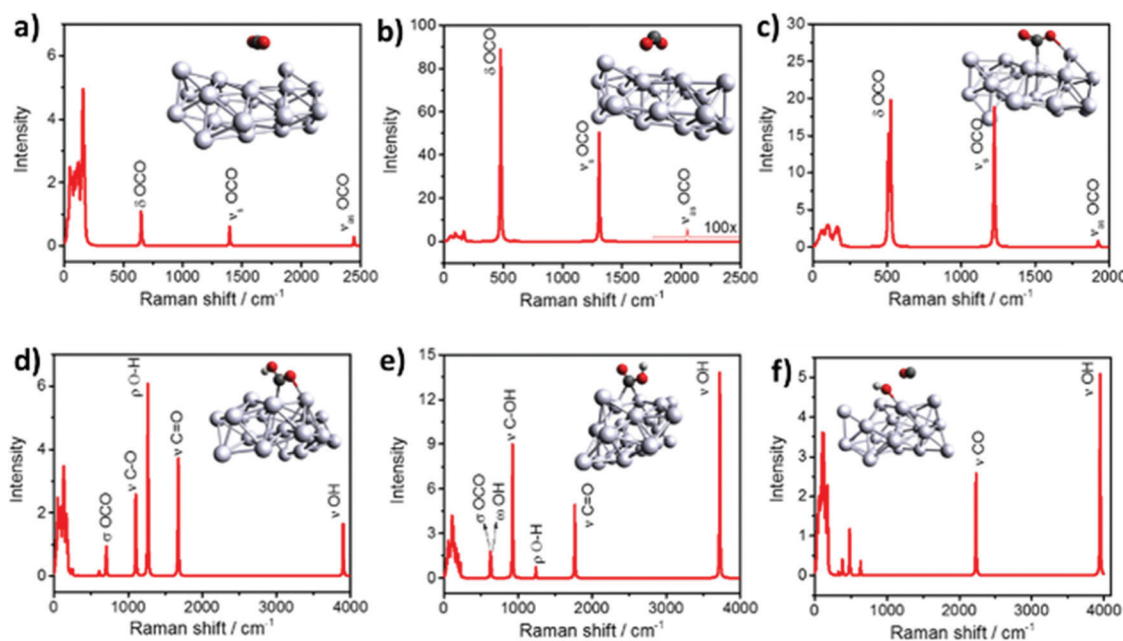
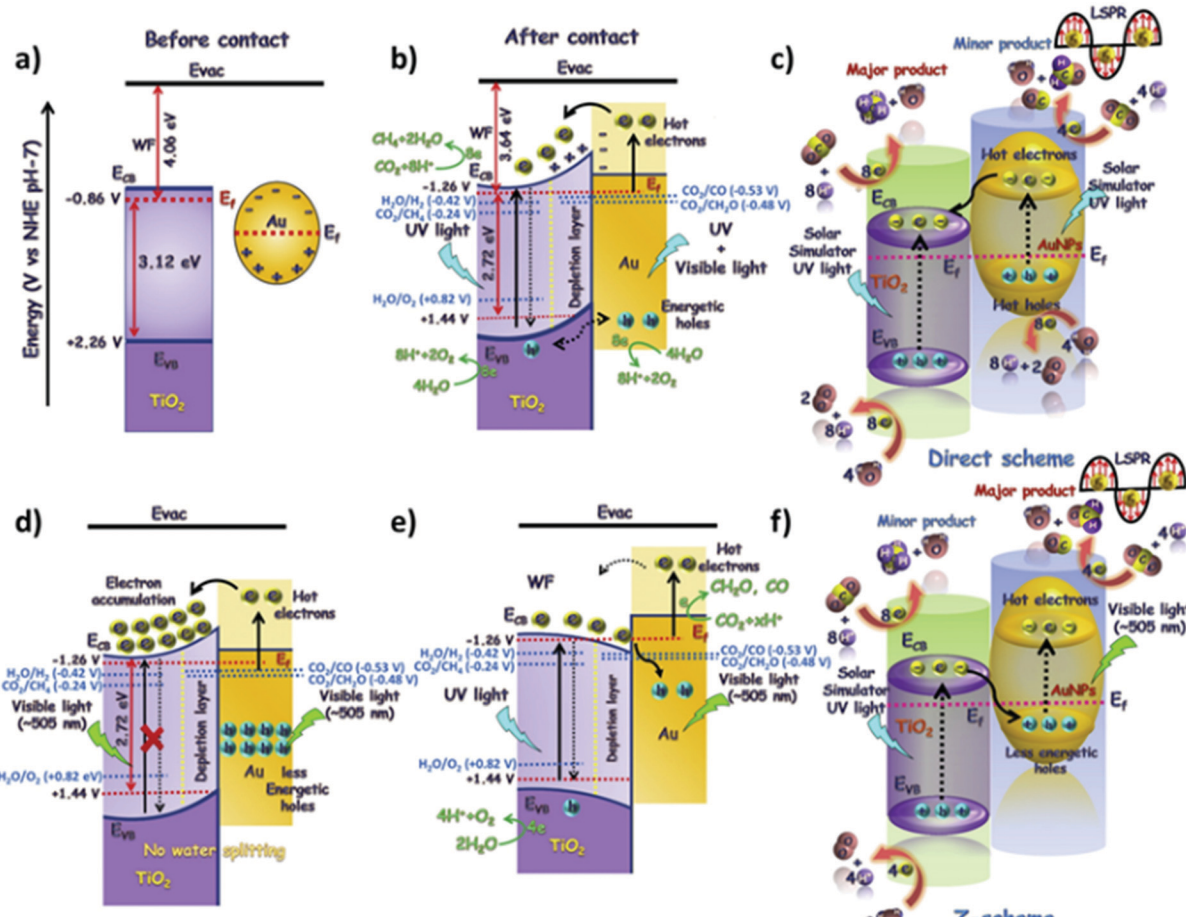


Fig. 22 (a) Physisorbed  $\text{CO}_2$ , (b)  $\text{CO}_2^{\delta-}$  anion with both O atoms facing the  $\text{Ag}^{\delta+}$  surface, (c)  $\text{CO}_2^{\delta-}$  anion binding to the  $\text{Ag}^{\delta+}$  surface via C and O atoms, (d)  $\text{HOCO}^*$  intermediate bound to the Ag surface via both C and O atoms, (e)  $\text{HOCO}^*$  intermediate bound to the Ag surface via a C atom, and (f) surface-bound  $\text{CO}^*$  and  $\text{OH}^*$  formed from dissociation of a  $\text{HOCO}^*$  intermediate with both O atoms facing the Ag surface. Reproduced with permission from ref. 396, Copyright 2018, American Chemical Society.





**Fig. 23** (a) Band energies of TiO<sub>2</sub> and Au before contact, (b) Schottky junction formation between Au and TiO<sub>2</sub> and their Fermi level alignment during CO<sub>2</sub> reduction under simulated sunlight (traditional SPR assisted scheme shown in the blue text), (c) schematic representation of CH<sub>4</sub> formation by Au-PMTiNTs under simulated sunlight, (d) hot-electron injection from Au NPs into TiO<sub>2</sub> across Schottky barrier under visible light by LSPR, (e) recombination of the accumulated electron in TiO<sub>2</sub> originated from the Au NP by LSPR, which forms the plasmonic Z-scheme, and (f) schematic illustration of overall Z-scheme for photocatalytic CO<sub>2</sub> photoreduction to CH<sub>2</sub>O. Reproduced with permission from ref. 398, Copyright 2020, Elsevier.

catalyst for CO<sub>2</sub> photoreduction, as shown in Fig. 23(a)–(f).<sup>398</sup> This catalyst was synthesized by charge-controlled pulsed anodization and provided tunable product selectivity. The photonic crystals were composed of TiO<sub>2</sub> nanotube arrays (referred to as periodically modulated titanium dioxide nanotube arrays (PMTiNTs)) decorated with the gold nanoparticle to form the plasmonic effect. The authors identified two pathways that afforded different selectivity.

Under simulated sunlight (AM 1.5G), CH<sub>4</sub> and CO were found to be the major and minor products, respectively. This indicated that direct charge transfer of sufficiently energetic electrons to the CB of TiO<sub>2</sub> and specific photonic bandgaps avoided the defect-mediated low-energy charge transfer that might produce other hydrocarbons, as shown in Fig. 23(c). In addition, owing to the lower reduction potential of CO<sub>2</sub>/CH<sub>4</sub> with respect to CO<sub>2</sub>/CO and CO<sub>2</sub>/CH<sub>2</sub>O, CH<sub>4</sub> formation may be thermodynamically favorable. Furthermore, when the Au NPs were illuminated with 532 nm light, strong absorption was observed owing to the LSPR. However, under visible-light irradiation, a slight positive shift of 25 mV is driven by hot-electron transfer

into CB energy of TiO<sub>2</sub> across the Schottky junction, followed by absorption and plasmonic dephasing as illustrated in Fig. 23(d); thereby leaving the positively charged holes on the Au NPs. Under simulated sunlight, an accumulation-type interfacial band alignment was formed that promoted strong electron transfer from TiO<sub>2</sub> to Au, as shown in Fig. 23(e) and (f).

Thus, a large flux of electrons recombines with holes produced from the Au by plasmonic damping, making the TiO<sub>2</sub> photocatalytically active. Although these hot electrons underwent thermalization within picoseconds, gas evolution indicated charge transfer to the CO<sub>2</sub> molecules. Thus, the key point of this study is that optically controlled product selectivity is a most delicate technique.

In conclusion, plasmonic photocatalysis provides an opportunity for the optimization of hydrocarbon products during CO<sub>2</sub> reduction. However, this field must still face the challenge of understanding the reaction mechanism for various photocatalysts. Its major drawbacks include the high energy input, low yield, and poor catalyst stability. Several *in situ* spectroscopy techniques may help elucidate the complex reaction mechanisms at the molecular level.

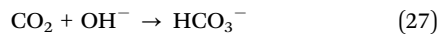
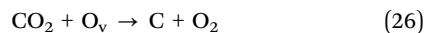
Table 8 Plasmonic materials for photocatalytic  $\text{CO}_2$  reduction

Catalyst	Feed gas composition	Light source	Reducing agent	Reaction conditions	Reactor	Yield	Ref.
Ag@Ni/SiO <sub>2</sub>	$\text{CO}_2 + \text{H}_2 + \text{N}_2$ (1:4:1)	405 nm laser light	$\text{H}_2$	50 mg sample	—	$\text{CH}_4$ selectivity: 55%	399
Au NP (TiO <sub>2</sub> /Au)	99.999% $\text{CO}_2 + \text{H}_2\text{O}$ (7:25)	UV	$\text{H}_2\text{O}$	100 mg sample, 50 °C	Flow reactor	$\text{CH}_4$ : 74.1 $\mu\text{mol g}^{-1}$ (15 h)	397
Au/Ag alloy coated on TiO <sub>2</sub>	$\text{CO}_2 + \text{H}_2$	150 mW $\text{cm}^{-2}$	$\text{H}_2$	10 mg sample	Batch reactor	CO: 1053 $\mu\text{mol g}^{-1} \text{h}^{-1}$	250
Au/g-C <sub>3</sub> N <sub>4</sub>	99.999% $\text{CO}_2 + \text{H}_2\text{O}$	300 W Xe lamp	$\text{H}_2\text{O}$	50 mg sample	Flow reactor	CH <sub>4</sub> : 1813 $\mu\text{mol g}^{-1} \text{h}^{-1}$	400
Au/TiO <sub>2</sub>	99.99% $\text{CO}_2 + \text{H}_2$	252 nm (150 mW $\text{cm}^{-2}$ )	$\text{H}_2$	Sample coated ceramic monolith	Monolith flow reactor	CO: 13.17 $\mu\text{mol g}^{-1}$ (2 h)	251
Pt/Au-SiO <sub>2</sub>	$\text{CO}_2 + \text{CH}_4$	Xe lamp (LA-251, 0.6 W $\text{cm}^{-2}$ )	—	20 mg sample	—	CH <sub>4</sub> : 42 $\mu\text{mol g}^{-1} \text{h}^{-1}$	401
Ag@TiO <sub>2</sub> core-shell	$\text{CO}_2 + \text{H}_2\text{O}$	300 W Xe	$\text{H}_2\text{O}$	—	Pyrex glass reactor	CO: 122.1 $\mu\text{mol g}^{-1} \text{min}^{-1}$	402
Au@TiO <sub>2</sub> yolk-shell hollow spheres	$\text{CO}_2 + \text{H}_2\text{O}$	300 W Xe lamp	$\text{H}_2\text{O}$	10 mg sample and 0.4 mL DI water	Flow reactor	CH <sub>4</sub> : 55.3 $\mu\text{mol g}^{-1} \text{min}^{-1}$	403
Au-Cu nanoalloy supported on TiO <sub>2</sub>	99.995% $\text{CO}_2 + \text{H}_2\text{O}$	1000 W Xe lamp	$\text{H}_2\text{O}$	Sample film	Batch reactor	CH <sub>4</sub> : 2.57 $\mu\text{mol g}^{-1} \text{h}^{-1}$	127
Ag-AgCl/C <sub>3</sub> N <sub>4</sub>	99.999% $\text{CO}_2 + \text{H}_2\text{O}$	15 W daylight lamp	$\text{H}_2\text{O}$	Sample coated on glass rods for immobilization	Tubular fixed-bed reactor	$\text{CH}_4$ : around 10 $\mu\text{mol g}^{-1}$ (10 h)	404

Nevertheless, plasmonic photocatalysis has immense potential for realizing high  $\text{CO}_2$  photoreduction yields in the near future. The photocatalytic  $\text{CO}_2$  reduction activity of plasmonic materials is summarized in Table 8.

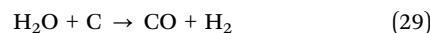
## 6 Origin of carbon in $\text{CO}_2$ photoreduction

Photocatalysts typically contain a certain amount of deposited carbonaceous species, especially on the surface, and various suggestions have been put forward for their origin. Literature reports have ascribed these species to a combination of the following factors: (i) the attachment of organic materials to the photocatalyst during synthesis, *e.g.*, the use of methanol as a hole scavenger during photodeposition; (ii)  $\text{CO}_2$  adsorption from the air to form various species such as “C”, “ $\text{CO}_3^{2-}$ ”, and “ $\text{HCO}_3^-$ ” as shown in eqn (26) and (27); and (iii) the adsorption of other organic molecules such as  $\text{HCOOH}$  from the air.<sup>405-408</sup> These species have been reported to be adsorbed by reactive surface sites, which are typically oxygen vacancies (Vo) and hydroxyl groups ( $\text{OH}^-$ ). The formation mechanism of these species has been reported to consume the surface defects as shown in eqn (26) and (27). In this regard, Zou and co-workers monitored the surface saturation of amorphous zinc germanate ( $\alpha$ -ZnGeO) with  $\text{CO}_2$  using C 1s X-ray photoelectron spectroscopy.<sup>408</sup> In addition, Diebold and co-workers observed the selective adsorption of  $\text{HCOOH}$  from the air by extremely clean TiO<sub>2</sub> under a controlled environment.<sup>405</sup>



The carbonaceous species, when illuminated under an inert or  $\text{CO}_2^-$  containing atmosphere, decompose to form hydrocarbon products similar to those generated by photocatalytic

$\text{CO}_2$  reduction. Moreover, in some cases, the yield under an inert atmosphere can even exceed that under  $\text{CO}_2$ , as reported by Xu and co-workers for their  $\text{Bi}_2\text{WO}_6$ -TiO<sub>2</sub> nanosheets (B-T) as shown in Fig. 24(a).<sup>407</sup> They also observed a photocatalytic yield under anhydrous conditions, as presented in Fig. 24(b), further confirming the presence of hydrocarbon residues. On this basis, the authors recommended the organic-free synthesis of photocatalytic materials. In a similar study, Mul and co-workers found that Cu(i)/TiO<sub>2</sub> synthesized using an organic compound (polyethylene glycol (PEG)) generated more CO compared to the same catalyst synthesized without PEG.<sup>409</sup> They thus attributed the CO to carbon deposits originating from the PEG and proposed the mechanism shown in eqn (28) and (29). In addition to organic compounds, surface-adsorbed  $\text{CO}_2$  and water can also be transformed into products. Under such circumstances, there is a need for the two reactions, *i.e.*, photodecomposition of the carbonaceous species and photocatalytic  $\text{CO}_2$  reduction, to be evaluated separately.



A photocatalyst with pre-adsorbed carbonaceous species may exhibit two types of activity depending upon the reactants consumed. The first is transient activity, in which the photocatalyst exhibits a sudden rise in photocatalytic yield during the initial minutes of photocatalytic  $\text{CO}_2$  reduction, and the second is steady-state activity, in which the photocatalyst displays a continuous low yield. The former originates from the consumption of pre-adsorbed species such as  $\text{HCO}_3^-$  and formate, while the latter results from the real photocatalytic sites mediating  $\text{CO}_2$  reduction.<sup>412</sup> Considering the participation of these two reactions, the overall yield determination could be misleading. Therefore, to evaluate the actual yield, it is essential to estimate the yield derived from the pre-adsorbed carbonaceous species.<sup>409,413</sup> In this regard,



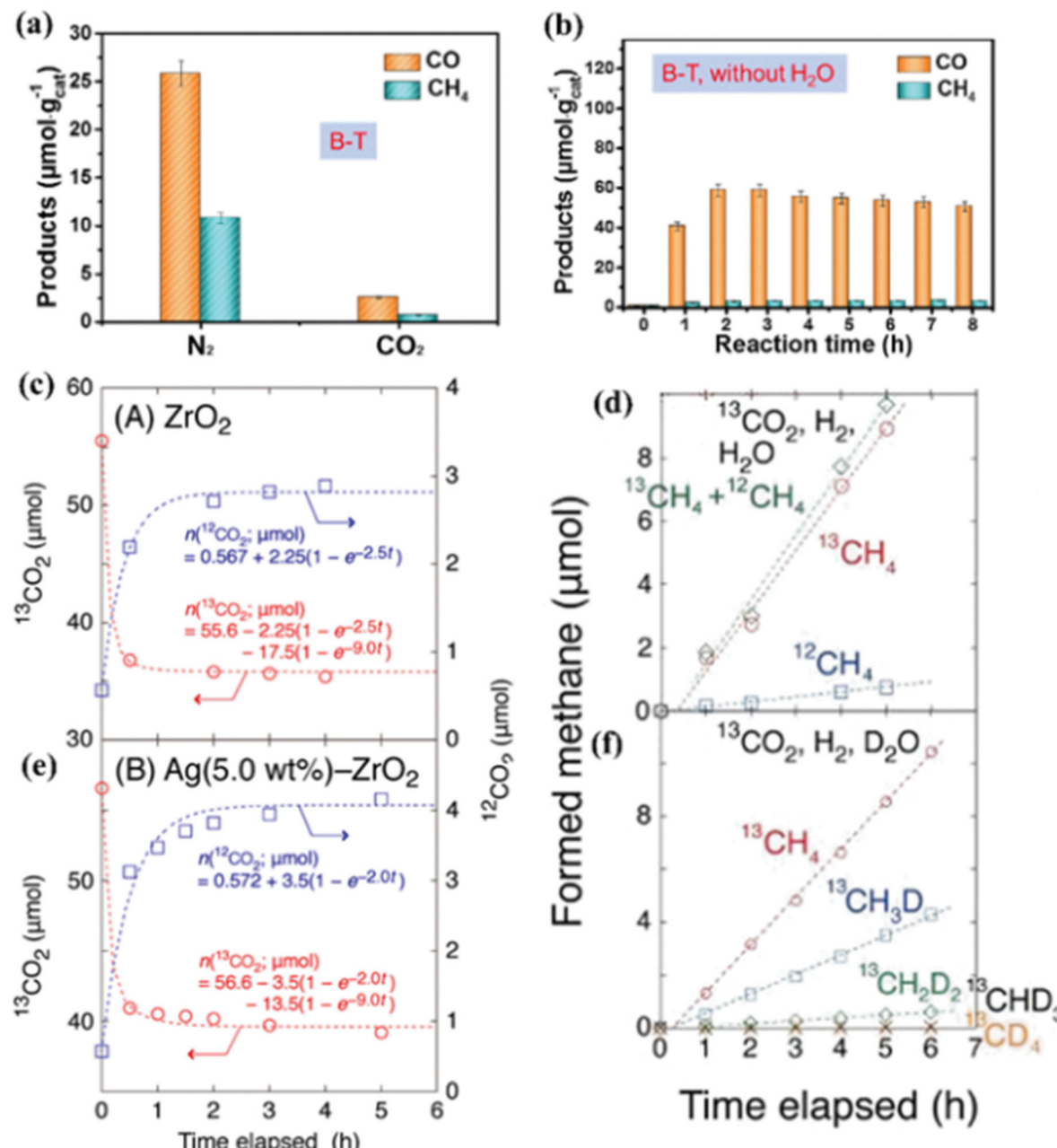


Fig. 24 (a) and (b) Photocatalytic yields exhibited by B-T under (a) humid  $\text{CO}_2$  and  $\text{N}_2$  and (b) anhydrous  $\text{N}_2$ . Reproduced with permission from ref. 407, Copyright 2018, Elsevier. (c) and (e)  $^{13}\text{CO}_2$  exchange reactions under UV-vis light for (c)  $\text{ZrO}_2$  and (e)  $\text{Ag}-\text{ZrO}_2$ . Reproduced with permission from ref. 410, Copyright 2019, American Chemical Society. (d) and (f) Photocatalytic yields from irradiation of  $\text{Ni}-\text{ZrO}_2$  under (d)  $^{13}\text{CO}_2$ ,  $\text{H}_2$ , and  $\text{H}_2\text{O}$ , and (f)  $^{13}\text{CO}_2$ ,  $\text{H}_2$ , and  $\text{D}_2\text{O}$ . Reproduced with permission from ref. 411, Copyright 2021, Wiley-VCH.

various treatment methods and spectroscopic techniques could be applied. There have been several reports of methods suitable for removing the carbonaceous/hydrocarbonaceous species, including thermal treatment, prolonged illumination, air/vacuum annealing, and washing with various solvents.<sup>252,414,415</sup> As far as the efficacy of such remedial methods is concerned, these species can be reduced using such techniques, but it is hard to completely eliminate them. For example, Mul and co-workers reported that under repeated cycles of irradiation the yield from the carbonaceous species decreased substantially but did not disappear.<sup>415</sup> Zou and

co-workers presented an interesting explanation for this behavior, noting the formation of oxygen vacancies in their  $\alpha\text{-ZnGeO}$  catalyst under light irradiation, which upon exposure to the ambient environment readily adsorbed  $\text{CO}_2$ .<sup>408</sup> This adsorbed  $\text{CO}_2$  may be the source of the photocatalytic yield under inert conditions. Therefore, these carbonaceous species are formed continuously and cannot be easily removed. Moreover, the discussed methods may result in alterations to the morphology and reactivity; thus, it is highly desirable to develop methods for solving this issue without altering the beneficial photocatalytic properties.



Isotopic labeling studies with  $^{13}\text{CO}_2$  have indicated that carbonate anions intercalated within layered double hydroxide (LDH) tend to exchange atmospheric  $\text{CO}_2$  *via* dynamic breathing.<sup>416</sup> Taking advantage of this phenomenon,  $^{13}\text{CO}_2$  can be used as a reactant molecule to trace the actual activity originating from photocatalytic  $\text{CO}_2$  reduction. In this regard, various studies have reported the utilization of  $^{13}\text{CO}_2$  as a tracer molecule, where the resulting products (*i.e.*,  $^{13}\text{CO}$  and  $^{13}\text{CH}_4$ ) definitively originate from the  $^{13}\text{CO}_2$  photoreduction reaction confirmed by gas chromatography–mass spectrometry (GC-MS). However, most of these studies were performed in batch reactors; although this permits determination of the relative contributions to the product yields, the reaction rate cannot be reliably calculated, which could lead to inaccurate kinetic real reaction rates of photocatalytic  $^{13}\text{CO}_2$  reduction by continuously monitoring the yields of  $^{13}\text{CO}$  and  $^{13}\text{CH}_4$ .<sup>410,411</sup> In addition, they also explored the exchange of  $^{13}\text{CO}_2$  with already adsorbed  $^{12}\text{CO}_2$  under irradiation. They found that the exchange of  $\text{CO}_2$  molecules eventually reached equilibrium, as shown in Fig. 24(c) and (e), and under irradiation this occurred rapidly.<sup>410</sup> Considering the presence of pre-adsorbed  $\text{CO}_2$  and other carbonaceous species, the yield originated from both sources, as shown in Fig. 24(d). They also noted the ratio of product formation rate is agreement with D (Deuterium) ratio in reactant (8.9%), as shown in Fig. 24(f). Under such circumstances, the pre-adsorbed water/hydroxyl groups acted as a source of  $\text{H}^+$ ; therefore, in addition to confirming the origin of carbon, the origin modeling of the reactions.<sup>5,407</sup>

Izumi and co-workers provided insights into the evaluation of the hydrogen are also important, which could be determined by following similar procedures.<sup>411</sup> In addition to isotopic analysis of the gaseous products, the intermediate products of  $^{13}\text{CO}_2$  over the surface of the photocatalyst could be analyzed by secondary-ion mass spectrometry (SIMS) to further confirm the origin of the products. One such study was performed by Zou and co-workers, in which they confirmed the presence of  $^{13}\text{C}$  on the surface of  $\alpha\text{-Zn-Ge-O}$  owing to its deposition during the reduction of  $^{13}\text{CO}_2$ .<sup>408</sup> Moreover, the participation of both hydrogen and carbon from  $\text{H}_2\text{O}$  and  $\text{CO}_2$ , respectively, has been confirmed by NMR studies.<sup>42,417</sup> In conclusion, understanding the origin of carbon in photocatalytic  $\text{CO}_2$  reduction is vital and it has been studied by state-of-art equipment such as GC-MS, SIMS, and NMR.

## 7 Economic/commercial viability

The worldwide sequestration of  $\text{CO}_2$  emissions currently accounts for a mere 1% of the total  $\text{CO}_2$  generated. The resulting continuous increase in atmospheric  $\text{CO}_2$  concentrations is placing increasing pressure on governments to restrict emissions, and the eventual implementation of regulations for  $\text{CO}_2$  capture is inevitable.<sup>418</sup> When this happens, the  $\text{CO}_2$  utilization landscape will be realigned and the trend will shift to  $\text{CO}_2$  capture, storage, and utilization technologies.<sup>419</sup> The resulting investments will largely go to technologies that are

not viable prior to these regulations. It is anticipated that investors will be primarily interested in technologies that offer maximum benefits by producing valuable chemicals or fuels from  $\text{CO}_2$ . To date, urea and methanol production facilities are the major industrial consumers of  $\text{CO}_2$ , but the scale of these industries is insufficient.<sup>420</sup> Hence, finding new opportunities for utilizing  $\text{CO}_2$  while producing value-added products will surely prove useful.<sup>421</sup>

Thermal power generation and the transportation sector account for two-thirds of  $\text{CO}_2$  emissions; therefore, finding viable  $\text{CO}_2$  conversion solutions for these sectors will enhance the scale of  $\text{CO}_2$  harvesting.<sup>422</sup> Various alternative technologies to  $\text{CO}_2$  reduction, such as photovoltaics, hydroelectricity, and wind power, are becoming increasingly popular because of their renewability and sustainability.<sup>423,424</sup> However, considering the current rate of adoption of these technologies, it may take some time to replace fossil energy and reduce its deleterious effects on the environment.<sup>425,426</sup> In addition, the energy garnered by these resources cannot be directly applied to the current transportation infrastructure until there is a large-scale shift to electric vehicles.<sup>427</sup> Therefore, the major portion of fossil utilities still requires viable, renewable, and eco-friendly solutions.<sup>424</sup> Under these circumstances, the continued use of fossil resources will necessitate carbon capture facilities, which will eventually make the use of fossil fuels expensive.<sup>428</sup> Thus, reversing the combustion reaction to produce fuels for transportation will eventually lead to mega-scale  $\text{CO}_2$  harvesting while producing high-value products.<sup>419</sup>

Photocatalytic  $\text{CO}_2$  reduction can be considered the reverse of combustion, enabling the transformation of  $\text{CO}_2$  to solar fuels using sunlight and water under ambient conditions.<sup>429</sup> Although the industrial-scale process of thermocatalytic  $\text{CO}_2$  reduction can also facilitate this transformation, these systems operate at elevated pressures and temperatures and require additional energy inputs and reducing agents such as  $\text{H}_2$ .<sup>430</sup> If these are not obtained from renewable resources, the net effects are not promising. Hence, photocatalytic  $\text{CO}_2$  reduction seems lucrative relative to its peers with respect to commercialization owing to its numerous environmental and economic benefits.<sup>431</sup> In this regard, considerable solar-to-fuel efficiencies (STF) have been achieved. For example, Rajh *et al.* reported an efficiency of 10.1% using their earth-abundant  $\text{Cu}_2\text{O}$  photocatalyst.<sup>432</sup> Although an STF of 10.1% is sufficient for commercialization, sustaining this efficiency over prolonged periods remains challenging. Therefore, despite the promise of these technologies, their commercialization is still hindered by catalyst instability.

High-value hydrocarbon products such as  $\text{C}_2\text{H}_4$  and  $\text{C}_2\text{H}_6$  provide another avenue for commercialization. However, the activity and stability remain low.<sup>433</sup>  $\text{C}_2$  products from photocatalytic  $\text{CO}_2$  reduction have a high market value compared to  $\text{C}_1$  products.<sup>434</sup> The production of longer-chain hydrocarbons with higher market value (*e.g.*, propane) could further enhance the possibilities.<sup>435</sup> With the remarkable recent advances in these technologies, there is currently great interest in converting  $\text{CO}_2$  to  $\text{C}_2$  and higher hydrocarbon products owing to their greater economic benefits.<sup>433</sup> However, realizing  $\text{C}_2$  selectivity is



challenging owing to the complex steps involved in the overall reaction.<sup>436</sup> Furthermore, by following this route the CO<sub>2</sub> harvesting scale will be low because specialty products are utilized in smaller volumes.<sup>419</sup>

Government subsidies are the major source of financing for emerging renewable technologies because these technologies are initially not competitive with respect to their well-established rivals; for example, biodiesel is subsidized to compete with mineral diesel.<sup>437,438</sup> However, to obtain such financial support, the technology should be at the pilot/bench scale with considerable efficiencies; for instance, KIT in Germany has successfully converted renewable energy to methane with 51.3% conversion efficiency under the “Power to Gas” project and is committed to extending the energy conversion efficiency to 80%.<sup>439,440</sup> Another example is high-temperature co-electrolysis to convert CO<sub>2</sub> and steam to syngas, which proceeds with an efficiency of up to 70%.<sup>419,441</sup> However, to the best of our knowledge, no pilot plant for photocatalytic CO<sub>2</sub> reduction has yet been established.

## 8 Outlook

The conversion of CO<sub>2</sub> into value-added chemicals using sunlight is now well established. Although many of the earlier studies into CO<sub>2</sub> photoconversion focused on improving the photocatalytic activity, there are also numerous other crucial parameters that warrant serious attention. For example, photocatalyst stability is as important as high activity.<sup>186</sup> However, in contrast to the extensive body of research focusing on achieving optimal activity, only limited information exists regarding the possible causes of deactivation.<sup>415</sup> These causes include loss of the active oxidation state under irradiation, the buildup of irreducible reaction intermediates, and morphological changes.<sup>87,408,442</sup> Various efforts have been made to circumvent these issues, such as the use of hole scavengers, construction of heterostructures to retain the desired oxidation states, and thermal and other treatments to remove the intermediates.<sup>252</sup> However, considerable work is still required to circumvent the need for non-renewable hole scavengers and ineffective and energy-intensive photocatalyst regeneration processes.<sup>90</sup>

In this review, various reasons have been discussed which contribute to destabilizing the photocatalyst. The widely identified reasons include losing active oxidation states of photocatalyst and accumulation of the reaction intermediates over the surface of the photocatalyst, *i.e.*, carbon. Therefore, it is mandatory to overcome these limitations to achieve commercial-scale viability. In this regard, photocatalyst is required to re-attain the active oxidation states without being taken out of the reactor. Literature suggests that single metal atom photocatalyst can regain their lost active oxidation states just by exposing them to air, which arises from metal–support interactions.<sup>443</sup> Moreover, intense UV irradiation under inert-humid conditions is believed to decompose the reaction intermediates. The protons generated from water oxidation will be utilized to reduce the already present carbonaceous species, and subsequently, activity can be restored. The researchers should focus on such developments which can make the photocatalytic reusable system simpler.

Besides stability, product selectivity is also underexplored, and in this regard, it is highly desirable to develop photocatalysts with the ability to mediate C–C coupling reactions by stabilizing the intermediate products. Several factors influence the product selectivity of CO<sub>2</sub> conversions, including the type of materials, band potentials of semiconductors, the intermediate stabilization, *etc.* Furthermore, the reaction medium has a crucial influence on product selectivity; for example, CH<sub>3</sub>OH, C<sub>2</sub>H<sub>5</sub>OH, and formaldehyde can be generated in an aqueous system, while CO, CH<sub>4</sub>, and C<sub>2</sub>H<sub>6</sub> production are more feasible in a gas phase system. In the literature, most of the photocatalysts have been reported for C<sub>1</sub> products like CO and CH<sub>4</sub>; however, limited studies have been carried out for C<sub>2</sub> selectivity. Literature suggests that metal nanoparticles like Pt, Pd, Au, *etc.*, deposited on semiconductors have selectivity for CH<sub>4</sub> formation due to their ability to supply sufficient protons. For the C<sub>2+</sub> product, the C–H bonds can be formed by C–O bond cleavage and continuous protonation. The density of photogenerated electrons/holes and the stability of intermediates also impact the reaction’s C<sub>2</sub> selectivity; for example, stabilization of •CH<sub>3</sub> radicals is beneficial for achieving C<sub>2</sub> selectivity. Theoretically, the breakage of the C–O bonds at the single-metal site is easier than at the dual-metal site because the dual-metal site has a higher charge density due to the charge transfer. Thus, the intermediates become more stable at the dual-metal site.<sup>444</sup> To prove the theoretical calculation, *in situ/operando* XAS analysis can provide the experimental observation on the local coordination environment and oxidation states of the metal center during the reaction. As a result, for C<sub>2</sub> selectivity, it is preferable to carefully design catalysts to regulate the reaction intermediates. The combination of graphene with other semiconducting materials has been reported to enhance the C<sub>2</sub> selectivity.

To achieve an industry-relevant photocatalytic CO<sub>2</sub> reduction, CO<sub>2</sub> capture, utilization, and storage also should be considered.<sup>445</sup> An effective solution is still needed to avoid such additional costs, despite the use of abundant and cheap reactants. Furthermore, if the photocatalytic CO<sub>2</sub> conversion-efficiency is low, then the CO<sub>2</sub> concentration in the products may be too high to permit their direct use, thus necessitating separation of the hydrocarbons and CO<sub>2</sub>.<sup>446</sup> One possible solution is passing the gaseous mixture through gas separation membranes, although the installation and operation of these systems would also lead to higher costs.<sup>447</sup> Therefore, it would be highly desirable to search for solutions that help avoid these extra processing steps.<sup>131</sup>

To avoid the construction of CO<sub>2</sub>-collecting infrastructure, CO<sub>2</sub> can be captured from the atmosphere. This abundant resource, if it can be harnessed, would provide many benefits: it avoids the purification and storage of CO<sub>2</sub>, and in some cases, it contains abundant moisture, thus avoiding the need for humidification.<sup>448</sup> However, the use of low concentration CO<sub>2</sub> is associated with its own disadvantages, such as low adsorption over a photocatalyst. On the other hand, strategies to minimize the need for post-reaction product purification are also needed, such as the development of photocatalysts that can adsorb CO<sub>2</sub> and H<sub>2</sub>O in higher amounts. Subsequently, the reactant-laden photocatalyst could be subjected to irradiation



under controlled conditions to yield a CO<sub>2</sub>-free product mixture. Therefore, it would be desirable to explore such photocatalysts that can selectively adsorb atmospheric CO<sub>2</sub> and H<sub>2</sub>O with high stability.

Thermal effects can also lead to an enhancement in the yield of the solar products of photocatalytic CO<sub>2</sub> reduction.<sup>41</sup> One possible way to exploit these effects is the concentration of solar light, which does not require the use of any fossil fuels. However, to enable photothermal reactions, special attention must be paid to the design of photoreactors and photocatalysts with good durability to withstand the harsh conditions. Fortunately, rather than raising the bulk temperature, the photocatalyst surface could be locally heated through LSPR. For example, Izumi and co-workers found that the temperature increased to 392 K owing to Ag LSPR. This dual role of light provides another avenue for enhancing the activity by taking advantage of synergistic effects, but this is only feasible with well-designed photocatalysts and must be explored further.<sup>410</sup> Furthermore, the use of renewable hole scavengers such as glycerol, a byproduct of biodiesel manufacture, would also be desirable. In addition, facile photocatalyst regeneration processes must be developed, as in the case of some single-metal-atom catalysts, for which regeneration can be conveniently accomplished simply by exposing the catalyst to the environment.<sup>47</sup>

Considering the immense potential of CO<sub>2</sub> reduction, huge investments are in place, and these will surely escalate in the near future. For instance, the Musk Foundation recently announced the \$100 million X PRIZE for carbon removal.<sup>449</sup> Similarly, the European Innovation Council has offered a €5 million prize for the development of a bench-scale prototype for artificial photosynthesis.<sup>450</sup> Therefore, considering the current and future investments, it can be anticipated that CO<sub>2</sub> reduction will eventually find a route to commercialization. In this regard, photocatalytic CO<sub>2</sub> reduction could make a strong impression in terms of attracting investment. Such heavy investments in this field will expedite further research and help realize the true potential of photocatalytic CO<sub>2</sub> reduction.

## Conflicts of interest

There are no conflicts to declare.

## Acknowledgements

The authors acknowledge financial support from the Ministry of Science and ICT in Korea (2021R1A2C2009459 and 2021M3I3A1085039). This paper is dedicated to Professor Michael R. Hoffman (Caltech, USA) and Professor Wan In Lee (Inha University, Korea), who have contributed to the research and development of photocatalytic fields throughout their lives.

## References

- Z. Wang, H. Song, H. Liu and J. Ye, *Angew. Chem., Int. Ed.*, 2020, **59**, 8016–8035.
- W.-H. Wang, Y. Himeda, J. T. Muckerman, G. F. Manbeck and E. Fujita, *Chem. Rev.*, 2015, **115**, 12936–12973.
- G. M. Hallegraeff, *J. Phycol.*, 2010, **46**, 220–235.
- J. He and C. Janáky, *ACS Energy Lett.*, 2020, **5**, 1996–2014.
- S. Sorcar, Y. Hwang, J. Lee, H. Kim, K. M. Grimes, C. A. Grimes, J.-W. Jung, C.-H. Cho, T. Majima, M. R. Hoffmann and S.-I. In, *Energy Environ. Sci.*, 2019, **12**, 2685–2696.
- S. S. Meryem, S. Nasreen, M. Siddique and R. Khan, *Rev. Chem. Eng.*, 2018, **34**, 409–425.
- U. Nations, 21st Conference of the Parties, United Nations Framework Convention on Climate Change, UNFCCC, Paris, 2015.
- S. Nitopi, E. Bertheussen, S. B. Scott, X. Liu, A. K. Engstfeld, S. Horch, B. Seger, I. E. L. Stephens, K. Chan, C. Hahn, J. K. Nørskov, T. F. Jaramillo and Ib Chorkendorff, *Chem. Rev.*, 2019, **119**, 7610–7672.
- T. Kong, Y. Jiang and Y. Xiong, *Chem. Soc. Rev.*, 2020, **49**, 6579–6591.
- P. Abbasi, M. Asadi, C. Liu, S. Sharifi-Asl, B. Sayahpour, A. Behranginia, P. Zapol, R. Shahbazian-Yassar, L. A. Curtiss and A. Salehi-Khojin, *ACS Nano*, 2017, **11**, 453–460.
- C. Hiragond, S. Ali, S. Sorcar and S.-I. In, *Catalysts*, 2019, **9**, 370.
- C. B. Hiragond, N. S. Powar and S.-I. In, *Nanomaterials*, 2020, **10**, 2569.
- J. Ye, J. Yu, Y. Zhang, M. Chen, X. Liu, S. Zhou and Z. He, *Appl. Catal., B*, 2019, **257**, 117916.
- S. K. Kuk, Y. Ham, K. Gopinath, P. Boonmongkolras, Y. Lee, Y. W. Lee, S. Kondaveeti, C. Ahn, B. Shin, J. Lee, S. Jeon and C. B. Park, *Adv. Energy Mater.*, 2019, **9**, 1900029.
- Q. Lu and F. Jiao, *Nano Energy*, 2016, **29**, 439–456.
- M.-Y. Lee, K. T. Park, W. Lee, H. Lim, Y. Kwon and S. Kang, *Crit. Rev. Environ. Sci. Technol.*, 2020, **50**, 769–815.
- R. C. Pullar, R. M. Novais, A. P. F. Caetano, M. A. Barreiros, S. Abanades and F. A. C. Oliveira, *Front. Chem.*, 2019, **7**, 601.
- X.-Y. Wu and A. F. Ghoniem, *Prog. Energy Combust. Sci.*, 2019, **74**, 1–30.
- J. Jia, P. G. O'Brien, L. He, Q. Qiao, T. Fei, L. M. Reyes, T. E. Burrow, Y. Dong, K. Liao, M. Varela, S. J. Pennycook, M. Hmadeh, A. S. Helmy, N. P. Kherani, D. D. Perovic and G. A. Ozin, *Adv. Sci.*, 2016, **3**, 1600189.
- X. Meng, T. Wang, L. Liu, S. Ouyang, P. Li, H. Hu, T. Kako, H. Iwai, A. Tanaka and J. Ye, *Angew. Chem., Int. Ed.*, 2014, **53**, 11478–11482.
- H. Li, W. Tu, Y. Zhou and Z. Zou, *Adv. Sci.*, 2016, **3**, 1500389.
- Y. Zhou, Z. Wang, L. Huang, S. Zaman, K. Lei, T. Yue, Z. Li, B. You and B. Y. Xia, *Adv. Energy Mater.*, 2021, **11**, 2003159.
- M. Halmann, *Nature*, 1978, **275**, 115–116.
- P. Zhang and X. W. Lou, *Adv. Mater.*, 2019, **31**, 1900281.
- X. Chang, T. Wang and J. Gong, *Energy Environ. Sci.*, 2016, **9**, 2177–2196.
- O. Ola and M. M. Maroto-Valer, *J. Photochem. Photobiol. C*, 2015, **24**, 16–42.
- D. Li, M. Kassymova, X. Cai, S.-Q. Zang and H.-L. Jiang, *Coord. Chem. Rev.*, 2020, **412**, 213262.

28 Y. Y. Lee, H. S. Jung and Y. T. Kang, *J. CO<sub>2</sub> Util.*, 2017, **20**, 163–177.

29 T. Yui, A. Kan, C. Saitoh, K. Koike, T. Ibusuki and O. Ishitani, *ACS Appl. Mater. Interfaces*, 2011, **3**, 2594–2600.

30 H. Zhang, G. Liu, L. Shi and J. Ye, *Adv. Energy Mater.*, 2018, **8**, 1701343.

31 X. Jiao, K. Zheng, Z. Hu, Y. Sun and Y. Xie, *ACS Cent. Sci.*, 2020, **6**, 653–660.

32 S. Trivedi, D. Prochowicz, A. Kalam, M. M. Tavakoli and P. Yadav, *Renewable Sustainable Energy Rev.*, 2021, **145**, 111047.

33 J. Ran, M. Jaroniec and S. Qiao, *Adv. Mater.*, 2018, **30**, 1704649.

34 K. Yang, Z. Yang, C. Zhang, Y. Gu, J. Wei, Z. Li, C. Ma, X. Yang, K. Song, Y. Li, Q. Fang and J. Zhou, *Chem. Eng. J.*, 2021, **418**, 129344.

35 M. Yang, M. Gao, M. Hong and G. W. Ho, *Adv. Mater.*, 2018, **30**, 1802894.

36 X. Xiang, F. Pan and Y. Li, *Adv. Compos. Hybrid Mater.*, 2018, **1**, 6–31.

37 T.-H. Lai, K. Katsumata and Y.-J. Hsu, *Nanophotonics*, 2021, **10**, 777–795.

38 M. Sachs, E. Pastor, A. Kafizas and J. R. Durrant, *J. Phys. Chem. Lett.*, 2016, **7**, 3742–3746.

39 J. Fu, K. Jiang, X. Qiu, J. Yu and M. Liu, *Mater. Today*, 2020, **32**, 222–243.

40 L. Liu, F. Gao, H. Zhao and Y. Li, *Appl. Catal., B*, 2013, **134**, 349–358.

41 F. Zhang, Y.-H. Li, M.-Y. Qi, Y. M. A. Yamada, M. Anpo, Z.-R. Tang and Y.-J. Xu, *Chem Catal.*, 2021, **1**, 1–26.

42 N. M. Dimitrijevic, B. K. Vijayan, O. G. Poluektov, T. Rajh, K. A. Gray, H. He and P. Zapol, *J. Am. Chem. Soc.*, 2011, **133**, 3964–3971.

43 M. E. Aguirre, R. Zhou, A. J. Eugene, M. I. Guzman and M. A. Grela, *Appl. Catal., B*, 2017, **217**, 485–493.

44 S. Ali, J. Lee, H. Kim, Y. Hwang, A. Razzaq, J.-W. Jung, C.-H. Cho and S.-I. In, *Appl. Catal., B*, 2020, **279**, 119344.

45 F. Zhang, Y.-H. Li, M.-Y. Qi, Z.-R. Tang and Y.-J. Xu, *Appl. Catal., B*, 2020, **268**, 118380.

46 L. Liu, C. Zhao, J. T. Miller and Y. Li, *J. Phys. Chem. C*, 2016, **121**, 490–499.

47 S. Ali, M. C. Flores, A. Razzaq, S. Sorcar, C. B. Hiragond, H. R. Kim, Y. H. Park, Y. Hwang, H. S. Kim, H. Kim, E. Gong, J. Lee, D. Kim and S.-I. In, *Catalysts*, 2019, **9**, 727.

48 S. Sorcar, S. Yoriya, H. Lee, C. A. Grimes and S. P. Feng, *Mater. Today Chem.*, 2020, **16**, 100264.

49 Y. Lin, C. Deng, L. Wu, Y. Zhang, C. Chen, W. Ma and J. Zhao, *Energy Environ. Sci.*, 2020, **13**, 2602–2617.

50 W.-J. Yin, B. Weng, J. Ge, Q. Sun, Z. Li and Y. Yan, *Energy Environ. Sci.*, 2019, **12**, 442–462.

51 S. Xie, W. Ma, X. Wu, H. Zhang, Q. Zhang, Y. Wang and Y. Wang, *Energy Environ. Sci.*, 2021, **14**, 37–89.

52 X. Li, J. Yu, M. Jaroniec and X. Chen, *Chem. Rev.*, 2019, **119**, 3962–4179.

53 A. Bavykina, N. Kolobov, I. S. Khan, J. A. Bau, A. Ramirez and J. Gascon, *Chem. Rev.*, 2020, **120**, 8468–8535.

54 G. Chen, G. I. N. Waterhouse, R. Shi, J. Zhao, Z. Li, L. Wu, C. Tung and T. Zhang, *Angew. Chem., Int. Ed.*, 2019, **58**, 17528–17551.

55 Z. Kovačić, B. Likozar and M. Huš, *ACS Catal.*, 2020, **10**, 14984–15007.

56 D. P. Van Vuuren, E. Stehfest, D. E. H. J. Gernaat, J. C. Doelman, M. Van den Berg, M. Harmsen, H. S. de Boer, L. F. Bouwman, V. Daioglou, O. Y. Edelenbosch, B. Girod, T. Kram, L. Lassaletta, P. L. Lucas, H. Meijl, C. Müller, B. J. Ruijven, S. v. d. Sluis and A. Tabeau, *Glob. Environ. Change*, 2017, **42**, 237–250.

57 A. Dechezleprêtre, R. Martin and S. Bassi, *Handbook on Green Growth*, Edward Elgar Publishing, 2019.

58 H. N. Larsen, C. Solli and J. Pettersen, *Energy Procedia*, 2012, **20**, 354–363.

59 T. Inui, M. Anpo, K. Izui, S. Yanagida and T. Yamaguchi, *Advances in chemical conversions for mitigating carbon dioxide*, Elsevier, 1998.

60 S.-E. Park, J.-S. Chang and K.-W. Lee, *Carbon Dioxide Utilization for Global Sustainability: Proceedings of the 7th International Conference on Carbon Dioxide Utilization, Seoul, Korea, October 12–16, 2003*, Elsevier, 2004.

61 B. Eliasson, P. Riemer and A. Wokaun, *Greenhouse gas control technologies*, Elsevier, 1999.

62 J. L. White, M. F. Baruch, J. E. Pander III, Y. Hu, I. C. Fortmeyer, J. E. Park, T. Zhang, K. Liao, J. Gu and Y. Yan, *Chem. Rev.*, 2015, **115**, 12888–12935.

63 H. Wang, H. Rong, D. Wang, X. Li, E. Zhang, X. Wan, B. Bai, M. Xu, J. Liu, J. Liu, W. Chen and J. Zhang, *Small*, 2020, **16**, 2000426.

64 P. D. Tran, L. H. Wong, J. Barber and J. S. C. Loo, *Energy Environ. Sci.*, 2012, **5**, 5902–5918.

65 W. Tu, Y. Zhou and Z. Zou, *Adv. Mater.*, 2014, **26**, 4607–4626.

66 H. Huang, B. Pradhan, J. Hofkens, M. B. J. Roeffaers and J. A. Steele, *ACS Energy Lett.*, 2020, **5**, 1107–1123.

67 L. Liang, X. Li, Y. Sun, Y. Tan, X. Jiao, H. Ju, Z. Qi, J. Zhu and Y. Xie, *Joule*, 2018, **2**, 1004–1016.

68 S. Rej, M. Bissetto, A. Naldoni and P. Fornasiero, *J. Mater. Chem. A*, 2021, **9**, 5915–5951.

69 L. Shi, X. Ren, Q. Wang, W. Zhou and J. Ye, *J. Mater. Chem. A*, 2021, **9**, 2421–2428.

70 X. Wang, F. Wang, Y. Sang and H. Liu, *Adv. Energy Mater.*, 2017, **7**, 1700473.

71 A. J. Cowan and J. R. Durrant, *Chem. Soc. Rev.*, 2013, **42**, 2281–2293.

72 T. M. Clarke and J. R. Durrant, *Chem. Rev.*, 2010, **110**, 6736–6767.

73 T.-H. Lai, K. Katsumata and Y.-J. Hsu, *Nanophotonics*, 2020, **10**, 777–795.

74 X. Chen, C. Li, M. Grätzel, R. Kostecki and S. S. Mao, *Chem. Soc. Rev.*, 2012, **41**, 7909–7937.

75 X. Wang, A. Kafizas, X. Li, S. J. A. Moniz, P. J. T. Reardon, J. Tang, I. P. Parkin and J. R. Durrant, *J. Phys. Chem. C*, 2015, **119**, 10439–10447.

76 C. Liu, K. Huang, W.-T. Park, M. Li, T. Yang, X. Liu, L. Liang, T. Minari and Y.-Y. Noh, *Mater. Horiz.*, 2017, **4**, 608–618.



77 X. Li, H. Liu, D. Luo, J. Li, Y. Huang, H. Li, Y. Fang, Y. Xu and L. Zhu, *Chem. Eng. J.*, 2012, **180**, 151–158.

78 O. K. Varghese, M. Paulose, T. J. LaTempa and C. A. Grimes, *Nano Lett.*, 2009, **9**, 731–737.

79 P. Reñones, A. Moya, F. Fresno, L. Collado, J. J. Vilatela and A. Víctor, *J. CO2 Util.*, 2016, **15**, 24–31.

80 P. Maity, O. F. Mohammed, K. Katsiev and H. Idriss, *J. Phys. Chem. C*, 2018, **122**, 8925–8932.

81 X. Meng, L. Liu, S. Ouyang, H. Xu, D. Wang, N. Zhao and J. Ye, *Adv. Mater.*, 2016, **28**, 6781–6803.

82 W. Chu, Q. Zheng, O. V. Prezhdo and J. Zhao, *J. Am. Chem. Soc.*, 2020, **142**, 3214–3221.

83 X. Li, Y. Sun, J. Xu, Y. Shao, J. Wu, X. Xu, Y. Pan, H. Ju, J. Zhu and Y. Xie, *Nat. Energy*, 2019, **4**, 690–699.

84 W.-J. Yin, B. Wen, Q. Ge, X.-B. Li, G. Teobaldi and L.-M. Liu, *Dalton Trans.*, 2020, **49**, 12918–12928.

85 P. Liu, X. Peng, Y.-L. Men and Y.-X. Pan, *Green Chem. Eng.*, 2016, **18**, 139–143.

86 C. B. Hiragond, S. Ali, S. Sorcar and S.-I. In, *Catalysts*, 2019, **9**, 370.

87 Y. Li, W. N. Wang, Z. Zhan, M. H. Woo, C. Y. Wu and P. Biswas, *Appl. Catal., B*, 2010, **100**, 386–392.

88 K. Tennakone, A. H. Jayatissa and S. Punchihewa, *J. Photochem. Photobiol. A Chem.*, 1989, **49**, 369–375.

89 F. Fresno, I. J. Villar-García, L. Collado, E. Alfonso-González, P. Reñones, M. Barawi and V. A. de la Peña O'Shea, *J. Phys. Chem. Lett.*, 2018, **9**, 7192–7204.

90 J. Low, J. Yu and W. Ho, *J. Phys. Chem. Lett.*, 2015, **6**, 4244–4251.

91 D. Chen, X. Zhang and A. F. Lee, *J. Mater. Chem. A*, 2015, **3**, 14487–14516.

92 L. Andronic and A. Enesca, *Front. Chem.*, 2020, **8**, 565489.

93 S. Sorcar, Y. Hwang, C. A. Grimes and S.-I. In, *Mater. Today*, 2017, **20**, 507–515.

94 V. Natu, R. Pai, M. Sokol, M. Carey, V. Kalra and M. W. Barsoum, *Chem*, 2020, **6**, 616–630.

95 S. Sorcar, J. Thompson, Y. Hwang, Y. H. Park, T. Majima, C. A. Grimes, J. R. Durrant and S.-I. In, *Energy Environ. Sci.*, 2018, **11**, 3183–3193.

96 C. B. Hiragond, J. Lee, H. Kim, J.-W. Jung, C.-H. Cho and S.-I. In, *Chem. Eng. J.*, 2020, **416**, 127978.

97 H. Wang, L. Zhang, Z. Chen, J. Hu, S. Li, Z. Wang, J. Liu and X. Wang, *Chem. Soc. Rev.*, 2014, **43**, 5234–5244.

98 S. N. Habisreutinger, L. Schmidt-Mende and J. K. Stolarczyk, *Angew. Chem., Int. Ed.*, 2013, **52**, 7372–7408.

99 Y. Ji and Y. Luo, *ACS Catal.*, 2016, **6**, 2018–2025.

100 W. Ong, L. K. Putri and A. R. Mohamed, *Chem. – Eur. J.*, 2020, **26**, 9710–9748.

101 E. Vahidzadeh, S. Zeng, A. P. Manuel, S. Riddell, P. Kumar, K. M. Alam and K. Shankar, *ACS Appl. Mater. Interfaces*, 2021, **13**, 7248–7258.

102 W. Tu, Y. Zhou, Q. Liu, S. Yan, S. Bao, X. Wang, M. Xiao and Z. Zou, *Adv. Funct. Mater.*, 2013, **23**, 1743–1749.

103 X. Chen, L. Liu, Y. Y. Peter and S. S. Mao, *Science*, 2011, **331**, 746–750.

104 N. Liu, V. Häublein, X. Zhou, U. Venkatesan, M. Hartmann, M. Mačković, T. Nakajima, E. Speecker, A. Osvet, L. Frey and P. Schmuki, *Nano Lett.*, 2015, **15**, 6815–6820.

105 A. Sinhamahapatra, J.-P. Jeon and J.-S. Yu, *Energy Environ. Sci.*, 2015, **8**, 3539–3544.

106 X. Zhou, N. Liu, J. Schmidt, A. Kahnt, A. Osvet, S. Romeis, E. M. Zolnhofer, V. R. R. Marthala, D. M. Guldi, W. Peukert, M. Hartmann, K. Meyer and P. Schmuki, *Adv. Mater.*, 2017, **29**, 1604747.

107 N. F. Mott, *Mathematical Proceedings of the Cambridge Philosophical Society*, Cambridge University Press, 1938, vol. 34, pp. 568–572.

108 W. Schottky, *Naturwissenschaften*, 1938, **26**, 843.

109 X. Wang, K. Maeda, A. Thomas, K. Takanabe, G. Xin, J. M. Carlsson, K. Domen and M. Antonietti, *Nat. Mater.*, 2009, **8**, 76–80.

110 A. B. Jorge, D. J. Martin, M. T. S. Dhanoa, A. S. Rahman, N. Makwana, J. Tang, A. Sella, F. Corà, S. Firth, J. A. Darr and P. F. McMillan, *J. Phys. Chem. C*, 2013, **117**, 7178–7185.

111 J. Fu, J. Yu, C. Jiang and B. Cheng, *Adv. Energy Mater.*, 2018, **8**, 1701503.

112 V. S. Vyas, F. Haase, L. Stegbauer, G. Savasci, F. Podjaski, C. Ochsenfeld and B. V. Lotsch, *Nat. Commun.*, 2015, **6**, 1–9.

113 L. Wang, Y. Wan, Y. Ding, S. Wu, Y. Zhang, X. Zhang, G. Zhang, Y. Xiong, X. Wu, J. Yang and H. Xu, *Adv. Mater.*, 2017, **29**, 1702428.

114 R. Asahi, T. Morikawa, T. Ohwaki, K. Aoki and Y. Taga, *Science*, 2001, **293**, 269–271.

115 H. Irie, Y. Watanabe and K. Hashimoto, *J. Phys. Chem. B*, 2003, **107**, 5483–5486.

116 G. Liu, J. Pan, L. Yin, J. T. S. Irvine, F. Li, J. Tan, P. Wormald and H. Cheng, *Adv. Funct. Mater.*, 2012, **22**, 3233–3238.

117 L. Zhang, M. S. Tse, O. K. Tan, Y. X. Wang and M. Han, *J. Mater. Chem. A*, 2013, **1**, 4497–4507.

118 N. O. Gopal, H.-H. Lo, T.-F. Ke, C.-H. Lee, C.-C. Chou, J.-D. Wu, S.-C. Sheu and S.-C. Ke, *J. Phys. Chem. C*, 2012, **116**, 16191–16197.

119 X. Yan, K. Yuan, N. Lu, H. Xu, S. Zhang, N. Takeuchi, H. Kobayashi and R. Li, *Appl. Catal., B*, 2017, **218**, 20–31.

120 Z. Sun, N. Talreja, H. Tao, J. Texter, M. Muhler, J. Strunk and J. Chen, *Angew. Chem., Int. Ed.*, 2018, **57**, 7610–7627.

121 M. Liu, L. Zheng, X. Bao, Z. Wang, P. Wang, Y. Liu, H. Cheng, Y. Dai, B. Huang and Z. Zheng, *Chem. Eng. J.*, 2021, **405**, 126654.

122 Y. J. Jang, J.-W. Jang, J. Lee, J. H. Kim, H. Kumagai, J. Lee, T. Minegishi, J. Kubota, K. Domen and J. S. Lee, *Energy Environ. Sci.*, 2015, **8**, 3597–3604.

123 G. Li, Y. Sun, Q. Zhang, Z. Gao, W. Sun and X. Zhou, *Chem. Eng. J.*, 2021, **410**, 128397.

124 N. Blommaerts, N. Hoeven, D. A. Esteban, R. Campos, M. Mertens, R. Borah, A. Glisenti, K. De Wael, S. Bals, S. Lenaerts, S. W. Verbruggen and P. Cool, *Chem. Eng. J.*, 2021, **410**, 128234.

125 Y. Zhu, Z. Xu, Q. Lang, W. Jiang, Q. Yin, S. Zhong and S. Bai, *Appl. Catal., B*, 2017, **206**, 282–292.

126 W.-N. Wang, W.-J. An, B. Ramalingam, S. Mukherjee, D. M. Niedzwiedzki, S. Gangopadhyay and P. Biswas, *J. Am. Chem. Soc.*, 2012, **134**, 11276–11281.

127 S. Nea  u, J. A. Maci  -Agull  , P. Concepc  n and H. Garcia, *J. Am. Chem. Soc.*, 2014, **136**, 15969–15976.

128 Q. Zhai, S. Xie, W. Fan, Q. Zhang, Y. Wang, W. Deng and Y. Wang, *Angew. Chem.*, 2013, **125**, 5888–5891.

129 R. Long, Y. Li, Y. Liu, S. Chen, X. Zheng, C. Gao, C. He, N. Chen, Z. Qi, L. Song, J. Jiang, J. Zhu and Y. Xiong, *J. Am. Chem. Soc.*, 2017, **139**, 4486–4492.

130 J. C. Wang, L. Zhang, W. X. Fang, J. Ren, Y. Y. Li, H. C. Yao, J. S. Wang and Z. J. Li, *ACS Appl. Mater. Interfaces*, 2015, **7**, 8631–8639.

131 G. Y. Yao and Z. Y. Zhao, *J. Mater. Chem. C*, 2020, **8**, 8567–8578.

132 L. Guo, Y. Wang and T. He, *Chem. Rec.*, 2016, **16**, 1918–1933.

133 Q. Xu, L. Zhang, J. Yu, S. Wageh, A. A. Al-Ghamdi and M. Jaroniec, *Mater. Today*, 2018, **21**, 1042–1063.

134 Q. Yuan, D. Liu, N. Zhang, W. Ye, H. Ju, L. Shi, R. Long, J. Zhu and Y. Xiong, *Angew. Chem.*, 2017, **129**, 4270–4274.

135 Y. Liu, B. Zhang, L. Luo, X. Chen, Z. Wang, E. Wu, D. Su and W. Huang, *Angew. Chem., Int. Ed.*, 2015, **54**, 15260–15265.

136 S. N. Talapaneni, G. Singh, I. Y. Kim, K. AlBahily, A. H. AlMuhtaseb, A. S. Karakoti, E. Tavakkoli and A. Vinu, *Adv. Mater.*, 2020, **32**, 1904635.

137 X. Meng, S. Ouyang, T. Kako, P. Li, Q. Yu, T. Wang and J. Ye, *Chem. Commun.*, 2014, **50**, 11517–11519.

138 J. Z. Y. Tan, S. Gavrielides, H. R. Xu, W. A. Thompson and M. M. Maroto-Valer, *RSC Adv.*, 2020, **10**, 27989–27994.

139 T. Xiong, W. Cen, Y. Zhang and F. Dong, *ACS Catal.*, 2016, **6**, 2462–2472.

140 Y. Liao, Z. Hu, Q. Gu and C. Xue, *Molecules*, 2015, **20**, 18847–18855.

141 Z. He, L. Wen, D. Wang, Y. Xue, Q. Lu, C. Wu, J. Chen and S. Song, *Energy Fuels*, 2014, **28**, 3982–3993.

142 A. Nakada, K. Koike, K. Maeda and O. Ishitani, *Green Chem.*, 2016, **18**, 139–143.

143 H. A. E. Omr, M. W. Horn and H. Lee, *Catalysts*, 2021, **11**, 418.

144 D. Voiry, H. S. Shin, K. P. Loh and M. Chhowalla, *Nat. Rev. Chem.*, 2018, **2**, 1–17.

145 J. Zhao, M. A. Holmes and F. E. Osterloh, *ACS Nano*, 2013, **7**, 4316–4325.

146 A. D. Yoffe, *Adv. Phys.*, 1993, **42**, 173–262.

147 K. A. S. Fernando, S. Sahu, Y. Liu, W. K. Lewis, E. A. Gulians, A. Jafariyan, P. Wang, C. E. Bunker and Y.-P. Sun, *ACS Appl. Mater. Interfaces*, 2015, **7**, 8363–8376.

148 M. Zhou, S. Wang, P. Yang, C. Huang and X. Wang, *ACS Catal.*, 2018, **8**, 4928–4936.

149 J. Sheng, Y. He, J. Li, C. Yuan, H. Huang, S. Wang, Y. Sun, Z. Wang and F. Dong, *ACS Nano*, 2020, **14**, 13103–13114.

150 C. Huang, J. Qiao, R.-N. Ci, X.-Z. Wang, Y. Wang, J.-H. Wang, B. Chen, C.-H. Tung and L.-Z. Wu, *Chem.*, 2021, **7**, 1244–1257.

151 J. A. Caputo, L. C. Frenette, N. Zhao, K. L. Sowers, T. D. Krauss and D. J. Weix, *J. Am. Chem. Soc.*, 2017, **139**, 4250–4253.

152 Z. Zhang, K. Edme, S. Lian and E. A. Weiss, *J. Am. Chem. Soc.*, 2017, **139**, 4246–4249.

153 Y. Deng, M. Chen, G. Chen, W. Zou, Y. Zhao, H. Zhang and Q. Zhao, *ACS Omega*, 2021, **6**, 4247–4254.

154 H. Li, X. Zhang and D. R. MacFarlane, *Adv. Energy Mater.*, 2015, **5**, 1401077.

155 M. Li, M. Wang, L. Zhu, Y. Li, Z. Yan, Z. Shen and X. Cao, *Appl. Catal., B*, 2018, **231**, 269–276.

156 H. Wu, X. Li, C. Tung and L. Wu, *Adv. Mater.*, 2019, **31**, 1900709.

157 J. Wang, T. Xia, L. Wang, X. Zheng, Z. Qi, C. Gao, J. Zhu, Z. Li, H. Xu and Y. Xiong, *Angew. Chem., Int. Ed.*, 2018, **57**, 16447–16451.

158 C. Huang, R. Guo, W. Pan, J. Tang, W. Zhou, X. Liu, H. Qin and P. Jia, *Appl. Surf. Sci.*, 2019, **464**, 534–543.

159 H. Zhu, X. Gao, Y. Lan, D. Song, Y. Xi and J. Zhao, *J. Am. Chem. Soc.*, 2004, **126**, 8380–8381.

160 A. Selmani, M.   padina, M. Plodinec, I. Dela   Marion, M. G. Willinger, J. L  tzenkirchen, H. D. Gafney and E. Redel, *J. Phys. Chem. C*, 2015, **119**, 19729–19742.

161 Q. Liu, Y. Zhou, J. Kou, X. Chen, Z. Tian, J. Gao, S. Yan and Z. Zou, *J. Am. Chem. Soc.*, 2010, **132**, 14385–14387.

162 W. Zhou, Z. Yin, Y. Du, X. Huang, Z. Zeng, Z. Fan, H. Liu, J. Wang and H. Zhang, *Small*, 2013, **9**, 140–147.

163 J. Huang, Y. Lai, F. Pan, L. Yang, H. Wang, K. Zhang, H. Fuchs and L. Chi, *Small*, 2014, **10**, 4865–4873.

164 M. Ge, C. Cao, J. Huang, S. Li, Z. Chen, K.-Q. Zhang, S. S. Al-Deyab and Y. Lai, *J. Mater. Chem. A*, 2016, **4**, 6772–6801.

165 Y. T. Liang, B. K. Vijayan, K. A. Gray and M. C. Hersam, *Nano Lett.*, 2011, **11**, 2865–2870.

166 Y. Li, Y.-L. Li, B. Sa and R. Ahuja, *Catal. Sci. Technol.*, 2017, **7**, 545–559.

167 Q. Xiang, B. Cheng and J. Yu, *Angew. Chem., Int. Ed.*, 2015, **54**, 11350–11366.

168 K. S. Novoselov, A. K. Geim, S. V. Morozov, D. A. Jiang, Y. Zhang, S. V. Dubonos, I. V. Grigorieva and A. A. Firsov, *Science*, 2004, **306**, 666–669.

169 K. Li, X. An, K. H. Park, M. Khraisheh and J. Tang, *Catal. Today*, 2014, **224**, 3–12.

170 M. Tahir and N. S. Amin, *Appl. Catal., A*, 2013, **467**, 483–496.

171 S. Delavari and N. A. S. Amin, *Appl. Energy*, 2016, **162**, 1171–1185.

172 M. Dilla, R. Schl  gl and J. Strunk, *ChemCatChem*, 2017, **9**, 696–704.

173 S. In, M. G. Nielsen, P. C. K. Vesborg, Y. Hou, B. L. Abrams, T. R. Henriksen, O. Hansen and I. Chorkendorff, *Chem. Commun.*, 2011, **47**, 2613–2615.

174 X. Zhan, C. Yan, Y. Zhang, G. Rinke, G. Rabsch, M. Klumpp, A. I. Sch  fer and R. Dittmeyer, *React. Chem. Eng.*, 2020, **5**, 1658–1670.

175 A. Visan, J. R. van Ommen, M. T. Kreutzer and R. G. H. Lammertink, *Ind. Eng. Chem. Res.*, 2019, **58**, 5349–5357.

176 E. Pipelzadeh, V. Rudolph, G. Hanson, C. Noble and L. Wang, *Appl. Catal., B*, 2017, **218**, 672–678.

177 Z. Xiong, C.-C. Kuang, K.-Y. Lin, Z. Lei, X. Chen, B. Gong, J. Yang, Y. Zhao, J. Zhang, B. Xia and J. C. S. Wa, *J. CO2 Util.*, 2018, **24**, 500–508.



178 X. An, K. Li and J. Tang, *ChemSusChem*, 2014, **7**, 1086–1093.

179 K. Adachi, K. Ohta and T. Mizuno, *Sol. Energy*, 1994, **53**, 187–190.

180 H. Yamashita, H. Nishiguchi, N. Kamada, M. Anpo, Y. Teraoka, H. Hatano, S. Ehara, K. Kikui, L. Palmisano, A. Sclafani, M. Schiavello and M. A. Fox, *Res. Chem. Intermed.*, 1994, **20**, 815–823.

181 T. V. Nguyen and J. C. S. Wu, *Appl. Catal., A*, 2008, **335**, 112–120.

182 J. C. S. Wu, T.-H. Wu, T. Chu, H. Huang and D. Tsai, *Top. Catal.*, 2008, **47**, 131–136.

183 A. A. Khan and M. Tahir, *J. CO<sub>2</sub> Util.*, 2019, **29**, 205–239.

184 Z. Xiong, Z. Lei, S. Ma, X. Chen, B. Gong, Y. Zhao, J. Zhang, C. Zheng and J. C. S. Wu, *Appl. Catal., B*, 2017, **219**, 412–424.

185 P.-Y. Liou, S.-C. Chen, J. C. S. Wu, D. Liu, S. Mackintosh, M. Maroto-Valer and R. Linforth, *Energy Environ. Sci.*, 2011, **4**, 1487–1494.

186 F. Li, L. Zhang, J. Tong, Y. Liu, S. Xu, Y. Cao and S. Cao, *Nano Energy*, 2016, **27**, 320–329.

187 H. Yamashita, K. Ikeue, T. Takewaki and M. Anpo, *Top. Catal.*, 2002, **18**, 95–100.

188 M. Xing, Y. Zhou, C. Dong, L. Cai, L. Zeng, B. Shen, L. Pan, C. Dong, Y. Chai, J. Zhang and Y. Yin, *Nano Lett.*, 2018, **18**, 3384–3390.

189 M. Subrahmanyam, S. Kaneko and N. Alonso-Vante, *Appl. Catal., B*, 1999, **23**, 169–174.

190 S. Poudyal and S. Laursen, *Catal. Sci. Technol.*, 2019, **9**, 1048–1059.

191 N. G. Moustakas and J. Strunk, *Chem. – Eur. J.*, 2018, **24**, 12739–12746.

192 B. Ohtani, *Phys. Chem. Chem. Phys.*, 2014, **16**, 1788–1797.

193 J. Colina-Márquez, F. Machuca-Martínez and G. L. Puma, *Environ. Sci. Technol.*, 2010, **44**, 5112–5120.

194 W. A. Thompson, E. Sanchez Fernandez and M. M. Maroto-Valer, *ACS Sustainable Chem. Eng.*, 2020, **8**, 4677–4692.

195 J. P. Perdew and A. Zunger, *Phys. Rev. B: Condens. Matter Mater. Phys.*, 1981, **23**, 5048.

196 J. P. Perdew, J. A. Chevary, S. H. Vosko, K. A. Jackson, M. R. Pederson, D. J. Singh and C. Fiolhais, *Phys. Rev. B: Condens. Matter Mater. Phys.*, 1992, **46**, 6671.

197 P. Verma and D. G. Truhlar, *Theor. Chem. Acc.*, 2016, **135**, 1–15.

198 E. E. Salpeter and H. A. Bethe, *Phys. Rev.*, 1951, **84**, 1232.

199 L. Hedin and S. Lundqvist, *Solid state physics*, Elsevier, 1970, vol. 23, pp. 1–181.

200 L. Li, R. Zhang, J. Vinson, E. L. Shirley, J. P. Greeley, J. R. Guest and M. K. Y. Chan, *Chem. Mater.*, 2018, **30**, 1912–1923.

201 J. Zhao, B. Liu, L. Meng, S. He, R. Yuan, Y. Hou, Z. Ding, H. Lin, Z. Zhang, X. Wang and J. Long, *Appl. Catal., B*, 2019, **256**, 117823.

202 S. S. Tafreshi, A. Z. Moshfegh and N. H. de Leeuw, *J. Phys. Chem. C*, 2019, **123**, 22191–22201.

203 S. E. Braslavsky, A. M. Braun, A. E. Cassano, A. V. Emeline, M. I. Litter, L. Palmisano, V. N. Parmon and N. Serpone, *Pure Appl. Chem.*, 2011, **83**, 931–1014.

204 S. Kozuch and J. M. L. Martin, *ACS Catal.*, 2012, **2**, 2787–2794.

205 T. Bligaard, R. M. Bullock, C. T. Campbell, J. G. Chen, B. C. Gates, R. J. Gorte, C. W. Jones, W. D. Jones, J. R. Kitchin and S. L. Scott, *ACS Catal.*, 2016, **6**, 2590–2602.

206 Y.-J. Yuan, Z.-J. Ye, H.-W. Lu, B. Hu, Y.-H. Li, D.-Q. Chen, J.-S. Zhong, Z.-T. Yu and Z.-G. Zou, *ACS Catal.*, 2016, **6**, 532–541.

207 C. T. K. Nguyen, N. Q. Tran, S. Seo, H. Hwang, S. Oh, J. Yu, J. Lee, T. A. Le, J. Hwang, M. Kim and H. Lee, *Mater. Today*, 2020, **35**, 25–33.

208 R. L. McCreery, *Chem. Rev.*, 2008, **108**, 2646–2687.

209 X.-M. Hu, H. H. Hval, E. T. Bjerglund, K. J. Dalgaard, M. R. Madsen, M.-M. Pohl, E. Welter, P. Lamagni, K. B. Buhl, M. Bremholm, M. Beller, S. U. Pedersen, T. Skrydstrup and K. Daasbjerg, *ACS Catal.*, 2018, **8**, 6255–6264.

210 H.-Y. Jeong, M. Balamurugan, V. S. K. Choutipalli, E. Jeong, V. Subramanian, U. Sim and K. T. Nam, *J. Mater. Chem. A*, 2019, **7**, 10651–10661.

211 K. Jiang, H. Wang, W.-B. Cai and H. Wang, *ACS Nano*, 2017, **11**, 6451–6458.

212 D. T. Whipple and P. J. A. Kenis, *J. Phys. Chem. Lett.*, 2010, **1**, 3451–3458.

213 J. Bullock, D. F. Sránkó, C. M. Towle, Y. Lum, M. Hettick, M. C. Scott, A. Javey and J. Ager, *Energy Environ. Sci.*, 2017, **10**, 2222–2230.

214 M. Jouny, W. Luc and F. Jiao, *Ind. Eng. Chem. Res.*, 2018, **57**, 2165–2177.

215 M. Zubair, H. Kim, A. Razzaq, C. A. Grimes and S. Il In, *J. CO<sub>2</sub> Util.*, 2018, **26**, 70–79.

216 T. Maschmeyer and M. Che, *Angew. Chem.*, 2010, **122**, 1578–1582.

217 S. Docao, A. R. Koirala, M. G. Kim, I. C. Hwang, M. K. Song and K. B. Yoon, *Energy Environ. Sci.*, 2017, **10**, 628–640.

218 P. Kar, S. Zeng, Y. Zhang, E. Vahidzadeh, A. Manuel, R. Kisslinger, K. M. Alam, U. K. Thakur, N. Mahdi, P. Kumar and K. Shankar, *Appl. Catal., B*, 2019, **243**, 522–536.

219 A. Fujishima and K. Honda, *Nature*, 1972, **238**, 37–38.

220 L. Liu, H. Zhao, J. M. Andino and Y. Li, *ACS Catal.*, 2012, **2**, 1817–1828.

221 J. Yu, J. Low, W. Xiao, P. Zhou and M. Jaroniec, *J. Am. Chem. Soc.*, 2014, **136**, 8839–8842.

222 A. Meng, S. Wu, B. Cheng, J. Yu and J. Xu, *J. Mater. Chem. A*, 2018, **6**, 4729–4736.

223 W. Yu, D. Xu and T. Peng, *J. Mater. Chem. A*, 2015, **3**, 19936–19947.

224 X. Li, H. Jiang, C. Ma, Z. Zhu, X. Song, H. Wang, P. Huo and X. Li, *Appl. Catal., B*, 2021, **283**, 119638.

225 M. F. Ehsan and T. He, *Appl. Catal., B*, 2015, **166**, 345–352.

226 H. Wang, L. Zhang, K. Wang, X. Sun and W. Wang, *Appl. Catal., B*, 2019, **243**, 771–779.

227 Z. Wang, K. Teramura, S. Hosokawa and T. Tanaka, *J. Mater. Chem. A*, 2015, **3**, 11313–11319.

228 M. Akatsuka, Y. Kawaguchi, R. Itoh, A. Ozawa, M. Yamamoto, T. Tanabe and T. Yoshida, *Appl. Catal., B*, 2020, **262**, 118247.

229 H. J. Yoon, J. H. Yang, S. J. Park, C. K. Rhee and Y. Sohn, *Appl. Surf. Sci.*, 2021, **536**, 147753.

230 Q. Han, X. Bai, Z. Man, H. He, L. Li, J. Hu, A. Alsaedi, T. Hayat, Z. Yu, W. Zhang, J. Wang, Y. Zhou and Z. Zou, *J. Am. Chem. Soc.*, 2019, **141**, 4209–4213.

231 C. Lu, X. Li, Q. Wu, J. Li, L. Wen, Y. Dai, B. Huang, B. Li and Z. Lou, *ACS Nano*, 2021, **15**, 3529–3539.

232 G. Yin, M. Nishikawa, Y. Nosaka, N. Srinivasan, D. Atarashi, E. Sakai and M. Miyauchi, *ACS Nano*, 2015, **9**, 2111–2119.

233 W. Wang, C. Deng, S. Xie, Y. Li, W. Zhang, H. Sheng, C. Chen and J. Zhao, *J. Am. Chem. Soc.*, 2021, **143**, 2984–2993.

234 L. Wang, J. Wan, Y. Zhao, N. Yang and D. Wang, *J. Am. Chem. Soc.*, 2019, **141**, 2238–2241.

235 S. Xie, Y. Wang, Q. Zhang, W. Deng and Y. Wang, *ACS Catal.*, 2014, **4**, 3644–3653.

236 L. Liu, Y. Jiang, H. Zhao, J. Chen, J. Cheng, K. Yang and Y. Li, *ACS Catal.*, 2016, **6**, 1097–1108.

237 L. Collado, A. Reynal, F. Fresno, M. Barawi, C. Escudero, V. Perez-Dieste, J. M. Coronado, D. P. Serrano, J. R. Durrant and V. A. de la peña O'Shea, *Nat. Commun.*, 2018, **9**, 4986.

238 W. Wang, D. Xu, B. Cheng, J. Yu and C. Jiang, *J. Mater. Chem. A*, 2017, **5**, 5020–5029.

239 J. Bian, Y. Qu, X. Zhang, N. Sun, D. Tang and L. Jing, *J. Mater. Chem. A*, 2018, **6**, 11838–11845.

240 J. Li, F. Wei, C. Dong, W. Mu and X. Han, *J. Mater. Chem. A*, 2020, **8**, 6524–6531.

241 F. You, J. Wan, J. Qi, D. Mao, N. Yang, Q. Zhang, L. Gu and D. Wang, *Angew. Chem.*, 2020, **132**, 731–734.

242 T. Ye, W. Huang, L. Zeng, M. Li and J. Shi, *Appl. Catal., B*, 2017, **210**, 141–148.

243 K. Wang, J. Lu, Y. Lu, C. H. Lau, Y. Zheng and X. Fan, *Appl. Catal., B*, 2021, **292**, 120147.

244 A. Meng, B. Cheng, H. Tan, J. Fan, C. Su and J. Yu, *Appl. Catal., B*, 2021, **289**, 120039.

245 Y. Ma, Q. Tang, W. Y. Sun, Z. Y. Yao, W. Zhu, T. Li and J. Wang, *Appl. Catal., B*, 2020, **270**, 118856.

246 J. Jin, S. Chen, J. Wang, C. Chen and T. Peng, *Appl. Catal., B*, 2020, **263**, 118353.

247 T. Butburee, Z. Sun, A. Centeno, F. Xie, Z. Zhao, D. Wu, P. Peerakiatkajohn, S. Thaweesak, H. Wang and L. Wang, *Nano Energy*, 2019, **62**, 426–433.

248 L. Wang, S. Duan, P. Jin, H. She, J. Huang, Z. Lei, T. Zhang and Q. Wang, *Appl. Catal., B*, 2018, **239**, 599–608.

249 Y. Wei, X. Wu, Y. Zhao, L. Wang, Z. Zhao, X. Huang, J. Liu and J. Li, *Appl. Catal., B*, 2018, **236**, 445–457.

250 M. Tahir, B. Tahir and N. A. S. Amin, *Appl. Catal., B*, 2017, **204**, 548–560.

251 M. Tahir, *Appl. Catal., B*, 2017, **219**, 329–343.

252 A. Razzaq, A. Sinhamahapatra, T.-H. Kang, C. A. Grimes, J.-S. Yu and S.-I. In, *Appl. Catal., B*, 2017, **215**, 28–35.

253 S. Bera, J. E. Lee, S. B. Rawal and W. I. Lee, *Appl. Catal., B*, 2016, **199**, 55–63.

254 M. Wang, D. Wang and Z. Li, *Appl. Catal., B*, 2016, **183**, 47–52.

255 T. Wang, X. Meng, P. Li, S. Ouyang, K. Chang, G. Liu, Z. Mei and J. Ye, *Nano Energy*, 2014, **9**, 50–60.

256 S. In, D. D. Vaughn and R. E. Schaak, *Angew. Chem., Int. Ed.*, 2012, **51**, 3915–3918.

257 H. Lin, L. Li, M. Zhao, X. Huang, X. Chen, G. Li and R. Yu, *J. Am. Chem. Soc.*, 2012, **134**, 8328–8331.

258 M. M. Rodriguez, X. Peng, L. Liu, Y. Li and J. M. Andino, *J. Phys. Chem. C*, 2012, **116**, 19755–19764.

259 H. G. Yang, C. H. Sun, S. Z. Qiao, J. Zou, G. Liu, S. C. Smith, H. M. Cheng and G. Q. Lu, *Nature*, 2008, **453**, 638–641.

260 F. He, B. Zhu, B. Cheng, J. Yu, W. Ho and W. Macyk, *Appl. Catal., B*, 2020, **272**, 119006.

261 X. Y. Kong, W. L. Tan, B.-J. Ng, S.-P. Chai and A. R. Mohamed, *Nano Res.*, 2017, **10**, 1720–1731.

262 X. Y. Kong, W. Q. Lee, A. R. Mohamed and S.-P. Chai, *Chem. Eng. J.*, 2019, **372**, 1183–1193.

263 J. Hao, D. Yang, J. Wu, B. Ni, L. Wei, Q. Xu, Y. Min and H. Li, *Chem. Eng.*, 2021, **423**, 130190.

264 M.-P. Jiang, K.-K. Huang, J.-H. Liu, D. Wang, Y. Wang, X. Wang, Z.-D. Li, X.-Y. Wang, Z.-B. Geng, X.-Y. Hou and S.-H. Feng, *Chem.*, 2020, **6**, 2335–2346.

265 H. Sheng, M. H. Oh, W. T. Osowiecki, W. Kim, A. P. Alivisatos and H. Frei, *J. Am. Chem. Soc.*, 2018, **140**, 4363–4371.

266 J. Wu, Y. Huang, W. Ye and Y. Li, *Adv. Sci.*, 2017, **4**, 1700194.

267 G. A. Ozin, *Adv. Mater.*, 2015, **27**, 1957–1963.

268 A. A. Balandin, S. Ghosh, W. Bao, I. Calizo, D. Teweldebrhan, F. Miao and C. N. Lau, *Nano Lett.*, 2008, **8**, 902–907.

269 C. Lee, X. Wei, J. W. Kysar and J. Hone, *Science*, 2008, **321**, 385–388.

270 X. Du, I. Skachko, A. Barker and E. Y. Andrei, *Nat. Nanotechnol.*, 2008, **3**, 491.

271 S. Cui, X. Sun and J. Liu, *ChemSusChem*, 2016, **9**, 1698–1703.

272 Z. Xiong, Y. Luo, Y. Zhao, J. Zhang, C. Zheng and J. C. S. Wu, *Phys. Chem. Chem. Phys.*, 2016, **18**, 13186–13195.

273 K. M. Cho, K. H. Kim, H. O. Choi and H.-T. Jung, *Green Chem.*, 2015, **17**, 3972–3978.

274 P. Li, Y. Zhou, H. Li, Q. Xu, X. Meng, X. Wang, M. Xiao and Z. Zou, *Chem. Commun.*, 2014, **51**, 800–803.

275 J. Yu, J. Jin, B. Cheng and M. Jaroniec, *J. Mater. Chem. A*, 2014, **2**, 3407–3416.

276 S. Xie, Y. Wang, Q. Zhang, W. Fan, W. Deng and Y. Wang, *Chem. Commun.*, 2013, **49**, 2451–2453.

277 L. Gu, J. Wang, H. Cheng, Y. Zhao, L. Liu and X. Han, *ACS Appl. Mater. Interfaces*, 2013, **5**, 3085–3093.

278 Y. Chen, H. Gao, J. Xiang, X. Dong and Y. Cao, *Mater. Res. Bull.*, 2018, **99**, 29–36.

279 W. Tu, Y. Zhou, Q. Liu, Z. Tian, J. Gao, X. Chen, H. Zhang, J. Liu and Z. Zou, *Adv. Funct. Mater.*, 2012, **22**, 1215–1221.

280 Y. Zhao, Y. Wei, X. Wu, H. Zheng, Z. Zhao, J. Liu and J. Li, *Appl. Catal., B*, 2018, **226**, 360–372.

281 A. Razzaq, C. A. Grimes and S.-I. In, *Carbon*, 2016, **98**, 537–544.

282 M. Xing, F. Shen, B. Qiu and J. Zhang, *Sci. Rep.*, 2014, **4**, 6341.

283 Q. Li, B. Guo, J. Yu, J. Ran, B. Zhang, H. Yan and J. R. Gong, *J. Am. Chem. Soc.*, 2011, **133**, 10878–10884.

284 P.-Q. Wang, Y. Bai, P.-Y. Luo and J.-Y. Liu, *Catal. Commun.*, 2013, **38**, 82–85.



285 M. Long, Y. Qin, C. Chen, X. Guo, B. Tan and W. Cai, *J. Phys. Chem. C*, 2013, **117**, 16734–16741.

286 Y. Tang, X. Hu and C. Liu, *Phys. Chem. Chem. Phys.*, 2014, **16**, 25321–25329.

287 S. Ali, A. Razzaq and S.-I. In, *Catal. Today*, 2018, **335**, 39–54.

288 M. Xing, W. Fang, X. Yang, B. Tian and J. Zhang, *Chem. Commun.*, 2014, **50**, 6637–6640.

289 L.-Y. Lin, Y. Nie, S. Kavadiya, T. Soundappan and P. Biswas, *Chem. Eng. J.*, 2017, **316**, 449–460.

290 I. Shown, H. C. Hsu, Y. C. Chang, C. H. Lin, P. K. Roy, A. Ganguly, C. H. Wang, J. K. Chang, C. I. Wu, L. C. Chen and K. H. Chen, *Nano Lett.*, 2014, **14**, 6097–6103.

291 P. Madhusudan, S. Wageh, A. A. Al-Ghamdi, J. Zhang, B. Cheng and Y. Yu, *Appl. Surf. Sci.*, 2020, **506**, 144683.

292 L.-L. Tan, W.-J. Ong, S.-P. Chai, B. T. Goh and A. R. Mohamed, *Appl. Catal., B*, 2015, **179**, 160–170.

293 W.-J. Ong, L.-L. Tan, S.-P. Chai and S.-T. Yong, *Chem. Commun.*, 2015, **51**, 858–861.

294 X. Wang, K. Li, J. He, J. Yang, F. Dong, W. Mai and M. Zhu, *Nano Energy*, 2020, **78**, 105388.

295 Y. F. Mu, W. Zhang, G. X. Dong, K. Su, M. Zhang and T. B. Lu, *Small*, 2020, **16**, 1–8.

296 L. Wang, H. Tan, L. Zhang, B. Cheng and J. Yu, *Chem. Eng. J.*, 2021, **411**, 128501.

297 X. Lin, S. Wang, W. Tu, H. Wang, Y. Hou, W. Dai and R. Xu, *ACS Appl. Energy Mater.*, 2019, **2**, 7670–7678.

298 Z. Otgonbayar, K. Y. Cho and W. C. Oh, *ACS Omega*, 2020, **5**, 26389–26401.

299 Z. Otgonbayar, Y. Liu, K. Y. Cho, C.-H. Jung and W.-C. Oh, *Mater. Sci. Semicond. Process.*, 2021, **121**, 105456.

300 R. Gusain, P. Kumar, O. P. Sharma, S. L. Jain and O. P. Khatri, *Appl. Catal., B*, 2016, **181**, 352–362.

301 C. Bie, B. Zhu, F. Xu, L. Zhang and J. Yu, *Adv. Mater.*, 2019, **31**, 1–6.

302 R. B. Lin, S. Xiang, H. Xing, W. Zhou and B. Chen, *Coord. Chem. Rev.*, 2019, **378**, 87–103.

303 Z. Ma, Q. Zhang, W. Zhu, D. Khan, C. Hu, T. Huang, W. Ding and J. Zou, *Sustainable Energy Fuels*, 2020, **4**, 2192–2200.

304 M. C. Singo, X. C. Molepo, O. O. Oluwasina and M. O. Daramola, *Energy Procedia*, 2017, **114**, 2429–2440.

305 L. Zhao, A. Wang, A. Yang, G. Zuo, J. Dai and Y. Zheng, *Int. J. Hydrogen Energy*, 2020, **45**, 31863–31870.

306 Y. P. Zhu, J. Yin, E. Abou-Hamad, X. Liu, W. Chen, T. Yao, O. F. Mohammed and H. N. Alshareef, *Adv. Mater.*, 2020, **32**, 1–8.

307 Y. Gao, J. Wu, J. Wang, Y. Fan, S. Zhang and W. Dai, *ACS Appl. Mater. Interfaces*, 2020, **12**, 11036–11044.

308 C. Lin, H. He, Y. Zhang, M. Xu, F. Tian, L. Li and Y. Wang, *RSC Adv.*, 2020, **10**, 3084–3091.

309 S. Bordiga, C. Lamberti, G. Ricchiardi, L. Regli, F. Bonino, A. Damin, K. P. Lillerud, M. Bjorgen and A. Zecchina, *Chem. Commun.*, 2004, 2300–2301.

310 D. Sun, Y. Gao, J. Fu, X. Zeng, Z. Chen and Z. Li, *Chem. Commun.*, 2015, **51**, 2645–2648.

311 R. Li, J. Hu, M. Deng, H. Wang, X. Wang, Y. Hu, H. Jiang, J. Jiang, Q. Zhang and Y. Xie, *Adv. Mater.*, 2014, **26**, 4783–4788.

312 Z. C. Kong, J. F. Liao, Y. J. Dong, Y. F. Xu, H. Y. Chen, D. Bin Kuang and C. Y. Su, *ACS Energy Lett.*, 2018, **3**, 2656–2662.

313 H. Q. Xu, J. Hu, D. Wang, Z. Li, Q. Zhang, Y. Luo, S. H. Yu and H. L. Jiang, *J. Am. Chem. Soc.*, 2015, **137**, 13440–13443.

314 H. Dong, X. Zhang, Y. Lu, Y. Yang, Y. P. Zhang, H. L. Tang, F. M. Zhang, Z. Di Yang, X. Sun and Y. Feng, *Appl. Catal., B*, 2020, **276**, 119173.

315 X. Liu, H. Yang, J. He, H. Liu, L. Song, L. Li and J. Luo, *Small*, 2018, **14**, 1704049.

316 K. S. Novoselov, A. Mishchenko, A. Carvalho and A. H. Castro Neto, *Science*, 2016, **353**, aac9439.

317 M. Xu, T. Liang, M. Shi and H. Chen, *Chem. Rev.*, 2013, **113**, 3766–3798.

318 Y. Sun, S. Gao and Y. Xie, *Chem. Soc. Rev.*, 2014, **43**, 530–546.

319 D. Voiry, J. Yang and M. Chhowalla, *Adv. Mater.*, 2016, **28**, 6197–6206.

320 Q. H. Wang, K. Kalantar-Zadeh, A. Kis, J. N. Coleman and M. S. Strano, *Nat. Nanotechnol.*, 2012, **7**, 699–712.

321 D. Voiry, A. Mohite and M. Chhowalla, *Chem. Soc. Rev.*, 2015, **44**, 2702–2712.

322 M. Asadi, K. Kim, C. Liu, A. V. Addepalli, P. Abbasi, P. Yasaee, P. Phillips, A. Behranginia, J. M. Cerrato, R. Haasch, P. Zapol, B. Kumar, R. F. Klie, J. Abiade, L. A. Curtiss and A. S. Khojin, *Science*, 2016, **353**, 467–470.

323 H. Schmidt, F. Giustiniano and G. Eda, *Chem. Soc. Rev.*, 2015, **44**, 7715–7736.

324 L. Cheng and Y. Liu, *J. Am. Chem. Soc.*, 2018, **140**, 17895–17900.

325 A. J. Meier, A. Garg, B. Sutter, J. N. Kuhn and V. R. Bhethanabotla, *ACS Sustainable Chem. Eng.*, 2018, **7**, 265–275.

326 F. Xu, B. Zhu, B. Cheng, J. Yu and J. Xu, *Adv. Opt. Mater.*, 2018, **6**, 1800911.

327 H. Jung, K. M. Cho, K. H. Kim, H.-W. Yoo, A. Al-Saggaf, I. Gereige and H.-T. Jung, *ACS Sustainable Chem. Eng.*, 2018, **6**, 5718–5724.

328 D. Long, J. Liu, L. Bai, L. Yan, H. Liu, Z. Feng, L. Zheng, X. Chen, S. Li and M. Lu, *ACS Photonics*, 2020, **7**, 3394–3400.

329 B. Khan, F. Raziq, M. B. Faheem, M. U. Farooq, S. Hussain, F. Ali, A. Ullah, A. Mavlonov, Y. Zhao and Z. Liu, *J. Hazard. Mater.*, 2020, **381**, 120972.

330 R. Kim, J. Kim, J. Y. Do, M. W. Seo and M. Kang, *Catalysts*, 2019, **9**, 998.

331 W. Tu, Y. Li, L. Kuai, Y. Zhou, Q. Xu, H. Li, X. Wang, M. Xiao and Z. Zou, *Nanoscale*, 2017, **9**, 9065–9070.

332 Y. Wang, Z. Zhang, L. Zhang, Z. Luo, J. Shen, H. Lin, J. Long, J. C. S. Wu, X. Fu and X. Wang, *J. Am. Chem. Soc.*, 2018, **140**, 14595–14598.

333 W. Dai, J. Yu, Y. Deng, X. Hu, T. Wang and X. Luo, *Appl. Surf. Sci.*, 2017, **403**, 230–239.

334 R. A. Geioushy, S. M. El-Sheikh, I. M. Hegazy, A. Shawky, S. El-Sherbiny and A.-H. T. Kandil, *Mater. Res. Bull.*, 2019, **118**, 110499.

335 C. Yang, Q. Tan, Q. Li, J. Zhou, J. Fan, B. Li, J. Sun and K. Lv, *Appl. Catal., B*, 2020, **268**, 118738.

336 J. Low, L. Zhang, T. Tong, B. Shen and J. Yu, *J. Catal.*, 2018, **361**, 255–266.

337 Y. Li, Z. Yin, G. Ji, Z. Liang, Y. Xue, Y. Guo, J. Tian, X. Wang and H. Cui, *Appl. Catal., B*, 2019, **246**, 12–20.

338 Q. Tang, Z. Zhou and Z. Chen, *Wiley Interdiscip. Rev.: Comput. Mol. Sci.*, 2015, **5**, 360–379.

339 M. Naguib, V. N. Mochalin, M. W. Barsoum and Y. Gogotsi, *Adv. Mater.*, 2014, **26**, 992–1005.

340 M. W. Barsoum, *Prog. Solid State Chem.*, 2000, **28**, 201–281.

341 M. Naguib, M. Kurtoglu, V. Presser, J. Lu, J. Niu, M. Heon, L. Hultman, Y. Gogotsi and M. W. Barsoum, *Adv. Mater.*, 2011, **23**, 4248–4253.

342 Y. Gogotsi and B. Anasori, *ACS Nano*, 2019, **13**, 8491–8494.

343 Q. Tang, Z. Zhou and P. Shen, *J. Am. Chem. Soc.*, 2012, **134**, 16909–16916.

344 M. Ghiddu, M. R. Lukatskaya, M.-Q. Zhao, Y. Gogotsi and M. W. Barsoum, *Nature*, 2014, **516**, 78–81.

345 W.-F. Chen, J. T. Muckerman and E. Fujita, *Chem. Commun.*, 2013, **49**, 8896–8909.

346 O. Mashtalir, K. M. Cook, V. N. Mochalin, M. Crowe, M. W. Barsoum and Y. Gogotsi, *J. Mater. Chem. A*, 2014, **2**, 14334–14338.

347 H. Huang, Y. Song, N. Li, D. Chen, Q. Xu, H. Li, J. He and J. Lu, *Appl. Catal., B*, 2019, **251**, 154–161.

348 Z. Guo, J. Zhou, L. Zhu and Z. Sun, *J. Mater. Chem. A*, 2016, **4**, 11446–11452.

349 K. Huang, C. Li, H. Li, G. Ren, L. Wang, W. Wang and X. Meng, *ACS Appl. Nano Mater.*, 2020, **3**, 9581–9603.

350 J. Wu, Y. Zhang, P. Lu, G. Fang, X. Li, W. Y. William, Z. Zhang and B. Dong, *Appl. Catal., B*, 2021, **286**, 119944.

351 J. Ran, G. Gao, F.-T. T. Li, T.-Y. Y. Ma, A. Du and S.-Z. Z. Qiao, *Nat. Commun.*, 2017, **8**, 1–10.

352 A. Pan, X. Ma, S. Huang, Y. Wu, M. Jia, Y. Shi, Y. Liu, P. Wangyang, L. He and Y. Liu, *J. Phys. Chem. Lett.*, 2019, **10**, 6590–6597.

353 S. Cao, B. Shen, T. Tong, J. Fu and J. Yu, *Adv. Funct. Mater.*, 2018, **28**, 1800136.

354 W. Sun, S. A. Shah, Y. Chen, Z. Tan, H. Gao, T. Habib, M. Radovic and M. J. Green, *J. Mater. Chem. A*, 2017, **5**, 21663–21668.

355 Z. Zeng, Y. Xu, Z. Zhang, Z. Gao, M. Luo, Z. Yin, C. Zhang, J. Xu, B. Huang, F. Luo, Y. Du and C. Yan, *Chem. Soc. Rev.*, 2020, **49**, 1109–1143.

356 A. Kumar, A. Kumar and V. Krishnan, *ACS Catal.*, 2020, **10**, 10253–10315.

357 J. C. Hemminger, R. Carr and G. A. Somorjai, *Chem. Phys. Lett.*, 1978, **57**, 100–104.

358 C. Luo, J. Zhao, Y. Li, W. Zhao, Y. Zeng and C. Wang, *Appl. Surf. Sci.*, 2018, **447**, 627–635.

359 K. Xie, N. Umezawa, N. Zhang, P. Reunchan, Y. Zhang and J. Ye, *Energy Environ. Sci.*, 2011, **4**, 4211–4219.

360 D. Li, S. Ouyang, H. Xu, D. Lu, M. Zhao, X. Zhang and J. Ye, *Chem. Commun.*, 2016, **52**, 5989–5992.

361 D. Mateo, J. Albero and H. García, *Joule*, 2019, **3**, 1949–1962.

362 J. Lin, J. Hu, C. Qiu, H. Huang, L. Chen, Y. Xie, Z. Zhang, H. Lin and X. Wang, *Catal. Sci. Technol.*, 2019, **9**, 336–346.

363 K. Teramura, S. Okuoka, H. Tsuneoka, T. Shishido and T. Tanaka, *Appl. Catal., B*, 2010, **96**, 565–568.

364 H. Zhou, P. Li, J. Guo, R. Yan, T. Fan, D. Zhang and J. Ye, *Nanoscale*, 2015, **7**, 113–120.

365 J. Qin, L. Lin and X. Wang, *Chem. Commun.*, 2018, **54**, 2272–2275.

366 S. Wang, Y. Hou and X. Wang, *ACS Appl. Mater. Interfaces*, 2015, **7**, 4327–4335.

367 H. Shi, G. Chen, C. Zhang and Z. Zou, *ACS Catal.*, 2014, **4**, 3637–3643.

368 A. Kumar, G. Sharma, M. Naushad, T. Ahamad, R. C. Veses and F. J. Stadler, *Chem. Eng. J.*, 2019, **370**, 148–165.

369 Y. Wang, M. Liu, W. Chen, L. Mao and W. Shangguan, *J. Alloys Compd.*, 2019, **786**, 149–154.

370 S. Tu, Y. Zhang, A. H. Reshak, S. Auluck, L. Ye, X. Han, T. Ma and H. Huang, *Nano Energy*, 2019, **56**, 840–850.

371 M. Que, Y. Zhao, Y. Yang, L. Pan, W. Lei, W. Cai, H. Yuan, J. Chen and G. Zhu, *ACS Appl. Mater. Interfaces*, 2021, **13**, 6180–6187.

372 S. S. Bhosale, A. K. Kharade, E. Jokar, A. Fathi, S. Chang and E. W.-G. Diau, *J. Am. Chem. Soc.*, 2019, **141**, 20434–20442.

373 F. Xu, K. Meng, B. Cheng, S. Wang, J. Xu and J. Yu, *Nat. Commun.*, 2020, **11**, 1–9.

374 Y.-F. Xu, M.-Z. Yang, B.-X. Chen, X.-D. Wang, H.-Y. Chen, D.-B. Kuang and C.-Y. Su, *J. Am. Chem. Soc.*, 2017, **139**, 5660–5663.

375 Y. Jiang, J.-F. Liao, Y.-F. Xu, H.-Y. Chen, X.-D. Wang and D.-B. Kuang, *J. Mater. Chem. A*, 2019, **7**, 13762–13769.

376 Y. Mu, W. Zhang, G. Dong, K. Su, M. Zhang and T. Lu, *Small*, 2020, **16**, 2002140.

377 S. Wan, M. Ou, Q. Zhong and X. Wang, *Chem. Eng. J.*, 2019, **358**, 1287–1295.

378 C. Tang, C. Chen, W. Xu and L. Xu, *J. Mater. Chem. A*, 2019, **7**, 6911–6919.

379 S. Shyamal, S. K. Dutta and N. Pradhan, *J. Phys. Chem. Lett.*, 2019, **10**, 7965–7969.

380 G.-X. Dong, W. Zhang, Y.-F. Mu, K. Su, M. Zhang and T.-B. Lu, *Chem. Commun.*, 2020, **56**, 4664–4667.

381 J. Zhu, Y. Zhu, J. Huang, L. Hou, J. Shen and C. Li, *Nanoscale*, 2020, **12**, 11842–11846.

382 Y.-F. Xu, M.-Z. Yang, H.-Y. Chen, J.-F. Liao, X.-D. Wang and D.-B. Kuang, *ACS Appl. Energy Mater.*, 2018, **1**, 5083–5089.

383 Z. Chen, Y. Hu, J. Wang, Q. Shen, Y. Zhang, C. Ding, Y. Bai, G. Jiang, Z. Li and N. Gaponik, *Chem. Mater.*, 2020, **32**, 1517–1525.

384 L. Wu, Y. Mu, X. Guo, W. Zhang, Z. Zhang, M. Zhang and T. Lu, *Angew. Chem., Int. Ed.*, 2019, **58**, 9491–9495.

385 M. Que, Y. Zhao, L. Pan, Y. Yang, Z. He, H. Yuan, J. Chen and G. Zhu, *Mater. Lett.*, 2021, **282**, 128695.

386 L. Zhou, Y. Xu, B. Chen, D. Kuang and C. Su, *Small*, 2018, **14**, 1703762.

387 Z. Liu, H. Yang, J. Wang, Y. Yuan, K. Hills-Kimball, T. Cai, P. Wang, A. Tang and O. Chen, *Nano Lett.*, 2021, **21**, 1620–1627.

388 Y. Wang, H. Huang, Z. Zhang, C. Wang, Y. Yang, Q. Li and D. Xu, *Appl. Catal., B*, 2021, **282**, 119570.



389 C. Lu, D. S. Itanze, A. G. Aragon, X. Ma, H. Li, K. B. Ucer, C. Hewitt, D. L. Carroll, R. T. Williams, Y. Qiu and S. M. Geyer, *Nanoscale*, 2020, **12**, 2987–2991.

390 R. Verma, R. Belgamwar and V. Polshettiwar, *ACS Mater. Lett.*, 2021, **3**, 574–598.

391 Y. Tamaki and O. Ishitani, *ACS Catal.*, 2017, **7**, 3394–3409.

392 C. Clavero, *Nat. Photonics*, 2014, **8**, 95–103.

393 X.-C. Ma, Y. Dai, L. Yu and B.-B. Huang, *Light Sci. Appl.*, 2016, **5**, e16017.

394 M. Wang, M. Ye, J. Iocozzia, C. Lin and Z. Lin, *Adv. Sci.*, 2016, **3**, 1600024.

395 S. Yu, A. J. Wilson, G. Kumari, X. Zhang and P. K. Jain, *ACS Energy Lett.*, 2017, **2**, 2058–2070.

396 G. Kumari, X. Zhang, D. Devasia, J. Heo and P. K. Jain, *ACS Nano*, 2018, **12**, 8330–8340.

397 L. Collado, A. Reynal, J. M. Coronado, D. P. Serrano, J. R. Durrant and V. A. De la Peña O’Shea, *Appl. Catal. B*, 2015, **178**, 177–185.

398 S. Zeng, E. Vahidzadeh, C. G. VanEssen, P. Kar, R. Kisslinger, A. Goswami, Y. Zhang, N. Mahdi, S. Riddell, A. E. Kobryn, S. Gusalov, P. Kumar and K. Shankar, *Appl. Catal. B*, 2020, **267**, 118644.

399 I. García-García, E. C. Lovell, R. J. Wong, V. L. Barrio, J. Scott, J. F. Cambra and R. Amal, *ACS Sustainable Chem. Eng.*, 2020, **8**, 1879–1887.

400 H. Li, Y. Gao, Z. Xiong, C. Liao and K. Shih, *Appl. Surf. Sci.*, 2018, **439**, 552–559.

401 H. Song, X. Meng, T. D. Dao, W. Zhou, H. Liu, L. Shi, H. Zhang, T. Nagao, T. Kako and J. Ye, *ACS Appl. Mater. Interfaces*, 2018, **10**, 408–416.

402 D. Hong, L.-M. Lyu, K. Koga, Y. Shimoyama and Y. Kon, *ACS Sustainable Chem. Eng.*, 2019, **7**, 18955–18964.

403 W. Tu, Y. Zhou, H. Li, P. Li and Z. Zou, *Nanoscale*, 2015, **7**, 14232–14236.

404 L. K. Putri, W.-J. Ong, W. S. Chang and S.-P. Chai, *Catal. Sci. Technol.*, 2016, **6**, 744–754.

405 J. Balajka, M. A. Hines, W. J. I. DeBenedetti, M. Komora, J. Pavelec, M. Schmid and U. Diebold, *Science*, 2018, **361**, 786–789.

406 G. W. Busser, B. Mei, A. Pougin, J. Strunk, R. Gutkowski, W. Schuhmann, M. Willinger, R. Schlögl and M. Muhler, *ChemSusChem*, 2014, **7**, 1030–1034.

407 L. Yuan, K. Q. Lu, F. Zhang, X. Fu and Y. J. Xu, *Appl. Catal. B*, 2018, **237**, 424–431.

408 B. Wang, X. Wang, L. Lu, C. Zhou, Z. Xin, J. Wang, X. K. Ke, G. Sheng, S. Yan and Z. Zou, *ACS Catal.*, 2018, **8**, 516–525.

409 C. C. Yang, Y. H. Yu, B. Van Der Linden, J. C. S. Wu and G. Mul, *J. Am. Chem. Soc.*, 2010, **132**, 8398–8406.

410 H. Zhang, T. Itoi, T. Konishi and Y. Izumi, *J. Am. Chem. Soc.*, 2019, **141**, 6292–6301.

411 H. Zhang, T. Itoi, T. Konishi and Y. Izumi, *Angew. Chem., Int. Ed.*, 2021, **60**, 9045–9054.

412 M. Borges Ordonífo and A. Urakawa, *J. Phys. Chem. C*, 2019, **123**, 4140–4147.

413 A. Bazzo and A. Urakawa, *ChemSusChem*, 2013, **6**, 2095–2102.

414 T. Yui, A. Kan, C. Saitoh, K. Koike, T. Ibusuki and O. Ishitani, *ACS Appl. Mater. Interfaces*, 2011, **3**, 2594–2600.

415 C. C. Yang, J. Vernimmen, V. Meynen, P. Cool and G. Mul, *J. Catal.*, 2011, **284**, 1–8.

416 S. Ishihara, P. Sahoo, K. Deguchi, S. Ohki, M. Tansho, T. Shimizu, J. Labuta, J. P. Hill, K. Ariga, K. Watanabe, Y. Yamauchi, S. Suehara and N. Lyi, *J. Am. Chem. Soc.*, 2013, **135**, 18040–18043.

417 K. Kamogawa, Y. Shimoda, K. Miyata, K. Onda, Y. Yamazaki, Y. Tamaki and O. Ishitani, *Chem. Sci.*, 2021, **12**, 9682–9683.

418 A. Rafiee, K. Rajab Khalilpour, D. Milani and M. Panahi, *J. Environ. Chem. Eng.*, 2018, **6**, 5771–5794.

419 M. A. Sabri, S. Al Jitan, D. Bahamon, L. F. Vega and G. Palmisano, *Sci. Total Environ.*, 2021, **790**, 148081.

420 M. Aresta, A. Dibenedetto and A. Angelini, *J. CO<sub>2</sub> Util.*, 2013, **3–4**, 65–73.

421 P. Gabrielli, M. Gazzani and M. Mazzotti, *Ind. Eng. Chem. Res.*, 2020, **59**, 7033–7045.

422 P. Nejat, F. Jomehzadeh, M. M. Taheri, M. Gohari and M. Z. A. Majid, *Renewable Sustainable Energy Rev.*, 2015, **43**, 843–862.

423 H. M. Wee, W. H. Yang, C. W. Chou and M. V. Padilan, *Renewable Sustainable Energy Rev.*, 2012, **16**, 5451–5465.

424 S. Ali, T. Fazal, F. Javed, A. Hafeez, M. Akhtar, B. Haider, M. S. ur Rehman, W. B. Zimmerman and F. Rehman, *J. Clean. Prod.*, 2020, **259**, 120729.

425 R. G. Newell, D. Raimi and G. Aldana, *Resources for the Future*, 2019, pp. 8–19.

426 T. Covert, M. Greenstone and C. R. Knittel, *J. Econ. Perspect.*, 2016, **30**, 117–138.

427 G. De Pietro, L. J. Gallo Robert Howlett and L. C. Jain, *Smart Innovation, Systems and Technologies 98 Intelligent Interactive Multimedia Systems and Services Proceedings of 2018 Conference*, 2018.

428 E. S. Rubin and H. Zhai, *Environ. Sci. Technol.*, 2012, **46**, 3076–3084.

429 X. Yang and D. Wang, *ACS Appl. Energy Mater.*, 2018, **1**, 6657–6693.

430 R. Snoeckx and A. Bogaerts, *Chem. Soc. Rev.*, 2017, **46**, 5805–5863.

431 S. Cheng and B. E. Logan, *Proc. Natl. Acad. Sci. U. S. A.*, 2007, **104**, 18871–18873.

432 Y. A. Wu, I. McNulty, C. Liu, K. C. Lau, Q. Liu, A. P. Paulikas, C. J. Sun, Z. Cai, J. R. Guest, Y. Ren, V. Stamenkovic, L. A. Curtiss, Y. Liu and T. Rajh, *Nat. Energy*, 2019, **4**, 957–968.

433 J. Albero, Y. Peng and H. García, *ACS Catal.*, 2020, **10**, 5734–5749.

434 T. Yui, Y. Tamaki, K. Sekizawa and O. Ishitani, *Top. Curr. Chem.*, 2011, **303**, 151–184.

435 Y. Mi, X. Peng, X. Liu and J. Luo, *ACS Appl. Energy Mater.*, 2018, **1**, 5119–5123.

436 H. Yamashita, K. Ikeue, T. Takewaki and M. Anpo, *Top. Catal.*, 2002, **18**, 95–100.

437 Y. Wang, S. Zhou and H. Huo, *Renewable Sustainable Energy Rev.*, 2014, **39**, 370–380.

438 M. H. Chakrabarti, M. Ali, S. Baroutian and M. Saleem, *Process Saf. Environ. Prot.*, 2011, **89**, 165–171.

439 F. Graf, *Power to gas – state of the art and perspectives. MARCOGAZ-General Assembly: Workshop New Developments, DVGW Research Center at Engler-Bunte-Institut of KIT*, 2014.

440 I. P. K. M. Oberdorf, *KIT-KIT-Media-Press Releases-Power to Gas: Storing the Wind and Sun in Natural Gas*, 2014.

441 C. C. Economy, The carbon cycle is broken . . . Can we close it again? . . . and how? 2021.

442 S. Docao, A. R. Koirala, M. G. Kim, I. C. Hwang, M. K. Song and K. B. Yoon, *Energy Environ. Sci.*, 2017, **10**, 628–640.

443 B.-H. Lee, E. Gong, M. Kim, S. Park, H. R. Kim, J. Lee, E. Jung, C. W. Lee, J. Bok, Y. Jung, Y. S. Kim, K.-S. Lee, S.-P. Cho, J.-W. Jung, C.-H. Cho, S. Lebègue, K. T. Nam, H. Kim, S.-I. In and T. Hyeon, *Energy Environ. Sci.*, 2021, DOI: 10.1039/d1ee01574e.

444 X. Li, Y. Sun, J. Xu, Y. Shao, J. Wu, X. Xu, Y. Pan, H. Ju, J. Xhu and Y. Xie, *Nat. Energy*, 2019, **4**, 690–699.

445 B. Kim, H. Seong, J. T. Song, K. Kwak, H. Song, Y. C. Tan, G. Park, D. Lee and J. Oh, *ACS Energy Lett.*, 2020, **5**, 749–757.

446 A. M. Yousef, W. M. El-Maghlany, Y. A. Eldrainy and A. Attia, *Energy*, 2018, **156**, 328–351.

447 S. Luo, Q. Zhang, L. Zhu, H. Lin, B. A. Kazanowska, C. M. Doherty, A. J. Hill, P. Gao and R. Guo, *Chem. Mater.*, 2018, **30**, 5322–5332.

448 A. Goeppert, M. Czaun, G. K. S. Prakash and G. A. Olah, *Energy Environ. Sci.*, 2012, **5**, 7833–7853.

449 Musk Foundation, \$100M Prize for Carbon Removal, 2021.

450 European Innovation Council, Fuel from the Sun: Artificial Photosynthesis.